UNIVERSITY OF BEIRA INTERIOR
Engineering

Assessing wood quality by spatial variability of transverse elastic properties within the stem: Case study on *P. pinaster* at the meso scale
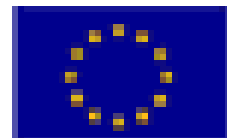
João Luís Esteves Pereira

Thesis for obtaining the degree of Doctor of Philosophy in
Mechanical Engineering
(3rd Cycle Studies)

Supervision: Doutor José Manuel Cardoso Xavier
Co-supervision: Prof. Doutor José Luís Penetra Cerveira Lousada
Co-supervision: Prof. Doutor Abílio Manuel Pereira da Silva

Covilhã, June 2013

"We may use wood with intelligence only if we understood wood",

Frank Lloyd Wright, 1928.

Aos meus Pais,

e

à Ana e à Margarida

Acknowledgements

Em primeiro lugar, quero deixar expresso o meu especial agradecimento ao Professor José Xavier, pela sua dedicação exclusiva e incansável na orientação deste trabalho. A sua competência e a sua persistência foram os atributos fundamentais para conseguirmos ultrapassar as diversas etapas desta maratona do conhecimento. Além disso, agradeço-lhe também pela sua amizade.

Quero agradecer também ao Professor José Morais e ao Professor José Lousada pelas suas superiores contribuições, indispensáveis ao desenvolvimento desta tese. Estou particularmente grato ao Professor José Morais pela sua sempre esclarecida e esclarecedora orientação nos momentos decisivos.

Ao Prof. Abílio Silva, agradeço a disponibilidade e prontidão com que sempre respondeu às minhas questões.

Agradeço com profunda emoção à minha família e amigos pelo apoio e pelo reforço positivo constante no que respeita ao presente e anteriores desafios que me fui propondo relativamente à minha formação académica. Em particular à Ana e à Margarida agradeço pela paciência e por terem sabido lidar com a privação da minha companhia e colaboração familiar.

A todos os colegas e amigos que de alguma forma contribuíram para este projeto, os meus sentidos agradecimentos pelo apoio e colaboração. Em particular, muito do alento veio da companhia e da amizade dos colegas Marcelo Oliveira e Fernando Silva.

Finalmente, queria agradecer ao Instituto Superior Politécnico de Viseu pelo suporte financeiro sem o qual teria sido mais difícil desenvolver este trabalho e também à Escola Superior de Tecnologia de Viseu pela disponibilização das instalações do LTIMM e ao Departamento de Engenharia de Madeiras pelo esforço na criação das condições possíveis, num contexto de dificuldades várias, para a realização deste trabalho.

Abstract

In this work the radial and longitudinal variations of maritime pine (*Pinus pinaster* Ait.) transverse elastic properties, within the stem, were investigated. Ring-oriented tensile tests through five radial positions and three height levels were carried out in 750 radial-tangential specimens, at the growth ring scale (meso scale). The strain fields over the gauge section were measured by digital image correlation. A suitable balance between accuracy and spatial resolution was achieved in order to reconstruct the gradient strain fields generated by the material heterogeneity at the growth rings level. A segmentation technique based on image processing and analysis was implemented in order to split each annual ring cross the region of interest, into three main tissue layers: resin channels, earlywood (EW) and latewood (LW). Accordingly, transverse elastic moduli of each EW and LW layers were then estimated by two different identification methods: the Anisotropic-based Method (AbM) and the Virtual Fields Method (VFM). The VFM was applied to directly identify in-situ Q_{11} and Q_{66} stiffness components associated to EW and LW. The AbM was applied to the global E_R and G_{RT} evaluation. These effective elastic properties were then used to infer the local ones as a function of mean density, combining the application of a micromechanical model (mixture law) and a unit cell model. The Q_{11} and Q_{66} LW/EW ratios were found in the order of 1.32 and 2.45, respectively. These ratios suggest a linear relationship between elastic properties and density. Furthermore, the spatial variability of the elastic properties was analysed and related to the meso structure heterogeneity, which was given namely by means of density measurements provided by X-ray microdensitometry. The results were found in good agreement, presenting significant correlations with density. Specifically, both effective E_R and G_{RT} were most often up to approximately 90% determined by mean density.

Keywords

Resumo

Neste trabalho investigou-se a variação radial e longitudinal das propriedades elásticas nas direções perpendiculares ao fio da madeira de pinho marítimo (*Pinus pinaster* Ait.) ao nível do tronco. Foram realizados ensaios de tracção na direcção radial utilizando 750 provetes com faces orientadas no plano radial-tangencial e à escala do anel de crescimento (escala meso). Os campos de deformação ocorridos na região de interesse foram medidos por correlação digital de imagem. Um equilíbrio entre a preçisão e a resolução espacial do método foi estabelecido, a fim de avaliar correctamente os gradientes dos campos de deformação gerados pela estrutura heterogénea do material à escala de observação. Uma técnica de segmentação baseada em processamento e análise de imagem foi implementada, no sentido de separar em cada anel as áreas correspondentes aos três tecidos principais: canais de resina, lenho inicial (LI) e lenho final (LF). Por conseguinte, as constantes elásticas transversais de cada tipo de lenho, dentro do anel, foram então estimadas através da aplicação de duas metodologias de identificação distintas: o método baseado na anisotropia (MbA) e o método dos campos virtuais (MCV).

O MCV foi aplicado na identificação directa das componentes da matriz de rigidez Q_{11} e Q_{66} associadas ao LI e ao LF e o MbA foi aplicado na identificação do módulo de elasticidade radial (E_R) e do módulo de corte (G_{RT}) globais. Estas propriedades elásticas efetivas foram depois utilizadas para inferir as respetivas propriedades locais do LI e do LF em função da densidade média, combinando a aplicação de um modelo micromecânico (lei de misturas) e um modelo celular unitário. Os rácios LF/LI obtidos para as componentes Q_{11} e Q_{66} foram 1.32 e 2.45, respetivamente, sugerindo a existência de uma relação linear entre as propriedades elásticas e a densidade. Por outro lado, foi analisada a variabilidade espacial das propriedades elásticas em função da heterogeneidade da meso estrutura, traduzida nomeadamente pelas medições de densidade que foram realizadas através de microdensitometria de raios-X. Os resultados demonstraram a existência de correlações significativas com a densidade. Concretamente, tanto o E_R como o G_{RT}

efetivos apresentaram determinações pela densidade muitas vezes na casa dos 90%.

Palavras-chave

Pinho marítimo, plano radial-tangencial, escala meso, ensaios de tração, correlação digital de imagem, método baseado na anisotropia, método dos campos virtuais, propriedades mecânicas, microdensitometria de raios-X.

Resumo Alargado

A madeira é um biomaterial de estrutura celular, com uma anatomia complexa e heterogénea. Esta heterogeneidade reflete-se em várias escalas de observação (Dinwoodie, 2000), incluindo a escala dos anéis de crescimento (escala meso) e a escala do tronco da árvore (escala macro). Na análise do comportamento mecânico da madeira é usual assumir-se um comportamento linear elástico ortotrópico, em que as direcções de simetria são a direcção longitudinal (L) das fibras, a direcção radial (R) dos anéis de crescimento e a direcção tangencial (T) aos anéis de crescimento. A identificação das propriedades mecânicas de um material fortemente heterogéneo e ortotrópico como a madeira, a um custo aceitável, coloca diversos problemas quer ao nível da mecânica experimental quer ao nível da modelação. Os métodos convencionais utilizados para a identificação das propriedades elásticas da madeira à escala macro baseiam-se em ensaios estaticamente determinados (nos quais o estado de tensão na região de interesse pode ser deduzido directamente a partir da força resultante aplicada) e em técnicas pontuais de medição dos deslocamentos ou deformações (Xavier et al., 2004). Esses métodos requerem a execução de vários ensaios independentes, cada um deles em amostras com um grande número de provetes, para a obtenção de resultados estatisticamente significativos. Esta é a abordagem adoptada na maioria dos trabalhos publicados sobre a variabilidade das propriedades elásticas da madeira à escala macro (Bao et al., 2001; Machado and Cruz, 2005). As limitações dos métodos convencionais podem em parte ser ultrapassadas recorrendo às técnicas óticas de medição dos campos cinemáticos (Grédiac, 2004). Entre elas conta-se a correlação digital de imagem (CDI), empregue por alguns autores para identificar as propriedades da madeira à escala macro e à escala meso (Dumail and Salmén, 2001; Farruggia and Perré, 2000; Ljungdahl et al., 2006; Shipsha and Berglund, 2007; Xavier, 2007). Porém, na esmagadora maioria destes trabalhos, os métodos óticos continuam associados a ensaios estaticamente determinados, os quais, além de não tirarem partido do potencial desses métodos de campo, são de difícil aplicação à madeira. Na verdade, a ortotropia da madeira e a variabilidade da sua estrutura anatómica, tornam difícil a realização de ensaios onde o estado de tensão seja acessível a partir das condições de fronteira, por via analítica (Keunecke et al., 2008). Aliás, pelas razões indicadas, as próprias condições de fronteira experimentais não são conhecidas a não ser aproximadamente. São escassos os trabalhos relativos aos métodos de identificação das propriedades elásticas da madeira a

partir de ensaios estaticamente indeterminados (Jernkvist and Thuvander, 2001; Xavier et al., 2007, 2009). Desde o trabalho pioneiro de Grédiac (1989), tem vindo a ser desenvolvido um método inverso, conhecido por Método dos Campos Virtuais (MCV), o qual só recentemente foi aplicado pela primeira vez à madeira (Xavier et al., 2007, 2009). O MCV foi também recentemente usado para determinar campos de propriedades em placas de materiais compósitos (Kim et al., 2007) e também em painéis de fibras de média densidade (Xavier et al., (in press)). A extensão do MCV na identificação de propriedades elásticas locais da madeira à escala meso será um contributo significativo para a compreensão da origem anatómica da variabilidade das propriedades da madeira, às escalas meso e macro. Além disso, o conhecimento das propriedades elásticas à escala meso é essencial para muitas áreas da mecânica da madeira, por exemplo, para o estudo do comportamento da madeira em fractura (de Moura et al., 2008; Thuvander et al., 2000), para análise do comportamento das ligações de peças de madeira por cavilha (Santos et al., 2009; Zink-Sharp et al., 1999) e dos processos tecnológicos de transformação da madeira (Holmberg et al., 1999).

Para caracterizar completamente o comportamento mecânico da madeira é necessário conhecer os modelos de variação dessas propriedades no referencial de simetria material (referencial LRT). Em particular, o estudo desses modelos no plano RT revela-se de redobrada importância já que é nele que se observam as principais fontes de variabilidade oriundas da estrutura do material e que por sua vez desempenham um papel preponderante no seu comportamento em fractura, no desempenho das ligações e também nas operações de transformação da madeira. Os ensaios mecânicos são um meio de obter essa informação, contudo, não só por motivos de economia mas também de rapidez e funcionalidade, importa evoluir para modelos de ensaio que permitam obter da mesma resposta mecânica o máximo de informação. De acordo com Jeong (2008), os métodos de identificação das propriedades mecânicas da madeira à escala macro podem ser melhorados se tiverem em linha de conta as características do material ao nível do anel de crescimento. É neste contexto que se insere esta tese, cujo objectivo se prende com a caracterização da madeira de pinho marítimo (*P. pinaster*) no plano transverso (RT) e à escala dos anéis de crescimento (escala meso).

O presente trabalho é apresentado ao longo de vários Capítulos, cujos temas se resumem em seguida. O Capítulo 1, está dividido em três secções, sendo que na primeira secção, é apresentada uma revisão sobre a estrutura anatómica da madeira, em particular da madeira das espécies resinosas, grupo ao qual pertence a madeira de *P. pinaster*, aqui em estudo. Escolheu-se esta espécie por ser a mais relevante no nosso País, tanto do ponto de vista comercial como social. De acordo com dados de 2010 (AIFF, 2010), o mercado do pinho, em Portugal, representa 62% do VAB da Fileira Florestal, com um volume de vendas de quase 3500 milhões de euros, dos quais 927 milhões de euros resultam das exportações e é responsável por cerca de 65000 empregos industriais diretos, envolvendo

89% das empresas do sector. Por outro lado, a madeira de *P. pinaster* é o suporte de grande parte das indústrias da fileira florestal nomeadamente da indústria de painéis, de segmentos específicos da indústria de celulose, das indústrias de paletes e de um vasto universo de pequenas e médias empresas de exploração florestal e indústrias de serração. A estrutura anatómica e o comportamento mecânico da madeira podem ser analisados de uma forma hierarquizada e a diferentes escalas de observação. Neste trabalho, a madeira será analisada à escala meso. A esta escala, a madeira é modelada como um sólido contínuo e heterogéneo, composto por camadas alternadas de lenho inicial (LI) formado na Primavera e lenho final (LF) formado no Verão. No LI, as células apresentam paredes celulares finas e amplos lumens, enquanto no LF, as paredes são mais espessas e os lumens escassos. Ao nível do anel de crescimento, as propriedades mecânicas acompanharão essa variação (Bigorgne, 2011). Na segunda secção, faz-se uma revisão sobre os ensaios mecânicos, de tração, de compressão e de corte, já aplicados à madeira, em trabalhos de caracterização das propriedades elásticas nas direções perpendiculares ao fio. Finaliza-se este capítulo, com uma revisão do ponto de vista da variabilidade espacial da estrutura anatómica da madeira e das suas propriedades físicas e mecânicas, procurando evidenciar as eventuais relações entre as propriedades e a estrutura bem como o seu contributo para a qualidade da madeira.

O Capítulo 2 é dedicado, por um lado, à análise do estado da arte no que refere aos métodos de identificação inversa, e, por outro lado, às técnicas óticas para medições de campo, com especial relevo para as técnicas não interferométricas, e em particular a correlação digital de imagem, utilizada neste trabalho. A identificação dos parâmetros materiais que figuram nas equações constitutivas é efetuada por via experimental através da aplicação de ensaios mecânicos adequados (Hodgkinson, 2000). O problema inverso na mecânica experimental consiste assim na caracterização dos parâmetros constitutivos desconhecidos assumindo-se o conhecimento da geometria da amostra, das condições de fronteira (ou, mais precisamente, das forças e os momentos resultantes) e das deformações (ou dos deslocamentos). Os ensaios normalizados são convencionalmente realizados de modo a alcançar um estado de tensão-deformação homogéneo na região de interesse da amostra onde são realizadas as medições. Convenientemente, este método leva a soluções baseadas em equações explícitas que relacionam os parâmetros desconhecidos com a força de carregamento e as deformações medidas (testes estaticamente determinados). Neste caso, os dispositivos pontuais, tais como extensómetros, são usualmente empregues na medição do estado de deformação do material. No entanto, na prática, a aplicação destes ensaios pode revelar-se difícil devido, por exemplo, à ocorrência de efeitos localizados, especialmente para materiais anisotrópicos e heterogéneos (Pierron et al., 1998). Além disso, vários métodos de ensaio independentes são necessários para lidar com o comportamento não isotrópico (Guitard, 1987), o que, na prática, exige um esforço adicional em termos de tempo e de custo. O desenvolvimento recente das técnicas óticas de campo

possibilitou uma nova abordagem ao nível dos ensaios de caracterização mecânica dos materiais (Grédiac, 2004). O princípio de base desta nova abordagem assume que na região de interesse (ROI) são gerados campos de deformação heterogéneos e complexos, de tal modo que vários parâmetros materiais estão embebidos na resposta mecânica do material (ensaios estaticamente indeterminados). Recorrendo a uma estratégia adequada de identificação inversa, todos os parâmetros envolvidos poderão ser convenientemente determinados. Na literatura, existem apenas alguns métodos de identificação propostos (Avril et al., 2008). A abordagem mais usual é baseada no método de actualização do modelo de elementos finitos (FEMUM). Este método consiste na construção de um modelo de elementos finitos do ensaio mecânico, considerando uma função objetivo com a diferença entre os resultados numéricos e experimentais (deslocamento ou deformação) sobre a ROI. A minimização desta função objetivo em relação aos parâmetros desconhecidos (variáveis de projeto), iterativamente atualizadas no modelo, proporciona a solução para o problema. Este método é flexível e não necessita propriamente de medições de campo. No entanto, uma vez que é iterativo, pode ser demorado e a convergência dependente da estimativa inicial das variáveis. Além disso, requer o conhecimento adequado das condições de fronteira a impor no modelo para evitar erros sistemáticos nos valores das variáveis identificadas. A presença de ruído nas medições também afetará a robustez deste método iterativo. Para ultrapassar as desvantagens associadas ao FEMUM, abordagens alternativas têm sido propostas. Entre elas, existem, por exemplo, o método baseado na anisotropia (MbA) (Majano-Majano et al., 2012), e o MCV (Pierron and Grédiac, 2012). Nesse sentido é proposto neste capítulo um ensaio de tracção em provetes com curvatura dos anéis variável para a caracterização, por um lado, das componentes ortotrópicas do *P. pinaster* no plano RT, e, por outro lado, das suas propriedades locais levando em consideração a heterogeneidade da própria estrutura da madeira à escala de observação. Este será o ensaio de base proposto neste trabalho. Para este ensaio específico, foram desenvolvidos dois métodos de identificação: o MbA e o MCV. Os princípios de base destes métodos de identificação são também descritos em detalhe neste capítulo.

O Capítulo 3 é dedicado à descrição do trabalho experimental, desde a seleção das árvores e dos toros, passando pelo desdobramento em tábuas, sua secagem e condicionamento até à obtenção dos provetes e posterior aplicação do padrão de speckle, necessário para uma adequada utilização da técnica de CDI. Apresenta-se também o procedimento inerente aos trabalhos de medição da densidade através da microdensitometria de raios X, bem como o *set-up* experimental envolvendo os ensaios mecânicos e a aquisição das imagens para a medição das deformações através da CDI. Os ensaios normalizados para a caracterização mecânica da madeira baseiam-se em provetes com geometria simples e em situações de carregamento elementares com base em estados de tensão/deformação simples ou homogéneos na zona de medição, para os quais existem equações explícitas para a identificação das propriedades. Pelo contrário, neste trabalho, é proposto um

método baseado na aplicação de um único ensaio de tração em provetes com diferentes orientações dos anéis, para identificar todas as propriedades, no plano transverso, definido pelas direções ortotrópicas R e T: E_R, E_T, ν_{RT} e G_{RT} onde E, ν e G se referem ao módulo de *Young*, coeficiente de *Poisson* e módulo de corte, respetivamente. Um esquema representativo da geometria do provete é apresentado na figura 3.1. O provete consiste num paralelepípedo com as dimensões nominais de 50(R)×5(T)×2(L) mm. Adotou-se esta solução que permite tirar partido de uma determinada orientação dos anéis em relação ao eixo de carregamento, definida por um ângulo médio θ, conforme ilustrado na figura 3.1. A madeira utilizada neste trabalho foi obtida de cinco árvores de *P. pinaster* com idades compreendidas entre os 65 e os 70 anos, provenientes de um povoamento não ordenado, localizado em Orgens, no concelho de Viseu (região centro-norte de Portugal). A seleção das árvores foi efetuada com base em aspetos macroscópicos essenciais da morfologia do fuste, como sejam a ausência de defeitos de conformação, a ausência de doenças, a maior linearidade vertical e a menor conicidade do fuste (Carvalho, 1996). Após o abate, as árvores foram seccionadas em diversos toros, tendo sido selecionados para este trabalho, apenas os cinco toros basais, com 2.8 metros de comprimento, por serem considerados os que fornecem madeira com melhor qualidade na árvore. Os toros foram desfiados em pranchas com 40 mm de espessura, que depois de devidamente empilhadas de forma a reconstituir cada toro (Fig. 3.2), foram submetidas a um processo de secagem natural, monitorizado através de medições regulares com um higrómetro GANN® HT 85T, até atingirem um teor em água entre 10 e 12%, sendo em seguida armazenadas no Laboratório de Tecnologia das Indústrias de Madeiras e Mobiliário da Escola Superior de Tecnologia e Gestão de Viseu, onde se procedeu á fabricação dos provetes. Para o trabalho experimental, foram fabricados 15 provetes para as medições de densidade com dimensões nominais de 3(L) x 5(T) mm e comprimento igual ao raio da prancha central, correspondendo a 5 árvores e 3 posições em altura para cada uma, e 750 provetes para os ensaios mecânicos, correspondendo a 5 árvores, 3 posições em altura, 5 posições radiais e 10 provetes para cada posição radial. Os ensaios mecânicos foram realizados numa máquina Instron® 5848 Microtester, a uma velocidade do travessão de $v = 0.2$ mm.min^{-1}. Considerando a distância entre amarras de $l_0 = 30$ mm, os ensaios foram executados a uma taxa de deformação de $\dot{\varepsilon} = v/l_0 = 1.1 \times 10^{-4}$ s^{-1}, para a qual o carregamento foi aplicado de forma contínua durante um período de tempo inferior a 3 minutos para evitar os efeitos viscoelásticos. A força aplicada foi medida por meio de uma célula de carga de 2 kN. Ao *set-up* usual do ensaio de tração, foi associado um sistema independente de aquisição e correlação de imagem formando no seu conjunto o *set-up* fotomecânico (Fig. 3.12). A aquisição da imagem durante o ensaio foi feita com um sistema ótico constituído por uma camara CCD (*Charge Coupled Device*) de 8 bits Baumer Optronic® FWX20 e uma lente telecêntrica Opto-Engineering TC 2309, cujas características são resumidas nas tabelas 3.1 e 3.2, respetivamente. Para a correlação de imagem utilizou-se o

código comercial ARAMIS® DIC-2D v6.0.2 da GOM mbH (ARAMIS; Xavier et al., 2012). No que respeita à densidade, as medições foram realizadas no Laboratório de Produtos Florestais do Departamento Florestal, da UTAD, de acordo com o procedimento descrito por (Lousada, 2000), utilizando um microdensitómetro de duplo feixe JOYCE LOEBEL® MK3 (Fig. 3.7) equipado com um gerador de raios-X SEIFERT® ISO-Debyeflex. As principais vantagens desta técnica de medição são, a elevada sensibilidade do fotomultiplicador do microdensitómetro, a elevada capacidade de resolução (de 10 a 200 valores por mm), a velocidade de processamento (3 cm/min) e o registo da informação numa pelicula radiofotográfica (Kodak® Industrex CX) que torna possível a realização de leituras as vezes que forem necessárias. A variação da densidade média na madeira das espécies resinosas (0.4 - 0.7 g.cm^{-3}) não é tão elevada como nas espécies de folhosas (0.2 - 1.2 g.cm^{-3}). Apesar desta enorme variabilidade, à parede celular das fibras é habitualmente atribuído um valor constante de 1.5 (Skaar, 1989) ou 1.53 (Tsoumis and Passialis, 1977) dependendo dos autores. Por isso, as diferenças referidas, apenas podem ser atribudas às diferenças verificadas nas proporções parede/lúmen de cada espécie. Para o *P. pinaster*, a variação da densidade média dentro do anel é considerada habitualmente entre 0.4 e 0.9 g.cm^{-3} (Lousada, 2000) em resultado das diferenças entre as camadas de LI e LF, nomeadamente o rácio entre o volume da parede celular e o volume total da célula.

O Capítulo 4 é dedicado, numa primeira fase, à identificação das propriedades elásticas perpendiculares ao fio e posteriormente à apresentação e discussão da anàlise da variabilidade dos parâmetros da densidade e das propriedades elàsticas do *P. pinaster* ao nível do tronco, quer em altura, quer em largura na direção radial. Além disso procura-se também identificar e descrever os eventuais padrões de correlação existentes entre eles. No que respeita à identificação das propriedades elásticas, neste capítulo aplica-se o MbA. Este método baseia-se na teoria da elasticidade anisotrópica e permite – assumindo um estado plano de tensão, que o material é contínuo, homogéneo e governado por um comportamento linear elástico ortotrópico – obter as componentes da matriz de flexibilidade explicitamente através das condições de fronteira determinadas diretamente dos ensaios experimentais. Uma vez identificadas as propriedades globais, utiliza-se uma lei de misturas baseada em modelos micromecânicos, desenvolvidos para os materiais compósitos, para estimar as constantes elásticas da madeira em função das propriedades elásticas dos constituintes individuais (Jones, 1999), que complementada com modelos celulares unitários relacionando as propriedades elásticas dos constituintes individuais com a densidade (Gibson and Ashby, 1997), nos permitem obter as propriedades mecânicas do LI e do LF. Na sequência da revisão realizada no primeiro capítulo e em resultado do próprio trabalho até aqui descrito, fica claro que é extremamente relevante o conhecimento dos padrões de variação das propriedades físicas e mecânicas da madeira, quando se perspetiva o desenvolvimento de qualquer estudo relacionado com a qualidade da madeira. No que respeita à densidade, e de acordo com Lousada (2000), existem muitas referências acerca

dos seus padrões de variação relativamente às espécies resinosas e em particular ao *P. pinaster*. De um modo geral, todas elas indicam que há mais variação dentro da árvore do que entre árvores. Normalmente os estudos sobre a variabilidade da densidade são realizados de acordo com três modelos de variação principais: (i) como varia a densidade radialmente ao nível do anel com base nas transições LI-LF, (ii) como varia a densidade radialmente de anel para anel desde a medula até ao câmbio e (iii) como varia a densidade longitudinalmente, considerando diferentes níveis de altura na árvore. Tendo em conta que a densidade da parede celular é constante (aproximadamente igual a 1.5 g.cm^{-3}) e que as variações da densidade são devidas, quase exclusivamente, às diferenças da proporção parede/lúmen, ou seja, à maior ou menor quantidade de parede celular presente num determinado volume de madeira, espera-se que as propriedades mecânicas, na condição de outros fatores permanecerem constantes, apresentem padrões de variação idênticos aos verificados para a densidade (Lousada, 2000; Zobel and Buijtenen, 1989).

As propriedades elásticas dos constituintes da madeira ao nível do anel de crescimento constituem informação fundamental para aplicação em outros estudos como, no comportamento da madeira em fratura nas direções perpendiculares ao fio da madeira (de Moura et al., 2008; Thuvander et al., 2000), no comportamento mecânico das ligações coladas na madeira (Santos et al., 2009; Zink-Sharp et al., 1999), nos fenómenos de formação e propagação de fendas em obras de arte quando expostas a grande variação de humidade (Dureisseix et al., 2011) e nos processos de maquinação da madeira (Holmberg et al., 1999). No entanto, a identificação das propriedades à escala meso coloca diversas dificuldades. As abordagens tradicionais baseiam-se na aplicação de ensaios estaticamente determinados, que por sua vez utilizam pequenas amostras de cada camada individual de LI e de LF (Cramer et al., 2005; Farruggia and Perré, 2000). Para aceder à variação espacial das propriedades elásticas ou para a sua representatividade estatística, estas abordagens requerem uma enorme quantidade de amostras. Esta limitação pode em parte ser ultrapassada utilizando uma abordagem diferente, baseada em ensaios mecânicos estaticamente indeterminados, a partir dos quais vários parâmetros podem ser identificados a partir de um único ensaio mecânico (Jernkvist and Thuvander, 2001; Xavier et al., 2007, 2009). Esta metodologia tira partido da cinemática das medições de campo (*i.e.*, deslocamento ou deformação) fornecidas por uma técnica ótica adequada em associação com um método inverso de identificação. Assim, no capitulo 5, apresenta-se a aplicação do método dos campos virtuais para um conjunto de dez provetes, correspondendo ao nível da altura do peito e à posição radial mais próxima do câmbio, no sentido de procurar validar esta metodologia.

Por fim apresentam-se as principais conclusões retiradas ao longo de todo o trabalho, e apresentam-se sugestões de trabalho complementar a desenvolver futuramente, muitas delas em consequência do enquadramento temporal em que um trabalho desta natureza tem que ser executado.

References

AIFF. Caracterização da fileira florestal 2010. Technical report, AIFF, 2010.

ARAMIS. *Commercial software*. GOM (www.gom.com).

S. Avril, M. Bonnet, A.-S. Bretelle, M. Grédiac, F. Hild, P. Ienny, F. Latourte, D. Lemosse, S. Pagano, E. Pagnacco, and F. Pierron. Overview of identification methods of mechanical parameters based on full-field measurements. *Experimental Mechanics*, 48(4): 381–402, 2008.

F. C. Bao, Z. H. Jiang, X. M. Jiang, X. X. Lu, X. Q. Luo, and S. Y. Zhang. Differences in wood properties between juvenile wood and mature wood in10 species grown in china. *Wood Science & Technology*, 35:363–375, 2001.

L. Bigorgne. *Mécanique et mécanismes de rupture dans le plan transverse du bois résineux*. PhD thesis, Institute National des Sciences Appliquées de Lyon, 2011.

A. Carvalho. *Madeiras Portuguesas: estrutura anatómica, propriedades, utilizações*. Instituto Florestal, 1996.

S. Cramer, D. Kretschmann, R. Lakes, and T. Schmidt. Earlywood and latewood elastic properties in loblolly pine. *Holzforschung*, 59(531-538):5, 2005.

M.F.S.F. de Moura, J.L. Morais, and N.M.M. Dourado. A new data reduction scheme for mode i wood fracture characterization using the dcb test. *Engineering Fracture Mechanics*, 75(13):3852–3865, 2008.

J.M. Dinwoodie. *Timber: Its nature and behaviour*. Van Nostrand Reinhold, 2000.

J.-F. Dumail and L. Salmén. Intra-ring variations in the rolling shear modulus of spruce wood. *Holzforschung*, 55(5):549–553, 2001.

D. Dureisseix, J. Colmars, A. Baldit, F. Morestin, and H. Maigre. Follow-up of a panel restoration procedure through image correlation and finite element modeling. *International Journal of Solids and Structures*, 48(6):1024–1033, 2011.

F. Farruggia and P. Perré. Microscopic tensile tests in the transverse plane of earlywood and latewood parts of spruce. *Wood Science and Technology*, 34(2):65–82, 2000.

L.J. Gibson and M.F. Ashby. *Cellular solids. Structure and properties*. Cambridge University Press, 1997.

M. Grédiac. Principe des travaux virtuels et identification. *Comptes Rendus de l'Académie des Sciences*, 309(2):1–5, 1989.

M. Grédiac. The use of full-field measurement methods in composite material characterization: Interest and limitations. *Composites Part A: Applied Science and Manufacturing*, 35(7-8):751–761, 2004.

D. Guitard. *Mécanique du matériau bois et composites*. Cepaduès-Editions, Collection Nabla, 1987.

J.M. Hodgkinson. *Mechanical testing of advanced fibre composites*. Cambridge, Woodhead Publishing Limited, 2000.

S. Holmberg, K. Persson, and H. Petersson. Nonlinear mechanical behaviour and analysis of wood and fibre materials. *Computers and Structures*, 72(4-5):459–480, 1999.

Gi Young Jeong. *Tensile properties of Loblolly pine strands using digital image correlation and stochastic finite element method*. PhD thesis, Faculty of Virginia Polytechnic Institute & State University, 2008.

L.O. Jernkvist and F. Thuvander. Experimental determination of stiffness variation across growth rings in Picea abies. *Holzforschung*, 55(3):309–317, 2001.

R. M. Jones. *Mechanics of composite materials*. Taylor and Francis, 2nd edition, 1999.

D. Keunecke, S. Hering, and P. Niemz. Three-dimensional elastic behaviour of common yew and norway spruce. *Wood Science and Technology*, 42(8):633–647, 2008.

J.-H. Kim, F. Pierron, M.R. Wisnom, and K. Syed-Muhamad. Identification of the local stiffness reduction of a damaged composite plate using the virtual fields method. *Composites Part A: Applied Science and Manufacturing*, 38(9):2065–2075, 2007.

J. Ljungdahl, L.A. Berglund, and M. Burman. Transverse anisotropy of compressive failure in european oak - A digital speckle photography study. *Holzforschung*, 60(2): 190–195, 2006.

J.L. Lousada. *Variação fenotípica e genética em características estruturais na madeira de Pinus pinaster Ait.* PhD thesis, Universidade de Trás-os-Montes e Alto Douro, Vila Real, Portugal, 2000.

J.S. Machado and H.P. Cruz. Within stem variation of maritime pine timber mechanical properties. *Holz als Roh - und Werkstoff*, 63(2):154–159, 2005.

A. Majano-Majano, J. Fernandez-Cabo, S. Hoheisel, and M. Klein. A test method for characterizing clear wood using a single specimen. *Experimental Mechanics*, 52:1079–1096, 2012.

F. Pierron and M. Grédiac. *The Virtual Fields Method*. Springer New York, 2012.

F. Pierron, E. Alloba, Y. Surrel, and A. Vautrin. Whole-field assessment of the effects of boundary conditions on the strain field in off-axis tensile testing of unidirectional composites. *Composites Science and Technology*, 58(12):1939–1947, 1998.

C.L. Santos, A.M.P. de Jesus, J.J.L. Morais, and J.L.P.C. Lousada. Quasi-static mechanical behaviour of a double-shear single dowel wood connection. *Construction and Building Materials*, 23(1):171–182, 2009. ISSN 0950-0618. doi: 10.1016/j.conbuildmat.2008.01.005.

A. Shipsha and L.A. Berglund. Shear coupling effects on stress and strain distributions in wood subjected to transverse compression. *Composites Science and Technology*, 67 (7-8):1362–1369, 2007.

C. Skaar. Shrinking and swelling. In A.P. Schniewind, editor, *Concise encyclopedia of wood and wood-based materials*, pages 243–245. Pergamon Press, 1989.

F. Thuvander, L.O. Jernkvist, and J. Gunnars. Influence of repetitive stiffness variation on crack growth behaviour in wood. *Journal of Materials Science*, 35(24):6259–6266, 2000.

G. Tsoumis and C. Passialis. Effect of growth rate and abnormal growth on wood substance and cell wall density. *Wood Science and Technology*, 1977.

J. Xavier. *Characterisation of the wood stiffness variability within the stem by the virtual fields method: application to P. pinaster in the LR plane.* PhD thesis, Art et Métiers ParisTech Châlons-en-Champagne, 2007.

J. Xavier, S. Avril, F. Pierron, and J. Morais. Novel experimental approach for longitudinal-radial stiffness characterisation of clear wood by a single test. *Holzforschung*, 61(5):573–581, 2007.

J. Xavier, S. Avril, F. Pierron, and J. Morais. Variation of transverse and shear stiffness properties of wood in a tree. *Composites Part A: Applied Science and Manufacturing*, 40:1953–1960, 2009. Special Issue: CompTest 2008.

J. Xavier, A.M.P. de Jesus, J.J.L. Morais, and J.M.T. Pinto. Stereovision measurements on evaluating the modulus of elasticity of wood by compression tests parallel to the grain. *Construction and Building Materials*, 26(1):207–215, 2012.

J. Xavier, U. Belini, F. Pierron, J. Morais, J. Lousada, and M. Tomazello. Characterisation of the bending stiffness components of mdf panels from full-field slope measurements. *Wood Science and Technology*, pages 1–19, (in press).

J.C. Xavier, N. Garrido, J. Oliveira, J. Morais, P. Camanho, and F. Pierron. A comparison between the Iosipescu and off-axis shear test methods for the characterization of *pinus pinaster* Ait. *Composites Part A: Applied Science and Manufacturing*, 35(7-8):827–840, 2004.

A. Zink-Sharp, J.S. Stelmokas, and H. Gu. Effects of wood anatomy on the mechanical behavior of single-bolted connections. *Wood and Fiber Science*, 31(3):249–263, 1999.

B.J. Zobel and J.P. Van Buijtenen. *Wood variation: Its causes and control.* Springer Series in Wood Science, Ed: Timell, T.E., Springer-Verlag, 1989.

Table of Contents

List of Figures

4   Identification of transverse elastic properties of *P. pinaster* by the anisotropic-based method

C Elastic properties-Density relationships

List of Tables

List of Abbreviations

AbM	Anisotropic-based method
AFN	Autoridade Florestal Nacional
CDI	Correlação digital de imagem
DBH	Diameter at breast height
DIC	Digital Image Correlation
D_{EW}	Earlywood mean density
D_{LW}	Latewood mean density
D_{max}	Annual ring maximum density
D_{mean}	Annual ring mean density
D_{min}	Annual ring minimum density
EW_W	Earlywood width
FEA	Finite element analysis
FEMUM	Finite element model updating method
HI	Heterogeneity index
IFN	Inventário Florestal Nacional
LTIMM	Laboratório de Tecnologia das Indústrias de Madeiras e Mobiliário
LW_W	Latewood width
$\%LW$	Latewood percentage
MbA	Método baseado na anisotropia
MCV	Método dos campos virtuais
MLS	Moving least squares
MPM	Material point method
NURBS	Non-uniform rational basis spline
PVW	Principle of virtual work
$Ring_W$	Annual ring width
SHPB	Split Hopkinson pressure bar
VAB	Valor acrescentado bruto
VFM	Virtual fields method

Introduction

Within Europe, there has been an increase in the use of wood for structural purposes, namely in the form of beams, pillars, joists, crossbars and laths. However, it is still very common to classify timber, particularly the Portuguese pine, with poor quality in terms of strength and durability or with less noble qualities, highlighting the fact that the spread of timber structures is conditioned on the assurance of their competitiveness with regard to other materials, especially by quality grading. This purpose of structural timber valuation can be achieved by increasing our knowledge on the mechanical behaviour of wood, with the elaboration of projects adequately grounded in concepts of structural safety and with a building system that meets the quality criteria, involving raw materials and manpower already adopted for steelwork and reinforced concrete.

As a natural composite material formed by trees, wood has a hierarchical structure which can be analysed and modelled at several length scales, starting from nano scale of chemical constituents up to the stem (Smith et al., 2003). Moreover, it has a complex and heterogeneous structure, resulting from the ability of the tree to change its morphology in response to variations in external forces acting during the growing process (Niklas, 1992). Thus, excepting for some simplified hypothesis (*e.g.* at the macro scale, clear wood has been modelled as a continuous, orthotropic and homogeneous material), wood can be regarded as a heterogeneous and anisotropic material. This means that the mechanical properties of wood can vary spatially within and among trees and along the direction of solicitation. Therefore, for wood quality assessment with regard to end-user applications in a politic of better preservation and management of the available natural resources, both bulk and spatial variation of mechanical properties of wood species within and among trees must be accurately characterised by suitable approaches. However, this characterisation poses several difficulties due to the inherent hierarchy, anisotropy and heterogeneity of wood. From an experimental point of view, for instance, conventional apparatus such as strain gauges for punctual strain measurements and standard mechanical test methods (based on homogeneous stress/strain fields) are most often very difficult to implement (*e.g.*, simplified and based assumptions difficult to guarantee in practice), expensive and very time consuming.

On the transverse cross-section of a softwood tree, concentric annual rings can be observed formed by the cambium at each growing season. At each point, two orthotropic

directions can be defined: the radial (R) and the tangential (T) directions, perpendicular and parallel to the growth rings structure, respectively. The anisotropy of wood in the radial-tangential (RT) plane has been explained by the reinforcement added by wood ray cells oriented radially across the stem (Ljungdahl et al., 2006), and by the more regular arrangement of cells along the radial direction than in the tangential one (Persson, 2000). At the stem level, the width and the number of the growth rings varies as a function of the tree growing rate, which is mostly controlled by external environment factors during growth. Moreover, the stem is usually split into juvenile and mature woods, regarding the cambial age in which wood cells have been formed. Although not yet fully understood, these aspects have been pointed out to justify the two significant radial variations of wood properties that can be observed in the transverse plane (Machado and Cruz, 2005; Xavier et al., 2009). At the magnification of the growth rings (1-10 mm), the cellular structure of wood can be resolved. It consists of a cellular tissue, aligned along the longitudinal direction of the stem. At this level, an individual annual growth ring can be assumed consisting of two principal layers called earlywood (springwood) and latewood (summerwood). The cells in the earlywood are characterised by thin walls and large diameters, whilst the latewood cells are smaller in diameter and have thick walls. Although this structural differentiation can support the local variability on density and mechanical properties (Hassel et al., 2009), the bulk properties of the wood cell itself remains roughly constant (Dinwoodie, 2000). The mechanical characterisation of wood at the growth ring scale is relevant because in many applications its behaviour is rather affected by the local heterogeneity verified at this level of observation. Such applications can include fracture mechanics (Dourado et al., 2008; Thuvander et al., 2000), the mechanical behaviour of bolted wood connections (Santos et al., 2009; Zink-Sharp et al., 1999), crack formation and propagation on culture heritage objects (*e.g.*, paintings) subjected to critical moisture content variations (Dureisseix et al., 2011), and wood transformation processes (Holmberg et al., 1999).

Full-field optical methods of displacement or strain measurement have become very useful tools in experimental solid mechanics. According to the physical phenomenon involved in the measurement, these methods can be sorted into white-light techniques (*e.g.*, digital image correlation and grid methods) and interferometric techniques (*e.g.*, speckle and moiré interferometry and shearography) (Grédiac, 2004). By comparison with more conventional punctual techniques (*e.g.*, strain gauges or extensometers) these methods have some important advantages: (*i*) they provide full-field data so gradient fields can be conveniently assessed; (*ii*) they are contact-free (eventually, they can require some preparation of the surface of interest). In parallel, novel identification methods have been developed in order to take advantage of the full-field measurements. A review of these methods can be found in (Avril et al., 2008). A novel application consists in measuring several parameters from a single test configuration. This integrated numerical-

experimental approach seems quite promising to wood mechanics because of its anisotropy and inherent variability (Jernkvist and Thuvander, 2001; Xavier et al., 2007, 2009).

In this framework, this thesis aims to effectively characterise the mechanical behaviour of wood in the RT plan and at growth rings scale (meso scale). In this work full-field measurements provided by digital image correlation (DIC) were coupled with identification strategies for assessing the radial variation of wood transverse elastic properties at the meso scale. Tensile tests at the tissue level were carried out on *P. pinaster*. Several tests were performed on samples cut at different radial positions within the stem and at three vertical locations. Five different trees were tested seeking representativeness of the spatial variation patterns within the stem.

From the point of view of its organization, this work is presented along several chapters divided into sections. The first chapter is divided into three sections, with the first one presenting a review of wood anatomical structure, especially of coniferous species, the group were the timber of *P. pinaster* here studied belongs. In the second section, a review on the tensile, compression and shear mechanical tests, already applied to wood in the transverse plane is presented. To end this chapter, spatial variability of wood anatomical structure and its physical and mechanical properties is revised, looking for evidence of any connections between the properties and structure as well as its contribution to wood quality definition. Chapter two is dedicated, on the one hand, to the analysis of identification methods applied to wood on the transverse plane at the meso scale, and, on the other hand, to full-field optical techniques with emphasis on non-interferometric techniques, including DIC, used in this work. On the third chapter, the experimental work is described in details. It starts by reporting the tasks since trees and logs selection, to the boards sawing, drying and conditioning procedure, until specimens manufacture. X-ray microdensitometry procedure for density measurements are then presented. A detailed description of the DIC technique applied to wood is then presented, with focus on the speckle pattern painting and selection of the optical devices and measuring parameters. To end with, the mechanical test and experimental setup is reported. Chapter four is dedicated, on a first step, to the transverse elastic properties identification by de anisotropic-based method on a global approach, followed by the local properties estimation based on a micromechanical model (mixtures law) coupled with a unit cell model with the respective earlywood and latewood mean density contribution. Besides, the spatial variation of both density and elastic properties is analysed and their relationships discussed. The identification of local transverse stiffness components within the annual rings by the virtual fields method is presented for a case study in Chapter five. Results are compared with the ones estimated on chapter four, based on the global identification. Finally, major conclusions throughout the work are drawn and perspectives for future work are outlined.

References

S. Avril, M. Bonnet, A.-S. Bretelle, M. Grédiac, F. Hild, P. Ienny, F. Latourte, D. Lemosse, S. Pagano, E. Pagnacco, and F. Pierron. Overview of identification methods of mechanical parameters based on full-field measurements. *Experimental Mechanics*, 48(4): 381–402, 2008.

J.M. Dinwoodie. *Timber: Its nature and behaviour*. Van Nostrand Reinhold, 2000.

N. Dourado, S. Morel, M.F.S.F. de Moura, G. Valentin, and J. Morais. Comparison of fracture properties of two wood species through cohesive crack simulations. *Composites Part A: Applied Science and Manufacturing*, 39(2):415–427, 2008.

D. Dureisseix, J. Colmars, A. Baldit, F. Morestin, and H. Maigre. Follow-up of a panel restoration procedure through image correlation and finite element modeling. *International Journal of Solids and Structures*, 48(6):1024–1033, 2011.

M. Grédiac. The use of full-field measurement methods in composite material characterization: Interest and limitations. *Composites Part A: Applied Science and Manufacturing*, 35(7-8):751–761, 2004.

B.I. Hassel, C.S. Modén, and L.A. Berglund. Functional gradient effects explain the low transverse shear modulus in spruce - full-field strain data and a micromechanics model. *Composites Science and Technology*, 69(14):2491–2496, 2009.

S. Holmberg, K. Persson, and H. Petersson. Nonlinear mechanical behaviour and analysis of wood and fibre materials. *Computers and Structures*, 72(4-5):459–480, 1999.

L.O. Jernkvist and F. Thuvander. Experimental determination of stiffness variation across growth rings in Picea abies. *Holzforschung*, 55(3):309–317, 2001.

J. Ljungdahl, L.A. Berglund, and M. Burman. Transverse anisotropy of compressive failure in european oak - A digital speckle photography study. *Holzforschung*, 60(2): 190–195, 2006.

J.S. Machado and H.P. Cruz. Within stem variation of maritime pine timber mechanical properties. *Holz als Roh - und Werkstoff*, 63(2):154–159, 2005.

K.J. Niklas. *Plant Biomechanics: An Engineering Approach to Plant Form and Function*. University of Chicago Press, 1992.

K. Persson. *Micromechanical modelling of wood and fibre properties*. PhD thesis, Division of Structural Mechanics, Lund Institute of Technology, Lund, Sweden, 2000.

C.L. Santos, A.M.P. de Jesus, J.J.L. Morais, and J.L.P.C. Lousada. Quasi-static mechanical behaviour of a double-shear single dowel wood connection. *Construction and Building Materials*, 23(1):171–182, 2009. ISSN 0950-0618. doi: 10.1016/j.conbuildmat.

2008.01.005.

I. Smith, E. Landis, and M. Gong. *Fracture and fatigue in wood.* John Wiley and Sons, 2003.

F. Thuvander, L.O. Jernkvist, and J. Gunnars. Influence of repetitive stiffness variation on crack growth behaviour in wood. *Journal of Materials Science*, 35(24):6259–6266, 2000.

J. Xavier, S. Avril, F. Pierron, and J. Morais. Novel experimental approach for longitudinal-radial stiffness characterisation of clear wood by a single test. *Holzforschung*, 61(5):573–581, 2007.

J. Xavier, S. Avril, F. Pierron, and J. Morais. Variation of transverse and shear stiffness properties of wood in a tree. *Composites Part A: Applied Science and Manufacturing*, 40:1953–1960, 2009. Special Issue: CompTest 2008.

A. Zink-Sharp, J.S. Stelmokas, and H. Gu. Effects of wood anatomy on the mechanical behavior of single-bolted connections. *Wood and Fiber Science*, 31(3):249–263, 1999.

Chapter 1

Characterisation of the transverse linear elastic behaviour of wood: anisotropy and heterogeneity

In this chapter, a review on the structure and transverse (*e.g.*, along the radial-tangential plane) mechanical behaviour of wood is presented. Particularly emphasis is given to the spatial variability of structure and transverse elastic properties of wood within and between trees. Assessing wood quality by eventual relationships between elastic properties and anatomical structure will be reviewed.

Contents

1.1   Hierarchical structure and modelling of wood

1.1.1   Introduction

Wood is a natural composite, characterised by a hierarchical structure of molecular units of cellulose, or its aggregates, embedded in a matrix of other phases (hemicelluloses and lignin) according to a multilevel architecture, ranging from molecular to structural scales, as schematically represented in Figure 1.1, that confer it specific characteristics and unique properties for multifunctional applications (Tirrel et al., 1994). That unique characteristics and abundant supply of wood have made it the most desirable building material throughout history since it has been widely used in building construction, boats, furniture and appliances and currently give it the potential to incorporate numerous materials synthesised by man through engineering. As an organic material derived from high anatomical complexity plants, wood has a cellular structure composed of fibres, arranged in preferable direction named wood fibre direction, corresponding to the axial length of the stem, parallel to the longitudinal direction (L) of material symmetry, that are traversed radially (R) by medullar rays, giving it different properties in its three main directions of symmetry (Fig. 1.2). For softwood species, as is the case of *P. pinaster*, more than 95% of the fibres that make up tissues, are elongated cells with 2-5 mm in length and with 10-80 μm in diameter called tracheids (Carvalho, 1996, pag. 59).

If the cross section of a log is analysed at the macroscopic scale, some major structural features of wood can be identified (Fig. 1.3), namely, two zones of different tonality, comprising a central dark region called heartwood and a bright area, forming an outer ring to the core, what is designated sapwood. The trunk section width occupied by each of these wood tissues, varies considerably depending on the age of the tree. Sapwood corresponds to the most recent wood formed by the cambium, and it is used by trees to perform water and nutrients transport from the roots to leaves, while heartwood, being the oldest part of the timber, is composed of sapwood tracheids that were losing their transport activity, moving the nutrients to form deposits, which however are metabolised in several types of extractives such as waxes, oils, resins, fats and tannins. In the case of *P. pinaster*, the process of heartwood formation is accompanied by synthesis and deposition of significant amounts of phenolic compounds, which generally exhibit toxicity in relation to biological organisms, pending on the main responsible for the greatest difficulty that xylophagous agents have to degrade the heartwood, ensuring their natural durability (Freitas et al., 2003). In the centre of the stem coinciding with the axis of the tree, a dark colour point corresponding to the pith can be distinguished, which in spite of its colour and position, is a spongy tissue, distinct from the core, resulting from the initial vertical growth of the tree. From the pith, on the overall transverse section with heartwood and sapwood, distinguished layers with alternating light-dark colour can be observed, organized in concentric rings arrangement, which layers correspond to the radial
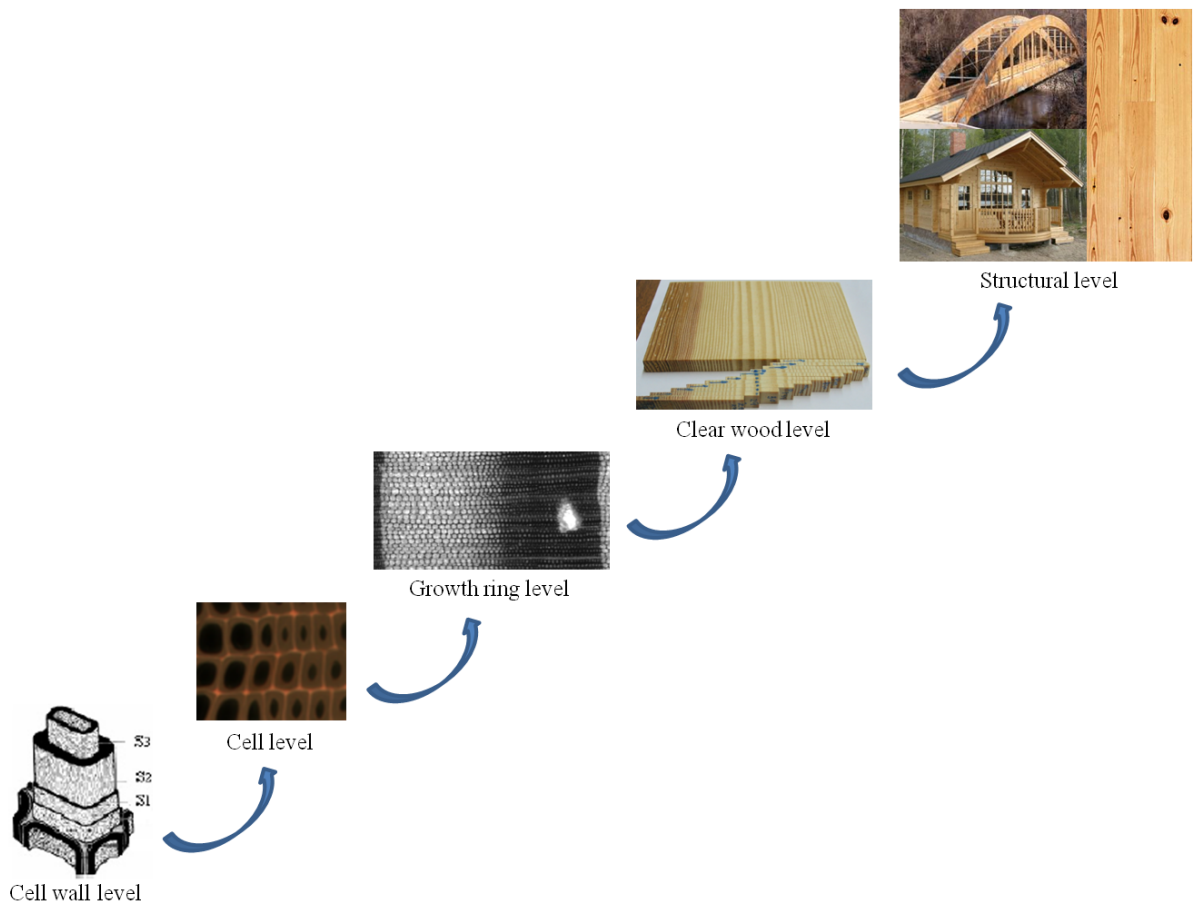
Figure 1.1: Wood chain from cell wall to structural level.
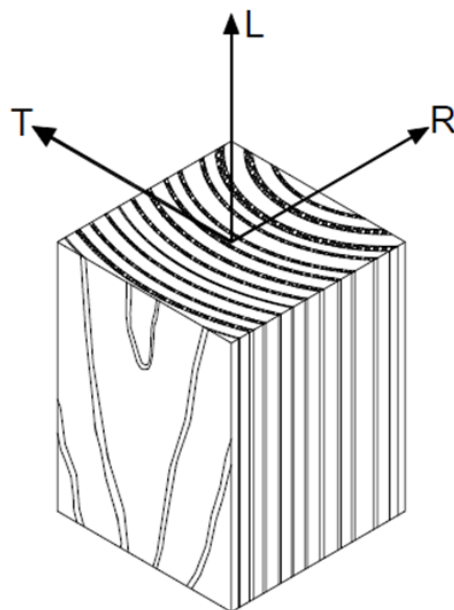
Figure 1.2: Material referential of symmetry (LRT).

season growth of the tree. Each pair of consecutive light-dark layers is called annual growth ring. The development of the tree does not occur uniformly throughout the year. Instead, depending on the seasons and on the availability of heat, light and water, cambial activity experiences large variations, so that the annual growth rings consisting of these two distinct areas of staining. The light layer formed during the spring, with favorable conditions of light, heat and water availability, is called earlywood (EW) or springwood, while the dark one, formed during the summer and autumn in less favorable soil and climatic conditions, is termed latewood (LW) or summer wood.

When increasing the magnification scale, entering the microscopic level of the wood structure, it is possible to identify, although in the transverse plane (RT plane), the arrangement and geometry of the cells, according to Figure 1.4.

The tree has a rather complex structure, whose high efficiency results from its need to adapt to withstand stresses to which it is subject throughout its lifetime. In this process, over time, the anatomical arrangement of timber is being adapted to create maximum resistance in the direction of loading, while in other directions has a much lower resistance. However, for an adequate characterisation of wood as a building material, its hierarchical anatomical structure must be analysed and modelled at different scales (Fig. 1.1) in order to optimise the mechanisms (expressed in the singularities of the material) involved in the action-reaction systems. Moreover, despite the timber engineering handles with properties and performance of the material as a structural component, the study of wood properties at macro scale (clear wood or defect free) and other scales of greater detail, is very important for the understanding of basic problems in wood engineering (Thelandersson and Larsen, 2003).

1.1.2   Structural scale

At the scale of observation of structural applications (1–10 m), in which wood is used as a component of a structural system with dimensions that cannot always relieve it of natural growth defects, such as resin pockets, reaction wood, crossing grain, etc., which tend to undervalue the material strength (Table 1.1), wood cannot be considered a homogeneous material (Thelandersson and Larsen, 2003). Furthermore, the number and the size of these anomalies ranging from board to board and consequently from element to element within the same structure, which means that the properties of lumber exhibit significant variability. Therefore, the mechanical behaviour of wood at structural scale cannot be achieved reliably, based only on the properties of clear wood. Conceptually, at this scale, the timber is modelled as a cylindrical orthotropic material having three planes of symmetry along their directions L, R and T (Fig. 1.2). However, by the dimensions involved at this scale, and for purposes of engineering design, wood can be considered as isotropic in the RT plane, since the anisotropy ratios in this plane, compared with the L
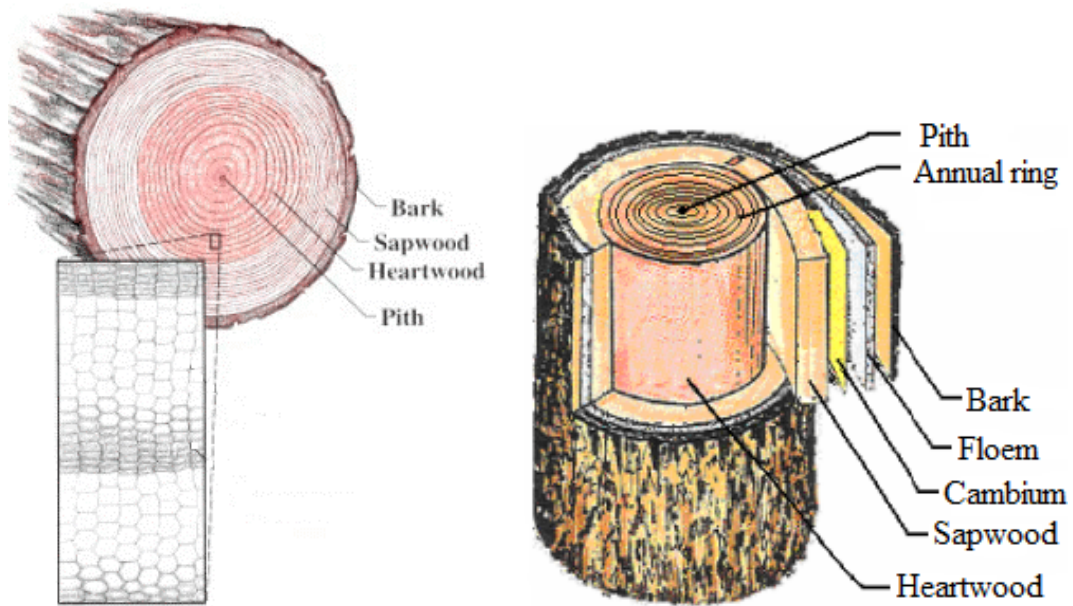
Figure 1.3: Major structural features of wood (adapted from Jozsa and Middleton (1994)).
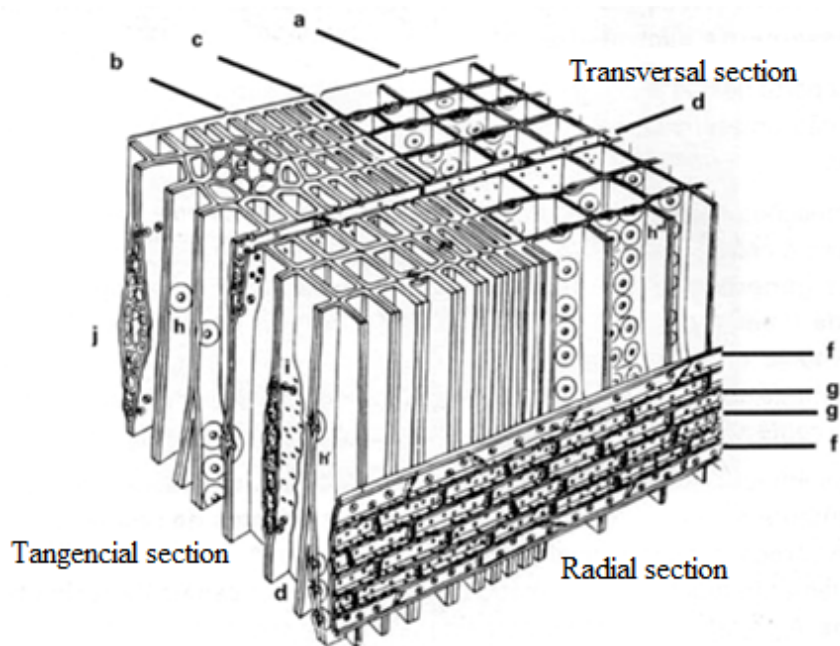
Figure 1.4: Microscopic structure of softwoods: a) earlywood; b) latewood; c) annual ring boundary d) ray e) resin duct; f) radial tracheid; g) parenchyma; h) bordered pits; i) cross-field pits; j) rays with horizontal resin duct.

Table 1.1: Strength/density ratios for some materials for structural applications.

Material	Density Kg/m^3	Strength MPa	Strength/Density 10^{-3} MPa.m^3/Kg
Structural steel	7800	400–1000	50–130
Aluminium	2700	100–300	40-110
Concrete, compression	2300	30–120	13-50
Clear softwood, tension	400–600	40–200	100-300
Clear softwood, compression	400–600	30–90	70–150
Structural timber, tension	400–600	15–40	30–80
Glass fibre in epoxi, typical value, tension	-	-	500
Carbon fibre in epoxi, typical value, tension	-	-	1000

direction, is relatively low.

1.1.3   Macro scale

At macroscopic scale of observation (1-10 cm), the volume of matter is sufficiently large compared with the volume of the unit cells or an equivalent volume of annual rings, so it can be assumed as a continuous material. Besides, clear wood can be assumed as a homogeneous material consisting of fibres oriented predominantly in the longitudinal direction. Each specimen of clear wood, representing an elementary volume of the material with uniform mechanical properties, is assumed as a continuous medium in which each material point is defined by three principal directions, defining the coordinate system of the material according to the referential of symmetry shown in Figure 1.2, the longitudinal direction parallel to the grain, the radial direction perpendicular to the grain and parallel to the rays, and the tangential direction, perpendicular to L and R and tangent to the growth rings.

1.1.4   Growth ring scale

The growth rate of the tree varies throughout the year depending on water and light availability and temperature, which is related to the seasons and introduces two sources of heterogeneity at the level of the anatomical structure of the wood formed, both at growth ring level. The first one consists on the formation of the woody tissue in different periods of spring (EW) and summer (LW) and the second is related to the growth rate as reflected in the amount of tissue that is formed at each station and consequently a differentiated thickness on the layers of annual growth. Therefore, at the growth ring scale of observation (meso scale; 1-10 mm), each ring comprises two main layers, one corresponding to the EW and another corresponding to the LW, as can be seen in Figure 1.5. As the EW is formed

during the spring, the structure of tracheid cells is characterised by large diameter thin walled while the *LW* has small cell diameters thick-walled. The transition between the *EW* and *LW* may be more or less smooth (in some cases it is even possible to distinguish a transition zone) while between the *LW* and *EW* of the following year the transition is always abrupt, and therefore well defined, due to the vegetative cessation that occurs during Winter.

At this scale of observation, the heterogeneity of wood structure becomes relevant, firstly, due to the large difference in stiffness between the tissues that make up the two layers that constitute a ring, and on the other hand, due to the presence of rays wrapped in parenchyma cells oriented in the radial direction and the presence of resin ducts oriented parallel to the fibre. The cell structure arrangement itself, more aligned in the radial direction and more interspersed in the tangential direction, contributes to the anisotropy of the material in this plane and implicitly to the wood mechanical response.

Within a ring, zooming to a single *EW* or *LW* layer, one can access to the cell scale (10-100 μm), where their size and geometry play an important role on the heterogeneity characterisation. Therefore, at this scale, wood is usually analysed and modelled as a cellular structure, applying unit cell models based on beam theory with different geometrical parameters to characterise the rigidity of wood.

1.1.5 Cell wall scale

On the scale of sub-microscopic observation (0.1-10 μm), the wood cell wall structure can be observed, whose basic unit, the microfibril, is only visible using electron microscopy, reaching the nanoscale (10^{-3} μm). The microfibril is a grouping of cellulose molecules chains $(C_6H_{12}O_5)_n$ (Fig. 1.6), where n (degree of polymerisation) equal to 5000-10000 (Haygreen and Bowyer, 1982) and hemicellulose molecules, strengthened by the lignin matrix. The microfibrils have rectangular section with 100-300 Å wide and 50-100 Å thick and several microns long. The subsequent aggregation of microfibrils bundles in layers with 300-600 Å reveals itself in the form of plates or layers that constitute the cell wall.

Figure 1.7 shows the structure of the cell wall of a wood fibre, which consists of the following layers: a tinny primary wall (P) and a thick secondary wall (S) divided into three sub-layers (S_1, S_2 and S_3). The connection between two adjacent cells is assured by the middle lamella (M) forming a structure of cell aggregates. The middle lamella is chemically characterised by the predominance of lignin which is a substance of phenolic nature, also present in the primary wall of adjacent tracheids, functioning as the cement binder. The primary wall is highly lignified and contains a considerable amount of hemicelluloses. According to (Kollman and Côté Jr., 1984), in this layer the cellulose content is relatively low, not exceeding 20 to 25%, and the microfibrils have no preferred orientation. In the
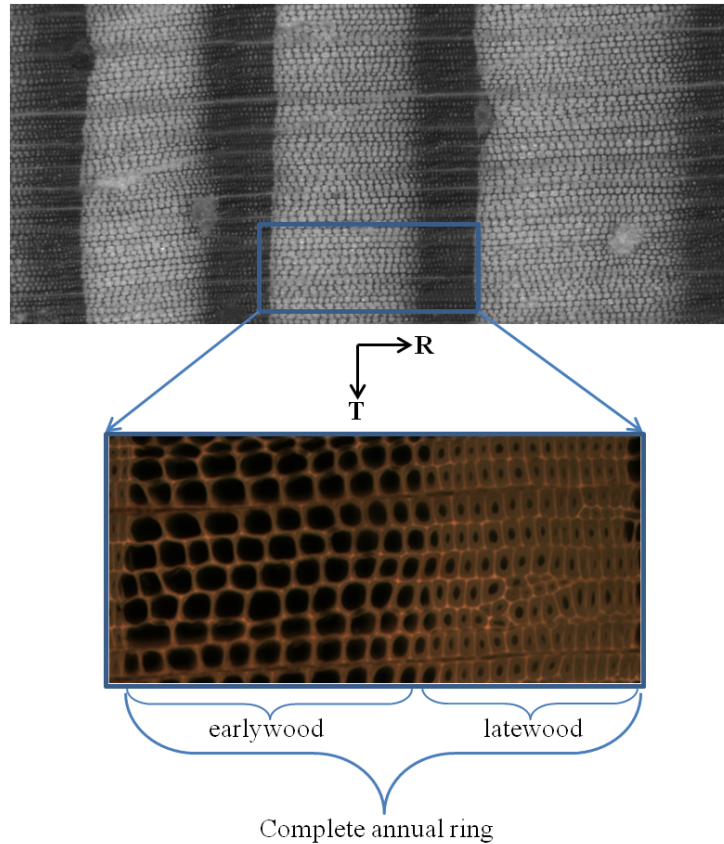
Figure 1.5: Annual rings and earlywood/latewood layers: meso scale.

secondary wall, predominant substances are cellulose, hemicelluloses and lignin, this one being scattered or associated to the hemicelluloses and to the cellulose. The S_1 and S_3 layers are formed by microfibrils spirals whose deviation to the tracheid axis varies between $50°$ and $90°$. In contrast, the S_2 layer shows the microfibrils oriented almost parallel to the same axis, with a deviation of only $10°$ to $30°$. Furthermore, the S_2 layer is the thickest among the layers of the secondary wall (3 to 15 times thicker than the S_1 and S_3 together) hence, it has a high influence on physical and mechanical behaviour of wood. On cells of mature wood, the microfibril angle of the S_2 layer is approximately $7°$ or less, while on the juvenile wood (as on compression wood) this angle may be up to $45°$ (Jozsa and Middleton, 1994).

From its chemical composition, wood can be defined as a reinforced composite, whose mechanical behaviour is a combination of high elasticity of the cellulose under short-term loads and plastic flow of the hemicelluloses and lignin under long-term loads, which is different from most other structural materials (Jeong, 2008).
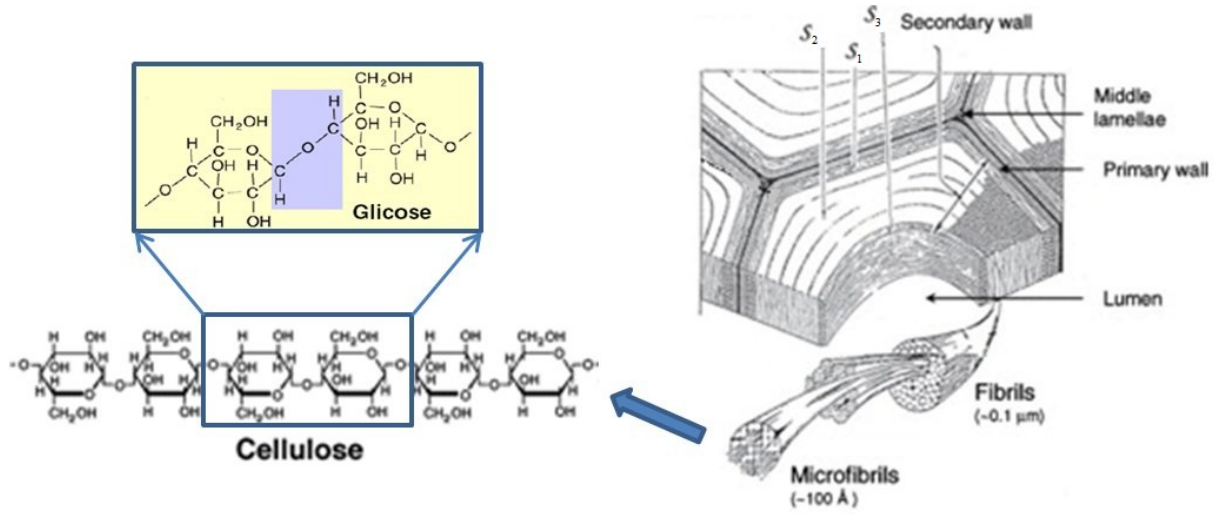
Figure 1.6: Fibrils e microfibrils: arrangement and composition.
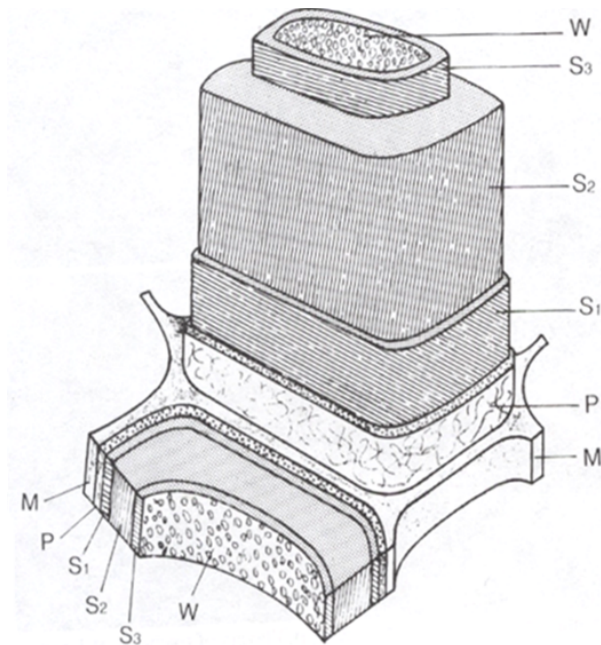
Figure 1.7: Cell wall structure: M) middle lamella; P) Primary wall; S1) Secondary wall (external layer); S2) Secondary wall (middle layer); S3) Secondary wall (internal layer); W) lumen (adapted from (Tsoumis, 1991).

1.1.6   Conclusions
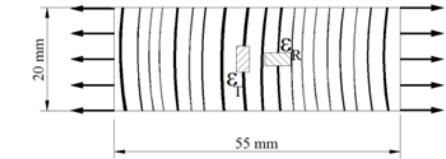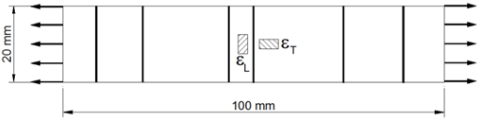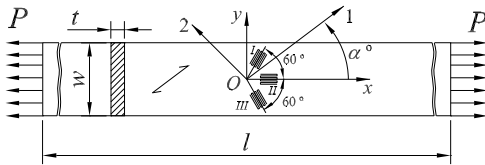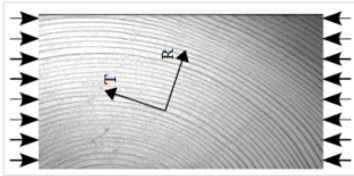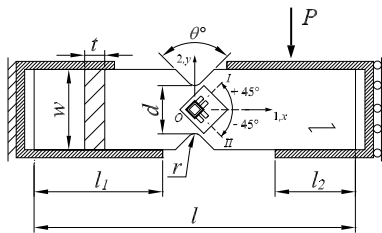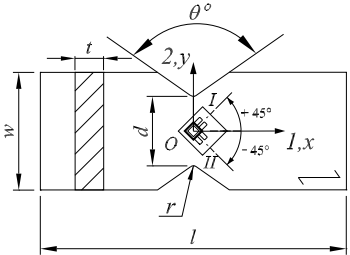
Trees can be distinguished by their anatomical structure into softwood and hardwood species. *Pinus pinaster*, was selected as the material for this work, because, it is the most relevant specie in our country, both from the economic and social points of view. According to 2010 data from AIFF, the pine market in Portugal represents 62% of the Forestry VAB, with a sales volume of almost 3500 million euros, from which 927 million euros in exportation and accounts for about 65000 direct manufacturing jobs, involving 89% of the industry. Furthermore, maritime pine is the support of the majority of industries including panels industry, specific segments of the cellulose industry, the industries of pallets and a large number of small and medium enterprises of forestry and sawmills. The anatomical structure and the mechanical behaviour of wood can be analysed hierarchically at several length scales. Models to predict mechanical properties of wood at the macro scale level could be improved by including the intra-ring characteristics but little research has explored the uncertainties of mechanical properties at the EW and LW layers (Jeong, 2008). In this work, wood will be analysed at the mesoscopic scale. At this scale, wood is modelled as a continuous (solid) and inhomogeneous material, consisting of alternate layers of EW and LW. In EW, the cells are characterised by thin walls and large lumens, whilst in LW, the walls are thicker and lumens are smaller. Within an individual growth ring, mechanical properties will follow that variation (Bigorgne, 2011). It is relevant to know these sets of local properties since they can play an important role in applications such as fracture mechanics (Dourado et al., 2008) to better understand fracture mechanisms, of wood joints by means of crack propagation (Santos et al., 2009) and wood machining, for instance.

1.2   Mechanical tests for wood characterisation in the transverse plane

1.2.1   Tensile tests

The elastic moduli of wood perpendicular to the grain (E_R and E_T) are considerably lower than the one parallel to the grain (E_L). Usually, the proposed tensile tests for wood transverse stiffness characterisation (*e.g.*, ASTM D143, 2007) only consider the strength evaluation. As an alternative to these standards, some authors have proposed different approaches, which consider the orthotropic behaviour of wood (Aicher et al., 2001; Pereira, 2005). Particularly, Pereira (2005) proposed two specimen geometries for radial and tangential characterisation, which can be observed in table 1.2(a) and (b) respectively. The tangential sample is made from two pieces of wood glued together in order to obtain a specimen with double symmetry. The uniaxial stress-strain field

Table 1.2: Classical mechanical tests for wood characterisation in the transverse plane.

Mechanical test		Elastic properties
(a) Tensile test in the R direction (Pereira, 2005)		E_R, ν_{RT}
(b) Tensile test in the T direction (Pereira, 2005)		E_T, ν_{TL}
(c) Off-axis tensile test (Garrido, 2004)		G_{RT}
(d) Transverse compression test (Simon, 2009)		E_R, ν_{RT}
(e) Iosipescu shear test (Xavier, 2003)		G_{RT}
(f) Arcan shear test (Oliveira, 2004)		G_{RT}

generated from wood mechanical response to the perpendicular tensile load, allow getting the engineering constants by applying the equations (1.1), where $1 - 2 \equiv R - T$, P is the applied load, A is the initial cross-section area, ε_i $(i = 1, 2)$ is the strain component in the i direction, E is the Young's modulus and ν is the *Poisson*'s ratio.

$$E_1 = \frac{P/A}{\varepsilon_1} \qquad \text{and} \qquad \nu_{12} = -\frac{\varepsilon_2}{\varepsilon_1}. \tag{1.1}$$

However, if the annual growth rings curvature is sharp across the region of interest (ROI) of the specimen a heterogeneous stress-strain field can occur as is stated by different authors (Aicher et al., 2001; Pedersen et al., 2003). Moreover, the degree of heterogeneity increases with the anisotropy ratio E_R/E_T and it is also dependent on the shear modulus of the material. Lower values of the shear modulus will raise the effect of the E_R/E_T ratio (Aicher et al., 2001; Pedersen et al., 2003). Pereira (2005) has proposed a numerical correction factor as a way to account with both stress and strain heterogeneous distributions for the properties determined directly from Eqs. (1.1).

1.2.2   Compression tests

The behaviour of wood in compression perpendicular to grain has been studied by several authors (Bigorgne, 2011; Gibson and Ashby, 1997; Majano-Majano et al., 2012; Nairn, 2007; Shipsha and Berglund, 2007; Simon, 2009). Different specimen dimensions and loading cases, leading to different stress distributions and stress-strain responses have been employed (see STEP, 1996, Figure 4, p. IV-2-4). As for the case of tensile tests carried out perpendicularly to the grain, the elastic properties of wood in transverse compression can be influenced by both shear coupling effects and by the cylindrical symmetry of the annual rings pattern. Simon (2009), held some compression tests on *Picea* specimens at macro scale, whose configuration can be seen in table table 1.2(d). In this test, the load applied to the specimen has approximately 45 degrees with the annual rings direction. As the softwoods are known by their low shear modulus compared to their radial and tangential stiffness, the intention was to take advantage on this relative weakness based on the heterogeneous strain fields on the central region of the sample in RT plane. Bigorgne (2011) has also made some studies on *Picea* applying standard compressive tests on the RT plane and at meso scale. In a more recent work, Majano-Majano et al. (2012) proposed a test method consisting of three different uniaxial compression loads application over the same rectangular prismatic specimen. The loads were applied along the three different directions defined by the edges of the specimen, which will define the general axes (xyz). A key point here was that the orientation of the material coordinate system (LRT) was not coincident with any of the three specimen directions. With this configuration, the compression loading applied along only one general axis, produces normal and shear stresses along the local material axes LRT. Their corresponding elongations and angular

distortions can therefore be measured simultaneously by a 3D optical digital measurement system and the material parameters determined based on an inverse method for obtaining the complete compliance matrix.

1.2.3 Shear tests

The characterisation of wood shear mechanical behaviour it's been a problem of experimental mechanics whose complexity as to do with the difficulty to define appropriate tests for obtaining a pure and uniform shear state. Some of the most relevant works on wood shear properties identification were developed under the application of three different tests: off-axis tensile, arcan and iosipescu. In the next sub-sections a review on them will be presented.

1.2.3.1 Off-axis tensile test

The off-axis tensile test was firstly proposed by Chamis and Sinclair (1977) for unidirectional fibrous composites. Lather, other studies with major developments were undertaken also on fibrous composites (Kawai et al., 1997; Pierron and Vautrin, 1996; Pierron et al., 1998; Pindera and Herakovick, 1986; Sun and Berreth, 1998; Sun and Chung, 1993). The application of this test to clear wood was also investigated by several authors (Ebrahimi and Sliker, 1981; Liu, 2002; Sliker and Yu, 1993; Xavier et al., 2004; Zhang and Sliker, 1991). The specimen consists basically of a rectangular coupon, whose geometrical directions (x, y) make an angle with the orthotropic directions of the material $(1, 2)$ as illustrated in the schematic representation of the off-axis tensile test in table 1.2(c). When a uniform and uniaxial load (P) is applied at the specimen ends along its longitudinal direction (x) in the central cross-section, the in-plane stress state, considering the specimen coordinate system, is equal to,

$$\sigma_{xx} = \frac{P}{A}, \qquad \sigma_{yy} = \sigma_{xy} = 0 \tag{1.2}$$

where A is the cross-section area of the specimen (with $A = w \times t$). Starting from the equation (1.2) and using classical formulae of matrix transformation, the stress components in the material coordinate system $(1, 2)$ can be written as

$$\sigma_1 = \frac{P}{A} \cos^2 \alpha, \qquad \sigma_2 = \frac{P}{A} \sin^2 \alpha, \qquad \sigma_6 = \frac{P}{A} \cos \alpha \sin \alpha. \tag{1.3}$$

representing the biaxial state of stress in the material axes, dependent on the off-axis angle generated by the initial uniaxial state of stress. To maximize the effect of the load on the material stress components and thus its shear behaviour, the best angle must be defined preliminarily. This calibration procedure can be achieved regarding to either the stiffness and strength properties of the material by evaluating the best angle corresponding to the

maximum $\varepsilon_6(\alpha)/\varepsilon_x$ ratio (ε_6 is the shear strain in the material axes and ε_x the strain along the specimen longitudinal direction) (Chamis and Sinclair, 1977) and normalising the stress components with respect to the material strength parameters and evaluate their variation from the α angle: $\sigma_1(\alpha)/X^+$, $\sigma_2(\alpha)/Y^+$ and $\sigma_6(\alpha)/S$, where X^+ and Y^+ are the transverse tensile strengths and and S is the shear strength (Alloba, 1997).

During the experimental procedure, specimens are clamped to the testing machine yielding some end effects on gripping zone traduced by the lack of rotation of the specimens. This constraint usually contributes to nonuniform strain field generation at the central region of the samples. To address this limitation, specimen faces at the gripping zone are reinforced by end tabs. To get the best result on the correction of the earlier mentioned localised end effects, oblique end tabs must be used instead of rectangular ones to avoid S-shape deformation of the specimen (Pierron and Vautrin, 1996; Pindera and Herakovick, 1986). In this case some authors have been proved that a uniform state of stress can be achieved across a larger region of the specimen (Kawai et al., 1997; Pierron and Vautrin, 1996; Pierron et al., 1998; Sun and Berreth, 1998; Sun and Chung, 1993). Thus, the correct identification of the shear modulus can be reached from

$$G_{12} = \frac{\sigma_6}{\epsilon_6}. \tag{1.4}$$

According to Sun and Chung (1993) the angle of the end tabs (β) can be determined by

$$\cot \beta = -\frac{\overline{S_{16}}}{\overline{S_{11}}} \tag{1.5}$$

where the $\overline{S}_{ij}$ ($i, j = 1, 6$) are the elements of the compliance matrix over the specimen coordinate system.

1.2.3.2   Iosipescu shear test

The iosipescu shear test was introduced in 1967 by Iosipescu for isotropic materials study. Since the 80s, has widely been used on fibrous composite materials (Adams and Walrath, 1987; Ho et al., 1993; Ifju, 1994; Morton et al., 1992; Pierron, 1998; Pierron and Vautrin, 1994; Pindera et al., 1987, 1990; Walrath and Adams, 1983) and was even adopted as a standard test (ASTM D5379, 1993). In 1991, it was applied for the first time to the wood shear behaviour identification, by Janowiak and Pellerin (1992), followed by several other authors for different species (De Magistris and Salmén, 2005; Dumail and Salmén, 2001; Dumail et al., 2000; Liu, 2000; Xavier et al., 2004; Yoshihara et al., 1999). On table 1.2(e) a schematic representation of the Iosipescu test method is presented. The sample consists of a small parallelepiped with two symmetric V-notches at its centre. During test procedure, the vertical cross-head movement of the testing machine is transferred

into a predominant shear loading at the central region, by a proper fixture. As the specific geometry based on the two notches allows a quasi-uniform distribution of the shear stress in that region, the mean shear stress (σ_6) is given by:

$$\sigma_6 = \frac{P}{A} \tag{1.6}$$

where P represents the resultant of the vertical load applied to the specimen, and A the area of the smallest cross-section between the notches ($A = d \times t$, in table 1.2(e)). As the shear strain (ε_6) it is usually measured with a biaxial rosette, bonded at the centre of the specimen at $\pm 45°$ with respect to the specimen longitudinal axis. Assuming that the shear stress is uniform in the section between notches, the shear modulus can be determined as

$$G_{12}^a = \frac{\sigma_6}{\varepsilon_6}. \tag{1.7}$$

However, several authors have shown that neither the stress distribution between V-notches nor the strain distribution over the area covered by the rosette, are uniform (Ho et al., 1993; Morton et al., 1992; Pierron, 1998; Pindera et al., 1987). Thus, the shear modulus identified from equation (1.7) is an apparent value. To overcome this limitation, numerical correction factors have been proposed by Pierron (1998) for the correct shear modulus determination:

$$G_{12}^c = \frac{\sigma_6^O}{P/A} \frac{\varepsilon_6^{sg}}{\varepsilon_6^O} G_{12}^a = CSG_{12}^a, \tag{1.8}$$

where G_{12}^c is the efective shear modulus, σ_6^O the shear stress value at the centre of the specimen, P/A the average shear stress between the notches, ε_6^{sg} the shear strain measured by the rosette, ε_6^O the shear strain at the centre of the specimen, CS are the shear stress correction factors determined by finite element analyses. Whilst C factor quantifies the degree of heterogeneity of the shear stress distribution between the notches, the S factor takes into account the heterogeneity of the shear strain distribution over the gauge area. For *P. pinaster* specimens oriented in the LR, LT and RT planes, the CS correction factor was determined respectively equal to 0.96 (-4%), 0.91 (-9%) and 1.02 (2%) (Xavier et al., 2003, 2004). Regarding to this, it can be concluded that the error in the shear modulus evaluation by using equation 1.7, is smaller or of the same order of magnitude of the scatter usually found experimentally in the characterisation of wood mechanical properties due to its peculiar variability.

The data reduction method presented above assumes that both stress and strain distributions are constant through the thickness of the specimen. However, some authors (Ifju, 1994; Morton et al., 1992; Pierron, 1998) have pointed out that strain measurements on both front and back surfaces of the specimen can be significantly different, thus leading to an additional scatter in the identification of the shear modulus. This effect assumes more

relevance when testing thick specimens or when the fibres direction is oriented parallel to the loading direction. Although, Pierron (1998) has demonstrated that this effect can be minimised by measuring the shear strain on both faces of the specimen and take their average for the determination of the shear modulus of the material.

1.2.3.3   Arcan shear test

The Arcan test was first proposed for the shear characterisation of plastic materials by Goldenberg et al. (1958). These authors proposed an S shaped specimen with a notch whose geometry leads to a predominant shear stress state in the transverse section of the specimen. Afterwards, both in the field of fibre-reinforced composite materials (Arcan et al., 1976; El-Hajjar and Haj-Ali, 2004; Hung and Liechi, 1997; Mohr and Doyoyo, 2003; Voloshin and Arcan, 1980) as well as for clear wood specimens (Liu and Ross, 2005; Oliveira, 2004; Rammer and Hernandez, 1988), the configuration was substituted by a butterfly shaped specimen. Oliveira (2004) configuration test is shown in table 1.2(f). The specimen is attached to a specific fixture, consisting of two separated supports mounted in a butterfly shape, used to impose a predominant shear stress across the central part of the specimen. This mooring system was emphasised on several studies (El-Hajjar and Haj-Ali, 2004; Hung and Liechi, 1997; Mohr and Doyoyo, 2003; Oliveira, 2004), since it has important effects on the specimen mechanical response. From the point of view of the experimental measurements, the Arcan test is rather close to the Iosipescu test, once both load and gauge strains are measured at the central region of the specimen. Afterwards, the average shear stress and the average shear strain are determined from those measurements. Finally, the shear modulus in the material coordinate system is simply determined through equation 1.8.

1.3   Spatial variability of wood structure and properties

1.3.1   Introduction

Wood is a material with biological origin, whose properties varies from species to species and, within species, from individual to individual. The variability of wood properties within species may be associated with genetic factors, soil and climate conditions, silvicultural practices, among other factors that affect the growth rate of the tree. Since most of the pine production is used for structural purposes, whether in the form of beams, joists, pillars, floors or other structural components subjected to stresses of varying intensity, the most interesting properties for wood structure designers, are the modules, the crush strength and the toughness of wood, featuring its rigidity and resistance. Because wood exhibits different properties in different directions (anisotropy), for an appropriate characterisation of its mechanical behaviour, it is necessary to take into account a large

number of analysis parameters, associated with the properties mentioned. Reducing them for only a few key parameters, sufficient to define the quality of wood would be of great interest.

As already mentioned in section 1, the most relevant aspect of the wood anatomy is its hierarchical organization at different scales, ranging from structural level, typical of structural applications, until the nano scale layers of the cell wall. Is this hierarchical structure which gives wood the heterogeneity, and explains its variable mechanical behaviour and its anisotropy. For example, in the longitudinal direction, the rigidity and strength of timber are large, when compared with other materials, if resistance is considered in relation to the material weight, while in the perpendicular directions is relatively soft and less resistant.

1.3.2   Sources of variability

It is known that almost all the characteristics of softwood vary significantly from the pith to the cambium (Lousada et al., 1994; Machado and Cruz, 2005). In terms of density, it follows a pattern of variation, increasing in the cambium direction, largely due to the formation of juvenile wood near the pith, through the influence of the crown of the tree, during youth (from 5 to 20 years). Juvenile wood (Figure 1.8) is characterised by having low density, grain deviation, low percentage of LW, shorter tracheids and thinner cell walls in comparison with the wood formed in the outer layers called mature wood (Lousada et al., 1994; Schweinbruger, 2007).

The results of Machado and Cruz (2005), showed a strong and consistent effect of the distance to pith on all mechanical properties studied, mainly because of the juvenile/mature wood heterogeneity influence on wood properties variability. A trend for the decrease of mechanical properties along the stem, from bottom to top, was detected. Moreover, they observed a general increase of strength and stiffness for distance to pith, from 10 to 90 % of the trunk radius. Also (Dumail and Castéra, 1997), studied the within tree variability related with juvenile wood occurrence on Maritime pine to demonstrate a decrease from the base to the top of the tangential shrinkage and the anisotropic ratio between RT dimensional variations. In another study of the same species, Dumail et al. (1998) concluded that the within-tree variations are significant for hardness, energy release rate and basic density when considering the radial position effect. They found a strong relationship between hardness and basic density. Summarizing, juvenile wood is an important wood quality attribute because it can have lower density and always has shorter fibres, larger fibril angle, and slightly lower cellulose content than mature wood.

As a tree grows, it responds to the environment in many ways. It inevitably develops anomalous features (defects) that reduce the strength of lumber cut from it. The worst of these defects are knots, cross grain (spiral, diagonal, interlocked and wavy) and reaction
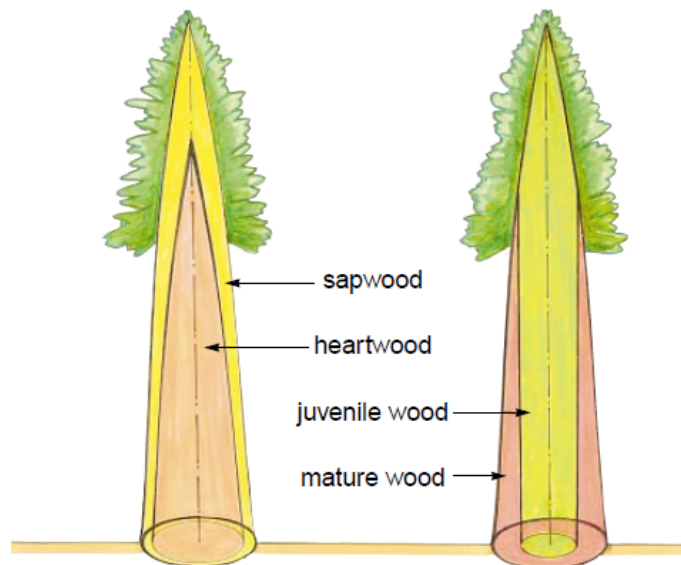
Figure 1.8: On stem juvenile/mature wood distribution(adapted from (Jozsa and Middleton, 1994)

wood. Knots in particular, reduce wood strength due to the occurrence of grain deviation, since the fibres of the node are generally perpendicular to the remaining timber. Furthermore it is very common the existence of cracks along the dried nodes, which reduces the material strength. Cross grain is a generic term describing wood fibres that are not aligned with the stem's longitudinal axis. Severe cross grain occurs when trees that have grown spirally or with pronounced taper are cut for lumber. Some cross grain is the inevitable result of cutting prismatic, rectangular pieces from a tapered mass of concentric cylinders. Cross grain drastically reduces the tensile strength of the lumber and can precipitate abrupt and early bending failures. Moreover, the elastic properties are significantly influenced by the existence of reaction of wood, which is normally associated to marrow eccentricity, and results from stem exposure to asymmetric effort, taking tree to produce (on the side subjected to compression) smaller and rounded tracheids with much thicker walls, particularly at S_2 layer where occurs large concentrations of lignin, as well as a great microfibril angle. This kind of wood is harder, heavier and more resistant to compression but less resistant to tensile stresses, being also more fragile. Most softwoods grow compression wood on the underside of the branches.

There are other sources of variability associated to the wood processing. For example, during wood drying, there may be checks, shakes, and splits which are fractures in the wood that open as the lumber loses water (Simpson, 1991). Checks align with the longitudinal axis of the piece and are normal to the growth rings. Splits run through checks and are usually found at the ends of timber. The worst of the splits are often trimmed off after the lumber is dried as a final step in cutting lumber. Improper kiln-drying can accentuate

splitting at the ends. Shakes are thin voids within the tree that seem to occur naturally as the tree is growing. Shakes also align with the axis of the tree, but they lie in plane with the growth rings. It is as if the tree had delaminated slightly at a transition between EW and LW. Timber's strength relies upon the connection between adjacent wood cells. Though checks, shakes, and splits may close, the cells never reconnect across the fracture. By physically separating pieces of lumber, checks, shakes, and splits are detrimental in many ways. Just what and how much effect these separations have, depends on the location and severity of the defects, and the end use of the timber.

1.3.3   Variability versus quality

Typically, wood quality is closely related to the variability that she presents, which in turn is related to its heterogeneity. Since the amount of variability is a key issue, both in the processing and in the performance of timber, the variation of basic density, stiffness and strength must be known for an intelligent application of wood. In practice, this variability of properties must be translated into quality grades according to their relevance for the intended use. In Portugal, structural timber of maritime pine is classified only with visual grading rules into two main grades: grade E for structural timber suitable for general applications and grade EE (corresponding to the higher strength) for structural timber to be applied in special structures. This classification is based on the Portuguese standard NP4305 (1995) that is compatible with the Eurocode 5 (ENV1995-1-1) (STEP, 1996).

According to Jozsa and Middleton (1994), "wood quality is defined in terms of attributes that make it useful for a given end use", so it can only have meaning when the final product and its use are known, due to their relationship with the cumulative effect of various wood properties in a product. For structural framing, joists, planks, beams, stringers, posts and other lumber products, strength and stiffness are the main characteristics to consider on grade definition. From the natural grade-setting properties, density is taken as one of the most relevant, because it provides an excellent means of predicting end-use properties of wood such as strength, stiffness, hardness, heating value, machinability, pulp yield an paper making quality. Not only the mean density but also the density variation can be important as a measure of wood suitability for some en uses. Regarding the same authors, another important natural grade-setting characteristic has to do with the amount of juvenile wood on stem. The proportion of juvenile/mature wood is an important wood quality attribute, because, it can have lower density and always has short fibres, larger fibril angle, and slightly lower cellulose content than mature wood. A higher proportion of juvenile wood can result in reduced lumber strength. In structural uses, where load bearing capability is vital, also the presence of compression wood can be used to downgrade timber because of its harmful effects on strength and shrinkage.

From Lousada et al. (1994), density is one of the most important indicator of wood

quality since, in addition to its strong correlation with other properties such as mechanical strength, shrink, resistance to biodegradation and paper quality, and provides very precise quantification of the amount of raw material present in a piece of wood. Tsehaye et al. (2000), also states that the density has always been considered the best parameter to define the intrinsic quality of wood, if is assumed as an indicator of strength, stiffness and other properties. However, as a result of their work comparing the density and stiffness parameters as parameters of wood selection for structural purposes concluded that rigidity is more adequate than density for measuring wood quality for structural applications.

1.3.4   Conclusions

Overall, at the individual level, the characteristics of timber depend on the relative position to the tree axis (in R direction), and with the relative position to the base of the stem (in L direction). The patterns and causes of density and mechanical properties variation have been widely studied in planes parallel to the grain, while on the perpendicular planes there is still little information available. Furthermore, the greatest differences occur in the radial direction (Baillères et al., 2005). On the basis of what was exposed on the wood anatomy, we can easily understand that the variability at the growth rings scale, where the timber may be considered as a bi-composite, is considered to be predominant in this context, because of the wide variation in geometric parameters of the cells and their typical arrangement along the R e T directions, and in particular due to the cell wall thickness variations, reflecting itself in all other scales.

References

D.F. Adams and D.E. Walrath. Current status of the Iosipescu shear test method. *Journal of Composite Materials*, 21(6):494–507, 1987.

S. Aicher, G. Dill-Langer, and L. Höfflin. Effet of polar anisotropy of wood loaded perpendicular to grain. *Journal of Materials in Civil Engineering*, 13(1):2–9, 2001.

E.I. Alloba. *Extensométrie optique: Aspects métrologiques et application à la mécanique expérimentale des composites*. PhD thesis, Univeristé Claude Bernard - Lyon I, 1997.

M. Arcan, Z. Hashin, and A. Voloshin. A method to produce uniform plane-stress states with applications to fiber-reinforced materials. *Experimental Mechanics*, 18(4):141–146, 1976.

ASTM D143. *Standard methods of testing small clear specimens of timber*. ASTM International, West Conshohocken, PA, 2007.

ASTM D5379. *Test method for shear properties of composite materials by the V-notched beam method*. American Society for Testing and Materials, Philadelphia, PA, USA, 1993.

H. Baillères, O. Vitrac, and T. Ramananantoandro. Assessment of continuous distribution of wood properties from a low number of samples: Application to the variability of modulus of elasticity between trees and within a tree. *Holzforschung*, 59:524–530, 2005.

L. Bigorgne. *Mécanique et mécanismes de rupture dans le plan transverse du bois résineux*. PhD thesis, Institute National des Sciences Appliquées de Lyon, 2011.

A. Carvalho. *Madeiras Portuguesas: estrutura anatómica, propriedades, utilizações*. Instituto Florestal, 1996.

C.C. Chamis and J.H. Sinclair. Ten degree off-axis test for shear properties in fiber composites. *Experimental Mechanics*, 17(9):339–346, 1977.

F. De Magistris and L. Salmén. Combined shear and compression analyis using a modified Iosipescu shear test device. Experimental studies on dry wood. *Holzforschung*, 59(5):539–545, 2005.

N. Dourado, S. Morel, M.F.S.F. de Moura, G. Valentin, and J. Morais. Comparison of fracture properties of two wood species through cohesive crack simulations. *Composites Part A: Applied Science and Manufacturing*, 39(2):415–427, 2008.

J. F. Dumail and P. Castéra. Transverse shrinkage in maritime pine juvenile wood. *Wood Science and Technology*, 1997.

J.-F. Dumail and L. Salmén. Intra-ring variations in the rolling shear modulus of spruce wood. *Holzforschung*, 55(5):549–553, 2001.

J. F. Dumail, P. Castéra, and P. Morlier. Hardness and basic density variation in the juvenile wood of maritime pine,. *Annals of Forest Science*, 1998.

J.-F. Dumail, K. Olofsson, and L. Salmén. An analysis of rolling shear of spruce wood by the Iosipescu method. *Holzforschung*, 54(4):420–426, 2000.

G. Ebrahimi and S. Sliker. Measurement of shear modulus in wood by a tension test. *Wood Science*, 13(3):171–176, 1981.

R. El-Hajjar and R. Haj-Ali. In-plane shear testing of thick-section pultruded FRP composites using a modified Arcan fixture. *Composites Part B: Engineering*, 35(5):421–428, 2004.

L. Freitas, J. Rodrigues, and J. Graça. Composição dos extrativos da madeira de pinheiro bravo: variação borne/cerne e lenho normal/lenho resinado. Technical report, ISA, Centro de Estudos Florestais, 2003.

N. Garrido. Identificação do comportamento mecânico da madeira através do ensaio de tracção fora dos eixos de simetria material. Master's thesis, Universidade de Trás-os-Montes e Alto Douro, Vila Real, Portugal, 2004.

L.J. Gibson and M.F. Ashby. *Cellular solids. Structure and properties*. Cambridge University Press, 1997.

N. Goldenberg, M. Arcan, and E. Nicolau. On the most suitable specimen shape for testing shear strength of plastics. In *International Symposium on Plastics Testing and Standardization, ASTM STP 247*, pages 115–121, 1958.

J. G. Haygreen and J. L. Bowyer. *Forest Products and Wood Science*. Iowa State University Press, 1982.

H. Ho, M.Y. Tsai, J. Morton, and G.L. Farley. Numerical analysis of the Iosipescu specimen for composite materials. *Composite Science and Technology*, 46(2):115–128, 1993.

S.-C. Hung and K.M. Liechi. An evaluation of the Arcan specimen for determining the shear moduli of fiber-reinforced composites. *Experimental Mechanics*, 37(4):460–468, 1997.

P.G. Ifju. The shear gage: For reliable shear modulus measurements of composite materials. *Experimental Mechanics*, 34(4):369–378, 1994.

J.J. Janowiak and R.F. Pellerin. Shear moduli determination using torsional stiffness measurements. *Wood and Fiber Science*, 24(4):392–400, 1992.

Gi Young Jeong. *Tensile properties of Loblolly pine strands using digital image correlation and stochastic finite element method*. PhD thesis, Faculty of Virginia Polytechnic Institute & State University, 2008.

L. A. Jozsa and G. R. Middleton. A discussion of wood quality attributes and their practical implications. Technical report, Forintek Canada Corp., 1994.

M. Kawai, M. Morishita, H. Satoh, S. Tomura, and K. Kemmochi. Effects of end-tab shape on strain field of unidirectional carbon/epoxy composite specimens subjected to off-axis tension. *Composites Part A: Applied Science and Manufacturing*, 28(3):267–275, 1997.

F.P.F. Kollman and W.A. Côté Jr. *Principles of wood science and technology – Solid wood*. Springer-Verlag, Berlin, 1984.

J.Y. Liu. Effects of shear coupling on shear properties of wood. *Wood and Fiber Science*, 32(4):458–465, 2000.

J.Y. Liu. Analysis of off-axis tension test of wood specimens. *Wood and Fiber Science*, 34 (2):205–211, 2002.

J.Y. Liu and R.J. Ross. Relationship between radial compressive modulus of elasticity and shear modulus of wood. *Wood and Fiber Science*, 37(2):201–206, 2005.

J. L. Lousada, F. Fonseca, and M. E. Silva. Relações entre componentes da densidade da madeira no lenho juvenil e no lenho adulto em pinus pinaster ait. Technical report, LPF, UTAD, 1994.

J.S. Machado and H.P. Cruz. Within stem variation of maritime pine timber mechanical properties. *Holz als Roh - und Werkstoff*, 63(2):154–159, 2005.

A. Majano-Majano, J. Fernandez-Cabo, S. Hoheisel, and M. Klein. A test method for characterizing clear wood using a single specimen. *Experimental Mechanics*, 52:1079–1096, 2012.

D. Mohr and M. Doyoyo. A new method for the biaxial testing of cellular solids. *Experimental Mechanics*, 43(2):173–182, 2003.

J. Morton, H. Ho, M.Y. Tsai, and G.L. Farley. An evaluation of the Iosipescu specimen for composite materials shear property measurement. *Journal of Composite Materials*, 26(5):708–750, 1992.

J.A. Nairn. A numerical study of the transverse modulus of wood as a function of grain orientation and properties. *Holzforschung*, 61(4):406–413, 2007.

NP4305. *Madeira serrada de pinheiro bravo para estruturas: classificação visual*. IPQ, 1995.

J.M. Oliveira. Caracterização do comportamento ao corte da madeira usando o ensaio de Arcan. Master's thesis, Universidade de Trás-os-Montes e Alto Douro, Vila Real, Portugal, 2004.

M.U. Pedersen, C.O. Clorius, L. Damkilde, and P. Hoffmeyer. A simple size effect model for tension perpendicular to the grain. *Wood Science and Technology*, 37(2):125–140, 2003.

J.L. Pereira. Comportamento mecânico da madeira em tracção nas direcções de simetria material. Master's thesis, Universidade de Trás-os-Montes e Alto Douro, Vila Real, Portugal, 2005.

F. Pierron. Saint-Venant effects in the Iosipescu specimen. *Journal of Composite Materials*, 32(22):1986–2015, 1998.

F. Pierron and A. Vautrin. Accurate comparative determination of the in-plane shear modulus of T300/914 by the Iosipescu and 45° off-axis tests. *Composite Science and Technology*, 51(1):61–72, 1994.

F. Pierron and A. Vautrin. The 10° off-axis tensile test: A critical approach. *Composites Science and Technology*, 56(4):483–488, 1996.

F. Pierron, E. Alloba, Y. Surrel, and A. Vautrin. Whole-field assessment of the effects of boundary conditions on the strain field in off-axis tensile testing of unidirectional

composites. *Composites Science and Technology*, 58(12):1939–1947, 1998.

M.-J. Pindera and C.T. Herakovick. Shear characterization of unidirectional composites with the off-axis tension test. *Experimental Mechanics*, 26(1):103–112, 1986.

M.-J. Pindera, G. Choksi, J.S. Hidde, and C.T. Herakovich. A methodology for accurate shear characterization of unidirectional composites. *Journal of Composite Materials*, 21 (12):1164–1184, 1987.

M.-J. Pindera, P. Ifju, and D. Post. Iosipescu shear characterization of polymeric and metal matrix composites. *Experimental Mechanics*, 30(1):101–108, 1990.

D. R. Rammer and R. Hernandez. Moiré analysis of the modified Arcan shear specimen. In J. Natterer and J.-L. Sandoz, editors, *5th World Conference on Timber Engineering*, volume 2, Montreux, Switzerland, 17-20 August 1988.

C.L. Santos, A.M.P. de Jesus, J.J.L. Morais, and J.L.P.C. Lousada. Quasi-static mechanical behaviour of a double-shear single dowel wood connection. *Construction and Building Materials*, 23(1):171–182, 2009. ISSN 0950-0618. doi: 10.1016/j.conbuildmat. 2008.01.005.

F.H. Schweinbruger. *Wood strucuture and environment.* Springer, 2007.

A. Shipsha and L.A. Berglund. Shear coupling effects on stress and strain distributions in wood subjected to transverse compression. *Composites Science and Technology*, 67 (7-8):1362–1369, 2007.

P. Simon. *Approche multiéchelle du comportement mécanique du bois dans le plan transverse.* PhD thesis, Institut national des sciences appliquées de Lyon, 2009.

W. T. Simpson. *Dry Kiln Operatorťs Manual.* US Department of Agriculture, Forest Products Laboratory, Madison, Wisconsin, w. t. simpson edition, August 1991. Agriculture hanbook 188.

A. Sliker and Y. Yu. Elastic constant for hardwoods measured from plate and tension tests. *Wood Fiber Science*, 25(1):8–22, 1993.

STEP. *Structures en bois aux états limites. Tome 1: Introduction à l'Eurocode 5, Matériaux et bases de calcul.* Eyrolles, 1996.

C.T. Sun and S.P. Berreth. A new end tab design for off-axis tension test of composite materials. *Journal of Composite Materials*, 22(8):766–779, 1998.

C.T. Sun and I. Chung. An oblique end-tab design for testing off-axis composite specimens. *Composites*, 24(8):619–623, 1993.

S. Thelandersson and H. J. Larsen. *Timber Engineering.* John Wyley & Sons, Ltd, 2003.

D. A. Tirrel, I. Aksay, E. Baer, P. D. Calvert, J. Capello, E. A. Dimarzio, E. A. Evans, J. Fessler, J. D. Hoffman, M. Jaffe, G. Mayer, V. C. Mow, and S. A. Waindwright. Hierarchical structures in biology as a guide for new materials technology. Technical report, National Academy of Sciences, USA, 1994.

A. Tsehaye, A.H. Buchanan, and J.C.F. Walker. Selecting trees for structural timber. *Holz als Roh- und Werkstoff*, 58(3):162–167, 2000.

G.T. Tsoumis. *Science and Technology of Wood: Structure, properties, utilization.* Van Nostrand Reinhold, 1991.

A. Voloshin and M. Arcan. Pure shear moduli of unidirectional fibre-reinforced materials. *Fibre Science and Technology*, 13(2):125–134, 1980.

D.E. Walrath and D.F. Adams. The Iosipescu shear test as applied to composite materials. *Experimental Mechanics*, 23(1):105–110, 1983.

J. Xavier. Caracterização do comportamento ao corte da madeira usando o ensaio de Iosipescu. Master's thesis, Universidade de Trás-os-Montes e Alto Douro, Vila Real, Portugal, 2003.

J. Xavier, J. Oliveira, J. Morais, P. Camanho, and F. Pierron. Measurement of the shear modulus of wood *pinus pinaster* Ait. by the Iosipescu test. In *Livro de Actas do VII Congresso Nacional de Mecânica Aplicada e Computacional*, Universidade de Évora, Portugal, 14 a 16 de Abril, 2003.

J.C. Xavier, N. Garrido, J. Oliveira, J. Morais, P. Camanho, and F. Pierron. A comparison between the Iosipescu and off-axis shear test methods for the characterization of *pinus pinaster* Ait. *Composites Part A: Applied Science and Manufacturing*, 35(7-8):827–840, 2004.

H. Yoshihara, H. Ohsaki, Y. Hubojima, and M. Ohta. Applicability of the Iosipescu shear test on the measurement of the shear properties of wood. *Journal of Wood Science*, 45 (1):24–29, 1999.

W. Zhang and A. Sliker. Measuring shear moduli in wood with small tension and compression samples. *Wood Fiber Science*, 23(1):58–68, 1991.

Chapter 2

Material parameter identification from full-field measurements

In this chapter, identification methods for extracting relevant constitutive parameters based on full-field measurements will be reviewed. Moreover, a survey on full-field optical techniques is presented, given emphasis on digital image correlation.

Contents

2.1   Identification methods

2.1.1   Introduction

The material parameters figuring in constitutive equations are determined experimentally using suitable mechanical tests (Hodgkinson, 2000). The typical inverse problem solved in experimental solid mechanics, is the characterisation of unknown constitutive parameters assuming to know specimen geometry, boundary conditions (or more precisely, resultant forces and moments) and the strains (or displacements). Standard tests are conventionally performed yielding to a homogeneous or simple state of stress-strain across the gauge area. Conveniently, this approach leads to closed-form solutions (explicit equations) relating the unknown material parameters to load and strain measurements (statically determined tests). In this case, punctual devices, such as strain gauges, are usually employed for measuring the strain state. However, in practice, the implementation of these tests can be difficult due to for instance end-effects, especially for anisotropic and heterogeneous materials (Pierron et al., 1998). Moreover, independent test methods are needed to deal with non-isotropic behaviour (Guitard, 1987), which demands an extra effort in both time and cost from a practical point of view.

The recent development of full-field optical techniques has enabled a new glance on mechanical tests for material characterisation (Grédiac, 2004). The basic assumption is that heterogeneous and complex strain fields are generated across the region of interest by proper specimen geometry and loading system. In this case, several material parameters can be activated at once in the mechanical response of the material (statically undetermined tests). By means of a suitable identification strategy all the involved material parameters can be determined. A few approaches exist in the literature for addressing this problem. A recent survey of this methods is presented in Avril et al. (2008). The most familiar approach may be the finite element model updating method (FEMUM). It consists in building a finite element model of the mechanical test and considering a cost function of the difference between numerical and experimental data (displacement or strain) over the region of interest. The minimisation of this cost function with respect to the unknown material parameters (design variables), iteratively updated in the model, provides the solution to the problem. This method is flexible and does not specifically require full-field measurements. However, as it is iterative, it can be time consuming and the convergence dependent on the initial guess of parameters. Moreover, accurate boundary conditions need to be modelled to avoid a bias on the identified parameters. The presence of noise in the measurements will also affect the robustness of the updating routine. To overcome the drawbacks associated to the FEMUM, alternative approaches have been proposed. Among them, there is for instance the anisotropic-based method (AbM) (Majano-Majano et al., 2012), and the virtual fields method (VFM) (Pierron and Grédiac, 2012). The principle of these identification strategies will be presented in the following

when applied to the global and local identification of the transverse elastic properties of wood at the meso scale based on ring-oriented tensile tests.

2.1.2 Ring-oriented tensile test at the meso scale

Standard tests for wood mechanical characterisation are based on simple specimen geometries and elementary loading cases relying on homogeneous or simple stress-strain states at the gauge section, in which closed-form solutions exists for parameter identification. Conversely, in this work, a single ring-oriented tensile test is proposed for the characterisation of wood properties in the transverse plane defined by the radial (R) and tangential (T) orthotropic directions. The mechanical model of this test method is schematically shown in Figure 2.1. A rectangular specimen with nominal dimensions L (length)$\times$ w (width) $\times$ b (thickness) ($b < w < L$) is submitted to a uniaxial stress state at its ends given by $\sigma_{xx}(t) = F(t)/wb$, where $F(t)$ is the resultant applied load at the instant t (measured experimentally using a load cell) and wb is the nominal cross-section area.

If a uniaxial tensile test is carried out on a prismatic specimen (Fig. 2.1(b)), the area integral of the longitudinal stress over each cross-section (free-body diagram) must be equal (in equilibrium) with the applied axial loading. This statement can be written as

$$\overline{\sigma}_{xx}(x,t) = \frac{1}{wb} \int_{-b/2}^{b/2} \int_{-w/2}^{w/2} \sigma_{xx}(x,y,z,t)dydz = \frac{F(t)}{wb} \tag{2.1}$$

where $\overline{\sigma}_{xx}(x,t)$ is the average longitudinal stress (engineering stress) at a given instant t, (y,z) are coordinates over the cross-section and x is the longitudinal axis along with tension is applied. It is worth noting that the integral constraint is less restrictive than the purely uniform stress assumption, since Eq. (2.1) is still valid even if σ_{xx} is not uniform across the cross-section. In plane stress assumption, σ_{xx} will be a function of only x and y coordinates. For a given cross-section, the equilibrium statement can then be written as

$$\int_{-w/2}^{w/2} \sigma_{xx}(x,y)dy = \frac{F}{b} \tag{2.2}$$

2.1.3 Anisotropic-based method

Let us assume a plane stress approach (i.e., $\sigma_{zz} = \sigma_{xz} = \sigma_{yz} = 0$). Moreover, polar coordinates r and θ will be used, as represented in Fig. 2.1(a); this coordinate system is more realistic with regard to the geometrical arrangement of the circumferential ring wood structure across the transverse plane. Cartesian and polar coordinates of a point P in the plane are simple related by
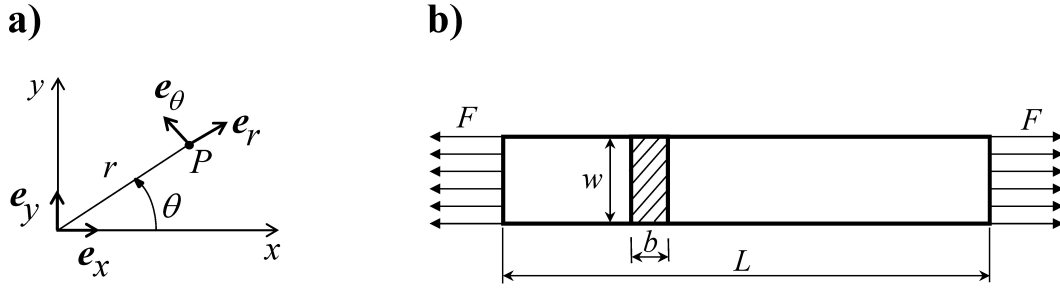
Figure 2.1: (a) polar coordinate system; (b) mechanical model of the tensile test.

$$x = r \cos \theta \quad \text{and} \quad y = r \sin \theta. \tag{2.3}$$

At a given point P on the plane, a polar orthonormal basis (e_r, e_θ) is defined by (Fig. 2.1(a))

$$\begin{Bmatrix} e_r \\ e_\theta \end{Bmatrix} = \begin{bmatrix} \cos \theta & \sin \theta \\ -\sin \theta & \cos \theta \end{bmatrix} \begin{Bmatrix} e_x \\ e_y \end{Bmatrix} = [Q] \begin{Bmatrix} e_x \\ e_y \end{Bmatrix} \tag{2.4}$$

where $[Q]$ represents the transformation matrix from cartesian to polar coordinates, in which the first and second rows contains, respectively, the cosine direction of the unit vectors e_r and e_θ in the Cartesian basis (e_x, e_y). This transformation matrix is proper-orthogonal: $[Q][Q]^T = [Q]^T[Q] = [I]$, with $\det([Q]) = 1$.

In a first approximation, it is assumed that the material is continuous, homogeneous and governed by a linear elastic orthotropic behaviour. In the case where material and specimen coordinate systems are coincident (*i.e.*, $\theta = 0$ in Fig. 2.1(b)), the Hooke's law writes as (in Voigt notation)

$$\begin{Bmatrix} \varepsilon_{rr} \\ \varepsilon_{\theta\theta} \\ \varepsilon_{r\theta} \end{Bmatrix} = \begin{bmatrix} S_{11} & S_{12} & 0 \\ S_{21} & S_{22} & 0 \\ 0 & 0 & S_{66} \end{bmatrix} \begin{Bmatrix} \sigma_{rr} \\ \sigma_{\theta\theta} \\ \sigma_{r\theta} \end{Bmatrix} \quad \Rightarrow \quad \{\bar{\varepsilon}\} = [\overline{S}] \{\bar{\sigma}\} \tag{2.5}$$

where $\{\bar{\varepsilon}\}$ is the reduced strain pseudo-vector, $\{\bar{\sigma}\}$ is the reduced stress pseudo-vector, and $[\overline{S}]$ is the reduced compliance matrix in the material coordinate system, defining at each material point a linear relationship between stress and strain. The components of the compliance matrix can be written explicitly as a function of engineering constants determined directly from experimental test methods as (Jones, 1999)

$$[\overline{S}] = \begin{bmatrix} 1/E_1 & -\nu_{21}/E_2 & 0 \\ -\nu_{12}/E_1 & 1/E_2 & 0 \\ 0 & 0 & 1/G_{12} \end{bmatrix}. \tag{2.6}$$

where E_i are Young's modulus, ν_{ij} the *Poisson*'s ration and G_{ij} the Shear modulus ($i, j = 1, 2$). Since the compliance matrix is symmetric ($S_{ij} = S_{ji}$), the following relationship must be verified $\nu_{ij}/E_i = \nu_{ji}/E_j$ ($i, j = 1,2$).

Let us move now to an off-axis tensile test configuration in which the material coordinates system (e_r, e_θ) has a given angle (the off-axis angle θ in Fig. 2.1(a)) with regard to the specimen coordinate system (e_x, e_y). In this case, the stress state in the material coordinate system (*e.g.*, polar coordinate system), $[\overline{\sigma}]$, is given with regard to the applied stress state, $[\overline{\sigma}']$, by the following transformation rule of second-order symmetric tensors

$$[\overline{\sigma}] = [Q][\overline{\sigma}'][Q]^T, \tag{2.7a}$$

with

$$[\overline{\sigma}] = \begin{bmatrix} \sigma_{rr} & \sigma_{r\theta} \\ \sigma_{r\theta} & \sigma_{\theta\theta} \end{bmatrix} \quad \text{and} \quad [\overline{\sigma}'] = \begin{bmatrix} \sigma_{xx} & \sigma_{xy} \\ \sigma_{xy} & \sigma_{yy} \end{bmatrix}. \tag{2.7b}$$

In Voigt notation, Eq. (2.7) writes (with $c = \cos\theta$; $s = \sin\theta$)

$$\begin{Bmatrix} \sigma_{rr} \\ \sigma_{\theta\theta} \\ \sigma_{r\theta} \end{Bmatrix} = \begin{bmatrix} c^2 & s^2 & 2cs \\ s^2 & c^2 & -2cs \\ -cs & cs & c^2 - s^2 \end{bmatrix} \begin{Bmatrix} \sigma_{xx} \\ \sigma_{yy} \\ \sigma_{xy} \end{Bmatrix} \quad \Rightarrow \quad \{\overline{\sigma}\} = [\overline{T_\sigma}] \{\overline{\sigma}'\}. \tag{2.8}$$

In the same way, the strain pseudo-vector (in Voigt notation) in the material coordinate system can be written as

$$\begin{Bmatrix} \varepsilon_{rr} \\ \varepsilon_{\theta\theta} \\ \varepsilon_{r\theta} \end{Bmatrix} = \begin{bmatrix} c^2 & s^2 & cs \\ s^2 & c^2 & -cs \\ -2cs & 2cs & c^2 - s^2 \end{bmatrix} \begin{Bmatrix} \varepsilon_{xx} \\ \varepsilon_{yy} \\ \varepsilon_{xy} \end{Bmatrix} \quad \Rightarrow \quad \{\overline{\varepsilon}\} = [\overline{T_\varepsilon}] \{\overline{\varepsilon}'\}. \tag{2.9}$$

The reduced transformation matrices of stress ($[\overline{T_\sigma}]$) and strain ($[\overline{T_\varepsilon}]$) satisfy the following properties

$$[\overline{T_\sigma}]^{-1} = [\overline{T_\varepsilon}]^T \quad \text{and} \quad [\overline{T_\varepsilon}]^{-1} = [\overline{T_\sigma}]^T. \tag{2.10}$$

The transformation of the compliance matrix $[\overline{S}]$, between material (e_r, e_θ) and specimen (e_x, e_y) coordinate systems, can be deduced from the above stress (Eqs. 2.8) and strain (Eqs. 2.9) transformations. Starting from Eq. (2.5) one gets

$$\{\overline{\varepsilon}\} = [\overline{S}] \{\overline{\sigma}\} \Leftrightarrow [\overline{T_\varepsilon}] \{\overline{\varepsilon}'\} = [\overline{S}][\overline{T_\sigma}] \{\overline{\sigma}'\} \Leftrightarrow \{\overline{\varepsilon}'\} = [\overline{T_\varepsilon}]^{-1}[\overline{S}][\overline{T_\sigma}] \{\overline{\sigma}'\}. \tag{2.11}$$

Therefore, in the off-axis configuration, the Hooke's law in the specimen coordinate system is given by

$$\begin{Bmatrix} \varepsilon_{xx} \\ \varepsilon_{yy} \\ \varepsilon_{xy} \end{Bmatrix} = \begin{bmatrix} S'_{11} & S'_{12} & S'_{16} \\ S'_{21} & S'_{22} & S'_{26} \\ S'_{16} & S'_{26} & S'_{66} \end{bmatrix} \begin{Bmatrix} \sigma_{xx} \\ \sigma_{yy} \\ \sigma_{xy} \end{Bmatrix} \quad \Rightarrow \quad \{\bar{\varepsilon}'\} = [\bar{S}']\{\bar{\sigma}'\} \tag{2.12a}$$

where,

$$[\bar{S}'] = [\bar{T}_\sigma]^T [S][\bar{T}_\sigma]. \tag{2.12b}$$

or in an expanding form

$$\begin{bmatrix} S'_{11} & S'_{12} & S'_{16} \\ S'_{21} & S'_{22} & S'_{26} \\ S'_{16} & S'_{26} & S'_{66} \end{bmatrix} = \begin{bmatrix} c^2 & s^2 & cs \\ s^2 & c^2 & -cs \\ -2cs & 2cs & c^2 - s^2 \end{bmatrix} \begin{bmatrix} S_{11} & S_{12} & 0 \\ S_{21} & S_{22} & 0 \\ 0 & 0 & S_{66} \end{bmatrix} \begin{bmatrix} c^2 & s^2 & cs \\ s^2 & c^2 & -cs \\ -2cs & 2cs & c^2 - s^2 \end{bmatrix}. \tag{2.12c}$$

The compliance matrix in the specimen coordinate system for an arbitrary off-angle configuration can be expressed as a function of engineering constants as (Jones, 1999)

$$[\bar{S}'] = \begin{bmatrix} 1/E_x & -\nu_{yx}/E_y & \eta_{x,xy}/G_{xy} \\ -\nu_{xy}/E_x & 1/E_y & \eta_{y,xy}/G_{xy} \\ \eta_{xy,x}/E_x & \eta_{xy,y}/E_y & 1/G_{xy} \end{bmatrix} \tag{2.13}$$

in which, by definition, $\eta_{i,ij} = \varepsilon_i/\varepsilon_{ij}$ and $\eta_{ij,i} = \varepsilon_{ij}/\varepsilon_i$. These constants are shear-extension coupling coefficients[1]. The coefficient $\eta_{i,ij}$ expresses the stretching in the i-direction caused by shear stress in the ij-plane, whilst $\eta_{ij,i}$ characterised the shearing in the ij-plane caused by normal stress in the i-direction.

From the anisotropic elasticity theory, it is possible to derive an explicit relationship linking unknown compliance coefficients with specimen dimensions, loading configuration and strain measurements as

$$\begin{bmatrix} c^2 & s^2 & cs \\ s^2 & c^2 & -cs \\ -2cs & 2cs & c^2 - s^2 \end{bmatrix} \begin{Bmatrix} \varepsilon_{xx} \\ \varepsilon_{yy} \\ \varepsilon_{xy} \end{Bmatrix} = \begin{bmatrix} S_{11} & S_{12} & 0 \\ S_{21} & S_{22} & 0 \\ 0 & 0 & S_{66} \end{bmatrix} \begin{bmatrix} c^2 & s^2 & 2cs \\ s^2 & c^2 & -2cs \\ -cs & cs & c^2 - s^2 \end{bmatrix} \begin{Bmatrix} \sigma_{xx} \\ \sigma_{yy} \\ \sigma_{xy} \end{Bmatrix} \tag{2.14a}$$

or, in compact form

$$[T_\varepsilon]\{\bar{\varepsilon}'\} = [S][T_\sigma]\{\bar{\sigma}'\} \tag{2.14b}$$

in which,

- $[T_\varepsilon]$ and $[T_\sigma]$: are transformation matrices whose elements are cosine directions defined in function of the off-axis angle between material and specimen coordinates systems;

---

[1]These constants can also be called coefficients of mutual influence.

- $\{\bar{\varepsilon}'\}$: lists the strain components across the gauge section;

- $\{\bar{\sigma}'\}$: is the applied stress state at the ends of the specimen.

In practice, the strain components at the gauge section ($\{\bar{\varepsilon}'\}$) can be determined by a suitable full-field optical method, as for instance, digital image correlation (see Section 2.2.2). Let us assume herein that a specimen with an off-axis configuration is submitted to a uniaxial stress ($\sigma_{yy} = \sigma_{xy} = 0$), as schematically represented in Fig. 2.1(b)

$$[\bar{\sigma}'] = \begin{bmatrix} \sigma_{xx} & 0 \\ 0 & 0 \end{bmatrix}. \tag{2.15}$$

The system of Eqs. (2.14) is undetermined since there are only three equations and eventually five unknowns (or at least four, if the compliance matrix symmetry is imposed at this stage). Let us rewrite Eqs. (2.14) as a function of the unknown compliance matrix as follows

$$\begin{bmatrix} \sigma_{xx}c^2 & \sigma_{xx}s^2 & 0 & 0 & 0 \\ 0 & 0 & \sigma_{xx}c^2 & \sigma_{xx}s^2 & 0 \\ 0 & 0 & 0 & 0 & -\sigma_{xx}cs \end{bmatrix} \begin{Bmatrix} S_{11} \\ S_{12} \\ S_{21} \\ S_{22} \\ S_{66} \end{Bmatrix} = \begin{Bmatrix} \varepsilon_{xx}c^2 + \varepsilon_{yy}s^2 + \varepsilon_{xy}cs \\ \varepsilon_{xx}s^2 + \varepsilon_{yy}c^2 - \varepsilon_{xy}cs \\ -2\varepsilon_{xx}cs + 2\varepsilon_{yy}cs + \varepsilon_{xy}(c^2 - s^2) \end{Bmatrix}$$

(2.16a)

or, in compact form

$$[A]\{S\} = \{b\} \tag{2.16b}$$

One way to solve the linear system of Eqs. (2.16) is carry out at least two independent tests with different off-axis angles

- Loading case 1 (off-axis angle θ_1): $[A^1]\{S\} = \{b^1\}$
- Loading case 2 (off-axis angle θ_2): $[A^2]\{S\} = \{b^2\}$

This approach yields to an overdetermined system of equations which can be solved with regard to the compliance components ($\{S\}$) using the concept of pseudo-inverse. Generically, if m loading cases are considered, Eqs. (2.16) write

$$\begin{bmatrix} [A^1] \\ [A^2] \\ \vdots \\ [A^m] \end{bmatrix} \{S\} = \begin{bmatrix} \{b^1\} \\ \{b^2\} \\ \vdots \\ \{b^m\} \end{bmatrix} \tag{2.17a}$$

or, in compact form

$$[R]\{S\} = \{q\}. \tag{2.17b}$$

Finally, Eqs. (2.17) can then be solved as

$$\{S\} = ([R]^T[R])^{-1}[R]^T\{q\}. \tag{2.18}$$

2.1.4 Virtual fields method

2.1.4.1 Constitutive equations

To start with, let us assume herein a plane stress approach (*e.g.*, $\sigma_{zz} = \sigma_{xz} = \sigma_{yz} = 0$). Moreover, polar coordinates r and θ will be used, as represented in Fig. 2.1(a); this coordinate system is more realistic with regard to the geometrical arrangement of the circumferential ring wood structure across the transverse plane. Cartesian and polar coordinates of a point P in the plane are simple related by

$$x = r\cos\theta \quad \text{and} \quad y = r\sin\theta. \tag{2.19}$$

At a given point P on the plane, a polar orthonormal basis (e_r, e_θ) is defined by (Fig. 2.1(a))

$$\begin{Bmatrix} e_r \\ e_\theta \end{Bmatrix} = \begin{bmatrix} \cos\theta & \sin\theta \\ -\sin\theta & \cos\theta \end{bmatrix} \begin{Bmatrix} e_x \\ e_y \end{Bmatrix} = [a] \begin{Bmatrix} e_x \\ e_y \end{Bmatrix} \tag{2.20}$$

where $[a]$ represents the transformation matrix from cartesian to polar coordinates, in which the first and second rows contains, respectively, the cosine direction of the unit vectors e_r and e_θ in the Cartesian basis (e_x, e_y). This transformation matrix is proper-orthogonal: $[a][a]^T = [a]^T[a] = [I]$, with $\det([a]) = 1$.

In a first approximation, it is assumed that the material is continuous, homogeneous and governed by a linear elastic orthotropic behaviour. In the case where material and specimen coordinate systems are coincident (*i.e.*, $\theta = 0$ in Fig. 2.1(b)), the Hooke's law can be written as (in Voigt notation)

$$\begin{Bmatrix} \sigma_{rr} \\ \sigma_{\theta\theta} \\ \sigma_{r\theta} \end{Bmatrix} = \begin{bmatrix} Q_{11} & Q_{12} & 0 \\ Q_{12} & Q_{22} & 0 \\ 0 & 0 & Q_{66} \end{bmatrix} \begin{Bmatrix} \varepsilon_{rr} \\ \varepsilon_{\theta\theta} \\ \varepsilon_{r\theta} \end{Bmatrix} \quad \Leftrightarrow \quad \{\sigma\} = [Q]\{\varepsilon\} \tag{2.21}$$

where $\{\sigma\}$ is the reduced stress pseudo-vector, $\{\varepsilon\}$ is the reduced strain pseudo-vector, and $[Q]$ is the reduced stiffness matrix in the material coordinate system, defining at each material point a linear relationship between stress and strain. The components of the stiffness matrix can be written explicitly as a function of engineering contacts determined directly from experimental test methods as (Jones, 1999)

$$Q_{11} = \frac{E_1}{1 - \nu_{21}\nu_{12}}, \quad Q_{22} = \frac{E_2}{1 - \nu_{21}\nu_{12}} \tag{2.22}$$

$$Q_{12} = \frac{\nu_{12}E_2}{1 - \nu_{21}\nu_{12}} = \frac{\nu_{21}E_1}{1 - \nu_{21}\nu_{12}}, \quad Q_{66} = G_{12}.$$

where E_i are Young's modulus, ν_{ij} the *Poisson*'s ration and G_{ij} the Shear modulus ($i, j = 1, 2$). Since the stiffness matrix is symmetric ($Q_{ij} = Q_{ji}$), the following relationship must be verified $\nu_{ij}/E_i = \nu_{ji}/E_j$ ($i, j = 1,2$).

Let us move now to an off-axis tensile test configuration in which the material coordinates system (e_r, e_θ) has a given angle (the off-axis angle θ in Fig. 2.1(a)) with regard to the specimen coordinate system (e_x, e_y). In this case, the stress state in the material coordinate system (*i.e.*, polar coordinate system), $[\sigma]$, is given with regard to the applied stress state, $[\sigma']$, by the following transformation rule of second-order symmetric tensors

$$[\sigma] = [a][\sigma'][a]^T, \tag{2.23a}$$

with

$$[\sigma] = \begin{bmatrix} \sigma_{rr} & \sigma_{r\theta} \\ \sigma_{r\theta} & \sigma_{\theta\theta} \end{bmatrix} \quad \text{and} \quad [\sigma'] = \begin{bmatrix} \sigma_{xx} & \sigma_{xy} \\ \sigma_{xy} & \sigma_{yy} \end{bmatrix}. \tag{2.23b}$$

In Voigt notation, Eq. (2.23) writes (with $c = \cos\theta$; $s = \sin\theta$)

$$\begin{Bmatrix} \sigma_{rr} \\ \sigma_{\theta\theta} \\ \sigma_{r\theta} \end{Bmatrix} = \begin{bmatrix} c^2 & s^2 & 2cs \\ s^2 & c^2 & -2cs \\ -cs & cs & c^2 - s^2 \end{bmatrix} \begin{Bmatrix} \sigma_{xx} \\ \sigma_{yy} \\ \sigma_{xy} \end{Bmatrix} \quad \Leftrightarrow \quad \{\sigma\} = [T_\sigma]\{\sigma'\}. \tag{2.24}$$

In the same way, the strain pseudo-vector (in Voigt notation) in the material coordinate system can be written as

$$\begin{Bmatrix} \varepsilon_{rr} \\ \varepsilon_{\theta\theta} \\ \varepsilon_{r\theta} \end{Bmatrix} = \begin{bmatrix} c^2 & s^2 & cs \\ s^2 & c^2 & -cs \\ -2cs & 2cs & c^2 - s^2 \end{bmatrix} \begin{Bmatrix} \varepsilon_{xx} \\ \varepsilon_{yy} \\ \varepsilon_{xy} \end{Bmatrix} \quad \Leftrightarrow \quad \{\varepsilon\} = [T_\varepsilon]\{\varepsilon'\}. \tag{2.25}$$

The reduced transformation matrices of stress ($[T_\sigma]$) and strain ($[T_\varepsilon]$) satisfy the following properties

$$[T_\sigma]^{-1} = [T_\varepsilon]^T \quad \text{and} \quad [T_\varepsilon]^{-1} = [T_\sigma]^T. \tag{2.26}$$

The transformation of the stiffness matrix $[Q]$, between material (e_r, e_θ) and specimen (e_x, e_y) coordinate systems, can be deduced from the above stress (Eqs. 2.24) and strain (Eqs. 2.25) transformations. Starting from Eq. (2.21) one gets

$$\{\sigma\} = [Q]\{\varepsilon\} \Leftrightarrow [T_\sigma]\{\sigma'\} = [Q][T_\varepsilon]\{\varepsilon'\} \Leftrightarrow \{\sigma'\} = [T_\varepsilon]^T[Q][T_\varepsilon]\{\varepsilon'\}. \quad (2.27)$$

Therefore, in the off-axis configuration, the Hooke's law in the specimen coordinate system is given by

$$\begin{Bmatrix} \varepsilon_{xx} \\ \varepsilon_{yy} \\ \varepsilon_{xy} \end{Bmatrix} = \begin{bmatrix} Q'_{11} & Q'_{12} & Q'_{16} \\ Q'_{12} & Q'_{22} & Q'_{26} \\ Q'_{16} & Q'_{26} & Q'_{66} \end{bmatrix} \begin{Bmatrix} \sigma_{xx} \\ \sigma_{yy} \\ \sigma_{xy} \end{Bmatrix} \quad \Leftrightarrow \quad \{\varepsilon'\} = [Q']\{\sigma'\} \qquad (2.28a)$$

where,

$$[Q'] = [T_\varepsilon]^T[Q][T_\varepsilon]. \qquad (2.28b)$$

or in an expanding form

$$\begin{bmatrix} Q'_{11} & Q'_{12} & Q'_{16} \\ Q'_{12} & Q'_{22} & Q'_{26} \\ Q'_{16} & Q'_{26} & Q'_{66} \end{bmatrix} = \begin{bmatrix} c^2 & s^2 & -2cs \\ s^2 & c^2 & 2cs \\ cs & -cs & c^2-s^2 \end{bmatrix} \begin{bmatrix} Q_{11} & Q_{12} & 0 \\ Q_{12} & Q_{22} & 0 \\ 0 & 0 & Q_{66} \end{bmatrix} \begin{bmatrix} c^2 & s^2 & cs \\ s^2 & c^2 & -cs \\ -2cs & 2cs & c^2-s^2 \end{bmatrix}.$$
$$(2.28c)$$

2.1.4.2   Growth ring segmentation

An image of the growth ring structure is shown in Fig. 2.2. This field of view corresponds to the region where full-field measurements will be provided (in this case using digital image correlation, see Section 2.2.2). The image of the growth ring structure will be analysed using image processing and analysis tools in order to identify each constituent in the structure. A binary or mask image can then be obtained, classifying earlywood (EW), latewood (LW) and resin channels (RC) subregions as schematically represented in Fig. 2.2. In a first approximation, resin channels will be removed and the identification performed on EW and LW tissues. It is chosen here to associate a given set of elastic properties ($[Q]$) to each sub-region. Therefore, the following relationship can be established

$$[Q(x,y)] = [Q^e]I_1 + [Q^l]I_2 \qquad (2.29a)$$

(where $e \equiv EW$ and $l \equiv LW$ for simplification) and

$$I_1 = \left[\frac{I(x,y) - I^l(x,y)}{I^e(x,y) - I^l(x,y)} \right], \quad I_2 = \left[\frac{I(x,y) - I^e(x,y)}{I^l(x,y) - I^e(x,y)} \right] \qquad (2.29b)$$

where $I(x,y)$ is the light intensity field (Fig. 2.2) and

$$I^e(x,y) = \begin{cases} 1 & \text{if } (x,y) \in \text{EW} \\ 0 & \text{otherwise} \end{cases}, \quad I^l(x,y) = \begin{cases} 1 & \text{if } (x,y) \in \text{LW} \\ 0 & \text{otherwise} \end{cases}. \quad (2.30)$$

2.1.4.3 Principle and choice of virtual fields

The virtual fields method (VFM) is based on the principle of virtual work (PVW). In absence of body forces and under static conditions, the PVW can be written as

$$\underbrace{-\int_V \sigma : \varepsilon^\star \, dV}_{W^\star_{int}} + \underbrace{\int_{\partial V} \mathbf{T} \cdot \mathbf{u}^\star \, dS}_{W^\star_{ext}} = 0 \quad (2.31)$$

where σ is the Cauchy stress tensor, $\varepsilon^\star$ is the virtual strain tensor, $\mathbf{T}$ is the vector of external surface tractions applied over the solid boundary ∂V and $\mathbf{u}^\star$ is the virtual displacement vector. Eq. (2.31) describes the static equilibrium of a body by balancing out the internal virtual work ($W^\star_{int}$) of internal loads and the external virtual work ($W^\star_{ext}$) of external loads, for any kinematically admissible (strain and displacement) virtual fields (*e.g.*, satisfying the boundary conditions and $\mathbf{u}^\star$ being a function of class C1).

Let us assume herein a uniaxial plane stress approach (Eq. 2.2). Under this assumption Eq. (2.31) simplify to

$$\int_{-w/2}^{w/2} \int_0^L \sigma_{xx} \varepsilon^\star_{xx} \, dxdy = \frac{1}{b} \int_{\partial V} \mathbf{T} \cdot \mathbf{u}^\star \, dS \quad (2.32)$$

where L is the length of the gauge section. In developing the VFM, a relevant constitutive equation must be assumed *a priori* and imputed in the PVW (Eq. 2.32). From Eqs. (2.21), (2.24), (2.25), (2.29), in the material coordinate system, the following relationship holds

$$[T_\sigma]\{\sigma'\} = [Q][T_\varepsilon]\{\varepsilon'\} \quad (2.33\text{a})$$
$$\Leftrightarrow \{\sigma'\} = [T_\varepsilon]^T[Q][T_\varepsilon]\{\varepsilon'\} \quad (2.33\text{b})$$
$$\Leftrightarrow \{\sigma'\} = [T_\varepsilon]^T([Q^e]I_1 + [Q^l]I_2)[T_\varepsilon]\{\varepsilon'\}. \quad (2.33\text{c})$$
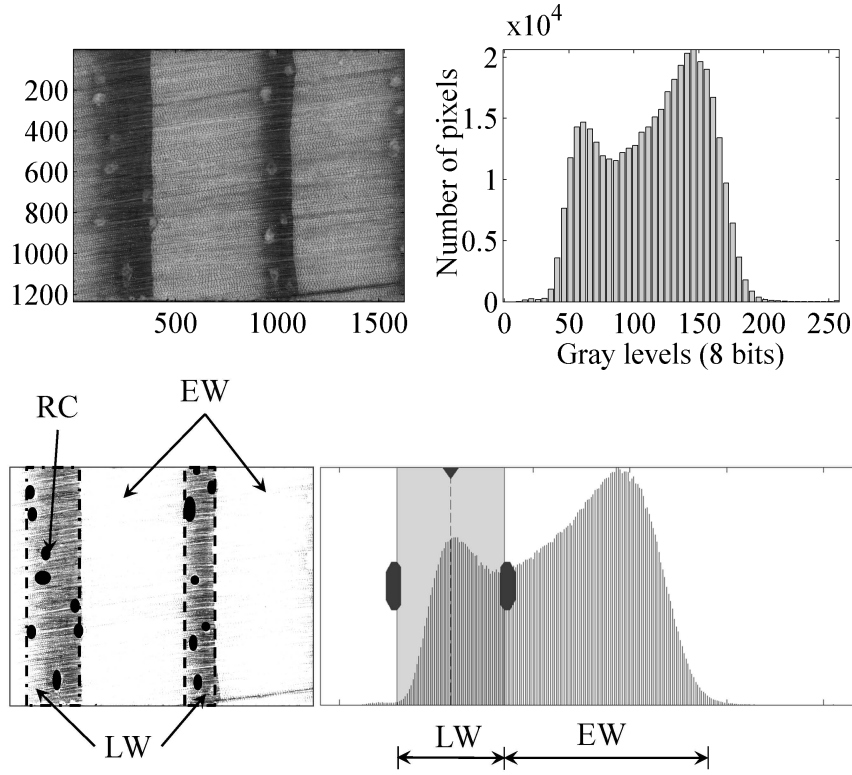
Figure 2.2: (up) growth ring structure: image and histogram; (bottom) illustration of the segmentation based on the histogram of the image.

From Eq. (2.33c), the σ_{xx} stress component can be written as

$$\sigma_{xx} = \{\varepsilon_I\}^T [T_I] \{Q_I\} \tag{2.34a}$$

where

$$\{\varepsilon_I\}_{[1\times6]} = \left\{ \varepsilon_{xx}I_1 \quad \varepsilon_{yy}I_1 \quad \varepsilon_{xy}I_1 \quad \varepsilon_{xx}I_2 \quad \varepsilon_{yy}I_2 \quad \varepsilon_{xy}I_2 \right\}^T \tag{2.34b}$$

and

$$[T_I]_{[6\times8]} = \begin{bmatrix} c^4 & s^4 & 0 & 0 & 0 & 0 & 0 & 0 \\ 0 & c^2s^2 & c^2s^2 & 0 & 0 & 0 & 0 & 0 \\ 0 & 0 & 0 & -2cs(c^2-s^2) & 0 & 0 & 0 & 0 \\ 0 & 0 & 0 & 0 & c^4 & s^4 & 0 & 0 \\ 0 & 0 & 0 & 0 & 0 & c^2s^2 & c^2s^2 & 0 \\ 0 & 0 & 0 & 0 & 0 & 0 & 0 & -2cs(c^2-s^2) \end{bmatrix} \tag{2.34c}$$

and

$$\{Q_I\}_{[8\times1]} = \left\{ Q_{11}^e \quad Q_{12}^e \quad Q_{22}^e \quad Q_{66}^e \quad Q_{11}^l \quad Q_{12}^l \quad Q_{22}^l \quad Q_{66}^l \right\}^T. \tag{2.34d}$$

Replacing Eq. (2.34a) into Eq. (2.32) the following equation is obtained

$$\int_{-w/2}^{w/2} \int_0^L \{\varepsilon_I\}^T [T_I] \{Q_I\} \varepsilon_{xx}^\star \, dxdy = \frac{1}{b} \int_{\partial V} \mathbf{T} \cdot \mathbf{u}^\star \, dS \qquad (2.35)$$

linking the unknown stiffness components for each EW and LW layers with strain field provided by some full-field optical technique, global growth ring orientation, specimen geometry, applied loading and any kinematically admissible virtual displacement and strain fields.

In order to solve Eq. (2.35) kinematically admissible virtual displacement and strain fields must be chosen. In a first approach, these virtual fields were chosen as summarised in Table 2.1. These virtual fields are illustrated in Fig. 2.3. Taking into account this set of virtual fields, Eq.(2.35) can be written for a given cross-section as

$$\int_{-w/2}^{w/2} \int_{x_0}^{x_0+\delta} \{\varepsilon_I\}^T [T_I] \{Q_I\} \, dxdy = \frac{\delta F(t)}{b} \qquad (2.36)$$

where δ represents the gauge length over which DIC measurements will be actually available (Fig. 2.3). In this case, the virtual fields were conveniently chosen to cancel out the integrals over the regions of the specimen were measurements were not provided. The integral forms in Eq.(2.36) can be approximated by summation (*e.g.* using rectangular method) assuming that enough spatial density of measurements is provided by DIC (spatial resolution)

$$\frac{1}{nm} \sum_{i=1}^n \sum_{j=1}^m \{\varepsilon_I(x_i, y_j)\}^T [T_I] \{Q_I\} = \frac{\delta F(t)}{b} \qquad (2.37)$$

where n and m are, respectively, the total number of data points in the horizontal and vertical directions obtained by DIC. This form of the VFM is equivalent to write that the average stress in each cross section is equal to the applied stress. Thus, for a given cross-section (x_i), Eq.(2.37) can be written as

$$\frac{1}{m} \sum_{j=1}^m \{\varepsilon_I(x_i, y_j)\}^T [T_I] \{Q_I\} = \frac{F(t)}{b} \quad \Leftrightarrow \quad [p_i]_{[1\times8]} \{Q_I\} = r. \qquad (2.38)$$

By taking all cross sections along the gauge length $(i = 1, \ldots, n)$ it follows that

Table 2.1: Selection of virtual fields (after (Sutton et al., 2008)).

Domain[a]	Virtual displacements	Virtual strains
▪ $0 < x < x_0$	$u_x^\star = 0$, $u_y^\star = 0$	$\varepsilon_{xx}^\star = 0$, $\varepsilon_{yy}^\star = 0$, $\varepsilon_{xy}^\star = 0$
▪ $x_0 < x < x_0 + \delta$	$u_x^\star = x$, $u_y^\star = 0$	$\varepsilon_{xx}^\star = 1$, $\varepsilon_{yy}^\star = 0$, $\varepsilon_{xy}^\star = 0$
▪ $x_0 + \delta < x < L$	$u_x^\star = \delta$, $u_y^\star = 0$	$\varepsilon_{xx}^\star = 0$, $\varepsilon_{yy}^\star = 0$, $\varepsilon_{xy}^\star = 0$

[a] where x_0 is a given location within the gauge length (L) and δ is any length such that $x_0 + \delta < L$.
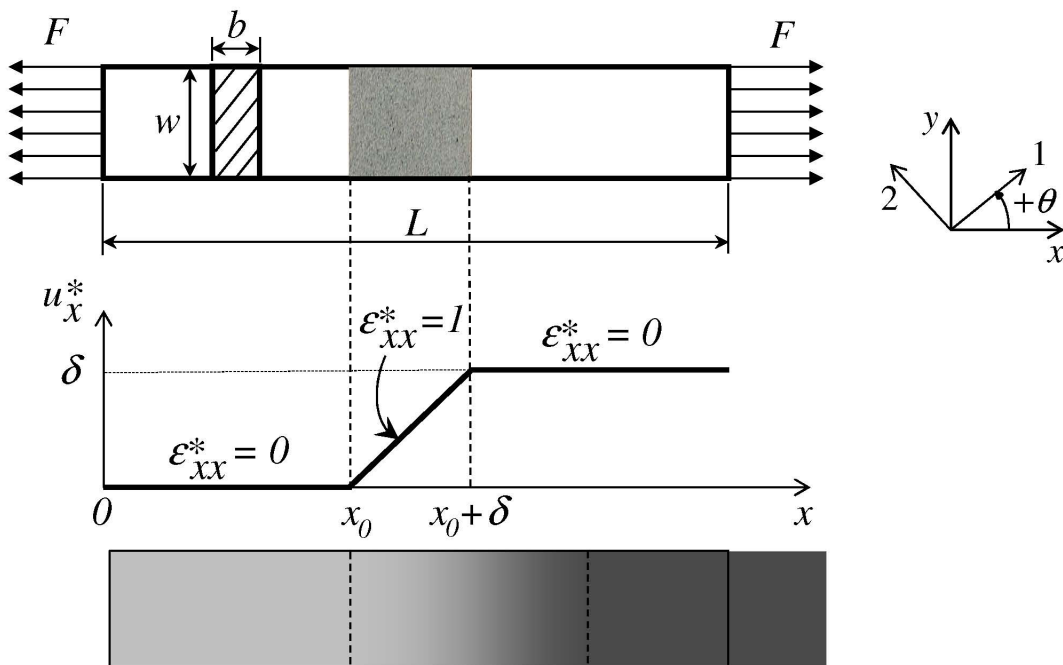

Figure 2.3: Mechanical model of the tensile test and illustration of the selected virtual fields.

$$\begin{bmatrix} [p_1] \\ \vdots \\ [p_n] \end{bmatrix} \{\overline{Q}\} = \begin{Bmatrix} r \\ \vdots \\ r \end{Bmatrix} \quad \Leftrightarrow \quad [P]_{[n\times 8]} \{Q_I\} = \{R\}_{[n\times 1]}. \tag{2.39}$$

Eq. (2.39) represents an overestimated system of equations that can be solved for the unknown orthotropic stiffness parameters of EW and LW constituents. For the purpose of identifiability and robustness of the method, however, additional information may be required for the full characterisation of material parameters. Therefore, for a given set of tests with different ring-orientation configurations, Eq. (2.39) can be built such as

$$\begin{bmatrix} [P_1] \\ \vdots \\ [P_t] \end{bmatrix} \{Q_I\} = \begin{Bmatrix} R_1 \\ \vdots \\ R_t \end{Bmatrix} \quad \Leftrightarrow \quad [\overline{P}]_{[(n\times t)\times 8]} \{Q_I\} = \{\overline{R}\}_{[(n\times t)\times 1]}. \tag{2.40}$$

where t is the total number of independent tests. This last equation can then be solved using the pseudo-inverse matrix as

$$\{Q_I\} = ([\overline{P}]^T [\overline{P}])^{-1} [\overline{P}]^T \{\overline{R}\}. \tag{2.41}$$

2.1.5 Conclusion

A new approach for material parameter characterisation based on full-field measurements was summarised in this section. Among different methods, the so-called anisotropic-based method and the virtual fields method were chosen for tackle the problem of identification of global and local transverse elastic properties of wood at the growth ring scale. The principle of these methods applied to the characterisation of wood at the meso scale was presented.

Table 2.2: Optical methods in experimental mechanics.

	White-light techniques	
Measurand[a]	Periodic pattern	Speckle pattern
u_x, u_y[b]	in-plane geometrical moiré (Cloud, 1995; Post et al., 1994)	digital speckle photography (Sjödahl, 1998)
	grid method (Surrel, 1999, 2004a)	digital image correlation (Pan et al., 2009b; Sutton et al., 2009)
	feature tracking method (Dahl and Malo, 2009; Franke et al., 2007)	
u_z	shadow and projection moiré (Cloud, 1995; Post et al., 1994)	–
	grid projection (Le Magorou et al., 2002)	–
u_x, u_y, u_z[c]	–	stereo-correlation (Orteu, 2009)
θ_x, θ_y[d]	reflection moiré (Cloud, 2006)	–
	deflectometry (Surrel, 2004b)	
	Interferometric techniques	
Measurand	Diffuse light	Diffracted light
u_x, u_y, u_z	speckle interferometry (Cloud, 1995)	moiré interferometry (Post et al., 1994)
ε_x, ε_y, ε_{xy}	speckle shearography (Hung and Ho, 2005)	grating shearography (Lee et al., 2004)

[a] u - displacement; θ - slope; ε - strain
[b] the in-plane (u_x, u_y) measurements are coupled with the out-of-plane (u_z) displacement
[c] the camera calibration is needed
[d] the slope measurements are coupled with position coordinates

2.2 Full-field optical techniques

2.2.1 Introduction

Experimental mechanics typically rely on surface deformation measurements (plane stress, plane strain or kinematic assumptions). Mechanical test methods are conventionally carried out using strain gauges (punctual) or extensometers (average). Data reduction schemes (closed-form solutions) are then proposed for determining material properties as a function of load, specimen dimensions and kinematic (displacement or strain) measurements (Hodgkinson, 2000). More recently, full-field optical methods of displacement and strain measurements have being proposed and increasingly used in experimental solid mechanics (Grédiac, 2004). In contrast to punctual or average techniques, these methods provide full-field data and are contact-free. A survey of these techniques is summarised in Table 2.2.

In white-light optical techniques, the geometrical deformation of a textured material surface is retrieved by analysing the spatial variation of light intensity observed during deformation (photometric measurements). It is assumed that the local luminance reflected at a given point is constant throughout the material deformation (optical flow constraint). Eventually, three classes of white-light techniques can be highlighted: (*i*) phase-measuring (based on periodic patterns); (*ii*) image correlation (based on random patterns); (*iii*) feature tracking (based on object marking) (Table 2.2).

The interferometric optical techniques are based on the phenomenon of interference of light waves. These methods require a monochromatic and coherent light source (*e.g.*, a laser). Considering the way light interacts with the material surface, these methods can be sorted into diffused light (speckle) and diffracted light (grating) interferometric techniques (Table 2.2). Speckle interferometry is based on the diffuse reflection of light from an optical rough surface, whereas grating interferometry is based on the diffraction of light over a grating on the object surface. Several configurations can be set-up by changing the directions of illumination and observation (sensitivity vector) for in-plane and out-of-plane displacement measurements. The moiré interferometry is a technique based on grating metrology allowing the measurement of both in-plane and out-of-plane displacements. Finally, shearography set-ups can be used (Table 2.2), providing directly the measurement of the (optical) derivatives of the displacement.

The selection of an optical method for a particular application may not be straightforward. Eventually, several guidelines can be considered taken into account the cost, the measurand (displacement, strain...), the scale of observation, the required performances (resolution, spatial resolution...), the simplicity of execution, and the expected values of deformation (*e.g.*, small or high strains). Among optical techniques (Table 2.2), digital image correlation (DIC) has becoming widely used (Pan et al., 2009b; Sutton et al., 2009). On the one hand, with regard to counterpart methods, this technique neither

requires specific and expensive optical devices (*e.g.*, lasers and anti-vibration tables) nor time-consuming surface preparation. On the other hand, DIC can be flexibly coupled with mechanical testing machines. Moreover, it can be conveniently applied from structural to micro or nano scale. In mechanical tests DIC-2D is usually used, whilst in structural applications DIC-3D (stereovision) can be preferable. The development of DIC has also followed closely the recent progress on computer science, automated image processing and digital cameras. In contrast with interferometric methods, phase analysis of the fringe images and phase unwrapping process are not required. Nevertheless, DIC measurements are usually unreliable near boundaries or discontinuities since subsets in the image are typically used for displacement evaluation through mathematical correlation (local approach). Taking into account the aforementioned considerations, in this work, the DIC method was deemed suitable for analysing the wood deformation at the growth ring scale. In the following, a review of the local approach of the DIC-2D method is presented.

2.2.2   Digital image correlation

A schematic representation of the photo-mechanical set-up coupling DIC-2D with a mechanical test is shown in Figure 2.4. A (quasi-)planar target object is imaged by a camera-lens optical system connected to a computer for real-time visualisation. In the DIC method the displacement of an object is measured by correlating images of the surface recorded at successive deformation stages. It is assumed that the surface of interest has a local, random textured pattern uniquely characterising the material surface. In estimating the object motion, the pinhole camera model (perspective projection) can be considered. It is defined by the magnification of the imaging system (mm/pixel), which is assumed constant during image acquisition (*e.g.*, out-of-plane movements are neglected and the object undergo only in-plane deformation). Besides, geometrical distortion induced by optical aberrations are assumed either negligible (differential measurements) or taken into account by a distortion correction method. After image recording, a matching (correlation) process is carried out between images taken before and after deformation as schematically shown in Figure 2.5. The reference (undeformed) image is divided by square or rectangular subsets with size $\Omega \equiv (2M + 1) \times (2N + 1)$ pixels, where M and N are number of pixels in the x and y image directions, respectively (Figure 2.5). In order to enhance the displacement spatial resolution (defined as the smaller distance separating two independent displacement measurements), subsets can slightly overlap by sharing some pixels. In this case, the subset step (f_d) will be smaller than the subset size (f_s). Adjacent ($f_s = f_d$) or spaced ($f_s < f_d$) subsets can also be selected depending on the purpose. The selection of these measuring parameters is a key issue because they will contribute to the spatial resolution (Δu) and the resolution (σ_u) associated to DIC measurements. Therefore, they should then be carefully chosen with regard to the application, in a com-

promise between correlation (small subsets) and interpolation (large subsets) errors. By locally minimising the difference on light intensity distribution between a pair of images, subset mapping in the deformed image is calculated allowing the definition of full-field displacements (a displacement vector is conventionally attached to each subset, $P(x_0, y_0)$ in Figure 2.5).

Several mathematical correlation criteria have been proposed for estimation of the displacement fields in the subset matching process. It has been shown that the zero-normalized sum of squared differences (ZNSSD) is a robust algorithm since it take into account offset and linear scale variations of light intensity and is most efficient when using iterative procedure for the minimisation problem (Pan et al., 2009b)

$$C_{\text{ZNSSD}}(\mathbf{p}) = \sum_\Omega \left[\frac{f(x_i, y_i) - f_m}{\sqrt{\sum_\Omega \left[f(x_i, y_i) - f_m \right]^2}} - \frac{g(x_i', y_j') - g_m}{\sqrt{\sum_\Omega \left[g(x_i', y_j') - g_m \right]^2}} \right]^2 \tag{2.42}$$

where Ω is the subset domain, $f(x_i, y_j)$ is the pixel grey level at (x_i, y_j) in the reference image, $g(x_i', y_j')$ is the pixel grey level at (x_i', y_j') in the deformed image, and f_m and g_m are the mean gray-level values over the subset in reference and deformed image, respectively, given by

$$f_m = \frac{1}{(2M+1)^2} \sum_{i=-M}^{i=M} \sum_{i=-N}^{i=N} f(x_i, y_j) \tag{2.43a}$$

$$g_m = \frac{1}{(2N+1)^2} \sum_{i=-M}^{i=M} \sum_{i=-N}^{i=N} g(x_i', y_j') \tag{2.43b}$$

Eq. (2.42) has to be solved (minimised) with regard to the deformation parameter ($\mathbf{p}$) which will characterise the mapping function (shape function). Both first-order and second-order shape functions have been commonly used, given respectively by (Pan et al., 2009b)

$$\begin{cases} x_i' - x_i = u_0 + \mathbf{u_1}^T \mathbf{d} \\ y_j' - y_j = v_0 + \mathbf{v_1}^T \mathbf{d} \end{cases} \tag{2.44}$$

with $\mathbf{u_1} = \left\{ \frac{\partial u}{\partial x}, \frac{\partial u}{\partial y} \right\}^T$, $\mathbf{v_1} = \left\{ \frac{\partial v}{\partial x}, \frac{\partial v}{\partial y} \right\}^T$, $\mathbf{d} = \{x_i - x_0, y_j - y_0\}^T$ and $\mathbf{p} = \{u_0, v_0, \mathbf{u_1}, \mathbf{v_1}\}^T$; and

$$\begin{cases} x_i' - x = u_0 + \mathbf{u_1}^T \mathbf{d} + \frac{1}{2} \mathbf{d}^T \mathbf{u_2} \mathbf{d} \\ y_j' - y = v_0 + \mathbf{v_1}^T \mathbf{d} + \frac{1}{2} \mathbf{d}^T \mathbf{v_2} \mathbf{d} \end{cases} \tag{2.45}$$
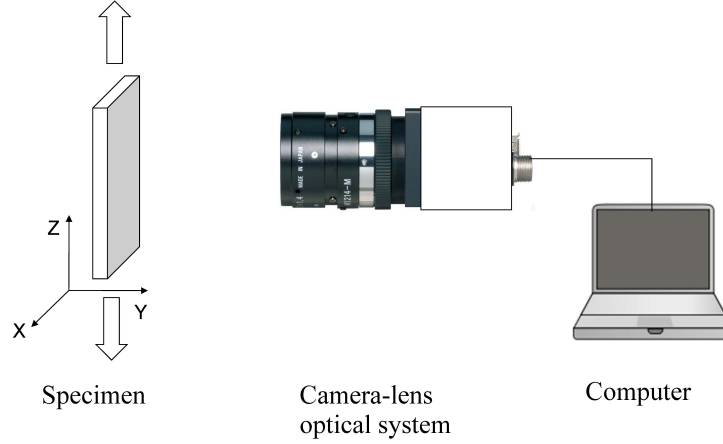
Figure 2.4: Photo-mechanical setup of the digital image correlation.

where $\mathbf{u_2} = [\frac{\partial u^2}{\partial x^2}, \frac{\partial u^2}{\partial x \partial y}; \frac{\partial u^2}{\partial x \partial y}, \frac{\partial v^2}{\partial y^2}]$, $\mathbf{v_2} = [\frac{\partial v^2}{\partial x^2}, \frac{\partial v^2}{\partial x \partial y}; \frac{\partial v^2}{\partial x \partial y}, \frac{\partial v^2}{\partial y^2}]$ and $\mathbf{p} = (u_0, v_0, \mathbf{u_1}, \mathbf{u_2}, \mathbf{v_1}, \mathbf{v_2})$. Iterative algorithm, *e.g.* Newton-Raphson or Levenberg-Marquardt, can then be used for finding optimal deformation parameter optimising the correlation coefficient (Bing et al., 2006; Pan et al., 2009b).

2.2.3   Strain field reconstruction

The digital image correlation technique provides displacements over a large set of discrete data points over a region of interest. Continuous strain fields, required in the parameter identification problem, are to be determined from this type of noisy displacements. Therefore, a suitable technique must be used to derive the strain field from the measured displacement field, according to the following relationships

$$
\begin{aligned}
\varepsilon_1(x, y) &= \frac{\partial u_x(x, y)}{\partial x} \\
\varepsilon_2(x, y) &= \frac{\partial u_y(x, y)}{\partial y} \\
\varepsilon_6(x, y) &= \frac{\partial u_x(x, y)}{\partial y} + \frac{\partial u_y(x, y)}{\partial x}.
\end{aligned}
\tag{2.46}
$$

It is worth noticing that the numerical differentiation of the measured displacement fields (Eqs. 2.46) is not straightforward since this procedure can amplify noise. For instance, direct differentiation using finite differences can lead to a strain resolution in the range of 10^{-3} (*e.g.*, for a displacement resolution of about 10^{-2} and a strain step of 5 subsets, a strain resolution of 2×10^{-3} is obtained using central finite differences), which is normally to high for practical use in mechanical tests. Several strategies can be then used to solve Eqs. (2.46). Most of them consists in approximating the data points using smooth

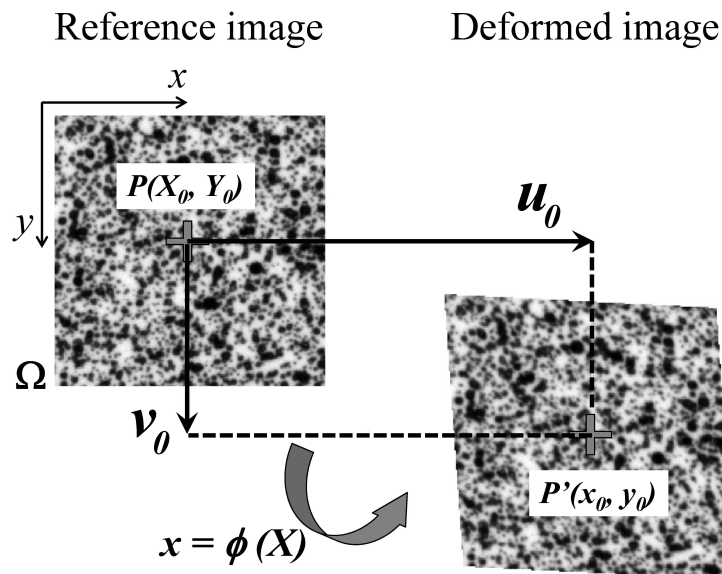Reference image   Deformed image

Figure 2.5: Principle of the digital image correlation technique.

basis functions. The differentiation of the data is then based on the differentiation of the approximated basis functions in the least-square sense. Generically these methods can be sorted on global and local strategies. Global approaches can be developed using 2D polynomial basis functions (Cordero and Roth, 2005; Pannier et al., 2006; Xavier et al., 2007), nonuniform rational B-spline (NURBS) basis functions (Elguedj et al., 2011; Réthoré et al., 2010) and global least-squares minimization using finite element shape basis functions (Avril et al., 2010). Local approaches can be developed using polynomial diffuse approximation (Avril et al., 2010), moving lest-squares (MLS) methods (Xiang et al., 2007), and point-wise local least-squares fitting (Pan et al., 2009a; Wattrisse et al., 2001). In order to capture the strain localisation due to the different constituents observed at the growth ring scale (namely, earlywood and latewood), this former local method was selected in this work. This approach used a first order shape function to locally approximate the displacement field measured by DIC. In this approach the regularisation parameters is the size of the strain window: $(2m + 1) \times (2m + 1)$. The value of m must be chosen in a compromise between level of low-pass filtering and accuracy of the representativeness of the strain field.

2.2.4 Conclusion

In this section, a brief survey of full-field optical methods was presented. Focus was given to the digital image correlation method, since this technique was chosen for this work. The basic principle of DIC as well as the numerical reconstruction of strain fields were presented. Identification methods such as VFM require full-field information, hence the relevance of using DIC.

References

S. Avril, M. Bonnet, A.-S. Bretelle, M. Grédiac, F. Hild, P. Ienny, F. Latourte, D. Lemosse, S. Pagano, E. Pagnacco, and F. Pierron. Overview of identification methods of mechanical parameters based on full-field measurements. *Experimental Mechanics*, 48(4): 381–402, 2008.

S. Avril, P. Feissel, F. Pierron, and P. Villon. Comparison of two approaches for differentiating full-field data in solid mechanics. *Measurement Science and Technology*, 21(1): 015703, 2010.

P. Bing, X. Hui-min, X. Bo-qin, and D. Fu-long. Performance of sub-pixel registration algorithms in digital image correlation. *Measurement Science and Technology*, 17(6): 1615–1621, 2006.

G.L. Cloud. Optical methods in experimental mechanics. Part 23: Reflection moiré. *Experimental Techniques*, 30(5):19–22, 2006.

G.L. Cloud. *Optical methods of engineering analysis*. Cambridge University Press, New York, 1995.

R.R. Cordero and P. Roth. On two methods to evaluate the uncertainty of derivatives calculated from polynomials fitted to experimental data. *Metrologia*, 42(1):39–44, 2005.

K.B. Dahl and K.A. Malo. Planar strain measurements on wood specimens. *Experimental Mechanics*, 49(4):575– 586, 2009.

Thomas Elguedj, Julien Réthoré, and Aurélien Buteri. Isogeometric analysis for strain field measurements. *Computer Methods in Applied Mechanics and Engineering*, 200: 40–56, 2011.

S. Franke, B. Franke, and K. Rautenstrauch. Strain analysis of wood components by close range photogrammetry. *Materials and Structures*, 40:37–46, 2007.

M. Grédiac. The use of full-field measurement methods in composite material characterization: Interest and limitations. *Composites Part A: Applied Science and Manufacturing*, 35(7-8):751–761, 2004.

D. Guitard. *Mécanique du matériau bois et composites*. Cepaduès-Editions, Collection Nabla, 1987.

J.M. Hodgkinson. *Mechanical testing of advanced fibre composites*. Cambridge, Woodhead Publishing Limited, 2000.

Y.Y. Hung and H.P. Ho. Shearography: An optical measurement technique and applications. *Materials Science and Engineering*, 49(3):61–87, 2005.

R. M. Jones. *Mechanics of composite materials*. Taylor and Francis, 2nd edition, 1999.

L. Le Magorou, F. Bos, and F. Rouger. Identification of constitutive laws for wood-based panels by means of an inverse method. *Composite Science and Technology*, 62 (4):591–596, 2002.

J.-R. Lee, J. Molimard, A. Vautrin, and Y. Surrel. Digital phase-shifting grating shearography for experimental analysis of fabric composites under tension. *Composites Part A: Applied Science and Manufacturing*, 35(7-8):849–859, 2004.

A. Majano-Majano, J. Fernandez-Cabo, S. Hoheisel, and M. Klein. A test method for characterizing clear wood using a single specimen. *Experimental Mechanics*, 52:1079–1096, 2012.

J.-J. Orteu. 3-D computer vision in experimental mechanics. *Optics and Lasers in Engineering*, 47(3-4):282–291, 2009.

B. Pan, A. Asundi, H. Xie, and J. Gao. Digital image correlation using iterative least squares and pointwise least squares for displacement field and strain field measurements. *Optics and Lasers in Engineering*, 47(7-8):865–874, 2009a.

B. Pan, K. Qian, H. Xie, and A. Asundi. Two-dimensional digital image correlation for in-plane displacement and strain measurement: a review. *Measurement Science and Technology*, 20(6):062001, 2009b.

Y. Pannier, S. Avril, R. Rotinat, and F. Pierron. Identification of the elastic-plastic constitutive parameters from statically undetermined tests using the Virtual Fields Method. *Experimental Mechanics*, 46(6):735–755, 2006.

F. Pierron and M. Grédiac. *The Virtual Fields Method*. Springer New York, 2012.

F. Pierron, E. Alloba, Y. Surrel, and A. Vautrin. Whole-field assessment of the effects of boundary conditions on the strain field in off-axis tensile testing of unidirectional composites. *Composites Science and Technology*, 58(12):1939–1947, 1998.

D. Post, G. Han, and P. Ifju. *High sensitivity moiré*. Springer Verlag, New York, 1994.

J. Réthoré, T. Elguedj, P. Simon, and M. Coret. On the use of nurbs functions for displacement derivatives measurement by digital image correlation. *Experimental Mechanics*, 50(7):1099–1116, 2010.

M. Sjödahl. Some recent advances in electronic speckle photography. *Optics and Lasers in Engineering*, 29(2-3):125–144, 1998.

Y. Surrel. Fringe analysis. In P.K. Rastogi, editor, *Photomechanics (Topics in Applied Physics)*, pages 57–104. Springer Verlag, 1999.

Y. Surrel. La technique de la grille pour la mesure de champs de déplacements et ses applications. *Instrumentation, Mesure, Métrologie*, 4(3-4):193–216, 2004a.

Y. Surrel. Deflectometry: A simple and effecient noninterferometric method for slope measurement. In *Xth SEM International Congress on Experimental Mechanics*. Society for Experimental Mechanics, 7-10 June in Costa Mesa, California, USA, 2004b.

M.A. Sutton, J. Yan, S. Avril, F. Pierron, and S. Adeeb. Identification of heterogeneous constitutive parameters in a welded specimen: Uniform stress and virtual fields methods for material property estimation. *Experimental Mechanics*, 48(4):451–464, 2008.

M.A. Sutton, J.-J. Orteu, and H. Schreier. *Image correlation for shape, motion and*

deformation measurements: Basic concepts, theory and applications. Springer, 2009.

B. Wattrisse, A. Chrysochoos, J.-M. Muracciole, and M. Némoz-Gaillard. Analysis of strain localization during tensile tests by digital image correlation. *Experimental Mechanics*, 41(1):29–39, 2001.

J. Xavier, S. Avril, F. Pierron, and J. Morais. Novel experimental approach for longitudinal-radial stiffness characterisation of clear wood by a single test. *Holzforschung*, 61(5):573–581, 2007.

G.F. Xiang, Q.C. Zhang, H.W. Liu, X.P. Wu, and X.Y. Ju. Time-resolved deformation measurements of the portevinŰle chatelier bands. *Scripta Materialia*, 56(8):721–724, 2007.

Chapter 3

Experimental work

This chapter describes the procedures of the experimental work carried out in the framework of this thesis. To start with, the selection, manufacturing and preparation of the wood material is presented. X-ray microdensitometry measurements are then described. To end with, the experimental set-up of the mechanical test coupled with the digital image correlation technique is carefully presented.

Contents

3.1   Material and specimens

3.1.1   Samples geometry

Standard tests for wood mechanical characterisation are based on simple specimen geometries and elementary loading cases relying on homogeneous or simple stress-strain states at the gauge section, in which closed-form solutions exists for parameter identification. Conversely, in this work, a single ring-oriented test method is proposed for the full characterisation of wood properties in the transverse plane defined by the radial (R) and tangential (T) orthotropic directions: E_R, E_T, ν_{RT} and G_{RT} where E, ν and G stand for *Young*'s modulus, *Poisson*'s ration and shear modulus, respectively. A schematic representation of the test method is presented on Figure 3.1. The specimen consists of a parallelepiped specimen with the dimensions of 50(R)×5(T)×2(L) mm. This solution has been adopted taking advantage of a particular orientation of the annual growth rings with regard to the loading axis, defined by an average angle θ (Fig. 3.1).

3.1.2   Trees selection and sampling

As it is well known, mostly of the Portuguese forest is not ordered, *i.e.*, is not subject to forestry management that lead to a favouring of the quality of its main raw material, that is wood. The stands of pine, except as the occasional patches of pine forest of Leiria, also did not escape this reality. Therefore, in this study, like others before (Garrido, 2004; Oliveira, 2004; Pereira, 2005; Xavier, 2003), we tried to use wood that would be representative of the majority that we can buy in commercial distribution, although we consider that it would be very important to change the mindset of the owners so as not systematically slaughtered best trees for use with low economic value, and even more to spread the advantages of performing thinning, and pruning to ensure some homogeneity between individuals of the farm, as a way of adding value to timber.

The material used in this study was obtained from five trees of *Pinus pinaster*, from a private stand located in Orgens in the municipality of Viseu (central-northern Portugal). In a first step, to the selection of the tree, based on the macroscopic morphology of the key shaft such as the absence of defects of structure, the absence of disease, higher or lower vertical linear taper of the stem (Carvalho, 1996).

After felled trees, aged between 65 and 70 years, they were split into several logs, having been selected for this work, only the basal logs of each, with 2.8 meters long, because they are considered to provide the best quality wood in the tree. Each log was numbered from 1 to 5 and transported to the sawmill, where was been outspread on to 40 mm thickness boards, following a continuous output sawing methodology held parallel to the line identified in diametrical cross section of the stem, with the aim to minimize the number of samples containing reaction wood.
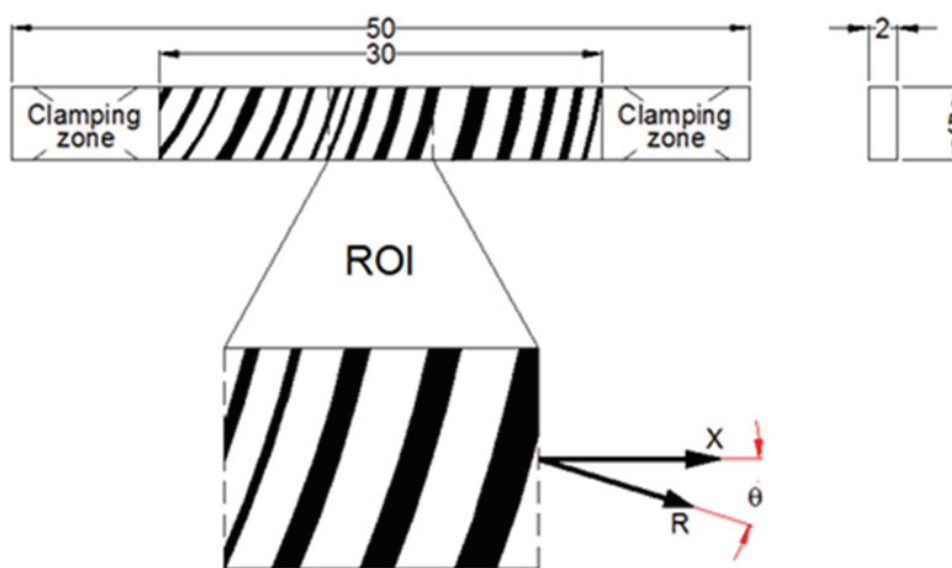
Figure 3.1: Sampling geometry for ring-oriented tensile test.

These boards, after being piled in order to reconstitute each log (Fig. 3.2) were subjected to natural drying process, monitored by regular measurements with a GANN® HT 85T hygrometer, until reaching a moisture content between 10 and 12% and then stored in the Laboratory of Wood and Furniture Industries Technologies of the School of Technology and Management of the Polytechnic Institute of Viseu, where were conditioned until samples manufacture.

3.1.3 Specimens sampling and manufacture

In each one of the logs already deployed, we selected the central plank, containing the pith, in which the positions to get the samples were defined and marked, both for the mechanical tests and for density measurements. According to the publications reviewed and in order to maximize the effects of longitudinal an radial variability at each stem selected, three positions in the longitudinal (L) direction (named L1, L2 and L3) were defined, as shown in Figure 3.3, and 5 positions in the radial (R) direction (designated R1, ..., R5) where established, as shown in Figure 3.4, and for each one of these radial positions 10 specimens were obtained with different ring orientations in order to take advantage of the natural heterogeneity (see table xx)

The three positions in height were identified and numbered in ascending order, towards the base of the tree to the crown, corresponding the L1 level to a height of 500 mm, the L2 level to a height of 1300 mm (DBH) and the L3 level to a height of 2300 mm.

In each of these height levels, after identifying the side of the board presenting a more regular and homogeneous rings distribution, in order to foil the presence of reaction wood
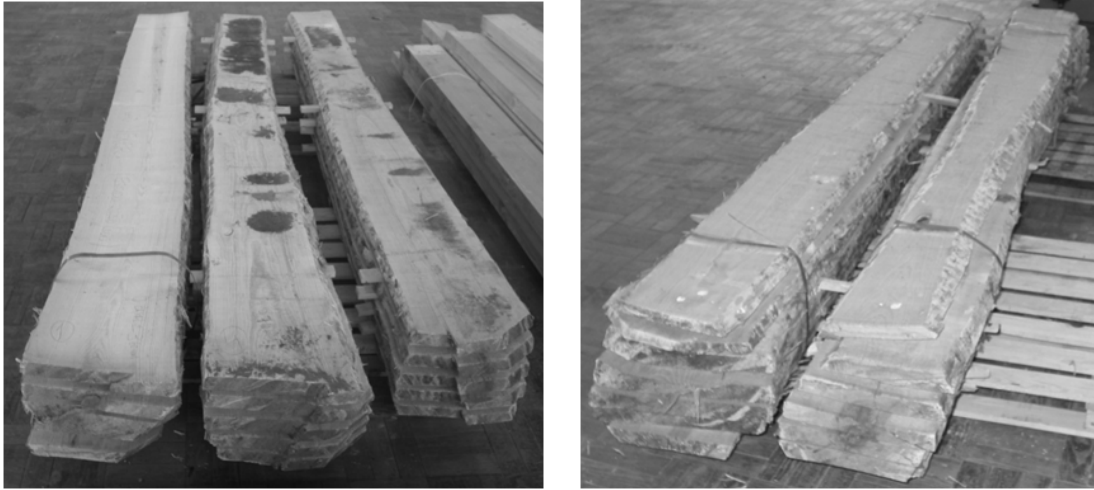
Figure 3.2: Logs after being sawn and dried.
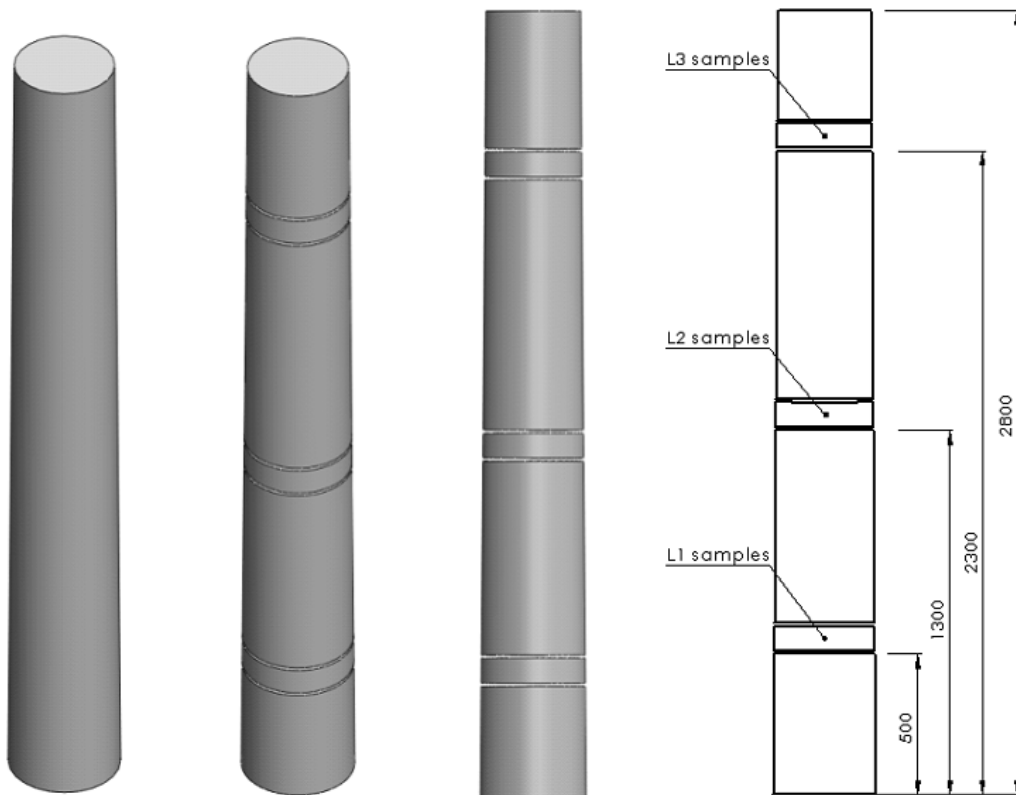
Figure 3.3: Sampling for along height variability on stem.
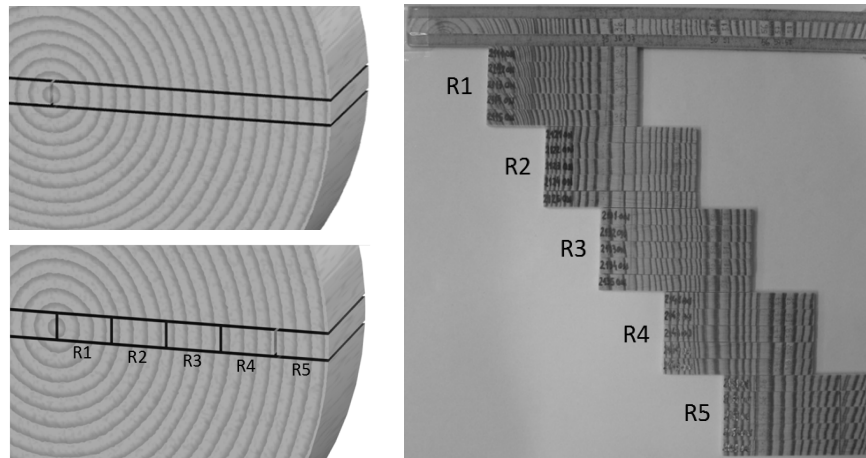
Figure 3.4: Sampling for radial variability on stem.

(compression wood), sixteen radial strips of wood were cut, containing all rings from the pith to the bark, with a length approximately equal to the radius of the stem (R direction) of about 3 mm thickness (L direction) and 5 mm width (T direction) as illustrated in Figure 3.4. One of these radial strips was used for density measurements (§ 3.2) and the other fifteen were used to obtain the specimens for mechanical tests. In this case, in each strip, five radial positions were identified and numbered in ascending order from the pith to the bark, each one corresponding to about 20% of the total length, from which we get a total of 10 specimens, in two groups of five with two main ring orientations, ensuring that its mid sections coincide with the radial position identified. Since the total length of five samples exceeded the radial length of the strip obtained we adopted a procedure of overlapping the specimens to ensure radial characterization of wood in the five positions identified (Fig. 3.4).

For ease of specimens identification for mechanical tests, a six-digit code was adopted, which identifies the tree, the height position, the radial position, the number of specimen and the orientation of growth rings in relation to the radial direction of material symmetry (Figure 3.5). Thus, the first digit ranges from 1 to 5, the second digit ranges from 1 to 3, the third digit ranges from 1 to 5, the fourth digit ranges from 0 to 9 and the last two will have two text options: ON or OF, concerning to ring orientation. For example, a specimen named 3241ON, was taken from the third tree (3), at breast height (2), from the fourth radial position (4), is specimen number (1) and has rings oriented next to the radial direction of material symmetry (ON). Resuming, for this study 15 specimens were manufactured to perform density measurements, corresponding to the five trees and the three height positions for each, and 750 specimens for mechanical tests, corresponding to the five trees, three height positions, five radial positions and ten specimens for each radial position. After obtaining the specimens for mechanical tests, we proceeded to the registration of its dimensions, using a Mitutoyo® digital caliper with a resolution of 0.01

mm and an accuracy of 0.02 mm.

3.2   X-ray microdensitometry measurements

3.2.1   Wood density

Despite density has been used for a long time as one of the most important property to characterize wood, is assumed as a feature widely floating, since it can vary not only from one species to another in a considerable proportion, but at the same species depending on the tree location, on the tree age, on the height level inside the stem, on the characteristics of ring formation year and, inside of the ring, on the season it was formed (spring or summer).

The variation of wood average density in softwoods (0.4 - 0.7 g.cm^{-3}) is not as high as between hardwoods (0.2 - 1.2 g.cm^{-3}). Although this variability, to the woody cell wall material is assigned a constant value of 1.5 g.cm^{-3} (Skaar, 1989) or 1.53 g.cm^{-3} (Tsoumis and Passialis, 1977), regarding the authors. So the differences just can be related to the differences in the wall/empty space proportions.

For *P. pinaster*, wood density variation inside the annual ring is normally considered between 0.4 and 0.9 g.cm^{-3} (Lousada, 2000) and it results from the differences between EW and LW layers, namely the ratio between cellular wall volume and the overall cellular volume.

3.2.2   X-ray microdensitometer technique

Traditional methods for density determining, based on weight/volume ratio are conditioned to application on specimens with measurable dimensions by traditional ways and gives only mean values for a given volume of wood. Furthermore, over the years has emerged the need for a more detailed characterization, namely between different rings and inside rings. Since the 60's, several techniques based on wood permeability to radiations have been developed, allowing determining, in addition to average density, several other density parameters, such as EW mean density (D_{EW}), LW mean density (D_{LW}), maximum density (D_{max}), minimum density (D_{min}) and the respective dimensions and fractions of EW and LW layers within the growth ring, namely, ring width ($Ring_W$), EW percentage (%EW), EW width (EW_W), LW percentage (%LW), LW width (LW_W) and heterogeneity index (HI). We apply a technique that takes advantage of wood permeability to x-rays. The main equipments, installed on the Forest Products Laboratory of UTAD, consist of a Joyce Loebl MK3 double-beam microdensitometer, equipped with a Seifert ISO-Debyeflex 1001 X-ray generator. The main advantages of this technique are the high sensitivity of the microdensitometer photomultiplier, the high resolution ca-
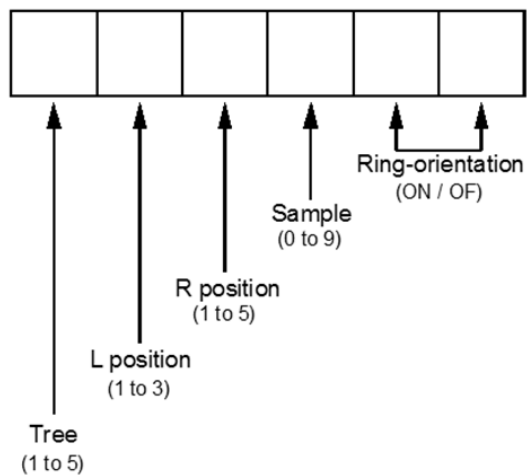
Figure 3.5: Samples codification and numbering scheme.

(a)
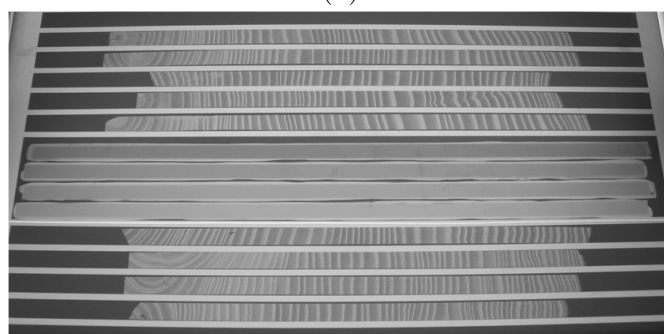
(b)

Figure 3.6: Wood and reference samples before X-ray (a) and after X-ray (b)bombardment.
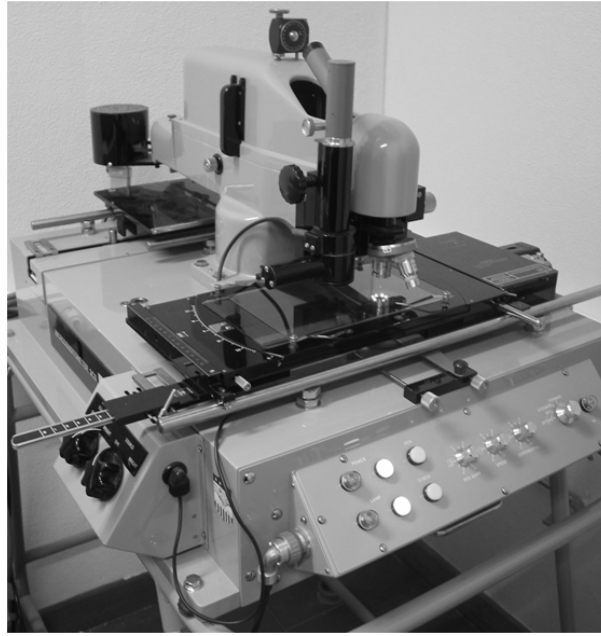
Figure 3.7: Microdensitometer Joyce Loebl MK3.

pability (from 10 to 200 values per mm), the processing speed (3 cm.min^{-1}), and the registry on a Kodak Industrex CX X-ray film that makes possible to take reads as often as necessary. The measurements were performed according to the procedure described in Lousada (2000) on samples with nominal dimensions of 3(L)×5(T) and length equal to the local radius of the central board, conditioned at 12% MC. Local density measurement of *Pinus pinaster* wood was performed with a spatial resolution of 0.1 mm (ten values per mm) and with an accuracy of $8{\times}10^{-4}$ g.cm^{-3}. Exposure time to radiation was 350 s at an intensity of 18 mA; accelerating tension of 12 kV was applied with a 2.5 m distance between the X-ray source and the film. After the samples bombardment with radiation we obtain the negative image of its structure printed on the film (Fig. 3.6b) representing their optical density that will be read from the microdensitometer (Fig. 3.7). Optical density will be then converted into wood density by a linear regression equation definition using the optical and the real density values of the reference samples.

From the local density profile across the overall length of the specimens, and after the growth rings limits determination based on the simultaneous observation of the specimen image on the x-ray film and the mean density values measured, the density parameters defined above, in the first paragraph, were then calculated. For the annual rings boundary definition, it was consider the value of 0.650 g.cm^{-3} as a limit between the EW and LW for the calculation of the EW and LW densities and respective percentages. That value was maintained besides the evidence from Lousada et al. (1994) that do not annul the existence of a high amount of transition wood which improves the amount and the influence of the LW percentage turning the EW density less accurate on the determination of mean

density.

3.3 Full-field displacement measurements

The full-field displacement of a (quasi-)planar target surface can be measured using the digital image correlation (DIC) method by processing images recorded before and after deformation. The digital images can be recorded using different apparatus depending on the scale of observation (*e.g.*, using a camera-lens optical system or a scanning electron microscope). The target surface of interest must have a textured pattern with suitable contrast (covering as much as possible the dynamic range of the camera sensor, but avoiding pixel saturation) and characteristic size (pixels per speckle) with regard to the field of view (region of interest). Moreover, the DIC measurement parameters (*i.e.*, subset size, subset step and base length for strain computation) must be chosen in order to fulfill a correct balance between spatial resolution (interpolation errors) and accuracy (correlation errors) with regard to the physical phenomenon or application under analysis. In this work the software ARAMIS DIC-2D v6.0.2 by GOM (ARAMIS) was used.

3.3.1 Camera-lens optical system

The mechanical tests carried out in this work were focused at the growth ring scale. In the hierarchical structure of wood, this level of magnification corresponds to a meso scale with a characteristic length within the range of about 1 up to 10 mm. Thus, a camera-lens optical system was still suitable for image grabbing. A 8-bit Charged Coupled Device (CCD) Baumer Optronic FWX20 camera was used (Table 3.1). This camera was coupled with an Opto-Engineering telecentric lens TC 23 09 whose characteristics are summarised in Table 3.2. Although this type of lens is more expensive, and eventually larger and heavier than normal lenses of similar focal length, the main advantage of a telecentric lens resides in the fact that the magnification is kept constant over a defined working-distance range. In performing in-plane displacement measurements by DIC, this feature is particular advantageous for avoiding errors induced by out-of-plane parasitic movements (Haddadi and Belhabib, 2008; Sutton et al., 2008). This camera-lens system leads to the following metrics:

- A conversion factor (pixel size on the object plane) of $f_c = 4.4$ μm/pixel ($1/f_c = 0.227$ pixel/μm) is obtained.

- If an image displacement accuracy of 10^{-2} pixels is assumed (Bornert et al., 2009), this configuration lead to an object displacement accuracy of 4.4×10^{-2} μm.

- To achieve a minimum image speckle size containing, for instance, 5 pixels, an average object speckle size of 21.9 μm must be guarantee in practice. If it is assumed

Table 3.1: Baumer Optronic FWX20 CCD camera.

Sensor format	1/1.8"
Number of pixel	1624×1236 pixels^2
Scan area	7.15×5.44 mm^2
Pixel size	4.4×4.4 μm^2

Table 3.2: Opto Engineering Telecentric lens TC 23 09.

Magnification	$1.0 \pm 3\%$
Field Of View (1/1.8")	7.1×5.4 mm^2
Working Distance	63.3 ± 2 mm
Working F-number	11
Telecentricity	$< 0.08°$
Field Depth	0.9 mm

that an image subset size must containing at least 3×3 speckles (*i.e.*, six bright and dark intensity transitions in each direction) to ensure suitable accuracy and isotropy in the subset matching process (minimum speckle inclusion criterion allowing maximum spatial resolution) (Sutton et al., 2009, p.237), this will define a subset of 15×15 pixels^2 = 225 pixels^2. This corresponds to a minimum spatial resolution of 66 μm.

3.3.2   Speckle pattern

To solve the correspondence problem in image matching, a target surface of interest must have a random (fingerprint uniqueness), isotropic (not having a preferred orientation) and contrasted (for computing image spatial derivatives) gray-level pattern (Sutton et al., 2009). This textured pattern is so-called speckle pattern, in similarity with the speckle image observed over a rough surface by coherent illumination. Such pattern can exist naturally on the material surface or, otherwise, must be created artificially using a suitable feature marking technique. For this purpose, different techniques – *e.g.*, using spray or airbrush paint, toner powder deposit or lithography (Sutton et al., 2000) – can be used, each of them eventually suitable for a given scale of observation from structural down to micro or nano scale. A suitable balance between region of interest (angle of view) and average (speckle) size of white-to-dark marks must be achieved in order to enhance the displacement spatial resolution (the smallest distance between independent measurements) associated to the DIC measurements. This can be particularly important when spatially gradient strain fields are expected to occur.

At the scale of the growth rings, the wood cellular structure can be resolved as shown in Figure 3.8. Therefore, in a first approach, the natural texture of the surface may be considered as a carrier pattern for DIC measurements. The surface was polished by using sandpaper with grit size decreasing from P180 up to P320. This procedure was fundamental for enhancing the details of the cellular tissue and therefore the image contrast. However, a uniform finishing across the growth rings was rather difficult to achieve, due to density variation between earlywood and latewood layers. In consequence,

a uniform contrast of the cellular texture (*i.e.* the cell walls with regard to lumen space) across the field of view was not possible. Particularly, in the latewood layer where the ratio lumen/cell wall is minimum, the image contrast was significantly reduced. This situation was disadvantageous because large subset windows need to be used in this case in order to define a suitable local pattern for DIC (aperture problem). Eventually a microtome of sliding knife could be used for sharp cutting of cells (enhancing contrast), but this machining operation was not easy to achieve in practice across the whole surface of the specimen $(50(R) \times 5(T)$ mm). To enhance the contrast of the cellular tissue image (*i.e.*, brightness difference between the wood substance in the cell wall and the lumen) obtained in a microscopy, Thuvander et al. (2000) have proposed to rubber a slurry of talcum powder into the surface to fill the lumen. At the magnification of the growth rings (meso scale) this procedure was not straightforward, and not improve significantly the contrast of the image. Furthermore, the rather regular texture of the cellular tissue may not guarantee the uniqueness of the subset texture pattern, which can lead to some mis-matching in the correlation algorithm.

Instead of using the natural cellular pattern, an artificial speckle pattern was painted on the wood surface. Firstly, a thin coating of white paint was applied uniformly over a polished region of interest. In order to guarantee a suitable detail of the dark marks with regard to the characteristic size of the field of view (Table 3.2), an airbrush was used for random distribution of dark spots. With this procedure a more uniform distribution of the speckle pattern was obtained. A different approach was proposed by Jernkvist and Thuvander (2001) using micron carbon toner particles spread over white background paint in radial tensile tests on spruce. The application of such particles may be however more tricky to achieve in practice than the airbrush, in order to guarantee a roughly uniform spatial distribution of random white-to-dark marks over the whole region of interest. Figure 3.9 shows the typical speckle pattern obtained using airbrush painting (an IWATA Custom Micron CM-B airbrush model was used with fluid nozzle of diameter 0.18 mm and spray range lower than 60 microns). As it can bee seen qualitatively from the image and histogram a suitable pattern for DIC was obtained.

3.3.3 Measuring parameters

In the DIC method some parameters such as subset size, subset step and base length for strain computation must be chosen *a priori*. These parameters directly influence the spatial resolution and accuracy associated to the measurements (Lecompte et al., 2006; Pan, 2011; Triconnet et al., 2009); therefore, they must be carefully chosen. In order to select this set of measuring parameters, a rigid-body translation test was proposed as guideline (at our best knowledge there are no standards available at the moment). The advantage of this type of test is that the kinematic fields are *a priori* known, *e.g.* the
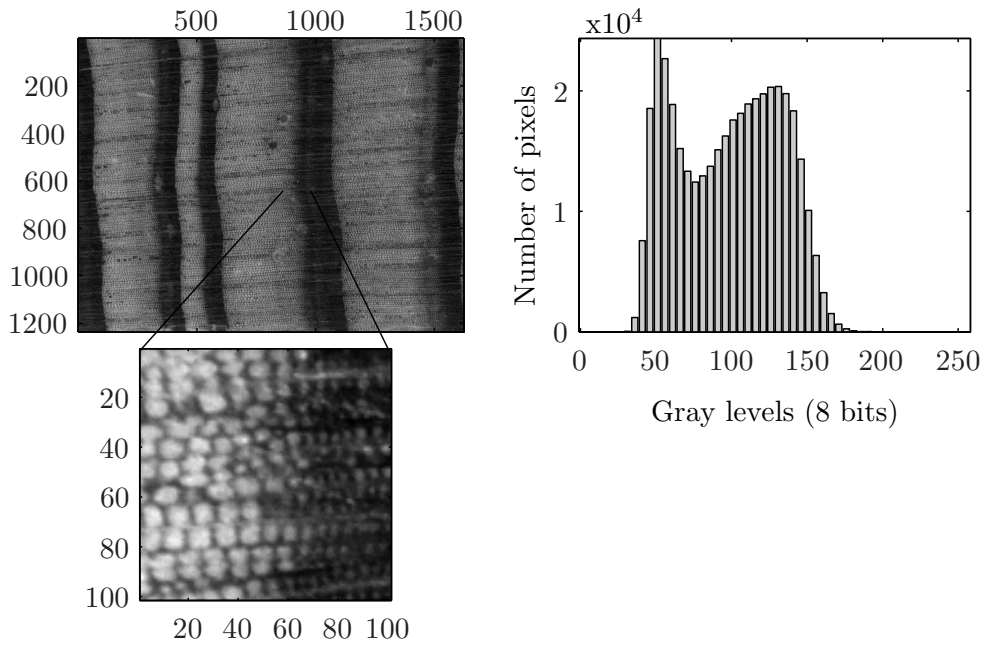
Figure 3.8: (left) natural texture of wood at the growth ring scale; (right) image histogram.
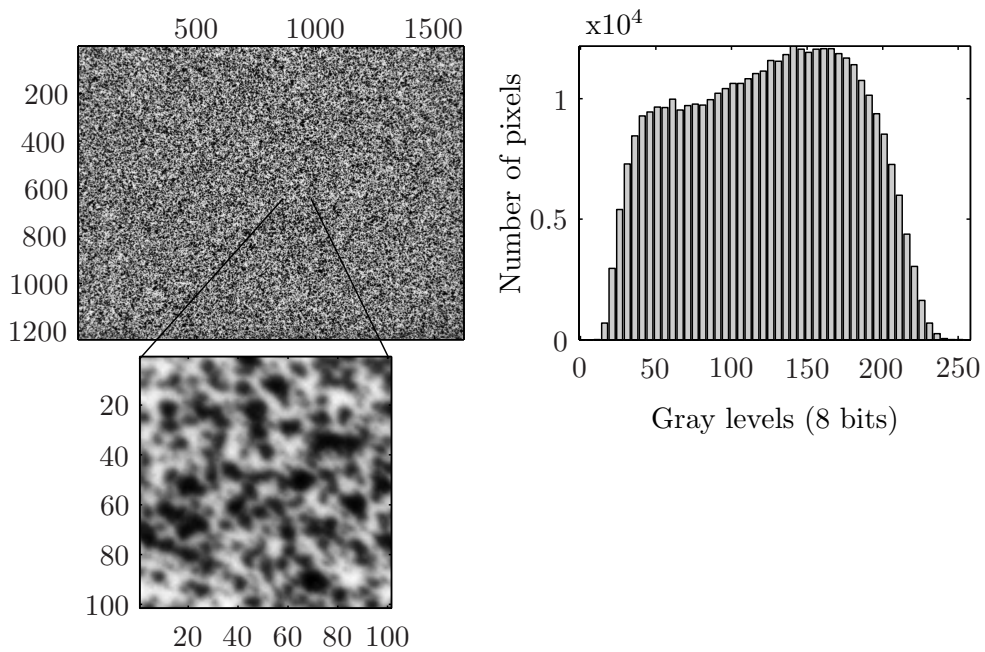
Figure 3.9: (left) speckle pattern across the growth rings; (right) image histogram.
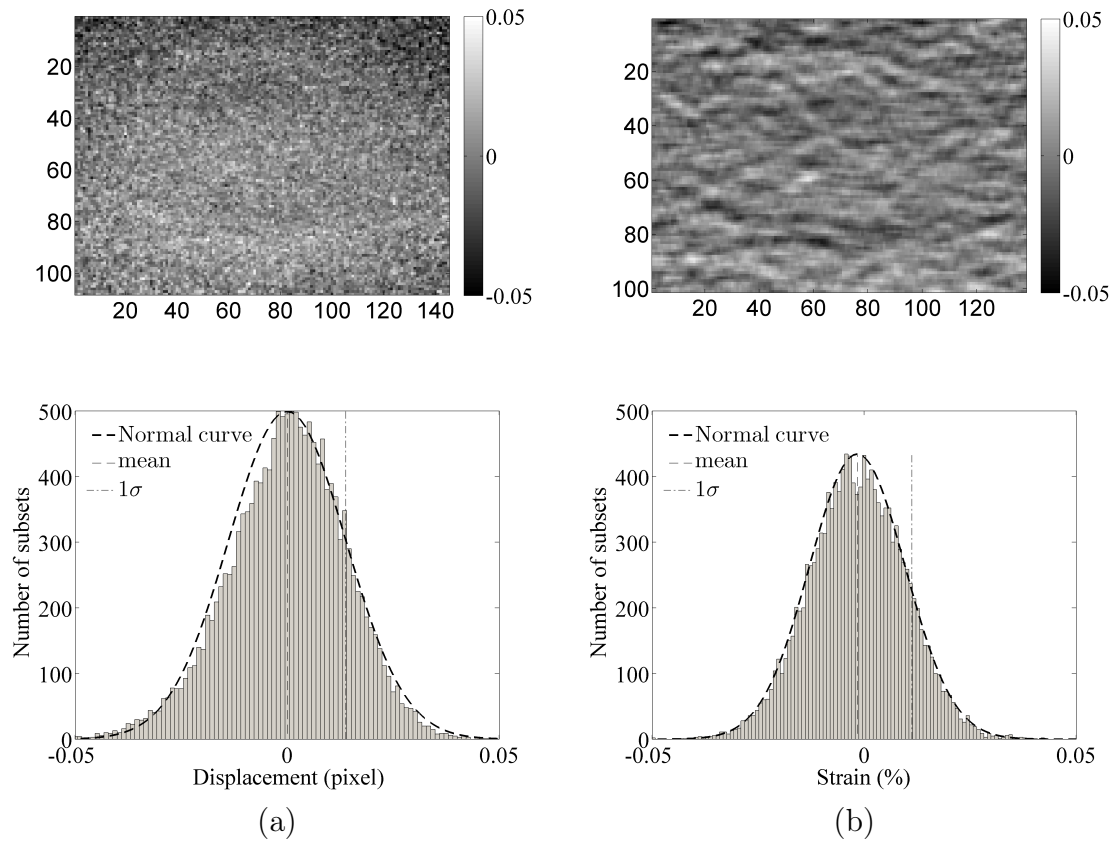
Figure 3.10: (a) $(U_X - \overline{U}_X)$ map and histogram; (b) ε_X map and histogram (subset size of 15×15 pixels, subset step of 11×11 pixels and strain gauge length of 7 subsets).

displacement field is theoretical constant (all subsets must have the same displacement value) and the strain field is expected to be zero. Thus, the DIC parameters can be arbitrarily chosen and their influence on the measuring errors, with regard to the theoretical solution, evaluated on a statistical basis. Square subsets of 9×9 (39.6×39.6), 11×11 (48.4×48.4), 15×15 (66×66), 21×21 (92.4×92.4) and 31×31 (136.4×136.4) pixels^2 (μm^2) were chosen for this analysis. Moreover, a strain gauge length of 3, 5, 7, 9 and 11 subsets was considered for the strain computation.

A translation test along the x (horizontal) direction was performed on a target speckle pattern object by recording two images, before and after deformation. The displacements between this pair of images were measured by the ARAMIS DIC-2D, taking different values of subset size. For each case study, the mean value of the displacement over the entire field (subsets) was calculated. In further processing, the displacement field was subtracted by the mean value, yielding residual map as shown, as an example, in Figure 3.10(a). As can be seen from the histogram of this map (a figure representing the number of subsets with given values of displacement), a roughly Gaussian noise distribution is obtained. Therefore, the standard deviation of this residual signal was considered for estimating the displacement resolution. The variation of this threshold value for displacement detection as a function of the subset (number of pixels per correlation window) is shown in Figure 3.11(a). As can be concluded, the correlation error decreases by increasing the subset size. This is, however, achieved by losing spatial resolution (interpolation errors). This analysis was extended to the strain fields. Figure 3.10(b) shows typical noisy strain map and histogram associated to the translation test measurements. The evaluation of the standard deviation (strain resolution) with regard to the gauge length used in the strain computation is shown in Figure 3.10(b), for the set of subsets selected. As can be expected, the strain resolution converge to the theoretical value of 0.01% as the gauge length increases, independently of the subset size used for displacement calculation. By analysing these results a compromise was found by choosing a subset size of 15×15 pixels, a subset step of 11×11 pixels (4 pixels overlapping between subsets), and a strain gauge length of 7 subsets (represented by a $'+'$ in Figure 3.11). The choice to slightly overlap the correlation windows by 4 pixels was to enhance spatial resolution associated to the measurements at the growth ring scale. Note that for a subset size of 15×15 pixels^2, a displacement spatial resolution of 66 μm was obtained, which corresponds roughly to the largest dimensions of wood cell (EW layer) of *P. pinaster*. In this case, the displacement resolution was about 1.75×10^{-2} pixels (0.066 μm). Besides, a strain spatial resolution of 0.461 mm was defined in order to guarantee some measuring points within each EW and LW layers (from X-ray microdensitometry measurements on *P. pinaster* the width of EW and LW layers was estimated to 0.3-3.4 mm and 0.5-3.6 mm, respectively). For this strain length, a strain resolution around 0.015% was obtained, which is still suitable for measuring the strains in the linear domain of the material mechanical response.
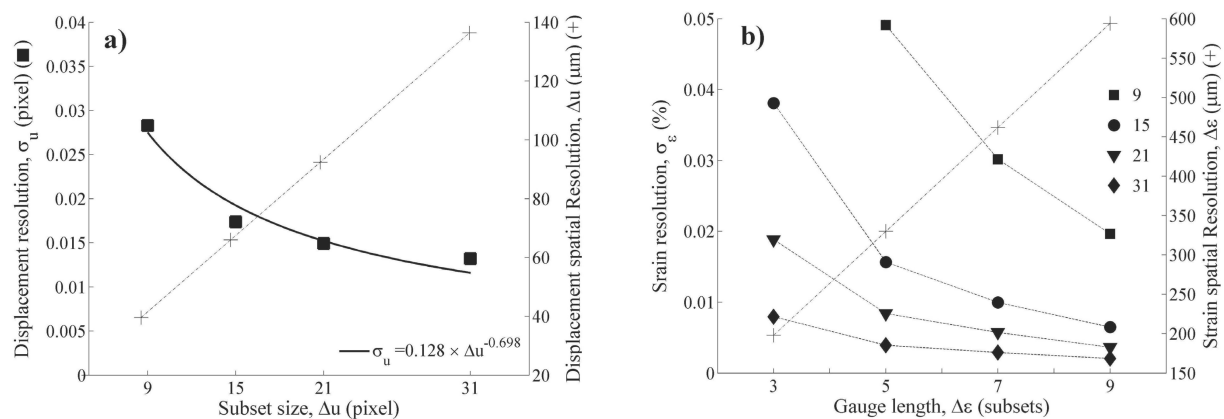
Figure 3.11: (a) evaluation of the displacement resolution (standard deviation) with regard to subset size; (b) evaluation of the strain resolution (standard deviation) with regard to gauge length (corresponding to a subset size of 15×15 pixels, a subset step of 11×11 pixels and a strain gauge length of 7 subsets).

3.4 Photo-mechanical set-up of the tensile test

The mechanical tensile tests were carried out in an Instron 5848 Microtester machine under displacement control at a rate of $v = 0.2$ mm.min^{-1}. Considering a free length between grips of $l_0 = 30$ mm, these tests were performed at a strain rate of $\dot{\varepsilon} = v/l_0 = 1.1 \times 10^{-4}$ s^{-1}. For this rate of deformation, the load was applied continuously throughout the test in less than 3 min allowing neglecting viscoelastic effects. The load was measured by means of a 2 kN load cell. The photo-mechanical set-up, coupling the tensile test with the digital image correlation technique, is shown in Figure 3.12. Two Raylux 25 white-light LED sources at about 45° with regard to the optical axis were used for uniform illumination of the specimen. The shutter time was typically set to 0.5 ms in order to use the maximum of the gray level distribution still avoiding pixel saturation. Taking a test velocity of $v = 0.2$ mm.min^{-1}, an exposure time of $t_e = 5 \times 10^{-4}$ s and a pixel size on the object plane of $p_O = 4.4$ μm.pixel^{-1}, a small displacement blurring in the image along the loading direction of $1.66 \times 10^{-3}\mu$m (*e.g.* 0.04% of the pixel size) is expected to occur. To help prevent both slippage of the specimen into the grips throughout the test and local crushing damage, sandpaper of P180 grit size was placed between the specimen loading faces and the tensile grip faces.

Painting a speckle pattern across the wood surface (Figure 3.9) had the disadvantage of hiding the annual growth ring structure (Figure 3.8). Therefore, the following procedure was implemented in order to recover the image of the growth rings. Both surfaces of the specimen were carefully polished. The speckle pattern was then painted on one face. The specimen was firstly mounted on the lower tensile grip into the testing machine with the natural growth rings surface towards the CCD camera (left image in Figure 3.12).
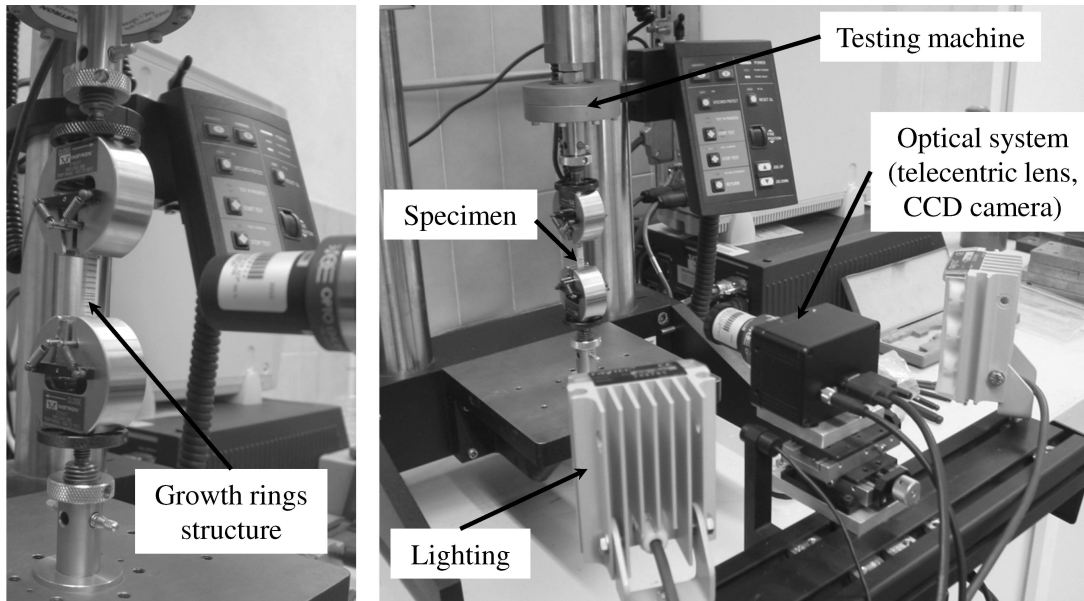
Figure 3.12: (left) image of the wood growth ring structure; (right) photo-mechanical set-up coupling the tensile test with the digital image correlation technique.

After focusing (fixing the working distance to 63.3 mm), one image of the growth ring structure was recorded. Finally, the specimen was rotated by 360° by rotating the whole lower tensile grip in order to image the opposite face with the speckle pattern (right image in Figure 3.12). It was assumed at this stage that the growth ring structure is invariant thought the thickness of the specimen; therefore the layout of growth ring structure could be retrieved after flipping images. Thus, the kinematic (displacement and strain) measurements provided by DIC could be associated afterwards to the local structure of the material at the growth ring level.

References

ARAMIS. *Commercial software.* GOM (www.gom.com).

M. Bornert, F. Brémand, P. Doumalin, J.-C. Dupré, M. Fazzini, M. Grédiac, F. Hild, S. Mistou, J. Molimard, J.-J. Orteu, L. Robert, Y. Surrel, P. Vacher, and B. Wattrisse. Assessment of digital image correlation measurement errors: Methodology and results. *Experimental Mechanics*, 49(3):353–370, 2009.

A. Carvalho. *Madeiras Portuguesas: estrutura anatómica, propriedades, utilizações.* Instituto Florestal, 1996.

N. Garrido. Identificação do comportamento mecânico da madeira através do ensaio de tracção fora dos eixos de simetria material. Master's thesis, Universidade de Trás-os-Montes e Alto Douro, Vila Real, Portugal, 2004.

H. Haddadi and S. Belhabib. Use of rigid-body motion for the investigation and estimation of the measurement errors related to digital image correlation technique. *Optics and Lasers in Engineering*, 46(2):185–196, 2008.

L.O. Jernkvist and F. Thuvander. Experimental determination of stiffness variation across growth rings in Picea abies. *Holzforschung*, 55(3):309–317, 2001.

D. Lecompte, A. Smits, S. Bossuyt, H. Sol, J. Vantomme, D. Van Hemelrijck, and A.M. Habraken. Quality assessment of speckle patterns for digital image correlation. *Optics and Lasers in Engineering*, 44(11):1132–1145, 2006.

J. L. Lousada, F. Fonseca, and M. E. Silva. Relações entre componentes da densidade da madeira no lenho juvenil e no lenho adulto em pinus pinaster ait. Technical report, LPF, UTAD, 1994.

J.L. Lousada. *Variação fenotípica e genética em características estruturais na madeira de Pinus pinaster Ait.* PhD thesis, Universidade de Trás-os-Montes e Alto Douro, Vila Real, Portugal, 2000.

J.M. Oliveira. Caracterização do comportamento ao corte da madeira usando o ensaio de Arcan. Master's thesis, Universidade de Trás-os-Montes e Alto Douro, Vila Real, Portugal, 2004.

B. Pan. Recent progress in digital image correlation. *Experimental Mechanics*, 51(7): 1223–1235, 2011.

J.L. Pereira. Comportamento mecânico da madeira em tracção nas direcções de simetria material. Master's thesis, Universidade de Trás-os-Montes e Alto Douro, Vila Real, Portugal, 2005.

C. Skaar. Shrinking and swelling. In A.P. Schniewind, editor, *Concise encyclopedia of*

wood and wood-based materials, pages 243–245. Pergamon Press, 1989.

M. Sutton, S. McNeill, J. Helm, and Y. Chao. Advances in two-dimensional and three-dimensional computer vision. In Pramod Rastogi, editor, *Photomechanics*, volume 77 of *Topics in Applied Physics*, pages 323–372. Springer Berlin / Heidelberg, 2000.

M.A. Sutton, J.H. Yan, V. Tiwari, H.W. Schreier, and J.J. Orteu. The effect of out-of-plane motion on 2d and 3d digital image correlation measurements. *Optics and Lasers in Engineering*, 46:746–757, 2008.

M.A. Sutton, J.-J. Orteu, and H. Schreier. *Image correlation for shape, motion and deformation measurements: Basic concepts, theory and applications*. Springer, 2009.

F. Thuvander, M. Sjödahl, and L.A. Berglund. Measurements of crack tip strain field in wood at the scale of growth rings. *Journal of Materials Science*, 35(24):6267–6275, 2000.

K. Triconnet, K. Derrien, F. Hild, and Didier Baptiste. Parameter choice for optimized digital image correlation. *Optics and Lasers in Engineering*, 47(6):728–737, 2009.

G. Tsoumis and C. Passialis. Effect of growth rate and abnormal growth on wood substance and cell wall density. *Wood Science and Technology*, 1977.

J. Xavier. Caracterização do comportamento ao corte da madeira usando o ensaio de Iosipescu. Master's thesis, Universidade de Trás-os-Montes e Alto Douro, Vila Real, Portugal, 2003.

Chapter 4

Identification of transverse elastic properties of *P. pinaster* by the anisotropic-based method

This chapter is dedicated to the identification of transverse elastic properties of *P. pinaster* by the anisotropic-based method (AbM). Density parameters and elastic properties will be discussed with regard to variability patterns within the stem. Besides, the possible correlations between the elastic constants and density parameters are investigated.

Contents

4.1   Introduction

Wood mechanical characterisation is made by experimental work with application of suitable tests to found its unknown constitutive parameters, based on specimen geometry, boundary conditions and displacements knowledge. However these tests can be of difficult implementation for such material because of some material particularities, like the anisotropic behaviour and anatomical heterogeneities. Trying to take advantage of those particularities, in this work, a single ring-oriented tensile test was applied for the material transverse elastic properties characterisation and the generated heterogeneous strain fields across de region of interest were measured with digital image correlation. In a first approach, all the transverse stiffness components available on mappings resulting from wood mechanical response, here considered as clear wood, were attempted to identify assuming a uniaxial stress state on the specimen coordinate system. In terms of wood quality, since it is closely related to its own heterogeneity, property variation patterns along the stem becomes a relevant issue once they can provide a measure of spatial variability and so, help on wood usefulness definition, both in terms of best processing and best applications. Hence, both density and elastic properties were patterned along the stem as well as their relationships were sought after.

4.2   Anisotropic-based method

4.2.1   On the identification of global elastic components

The identification strategy used in this work was based on anisotropic elasticity theory. The general framework was firstly proposed by Majano-Majano et al. (2012). This method will be called hereafter anisotropic-based method (AbM) (§ 2.1.3). Wood on the RT plane will be assumed as an orthotropic linear elastic material. Moreover, the continuum assumption will be kept, even if at the magnification of the growth rings the wood cellular structure can be resolved. Therefore, the orthotropic medium is characterised by four independent stiffness components. Due to the natural cylindrical shape of the stem, the constitutive law will be developed in polar coordinates.

For a given identification of global compliance components on the transversal plane, ten specimens per position were simultaneously processed by the AbM. To start with, results from a given position in the stem were analysed for validation purposes. The axial stress-strain curves associated to each specimen are plot in Fig. 4.1(a). In this case, the axial stress was simply determined as load divided by initial cross-section, whilst the axial strain was determined as the integral (mean) of the axial strain field over the region of interest (virtual gauge section). The difference on the non-linear behaviour observed on the stress-strain curves was strictly related to the variation of the off-axis angle (rings

curvature), which was in this case within the range of 4–42°. An example of the strain fields on the material coordinate system obtained from the ring-oriented tensile test is given in Fig. 4.2, corresponding to a specific level of loading. The histogram of the strain fields are also shown. As it can be seen, heterogeneous strain fields are obtained according to the structure heterogeneity itself at the scale of observation. Moreover, all the three components exist in the material coordinate system, although with different amplitude. A more detailed description on the strain fields will be given in Chapter 5, when local parameter identification will be discussed (§ 5.3). It is worth noticing that punctual measurements provided by, for instance, strain gauges will be more sensitivity to earlywood and latewood constituents (*e.g.*, Micro-Measurement CEA-06-125WT-350 0/90 rosettes have a gauge area of 3.18×4.57 mm^2 (Xavier et al., 2004)) than the global average carried out here from full-field measurements across the entire region of interest, therefore less scatter in the identification is expected (Xavier et al., 2012). From this set of data, the four stiffness components were determined directly by applying the AbM as shown in Fig. 4.1(b). The elastic components were here converted into engineering constants (see explicit relationships in Eq. (2.6), § 2.1.3) for comparison purposes with reference values, which are summarised in Table 4.1 (Forest Products Laboratory, 1999; Xavier et al., 2004). As it can be concluded, the identification of all engineering constants are in agreement with reference values determined at the macro scale.

The identification strategy aims at identifying simultaneously all the elements of the compliance matrix and therefore all independent engineering constants in the material coordinate system. However, the robustness of the approach must be verified. For that purpose, a second example is represented in Fig. 4.3. In this case, as it can be concluded from the axial stress-strain curves (Fig. 4.3(a)), the ten specimens have an off-axis angles rather similar, *e.g.*, among the specimens there are not much curvature variation. Indeed, in this case the off-axis angles vary in the range of 4–11°. As a result, the identification is not suitable, for instance, for E_T as it may be expected (Fig. 4.3(b)). For the purpose of identifiability and robustness of the method, these off-axis angles can be eventually optimised or chosen with some criterion. For instance, for the identification of the shear modulus ($S_{66} = 1/G_{RT}$) the off-axis angle (ring orientation) can be chosen so that shear behaviour in the material coordinate system is enhanced (Chamis and Sinclair, 1977). For this purpose the following relationships can be used where the strain components in the material coordinate system (ε_{rr}, $\varepsilon_{r\theta}$ and $\varepsilon_{\theta\theta}$) are normalised with regard to the axial applied strain (ε_{xx})

$$\begin{cases} \varepsilon_{rr}/\varepsilon_{xx} = (S_{11}c^2 + S_{12}s^2)/\Delta \\ \varepsilon_{\theta\theta}/\varepsilon_{xx} = (S_{12}c^2 + S_{22}s^2)/\Delta \\ \varepsilon_{r\theta}/\varepsilon_{xx} = S_{66}cs/\Delta \end{cases} \tag{4.1a}$$

(a)

(b)
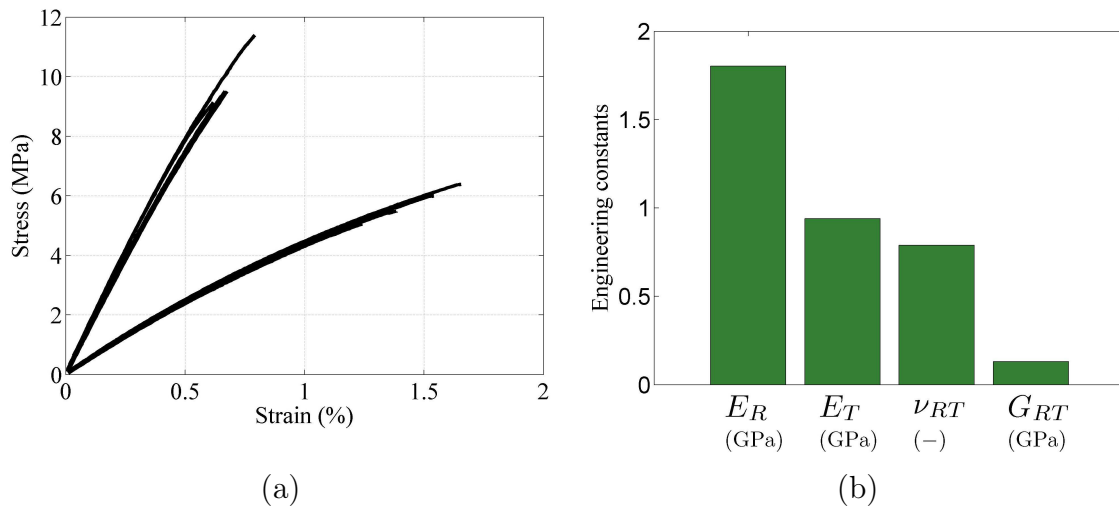
Figure 4.1: Example 1 of (a) stress-strain curves on the specimen coordinate system; (b) engineering elastic properties in the RT plate determined by the anisotropic-based method.

(a)

(b)

(c)
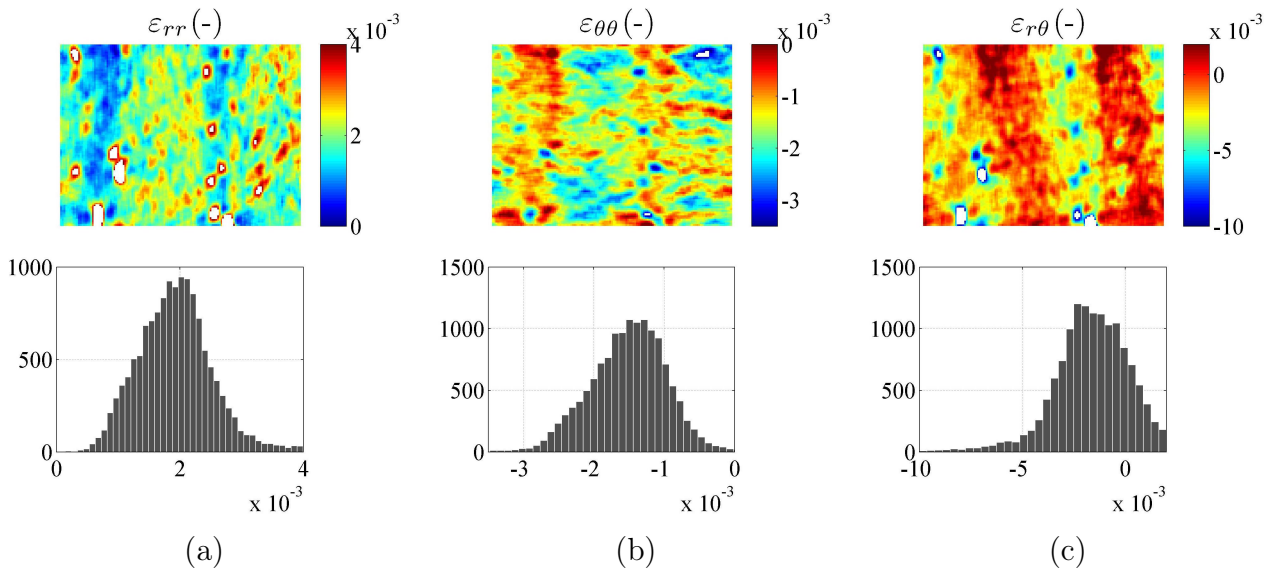
Figure 4.2: Strain field components on the material coordinate system (a) ε_{rr}, (b) $\varepsilon_{\theta\theta}$, (c) $\varepsilon_{r\theta}$ (load = 50 N).
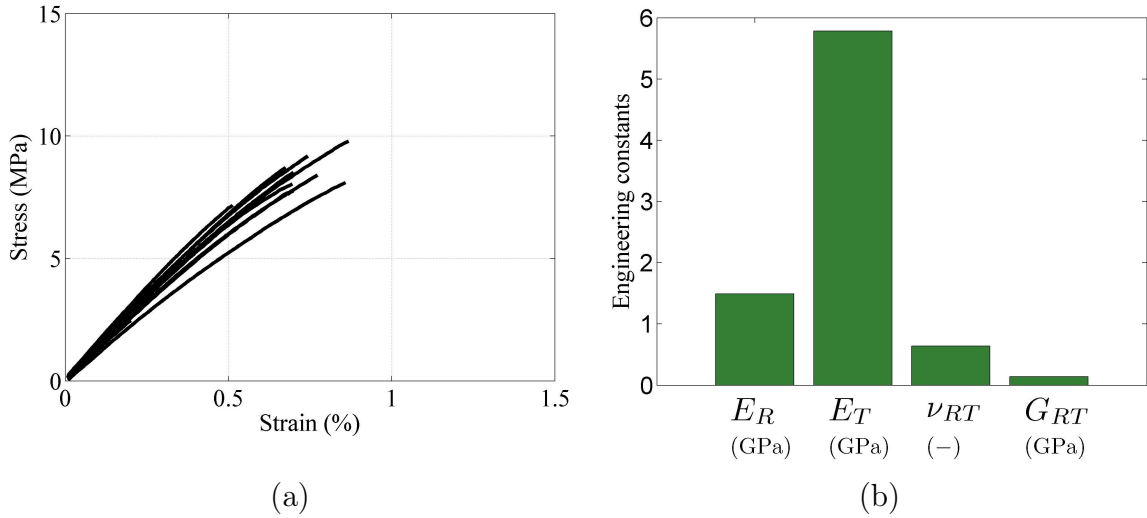
Figure 4.3: Example 2 of (a) stress-strain curves on the specimen coordinate system; (b) engineering elastic properties in the RT plate determined by the anisotropic-based method.

Table 4.1: Reference (after (Forest Products Laboratory, 1999; Xavier et al., 2004)) and identified properties of *P. pinaster* in the RT plane.

Elastic properties	Reference		AbM	
	min – max	mean	min – max	mean$\pm$ std[a]
E_R (GPa)	1.5 - 1.9	1.7	1.4-2.6	1.8$\pm$ 0.23
E_T (GPa)	0.8 - 1.4	1.1	0.4-1.5	0.9$\pm$ 0.24
ν_{RT} (-)	0.68 - 0.71	0.7	0.53-0.95	0.7$\pm$ 0.09
G_{RT} (GPa)	0.255 - 0.280	0.268	0.110-0.333	0.175$\pm$ 0.04

[a] Standard deviation

with,

$$\Delta = S_{11}c^4 + 2(S_{11} + 1/2S_{66})c^2s^2 + S_{22}s^4. \tag{4.1b}$$

These equations (4.1) are dependent on the material properties and the off-axis angle. Fig. 4.4 plots the evaluation of equations (4.1) for *P. pinaster*; the elastic properties of reference where taken from (Xavier et al., 2004). In terms of test optimisation a cost function can be used defined as follows,

$$\phi(\theta) = \frac{(\varepsilon_{rr} - \varepsilon_{\theta\theta})^2 + (\varepsilon_{rr} - \varepsilon_{r\theta})^2 + (\varepsilon_{\theta\theta} - \varepsilon_{r\theta})^2}{3(\varepsilon_{rr}^2 + \varepsilon_{\theta\theta}^2 + \varepsilon_{r\theta}^2)}. \tag{4.2}$$

Figure 4.5 plots the cost function (Eq. 4.2) as a function of the off-axis angle. As it can be concluded strain components in the material coordinate system are balanced out for angles as high as 60°.

From these results, only E_R and G_{RT} were kept for further analysis regarding spatial variability within the stem. Complementary tests on specimens preferentially oriented on the T direction should be systematically used for complete identification of all orthotropic stiffness componentes. In alternative, a more heterogeneous test should be proposed eventually using rectangular (unnotched) specimens loading in the Iosipescu test (Xavier et al., 2007) or a kind of compression test over a small disc.

4.2.2   On the estimation of local elastic components

There are in the literature few experimental data for mechanical properties of EW and LW layers (Cramer et al., 2005; Farruggia and Perré, 2000; Jernkvist and Thuvander, 2001). An indirect evaluation was proposed here in order to estimate local elastic properties of EW and LW from the global identification obtained by AbM. For this purpose, the following basis equations and approach were used. Micromechanical models that have been developed in the framework of composite materials aiming to estimate elastic constants as a function of the elastic properties of individual constituents (Jones, 1999), where applied to estimate EW and LW properties. The motivation for such analytical models was to reduce cost and time required in the experimental evaluation of these constituent parameters.

The transverse Young's modulus E_R can be developed according to the following relationship

$$\frac{1}{E_R} = \frac{v^{\mathrm{EW}}}{E_R^{\mathrm{EW}}} + \frac{v^{\mathrm{LW}}}{E_R^{\mathrm{LW}}} \tag{4.3}$$

where v^α represent the volume fraction and E_R^α the constituent Young's moduli (with $\alpha = $ EW,LW). In solving Eq. (4.3) for the EW and LW constituents elastic constants, an addition equation can be assumed based on unit cell models. Regular honeycomb
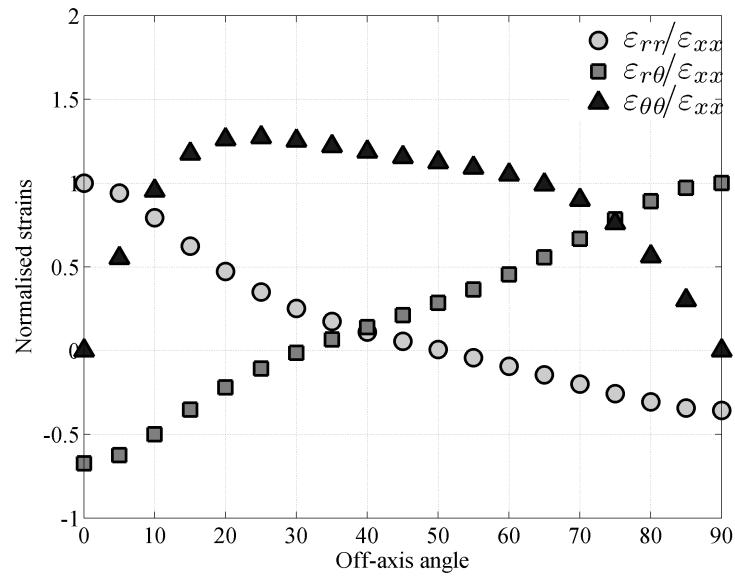
Figure 4.4: Variation of strain components in the material coordinate system with regard to the off-axis angle for *P. pinaster.*
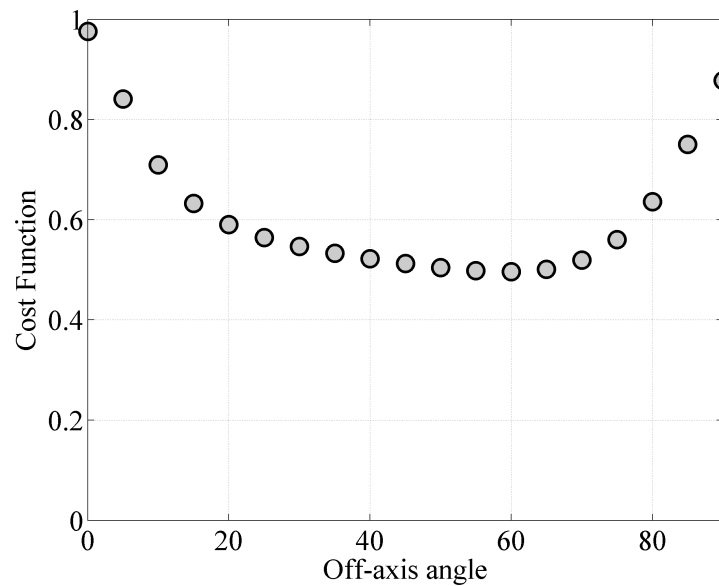
Figure 4.5: Cost function versus off-axis angle, balancing out strain components on the material coordinate system.

Table 4.2: Local transverse elastic properties of *P. pinaster* estimated from the global properties.

Elastic properties	Global Identification		Local Estimation	
	min – max	mean	EW± std[a]	LW± std
E_R (GPa)	1.4 - 2.6	1.8	1.5 ± 0.20	2.5 ± 0.34
G_{RT} (GPa)	0.110 - 0.333	0.175	0.146 ± 0.04	0.243 ± 0.05

[a] Standard deviation

models have been generically applied to wood in order to provide an estimation of elastic constants as a function of geometry, properties and density of cellular wood (cell wall) tissue (Gibson and Ashby, 1997). From these models the transverse moduli can be related as

$$\frac{E_R^{\text{LW}}}{E_R^{\text{EW}}} = \left(\frac{\rho^{\text{LW}}}{\rho^{\text{EW}}}\right)^a \qquad (4.4)$$

The a exponent is commonly chosen equal to 3 (Gibson and Ashby, 1997), but recent experiments has evidenced that this scaling should be close to a linear variation (Modén and Berglund, 2008). Therefore, for the radial moduli $a = 1.5$ was chosen in this work. In turn, the transverse shear modulus G_{RT} was determined according to the following rule of mixtures

$$\frac{1}{G_{RT}} = \frac{v^{\text{EW}}}{G_{RT}^{\text{EW}}} + \frac{v^{\text{LW}}}{G_{RT}^{\text{LW}}} \qquad (4.5)$$

where G_{RT}^{α} are the constituent shear moduli (with $\alpha = $ EW,LW). For this material parameter, the following relationship between shear moduli and density was assumed

$$\frac{G_{RT}^{\text{LW}}}{G_{RT}^{\text{EW}}} = \left(\frac{\rho^{\text{LW}}}{\rho^{\text{EW}}}\right)^3 \qquad (4.6)$$

Table 4.2 resumes the local properties for both EW and LW layers of the annual ring, estimated from the AbM global elastic properties. By the reasons presented earlier regarding the identifiability, only the values for E_R and G_{RT} were estimated.

4.3   Variability of wood properties within the stem

From the revision made in the first chapter and as a result of the work described so far, this chapter aims to investigate patterns of variability of wood properties within the stem in order to assess possible grade parameters to define wood quality for structural applications.

As regards density, and according to Lousada (2000), there are many references about their variation patterns concerning softwood species and in particular the *P. pinaster*. In general, all indicate that there is more variation within the tree than among trees. Usually, density studies are developed regarding on three radial and axial variation models: (*i*) one radial variation model inside the rings based on EW/LW transitions, (*ii*)another radial variation model between the growth rings from pith to cambium and (*iii*) one axial variation model associated to different levels of height on tree.

Considering that cell wall density is constant (approximately equal to 1.5 g.cm^{-3}, density variations on wood are due, almost exclusively, by the differences on wall-lumen ratio, *i.e.*, greater or lesser quantity of cell wall present in a given portion of wood. Thus, the mechanical strength and stiffness of wood is directly dependent on the strength and stiffness of the cell wall, wherein further wall, higher density, greater resistance and rigidity. Thus, it is understood that for the conditions under which the variation of other factors remain constant, the patterns of variation of mechanical properties closely follow the patterns of density variation (Lousada, 2000; Zobel and Buijtenen, 1989).

4.3.1 Variability of density

From the anatomical point of view, radial variation from pith to cambium origin is not a function of the distance to pith but of the cambium physiological age which generates the cells. It is worth noticing that the five radial positions of interest were defined effectively in terms of distance to pith but considering always, approximately, the same physiological age for each one.

To asses density variation patterns inside the stem, density measurements of, approximately, 135 to 190 mm long samples cut from the five trees according to the procedure described in Chapter 3, were made. The density measurements were performed by means of X-ray microdensitometry. In the raw data interpretation, a multiple regression analyzes was applied, following the procedure presented by Lousada (2000).

Figure 4.6 shows de mean density (D_{mean}) variation along the radius for all the trees and at all height levels studied. Although it gives only a global overview, it is possible to see that, in the juvenile wood, closer to the pith D_{mean} is low, increasing near to the heartwood/sapwood border and decreasing slightly towards the cambium. Nevertheless, sometimes, very close to the pit, D_{mean} values seemed to be higher than in the surrounding wood.

When looking deeper inside those values and concentrate on just one tree, through the Figures 4.7, 4.8, 4.9 and 4.10, showing the variation patterns for the different density parameters analysed (see Chapter 1, section 3.2), we can easily reinforce the radial previously mentioned pattern variation within the stem, especially concerning to the greater density values observed in the first rings (approximately the first 50 mm from the pith)
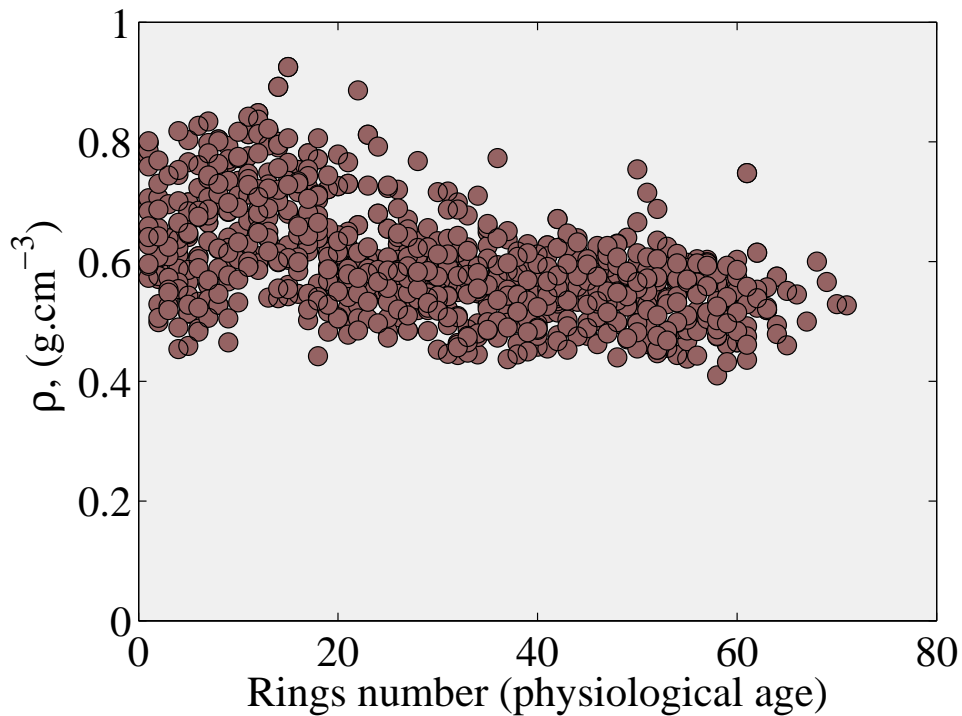
Figure 4.6: Density over-ring distribution: all trees at all height levels.

which are due to heartwood presence, resulting from the extractives deposition. This effect is much more evident in the first level (L1). At the higher levels on the stem, the amount of heartwood decreases, making D_{mean} radial pattern more stable. In fact, on height, and for each radial position, there is a decrease on D_{mean} from L1 to L3 positions. As can be seen on appendix A, this is true for all the five trees and is in agreement with literature.

Since it is a density parameter with greatest influence on radial variability within the ring, figure 4.9 shows the latewood percentage ($\%LW$) variation. Combining the analyses with figure 4.7, it is possible to see that, despite the position in height, the great values of this parameter are coincident to the greater values of D_{mean} on radial pattern. Besides, concerning to the variation on height, there is a slight fluctuation of this density parameter, increasing from base to the top.

More or less consistent with the variation of the $\%LW$, also the annual ring width ($Ring_W$) exhibits a pattern of apparent decrease with the height in the stem (Fig. 4.10). Recently one method widely used to quantify the density variation (the heterogeneity) at meso scale has been proposed by Ferrand (1982) and is based on standard deviation determination for all individual values of density in each ring, which is designated heterogeneity index (HI). In Figure 4.11 the HI variation pattern for tree number one in the direction of the beam as in height is presented. As it can be seen, radially, HI increases from pith to the periphery, with a tendency to stabilize or even decrease slightly near the
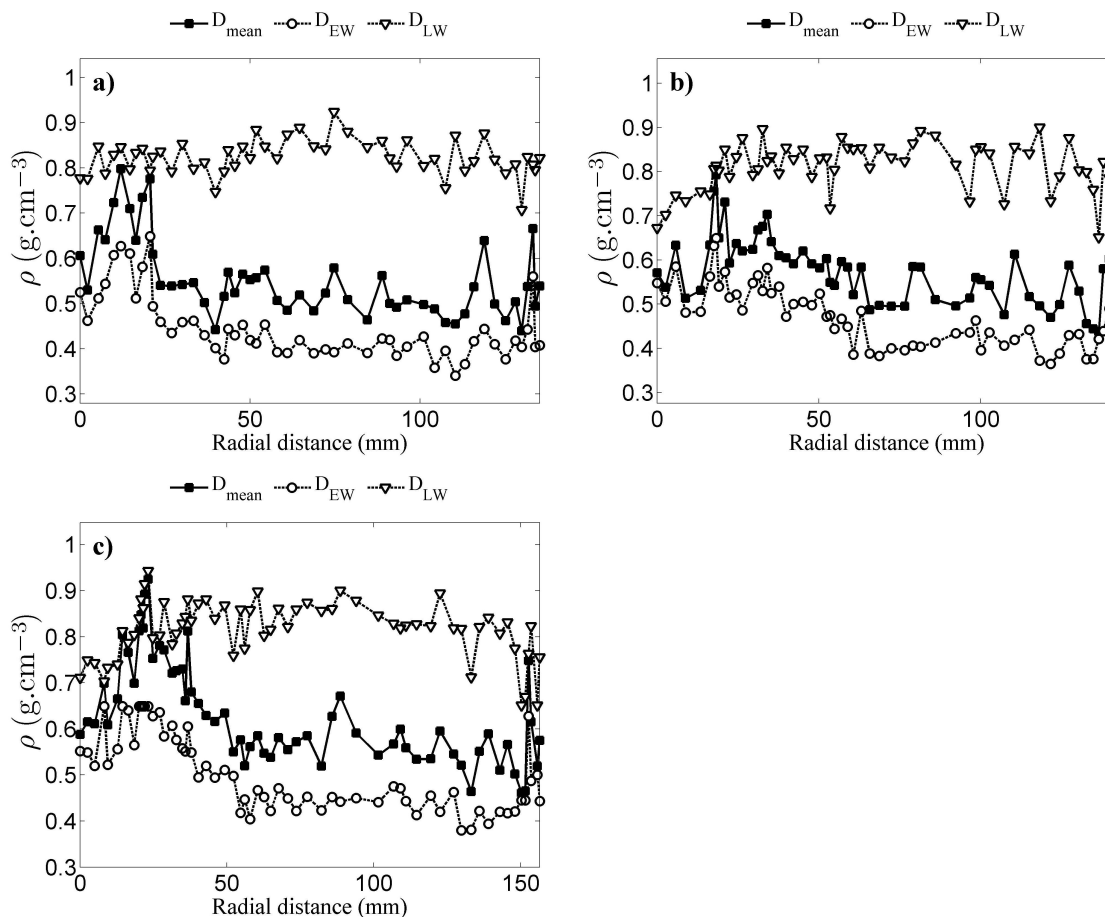
Figure 4.7: D_{mean}, D_{EW}, D_{LW} radial variation: tree number 1 - (a) L3, (b) L2, (c) L1.

cambium.

4.3.2 Variability of transverse elastic properties

Concerning to the variability of the elastic properties, the variation patterns for those obtained from AbM method, will be presented. No matter our initial perspective to determine all the four constants, E_R, E_t, ν_{RT} and G_{RT}, for the reasons identified earlier, at this time, with this set-up configuration and with this identification strategy, we only could get three of them, namely, E_R, ν_{RT}, G_{RT}. Furthermore, we will only present the within stem variation patterns for E_R and G_{RT}. The spatial variability by means of radial and longitudinal variations of those mentioned elastic properties will be presented in the next pages, regarding to the global properties identification and for tree number one. The results for the other four trees will be presented in the appendix B, following the same methodology presentation.

RADIAL VARIABILITY
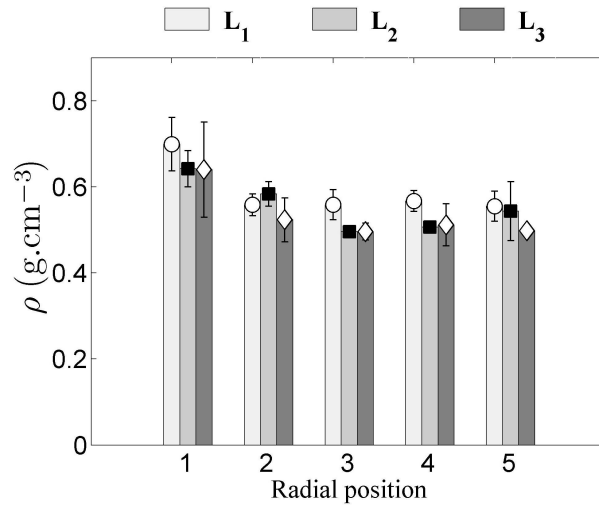
Figure 4.8: D_{mean} over radial and longitudinal positions variation: tree number 1.
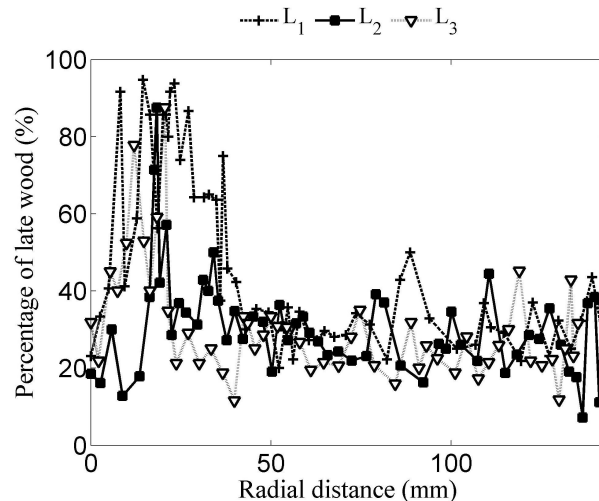
Figure 4.9: $\%LW$ over radial and longitudinal positions distribution: tree number 1.

As in the previous section for density, also the elastic properties radial variation from pith to cambium was analysed as a function of the cambium physiological age which generates the cells. So, the annual growth ring(s) whose elastic properties were identified on each specimen were the same for one specific radial position. Once more, that was guaranteed by counting and numbering the rings from the cambium to the pith to fix the radial position (physiological age) along the stem height.

For each level defined along the stem height, the mean values of the three elastic properties were calculated and analysed over the five radial positions.

The set of images shown on figure 4.12 reveal the variation along the radius for E_R. The first result of the evaluation of the pattern achieved relies on the global decrease of the transverse radial modulus from the first position (closer to the pith) to the fifth position
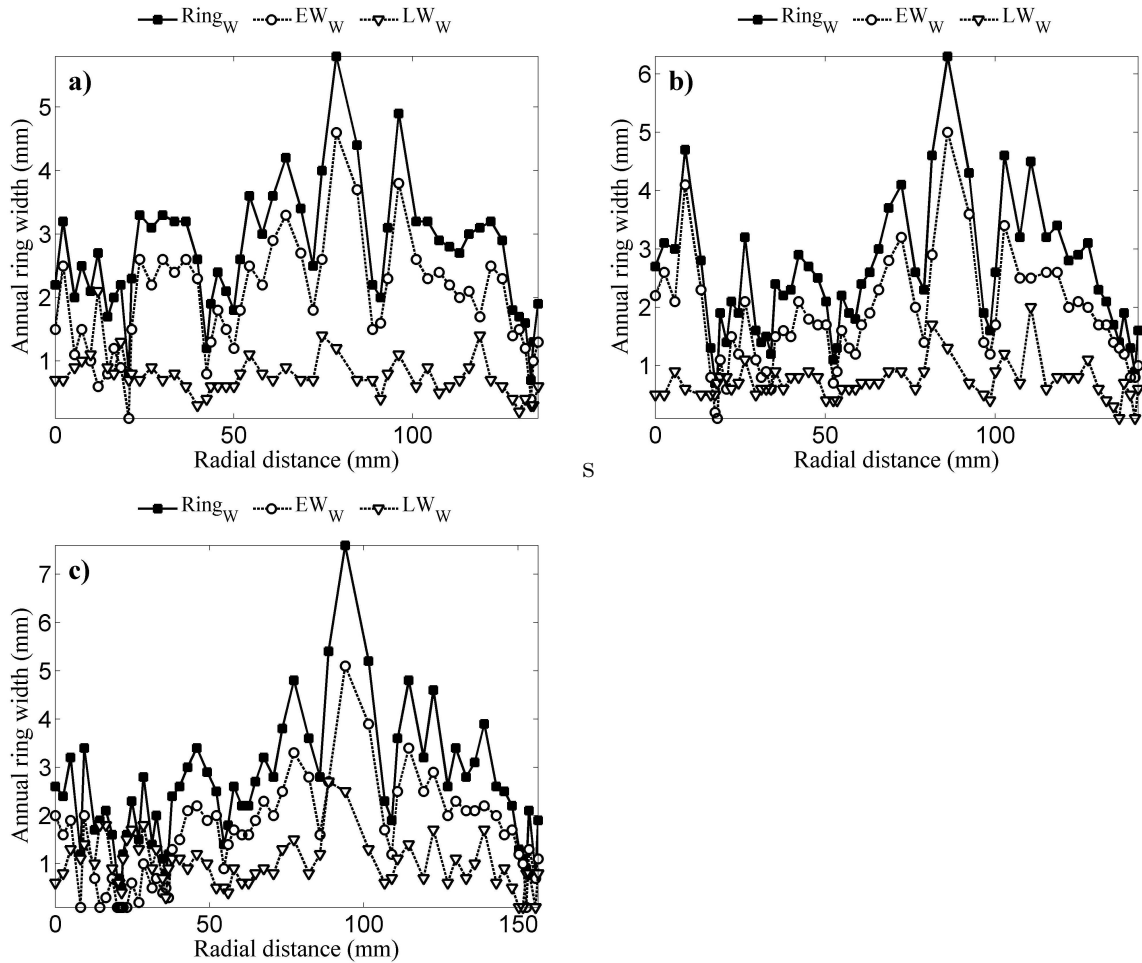
Figure 4.10: $Ring_W$, EW_W, LW_W radial variation: tree number 1 - (a) L3, (b) L2, (c) L1.

(closer to the cambium). This is valid independently on the stem height considered.

Concerning to the shear modulus variation, the figures Figure 4.13, shows a general pattern of variation on radial direction consistent with the E_R pattern, which is resumed by a decrease from pith to cambium.

LONGITUDINAL VARIABILITY

For each position defined along the stem radius, the mean values of the mentioned elastic properties were calculated and analysed over the three height levels. As obtained for the radial variation, also for the longitudinal one, the E_R and the G_{RT} modulus showed a trend of reduction from the base to the top of the stem (Fig. 4.14) despite along the stem height the decrease sometimes follow different fluctuations.
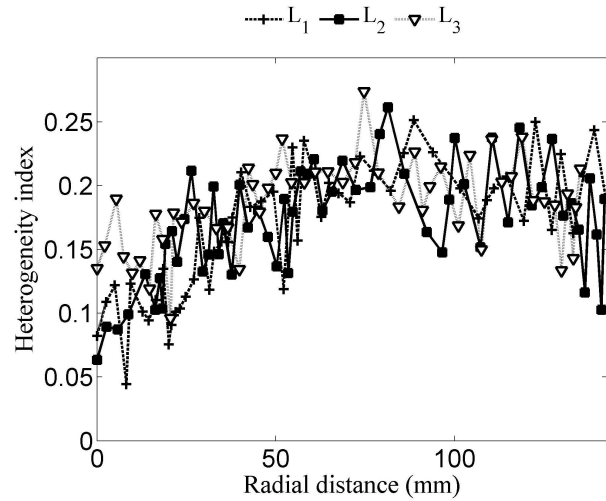
Figure 4.11: *HI* over radial and longitudinal positions distribution: tree number 1.
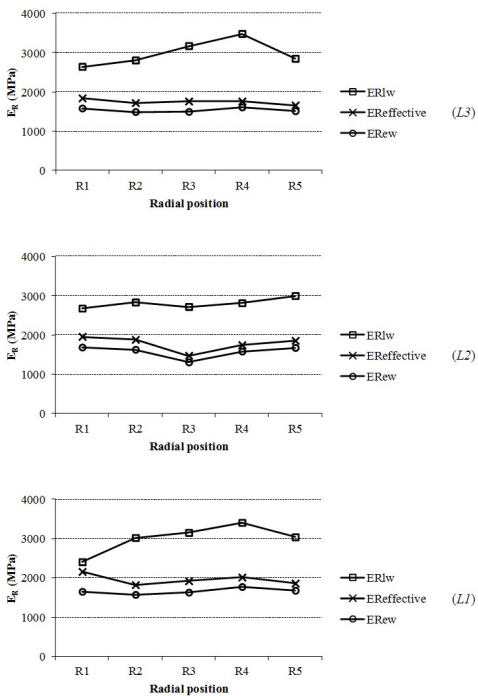
Figure 4.12: E_R over radial positions dis-
tribution: tree number 1
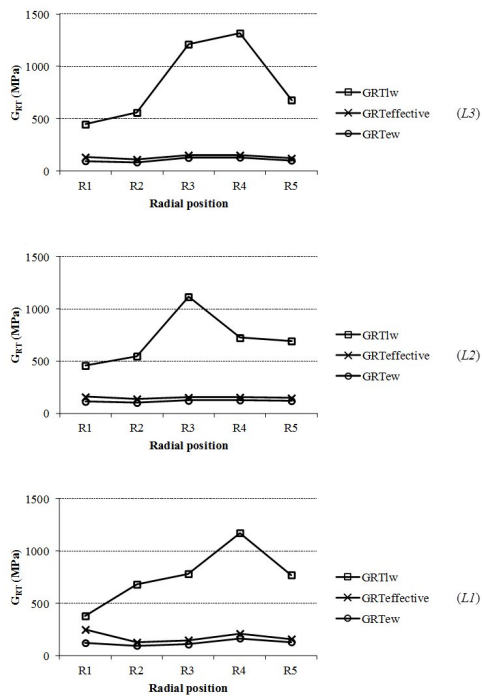
Figure 4.13: G_{RT} over radial positions
distribution: tree number 1
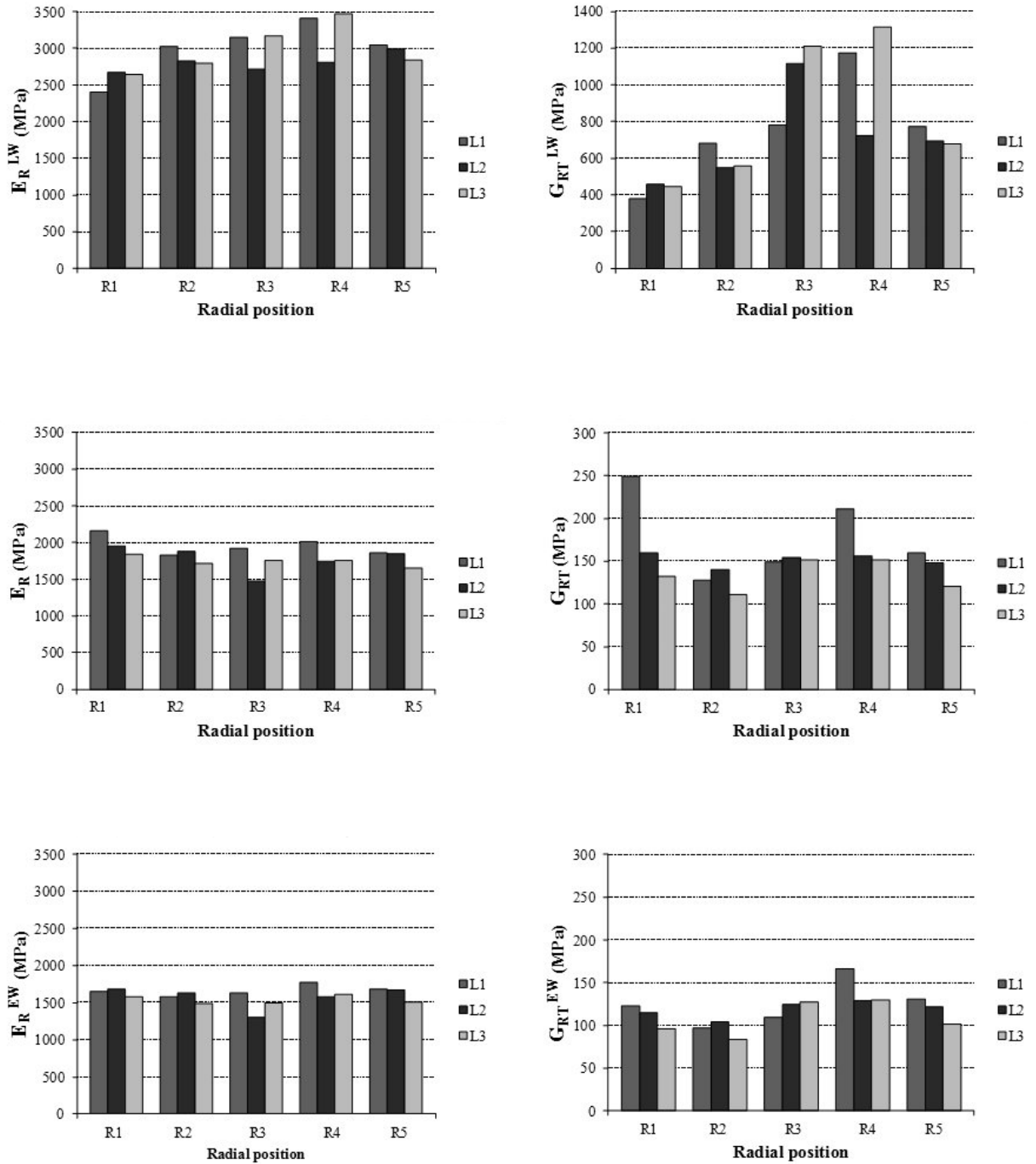
Figure 4.14: E_R and G_{RT} radial and longitudinal variation: tree number 1

4.4   Elastic properties-density relationships

More than finding the global trends of variation, relationships between elastic properties patterns of variation in radial and longitudinal and homologous patterns of the material anatomical characteristics must be understood, particularly expressed by the density. Regarding on the figure 4.14, the global E_R and G_{RT} radial variations follow that one presented by the mean density (Fig. 4.8), concerning to a general decrease from the innermost (R1) to the outermost positions (R5). Looking to find some cause-effect relationships between both elastic properties and density variations founded, linear fit correlations were performed for the same test conditions (fixing cambial age and level). Only the random factors associated to the tree life itself were varied, considering the five trees values of the same elastic property over each of the density parameters, one at a time. Considering the whole mesostructure over ROI, the complete annual growth rings visible on that region (varying from one to four), for the ten specimens corresponding to each radial position studied, were identified and their density parameters mean values established to relate with the respective E_R and G_{RT} mean values.

Analyzing the obtained determination coefficient values for the case here presented, and despite the positive or negative correlations verified, it can be appreciated that, in general, both ER showed good relations with four of the density parameters, presenting determination coefficients always between 66.44% and 96.61%. Those parameters are D_{mean}, D_{min}, D_{EW} and $\%LW$. From all of them, D_{mean} is the parameter that more consistently explains the variation for the three elastic properties, especially for E_R and G_{RT}. Curiously, the annual ring width, often used as major aspect on wood quality definition (Fernandez-Golfin and Diez, 1994), does not reveal much appetence to explain the elastic properties here studied. Regarding to the ring width fractions, whenever both present significant correlations with E_R and G_{RT}, for the EW_W it is mostly negative whereas for the LW_W is positive. Also is confirmed that the greater determination coefficients were observed in the positions closer to the pith. By organization and optimization reasons, doing to the great number of images, only the study referring to one density parameter (D_{mean}), for all physiological ages and eight levels, were presented in this section, regarding to the E_R and G_{RT} relationships (Figs. 4.15, 4.16, 4.17, 4.18, 4.19), presenting the remaining on appendix C. However, the complete results of determination coefficients (in percentage) are presented in Table 4.3. Analyzing the extreme situations, concerning to the D_{mean} correlation with E_R and G_{RT}, sometimes determination coefficient reaches values above 90%. Nevertheless, from table 4.3, although D_{mean} presents most often the highest determination coefficient values, none of the studied density parameters shows a stable correlation pattern for any of the elastic properties revealing the mesostructure heterogeneity.
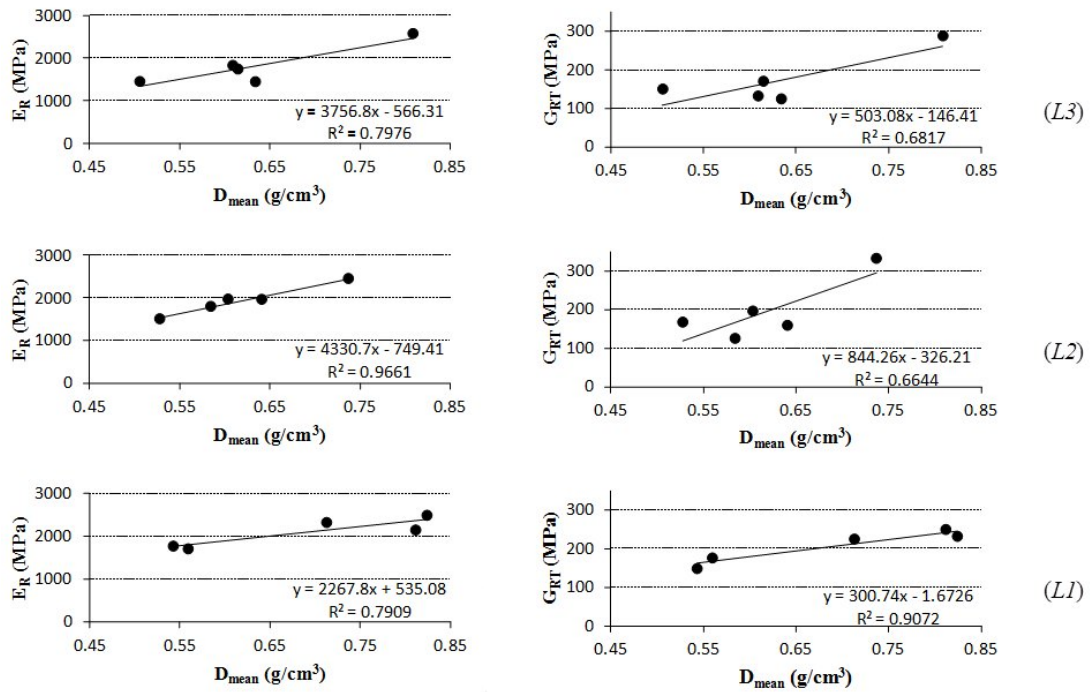
Figure 4.15: Linear fitting between E_R, G_{RT}, and D_{mean}: all trees at R1 position
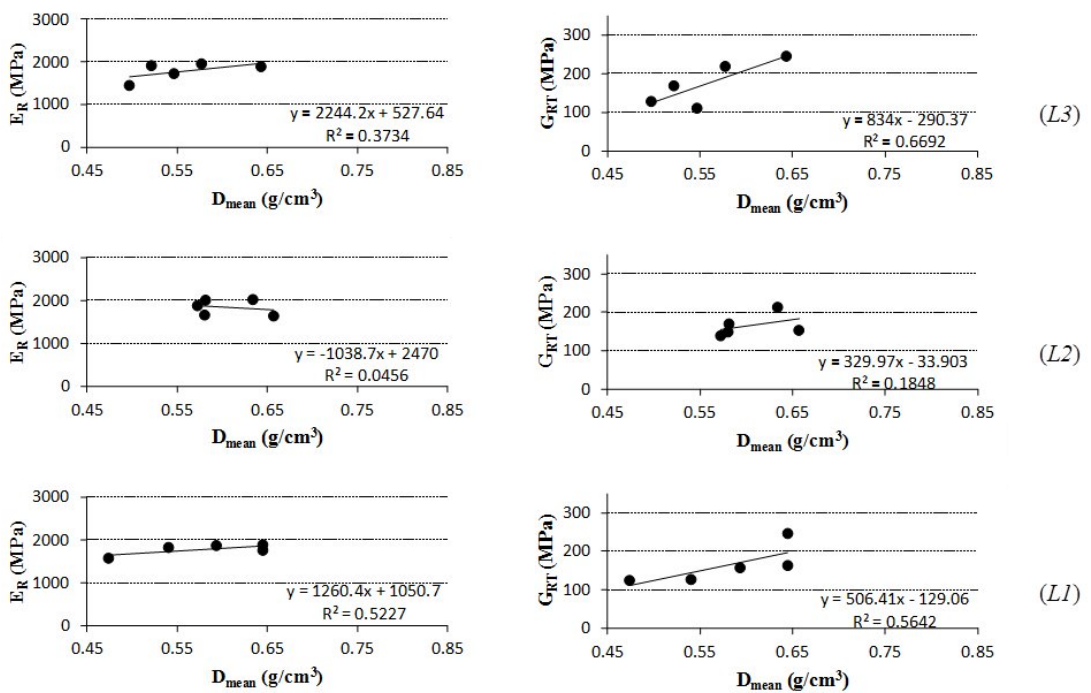
Figure 4.16: Linear fitting between E_R, G_{RT}, and D_{mean}: all trees at R2 position
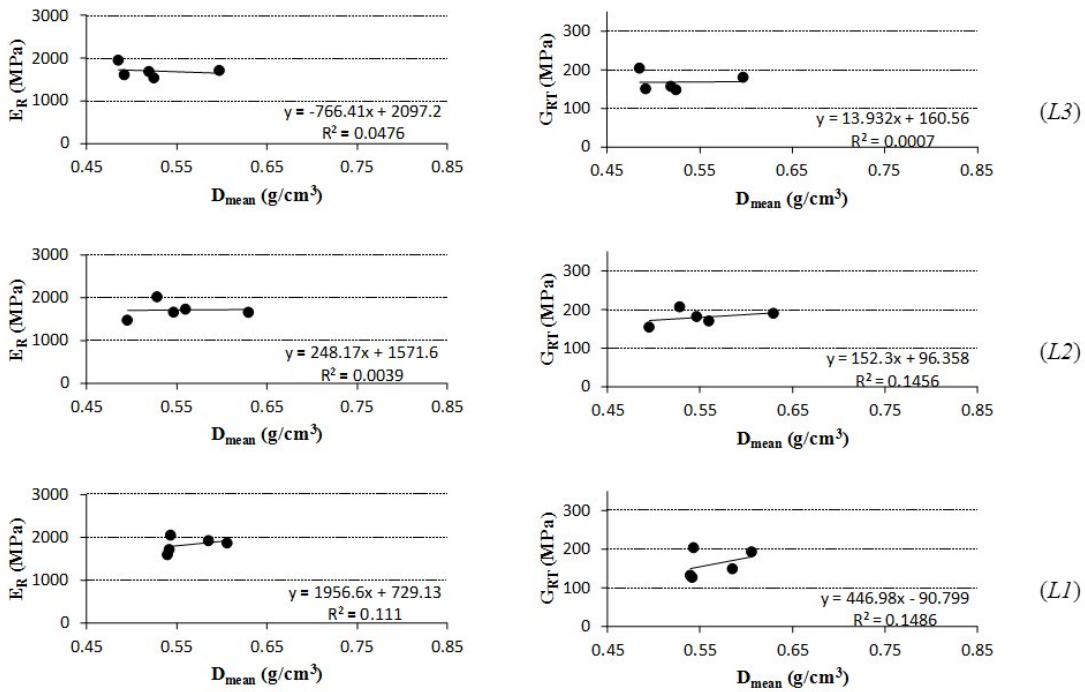
Figure 4.17: Linear fitting between E_R, G_{RT}, and D_{mean}: all trees at R3 position
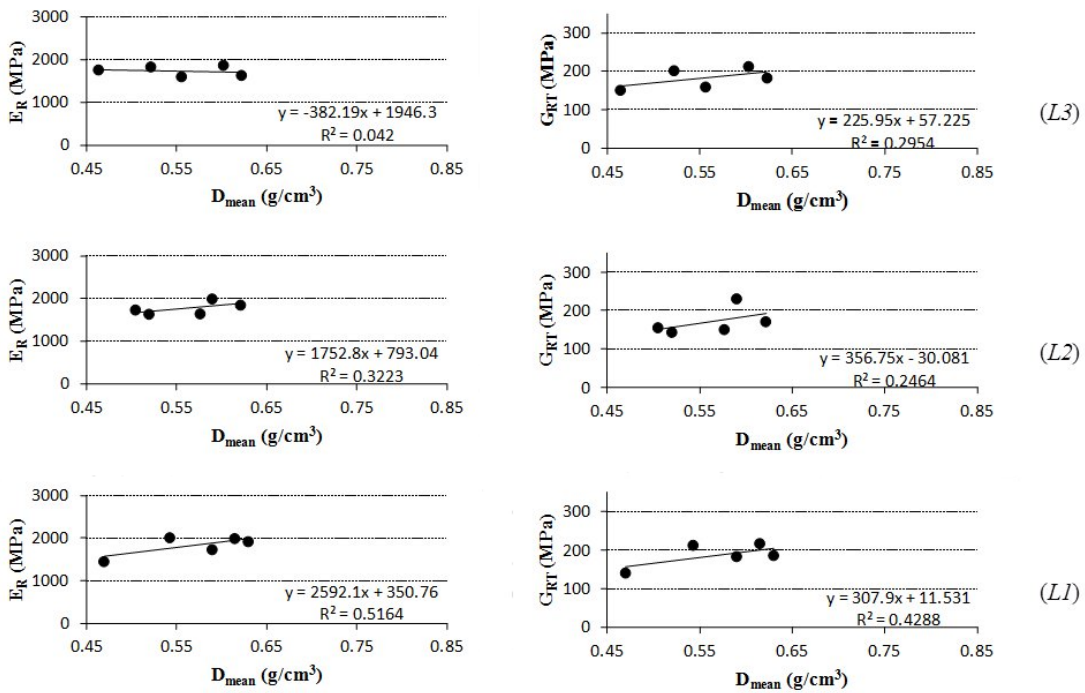
Figure 4.18: Linear fitting between E_R, G_{RT}, and D_{mean}: all trees at R4 position
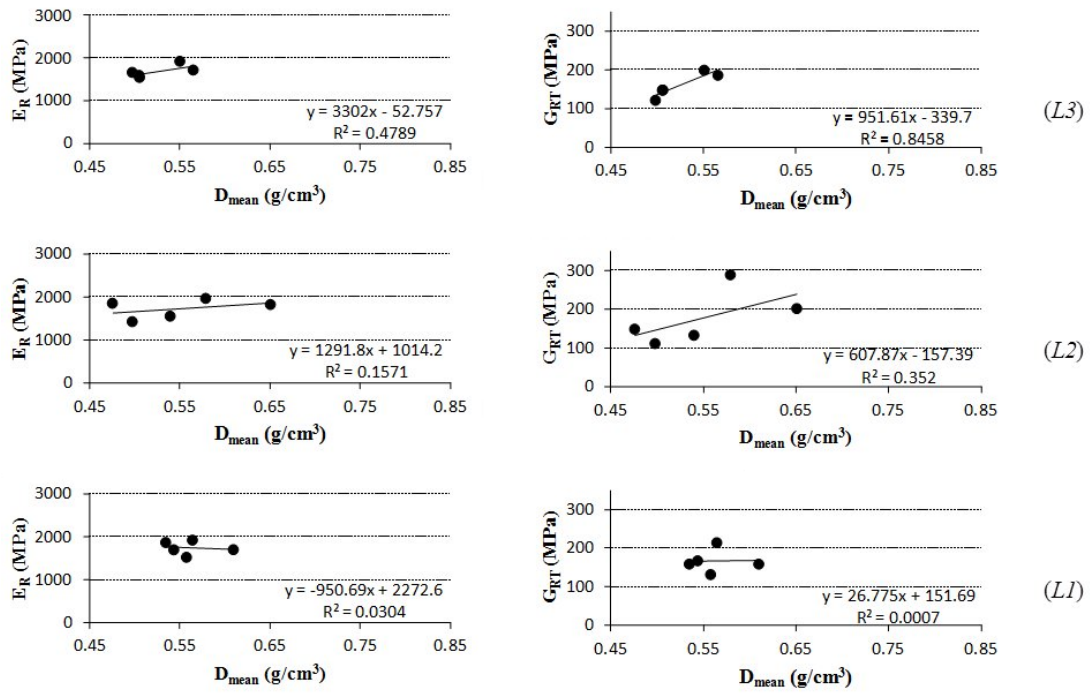
Figure 4.19: Linear fitting between E_R, G_{RT}, and D_{mean}: all trees at R5 position

4.5   Conclusion

Concerning to the elastic properties identification, the AbM method reveals suitable for global E_R, E_T, ν_{RT} and G_{RT} determination, achieving consistent values that are in accordance with references (Table 4.1), notwithstanding the initial hypothesis assumed of uniaxial tension state. However, some identifiability problems were reported for the E_T when the ring orientation was less variable within the specimens characterising the same position. The local elastic properties concerning to the EW and LW tissues were then estimated from the global properties, as a function of mean density, combining the application of a micromechanical model (mixture law) and a unit cell model (Table 4.2).

Generally, correlations between D_{mean} and E_R and G_{RT} were positive and statistically significant allowing the use of D_{mean} as mediator to infer local elastic properties. Besides the average density, sometimes also other parameters showed significant correlations with the elastic constants. Specifically, D_{min}, LW_W and D_{EW} presented substantial and positive determination of E_R and G_{RT}. With regard to EW_W , when presented significant correlation with the moduli, it was always negative which, physically, makes sense because the greater the contribution of the EW fraction in the annual ring, the lower the E_R and G_{RT}. From table 4.3, where all the determination coefficients are resumed, one can conclude that, despite D_{mean} is the parameter that more frequently explains the elastic behaviour, there are several others that alternately assume that role, which reveals the great variability of the mesostructure from specimen to specimen. The scale here studied is not the one

of the material but that of mesostructure. So, over the ROI, the representative element (the annual ring) varies in number (from one to four) and implicitly in width. Against this, becomes evident the interest and the benefit of a local analyses made point by point, in which the correlations will be more reliable, once both density and elastic properties result from the equivalent quantity (one facet size), against the ones here presented: elastic properties were identified from the average of 10 specimens mechanical response, over a $7.1 \times 5.4 \text{mm}^2$ region, whilst density was measured on a single specimen and with a 100 micron frequency.

The radial an the longitudinal within stem variability of E_R and G_{RT} was generally characterized by a decrease pattern. Radially, the trends of variation determined were: E_R varied from 10-35% and G_{RT} varied from 7-41% whilst longitudinally E_R varied from 4-12% and G_{RT} varied from 7-28%.

Table 4.3: Correlations between (E_R) and (D_{mean}, D_{min}, D_{max}, D_{EW}, D_{LW}, %LW, EW_W, LW_W, $Ring_W$, HI) for all trees.

Elastic Property	Radial position	Height level	Density parameters									
			D_{mean}	D_{min}	D_{max}	D_{EW}	D_{LW}	%LW	EW_W	LW_W	$Ring_W$	HI
	1	L1	79.09	86.00	52.45	81.41	34.31	83.92	79.81	45.51	14.65	31.63
		L2	96.61	93.45	18.50	96.04	2.20	89.39	84.74	52.49	39.12	54.83
		L3	79.76	77.17	43.20	80.56	22.15	87.80	72.63	65.16	13.91	15.44
	2	L1	52.27	21.15	31.80	22.50	44.07	63.78	66.24	15.07	22.46	16.46
		L2	4.56	8.52	28.13	3.76	31.09	27.87	8.24	19.66	12.46	52.66
		L3	37.34	35.10	0.83	56.56	11.05	20.64	1.91	14.56	0.27	28.36
E_R	3	L1	11.10	1.46	3.85	17.72	0.63	2.11	22.43	24.71	25.78	0.12
		L2	0.39	7.72	65.27	14.06	58.58	1.17	5.67	31.47	10.23	65.53
		L3	4.76	1.46	8.02	0.74	3.32	3.85	6.47	49.58	10.98	10.08
	4	L1	51.64	12.16	57.09	23.75	51.24	32.10	21.24	81.67	37.72	17.23
		L2	32.23	45.76	39.52	68.07	21.43	3.83	0.13	12.26	3.99	0.01
		L3	4.20	14.36	6.51	8.12	8.65	5.50	10.82	6.40	16.38	7.42
	5	L1	3.04	35.29	20.27	50.51	27.37	45.56	10.06	40.45	20.19	47.43
		L2	15.71	44.83	3.27	38.94	3.37	0.41	9.30	0.01	4.37	24.43
		L3	47.89	90.99	22.66	87.52	25.89	6.90	24.37	11.51	22.81	62.46

Table 4.4: Correlations between (G_{RT}) and (D_{mean}, D_{min}, D_{max}, D_{EW}, D_{LW}, %LW, EW_W, LW_W, $Ring_W$, HI) for all trees.

Elastic Property	Radial position	Height level	Density parameters									
			D_{mean}	D_{min}	D_{max}	D_{EW}	D_{LW}	%LW	EW_W	LW_W	$Ring_W$	HI
	1	L1	90.72	75.87	70.18	80.36	52.07	79.31	60.89	23	17.94	10.84
		L2	66.44	83.99	8.94	80.18	8.13	81.95	34.03	72	3.57	74.74
		L3	68.17	70.29	17.36	75.68	4.81	83.87	50.2	71.96	2.6	43.34
	2	L1	56.42	64.24	19.95	63.72	3.52	48.5	0.02	62.49	15.58	17.45
		L2	18.48	76.53	1.8	50.77	2.22	0.09	14.21	14.96	15.38	29.72
		L3	66.92	80.94	32.03	86.15	8.67	39.93	18.77	71.5	39.59	1.81
E_R	3	L1	14.86	29.82	10.82	71.65	21.97	15.78	0.02	4.3	0.66	21.16
		L2	14.56	30.38	77.42	36.27	94.44	9.73	29.5	14.28	34.68	92
		L3	0.07	3.2	13.82	2.53	7.58	0.11	20.03	56.99	26	31.33
	4	L1	42.88	19.58	35.33	30.24	25.51	28.57	21.88	68.96	35.82	3.73
		L2	24.64	68.95	18.84	78.48	6.69	1.09	5.31	1.42	1.22	6.39
		L3	29.54	12.48	3.8	18.6	4.45	24.12	16.2	26.4	2.9	1.83
	5	L1	0.07	81.36	67.58	86.44	69.28	18.68	63.23	60.49	71.06	84.73
		L2	35.2	84.82	11.93	86.92	5.5	1	59.14	3.76	36.73	43.41
		L3	84.58	68.47	32.65	74.09	29.81	6.05	49.84	1.81	33.18	39.69

References

C.C. Chamis and J.H. Sinclair. Ten degree off-axis test for shear properties in fiber composites. *Experimental Mechanics*, 17(9):339–346, 1977.

S. Cramer, D. Kretschmann, R. Lakes, and T. Schmidt. Earlywood and latewood elastic properties in loblolly pine. *Holzforschung*, 59(531-538):5, 2005.

F. Farruggia and P. Perré. Microscopic tensile tests in the transverse plane of earlywood and latewood parts of spruce. *Wood Science and Technology*, 34(2):65–82, 2000.

J. I. Fernandez-Golfin and M. R. Diez. Influencia da la anchura del anillo de crecimiento en la densidade y otras propriedades físico-mecanicas de la madera estructural de diversas espécies. Technical report, Centro de invetigación Florestal (CIFOR-INIA), 1994.

J. C. Ferrand. Réflexions sur la densité du bois. 2ere partie: Calcul de la desnsité et de son heterogeneite. *Holzforschung*, 36(3):153–157, 1982.

Forest Products Laboratory. *Wood handbook: Wood as an engineering material*. Gen. Tech. Rep. FPL-GTR-113, US Department of Agriculture, 1999.

L.J. Gibson and M.F. Ashby. *Cellular solids. Structure and properties*. Cambridge University Press, 1997.

L.O. Jernkvist and F. Thuvander. Experimental determination of stiffness variation across growth rings in Picea abies. *Holzforschung*, 55(3):309–317, 2001.

R. M. Jones. *Mechanics of composite materials*. Taylor and Francis, 2nd edition, 1999.

J.L. Lousada. *Variação fenotípica e genética em características estruturais na madeira de Pinus pinaster Ait.* PhD thesis, Universidade de Trás-os-Montes e Alto Douro, Vila Real, Portugal, 2000.

A. Majano-Majano, J. Fernandez-Cabo, S. Hoheisel, and M. Klein. A test method for characterizing clear wood using a single specimen. *Experimental Mechanics*, 52:1079–1096, 2012.

C.S. Modén and L.A. Berglund. A two-phase annual ring model of transverse anisotropy in softwoods. *Composites Science and Technology*, 68(14):3020–3026, 2008.

J. Xavier, S. Avril, F. Pierron, and J. Morais. Novel experimental approach for longitudinal-radial stiffness characterisation of clear wood by a single test. *Holzforschung*, 61(5):573–581, 2007.

J. Xavier, A.M.P. de Jesus, J.J.L. Morais, and J.M.T. Pinto. Stereovision measurements on evaluating the modulus of elasticity of wood by compression tests parallel to the grain. *Construction and Building Materials*, 26(1):207–215, 2012.

J.C. Xavier, N. Garrido, J. Oliveira, J. Morais, P. Camanho, and F. Pierron. A comparison

between the Iosipescu and off-axis shear test methods for the characterization of *pinus pinaster* Ait. *Composites Part A: Applied Science and Manufacturing*, 35(7-8):827–840, 2004.

B.J. Zobel and J.P. Van Buijtenen. *Wood variation: Its causes and control.* Springer Series in Wood Science, Ed: Timell, T.E., Springer-Verlag, 1989.

Chapter 5

Identification of transverse stiffness properties of *P. pinaster* by the virtual fields method

In this chapter, the in-situ characterisation of elastic properties of earlywood (EW) and latewood (LW) constituents of *P. pinaster* by the virtual field method (VFM) was investigated. The meso structure was classed using image processing and analysis tools based on segmentation (classification) and contour detection. The material defining each EW and LW layers was considered homogeneous, continuous and with a linear elastic orthotropic behaviour.

Contents

5.1 Introduction

The elastic properties of EW and LW constituents represent fundamental data in applications such as the transverse fracture behaviour of wood (Bigorgne, 2011; Thuvander et al., 2000), the mechanical behaviour of bolted wood connections (Santos et al., 2009; Zink-Sharp et al., 1999) and wood transformation processes (Holmberg et al., 1999). However, the correct evaluation of wood properties at the growth ring scale poses several difficulties. The conventional approach make use of statically determined tests, which therefore are based on testing small samples of each individual layer (Cramer et al., 2005; Farruggia and Perré, 2000). For statistical representativeness or spatial variation assessment of elastic properties, this approach requires testing a huge amount of samples. This limitation can be in part surmounted by a different approach based on statistically undetermined mechanical tests, from which several parameters can be identified from a single test (Jernkvist and Thuvander, 2001; Xavier et al., 2007, 2009). This methodology relies on full-field kinematic measurements (*e.g.*, displacement or strain) provided by a suitable optical technique, coupled with an inverse identification method. In this chapter, the identification of orthotropic elastic properties at the growth ring will be investigated. The approach combines the virtual fields method with full-field measurements provided by digital image correlation (DIC). This analysis represents a first approach for direct evaluation of stiffness components at each EW and LW constituents at the growth ring scale (§ 2.1.4). In order to validate the identification strategy, a given position on a tree was selected, from which ten specimen with different ring-orientation were processed. As case study, the first tree, at the breast height and outermost radial position was chosen.

5.2 Classification of the growth ring structure by image processing

Images of the growth ring structure at the central part of the specimens were taken just before testing. The size of the region of interest was fixed by the telecentric lens to 7.1×5.4 mm^2, which typically covered a few annual rings. It is worth noticing that this region corresponds to the one observed when performing DIC measurements, so a direct correspondence can be established between strain fields and constituent layers at the meso scale.

In processing the images of the wood structure at the annual growth rings, binary (mask) images were defined for classifying relevant constituents at the scale of observation. Taking into account the magnification of the optical system, by default, three regions were assumed: (i) resin channels (RC); (ii) EW and (iii) LW. The algorithm for image processing and analyses was implemented in Matlab according to the flowchart of Fig. 5.1, described as follows (Fig 5.2):
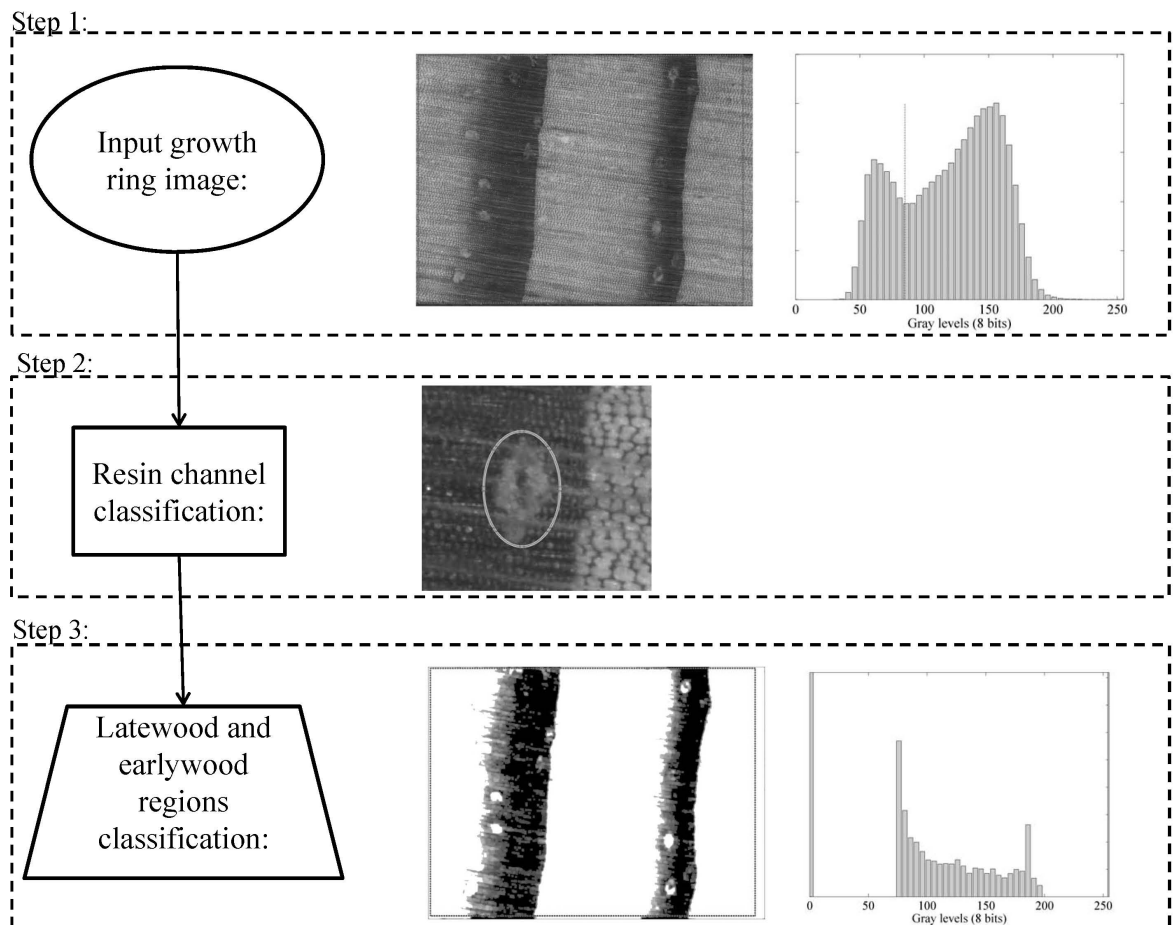
Figure 5.1: Image processing and analyses flowchart yielding the annual growth ring classification.

(i) Input and flip-up the raw image of the growth ring structure. Selection of the region of interest within the field of view corresponding to the region analysed by DIC (Fig 5.2a).

(ii) Detection of each resin channel in the image by means of an elliptical contour. This operation was found more accurate to be done manually by the user because the pixel gray-level of these elements was not unique and constant throughout the image, thus introducing difficulties in the automatisation of this process (Fig 5.2b). This step was deemed necessary in order to remove these elements on the identification process of EW and LW tissues afterwards.

(iii) Several algorithms have been proposed in the literature for image segmentation based on histogram bilevel thresholding (Dirami et al., 2013). Eventually, they can be computationally time consuming and their effectiveness and accuracy can be significantly reduced when applied to a complex image such as one of the wood
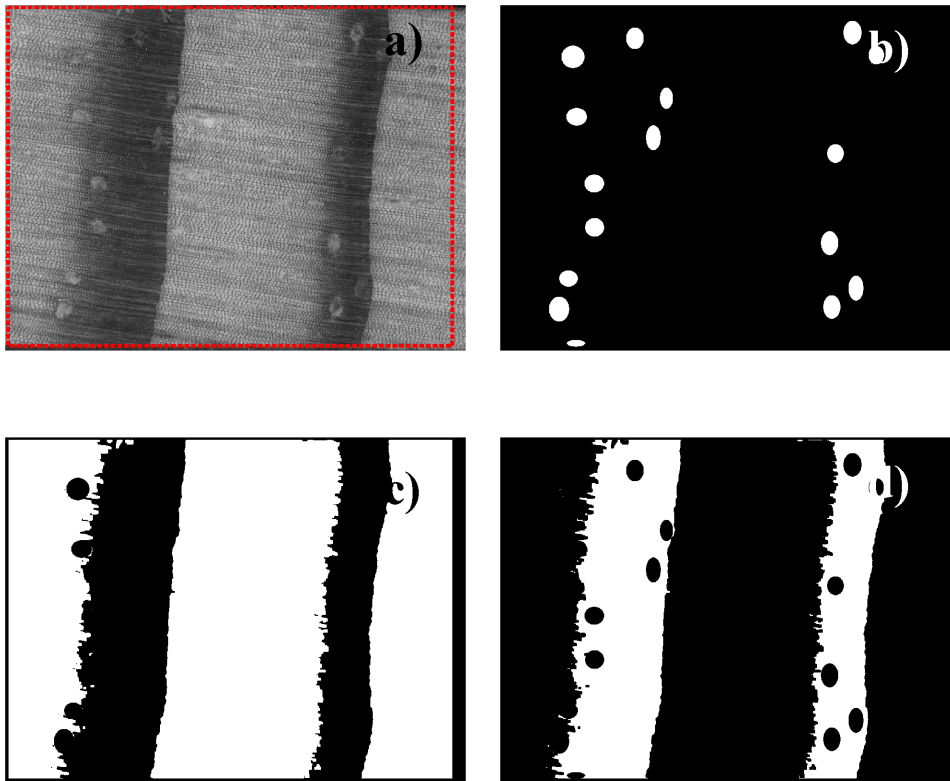
Figure 5.2: (a) growth ring structure across the gauge section, (b) resin channels mask; (c) earlywood mask; (d) latewood mask.

structure at the growth ring level. In this work, the definition of the EW and LW layers was achieved by iterative thresholding. At each step, pixels outside a given interval in the histogram were set either to 0 (EW) or 255 (LW) (see step 3 in Fig. 5.1). This procedure was required to clean up EW and LW layers, since the original images had no clear pixel gray-level separation between them (note that the pixel gray-level of the cell wall was naturally presented across the entire growth rings). Besides, rays were eventually visible across the field of view introducing an additional ambiguity. In this iterative processing, the histogram of the output image was analysed at each step until clear definition of the latewood layer was achieved (Fig 5.2d). The EW regions were then assumed as the counterpart of LW (Fig 5.2c).

The output binary images where then converted into mask matrices at each data point where displacement and strain values are given by the DIC analysis. An overview of this discretisation over the region of interest is shown in Fig. 5.3. As it can be seen the optical system was enough resolution to sort out each relevant constituents at the scale of observation. In a first approximation, an average off-axis angle was used to take into account the global orientation of the annual rings structure. This approximation is more accurate when the curvature of the growth rings (polar coordinate system) can be
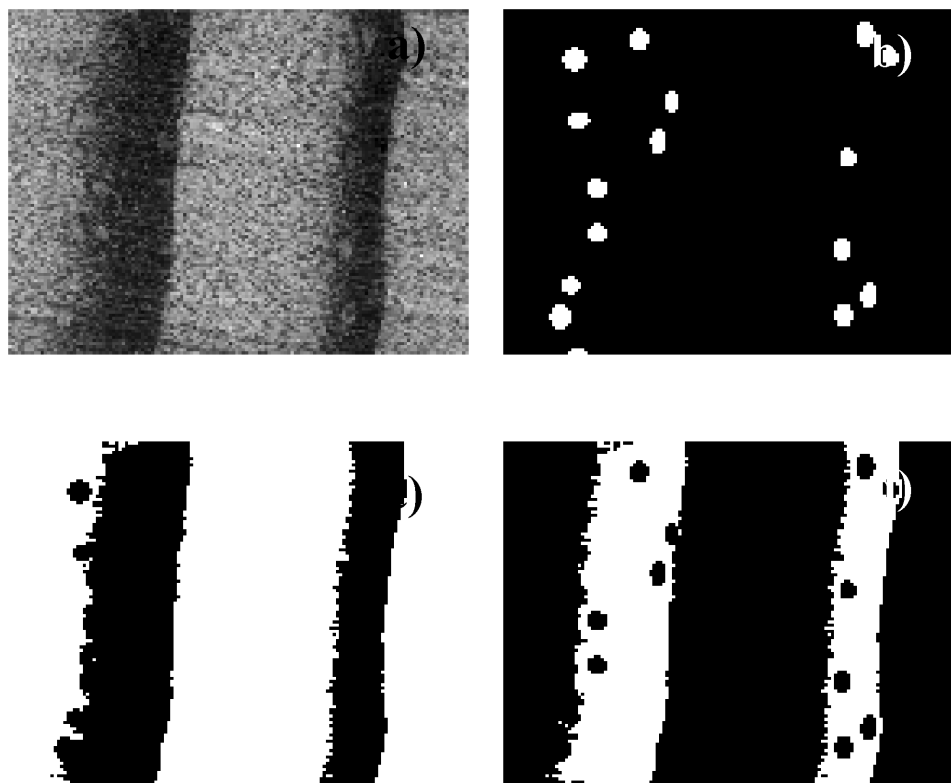
Figure 5.3: (a) growth ring structure across the gauge section, (b) resin channels mask; (c) earlywood mask; (d) latewood mask.

reasonably approximated by a straight line (cartesian coordinate system). However, in future work an image-based algorithm should be implemented for attribute a local off-axis angle at each point in the image corresponding to the DIC spatial resolution.

5.3 Identification of local stiffness components at the growth rings scale

For the purpose of validation, a given location within the stem was selected corresponding to the first tree, at breast height and outermost radial position. Considering the identifiability study previously carried out in § 4.2, only Q_{11} and Q_{66} stiffness components of EW and LW layers were eventually expected to be identified. This was confirmed in the current analyses in which inconsistent values of Q_{12} and Q_{22} were systematically obtained. For the purpose of complete identification of these latter stiffness components, complementary tests would be needed in which the loading system will privilege the mechanical deformation along those axes and planes of symmetry. However, this issue will not be explicitly addressed in this work, being invoked in future work.

An example of the strain fields on the specimen coordinate system together with the
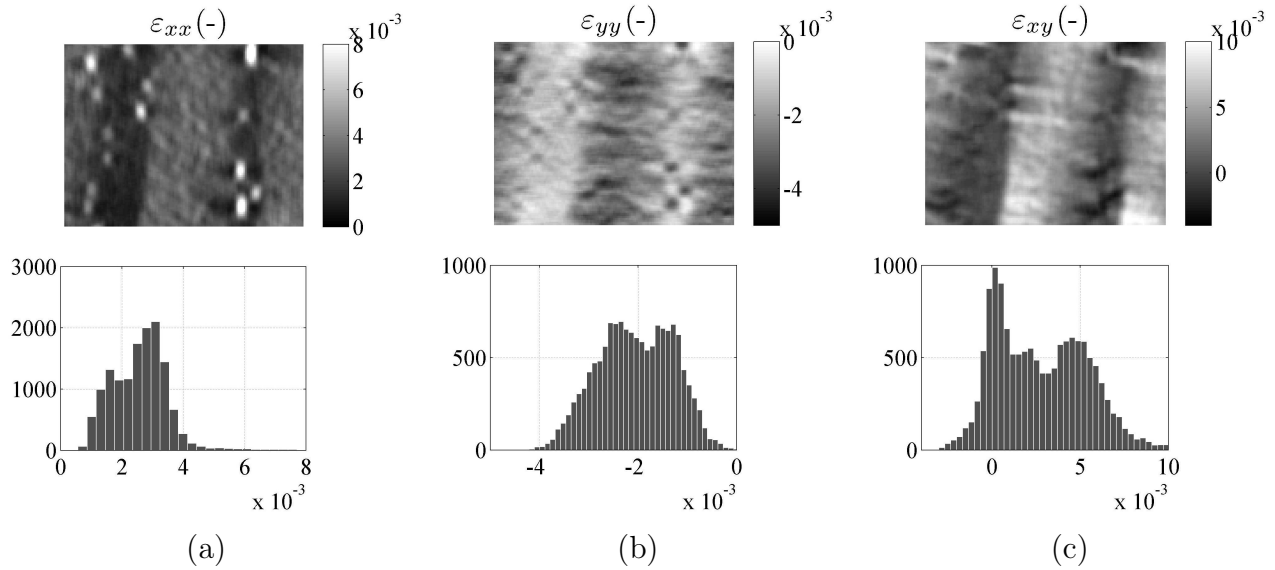
Figure 5.4: Strain field components on the material coordinate system (a) ε_{xx}, (b) ε_{yy}, (c) ε_{xy} (load = 55 N).

histogram of the strain maps is given in Fig. 5.4, for an applied load of about 55 N. To start with, heterogeneous strain fields were obtained following the heterogeneity of the wood structure at the growth ring level (Fig. 5.3). Moreover, all three components of the strain field exist (*i.e.*, they are different than zero), although with different amplitudes and locations within the region of interest. As expected, the local strain values are much influenced by the complex wood structure at the scale of observation. This is evidenced on the bipolar strain histograms of Fig. 5.4. Considering as example the ε_{xx} map (Fig. 5.4(a)), an average value of 1.7×10^{-3} of axial deformation was obtained for the LW layer, whilst a value of 3.4×10^{-3} was reached in the EW tissue. In this case, in average, the ratio between LW and EW strain values is equal to 2. This is consistent with an average density ratio of 1.8 g/cm^3 between LW and EW tissues measured by X-ray micro-densitometry. Farruggia and Perré (2000) have reported similar levels of axial (radial) strain, for the same range of applied stress, when performing micro-mechanical tensile tests on isolated tissues of EW and LW on spruce wood. A similar ratio between strain values associated to each EW and LW layers was obtained for ε_{yy} (Fig. 5.4(b)) and ε_{xy} (Fig. 5.4(c)).

Another important issue concerning the reconstruction of strain fields at the growth ring level can be discussed based, for instance, in the ε_{xx} component (Fig. 5.4(a)). At a given applied axial stress, it is physically plausible to assume that regions of pure EW tissue deforms more than region of pure LW (the former having a higher signal-to-noise ratio than the latter). This has been consistently observed in previous studies at a suitable scale of observation (Garab et al., 2010; Hassel et al., 2009a,b; Réthoré et al., 2010). Nevertheless, although this hypothesis seems globally verified across the region of interest (Fig. 5.4), there are some data points, specially within the LW tissue, that have
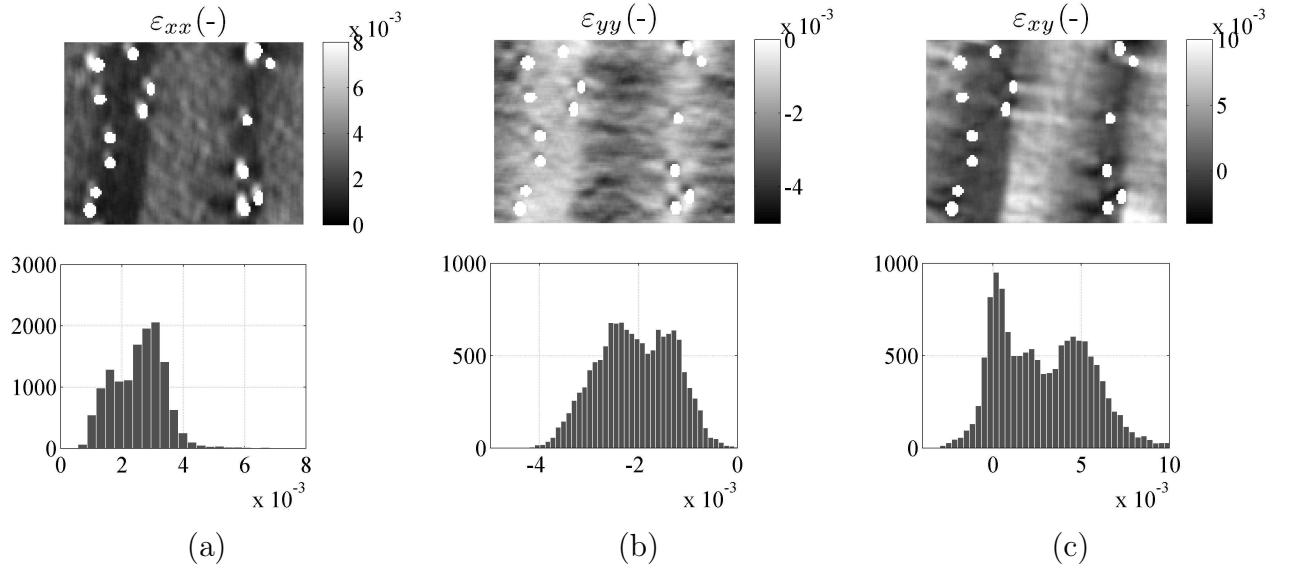
Figure 5.5: Strain field components on the specimen coordinate system (a) ε_{rr}, (b) $\varepsilon_{\theta\theta}$, (c) $\varepsilon_{r\theta}$ (load = 55 N).

an apparently very high level of strain, which is usually even higher than the strains at the EW tissue. This is, however, physically inconsistent with the characteristics of the tissues itself. This measurement clearly demonstrates the difficulties on the reconstruction of the local strains (balance between spatial resolution and resolution) in a very complex structure such as the one observed across a few annual growth rings of *P. pinaster*. These locations within the region of interest associated to an apparent high level of strain can be, however, systematically correlated with resin channels. Therefore, it is not surprising that these locations of high strain level occur preferentially at the latewood layer since it is within this tissue (and in the transition between EW and LW) that resin channels usually forms during the seasonal growing period of *P. pinaster* wood (Carvalho, 1996). Therefore, some regularisation must be taken into account when processing these strain fields for the purpose of in-situ identification of EW and LW tissues. This contrast with the global identification by the anisotropic-based method § 4.2, in which this regularisation was not found significant due to the integration effect of considering average strain values over the region of interest (*i.e.*, a virtual strain gauge). It is interesting to notice that regularisation of the estimated kinematic (*e.g.*, displacement, strain or velocity) fields is a common practice, for instance, in processing medical imaging. As an example, when processing ultrasound imaging of the myocardial tissue by speckle tracking methods, the velocity fields are in general noisy and may require correction before further processing (D'hooge, 2007). A possible way is to take into account additional boundary conditions based on *a priori* knowledge about the characteristics of the velocity field. For instance, it may be assumed *a priori* that neighboring pixels must have similar velocity vectors in both amplitude and direction during the regularization process.
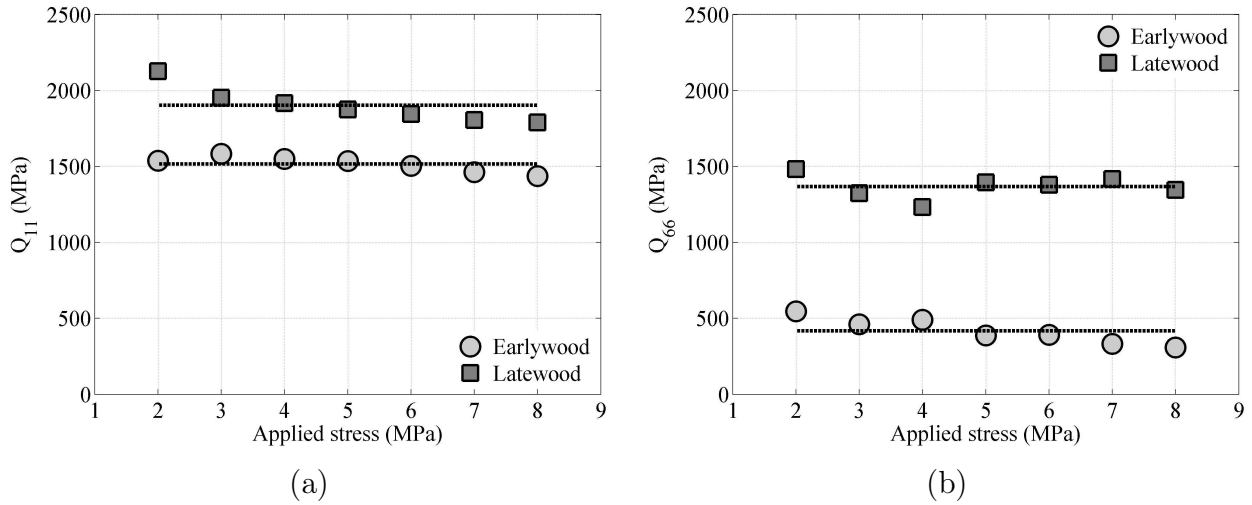
Figure 5.6: Stiffness components of earlywood and latewood constituents: (a) Q_{11}, (b) Q_{66} as a function of the applied stress.

For the local identification, to start with, the region of resin channels were systematically removed across the region of interest. In this procedure, the mask of the resin channels previously defined using image processing and analysis was applied (Fig. 5.3(b)). Regions of each EW and LW layers were then defined by applying their respective masks (Fig. 5.3(c) and Fig. 5.3(d), respectively). In addition, extra data points were rejected based on statistical representativeness, in order to exclude a radius of influence of the resin channels on the EW and LW deformations. For a given layer, the mean (μ) and standard deviation (σ) over the segmented strain components were computed. Values outside the interval of $|\mu \pm \sigma|$ were then systematically removed (low-pass filtering effect). In this way, some regularisation was taken into account by removing erroneous data points in the vicinity of the resin channels. Indeed, this issue points out one major drawback of DIC (local subset approach) when dealing with boundaries or discontinuities. The resin channels are weakness zones within the growth rings, which most often promote the rupture of the tissue. Usually resin channels are empty, but eventually they can be filled with resin. Nevertheless, these elements can be seen as a discontinuity within the tissue and, therefore, inaccurate values measured by DIC are excepted at these participar locations. This situation is similar when applying the DIC technique to fracture mechanical tests, in which the formation and propagation of a crack is observed (Xavier et al., 2012; Zhang and He, 2012). In these cases, a possible way to process the displacement (strain) fields is just by removing erroneous or inaccurate data points (Pan, 2011). An example of the strain fields obtained by removing erroneous data points, following the algorithm described above, is presented in Fig. 5.5. As it can be seen, data points within EW and LW tissues have seen systematically removed. In future work, other approaches can be

Table 5.1: Comparison between virtual fields method (VFM) and anisotropic-based method (AbM) identification methods for estimating local elastic engineering constants of earlywood (EW) and latewood (LW).

	E_R					
	VFM			AbM		
	EW	LW	LW/EW	EW	LW	LW/EW
Mean (MPa) (%)	1272.8	1677.9	1.32	1673.8	2993.0	1.79
Rel. dif.[a] (%)				31.51%	78.37%	35.64%

	G_{RT}					
	VFM			AbM		
	EW	LW	LW/EW	EW	LW	LW/EW
Mean (MPa)	490.7	1203.6	2.45	121.4	693.9	5.72
Rel. dif. (%)				75.27%	42.34%	133.11%

[a] Relative difference (Rel. dif.)

sought to address this strain field regularisation problem, using for instance a global DIC approach using NURBS base functions (Réthoré et al., 2010).

For the local material parameter identification, stages at an applied axial stress of 1 up to 8 MPa were considered. The strain fields were processed using the VFM for extracting in-situ transverse orthotropic elastic components as described in details in § 2.1.4. Fig. 5.6 shown results for Q_{11} and Q_{66} components of each EW and LW components as a function of the applied axial stress. As it can be seen, the stiffness values are more stable with regard to the applied loading for the EW identification. This is consistent with the fact that the regularisation of strain field is more sensitive for LW regions. Indeed these regions not only represent a smaller volume (area) fraction (*e.g.*, the %LW is 30% from X-ray micro-densitometry analyses), with regard to EW within the region of interest, but have also a lower signal-to-noise ratio. Nevertheless, it is still clear that LW is stiffer than EW, as one may expect.

The results of the local stiffness values determined by the VFM were discussed with regard to the estimation made indirectly using cellular models and based on global parameter identified by the anisotropic-based method taking into account rule of mixtures and local density information provided by X-ray micro-densitometry, as discussed in § 4.2. This comparison is summarised in Table 5.1. For comparison purposes, Q_{11} and Q_{66} stiffness components where transferred, respectively, into $E_R(= Q_{11}\Delta)$ and $G_{RT}(= Q_{66})$ engineering constants (according to the explicit relationship in Eq. 2.22), assuming that $\Delta \equiv \Delta_{EW} \equiv \Delta_{LW} = 1 - \nu_{TR}\nu_{RT} = 0.819$ (in which $\nu_{RT} = 0.586$ and $\nu_{TR} = 0.309$ for *P. pinaster* wood (Xavier et al., 2004)). In terms of E_R, a LW/EW ratio of 1.32 is obtained

from stiffness values identified by the VFM, whilst a slightly high value of 1.79 is obtained based on the global identification by the AbM. The LW/EW ratio of mean densities is 1.92 (estimated from X-ray micro-densitometry measurements), *i.e.*, in the same order of magnitude of the radial Young's modulus. In turn, the G_{RT} shear modulus has a LW/EW ratio of 2.45 by the VFM, whilst a value of 5.72 is obtained based on the global identification by the AbM. In the latter case, the higher different is justified by the fact that an exponential of 3 was used for estimating local properties based on the ratio: $(\rho_{LW}/\rho_{EW})^3$. However, direct results from the VFM indicates that this exponential term is too high. Nevertheless, these results indicate that the ratio of shear modulus between EW and LW is about the twice the one of the radial Young's modulus.

5.4   Conclusion

For validation purposes, a case study was analysed by applying the VFM to directly identify in-situ Q_{11} and Q_{66} stiffness components associated to EW and LW constituents within the annual ring structure. Image processing and analyses were carried out over the complex wood structure at the meso scale for classifying relevant constituents. At the scale of observation, three layers were resolved: resin channels, EW and LW. Binary (mask) images were then used to sort the strain fields for each layer. A regularisation procedure was proposed in order to extract representative strains associated to EW and LW layers. This regularisation of the strain fields was found crucial because erroneous values were estimated in the vicinity of resin channels, since these regions within the annual ring represent a discontinuity on the tissue and therefore displacements measured by DIC are inaccurate (assumption: continuous based functions). These classified strain fields were processed by the VFM for local identification of stiffness parameters. The Q_{11} and Q_{66} LW/EW ratios were found in the order of 1.32 and 2.45, respectively. These ratios suggest a linear relationship between elastic properties and density, rather than a cubic one based on cellular honeycomb models (Gibson and Ashby, 1997).

As a future work this analysis should be extended to further position in the tree for assessing spatial variability of local properties within the stem. This is intended to be relevant data for assessing wood quality based on pattern variations of properties within the stem. Moreover, this information can be of major importance to validate multi-scaling modelling, which take into account the spatial variability of cell wall constituents within the stem (*e.g.*, micro-fibril angle, chemical composition, local density....) (Wagner et al., (in press). Moreover, the numerical study carried you by Nairn (2007) using the material point method (morphological based model) of the transverse modulus of wood as a function of ring orientation and elastic properties taking into account heterogeneity and anisotropy could be properly validated. In addition, the regularisation of the strain fields can be eventually improved using different approaches, such as global digital image

correlation using regular displacement fields that are consistent with the period pattern of deformation within the annual growth ring, in a similar approach as proposed in (Leclerc et al., 2009). This issue is of relevance since the identification is rather affected when processing local strains associated to each constituent within each annual growth ring structure.

References

J. D'hooge. *Myocardial Imaging: Tissue Doppler and Speckle Tracking*, chapter Principles and different techniques for speckle tracking, pages 17–25. Blackwell Publishing Ltd, 2007.

L. Bigorgne. *Mécanique et mécanismes de rupture dans le plan transverse du bois résineux*. PhD thesis, Institute National des Sciences Appliquées de Lyon, 2011.

A. Carvalho. *Madeiras Portuguesas: estrutura anatómica, propriedades, utilizações*. Instituto Florestal, 1996.

S. Cramer, D. Kretschmann, R. Lakes, and T. Schmidt. Earlywood and latewood elastic properties in loblolly pine. *Holzforschung*, 59(531-538):5, 2005.

A. Dirami, K. Hammouche, M. Diaf, and P. Siarry. Fast multilevel thresholding for image segmentation through a multiphase level set method. *Signal Processing*, 93(1):139–153, 2013.

F. Farruggia and P. Perré. Microscopic tensile tests in the transverse plane of earlywood and latewood parts of spruce. *Wood Science and Technology*, 34(2):65–82, 2000.

J. Garab, D. Keunecke, S. Hering, J. Szalai, and P. Niemz. Measurement of standard and off-axis elastic moduli and poisson's ratios of spruce and yew wood in the transverse plane. *Wood Science and Technology*, 44(3):451–464, 2010.

L.J. Gibson and M.F. Ashby. *Cellular solids. Structure and properties*. Cambridge University Press, 1997.

B.I. Hassel, P. Berard, C.S. Modén, and L.A. Berglund. The single cube apparatus for shear testing - full-field strain data and finite element analysis of wood in transverse shear. *Composites Science and Technology*, 69(7-8):877–882, 2009a.

B.I. Hassel, C.S. Modén, and L.A. Berglund. Functional gradient effects explain the low transverse shear modulus in spruce - full-field strain data and a micromechanics model. *Composites Science and Technology*, 69(14):2491–2496, 2009b.

S. Holmberg, K. Persson, and H. Petersson. Nonlinear mechanical behaviour and analysis of wood and fibre materials. *Computers and Structures*, 72(4-5):459–480, 1999.

L.O. Jernkvist and F. Thuvander. Experimental determination of stiffness variation across growth rings in Picea abies. *Holzforschung*, 55(3):309–317, 2001.

H. Leclerc, J.-N. Périé, S. Roux, and F. Hild. Integrated digital image correlation for the identification of mechanical properties. In A. Gagalowicz and W. Philips, editors, *Computer Vision/Computer Graphics CollaborationTechniques*, volume 5496 of *Lecture Notes in Computer Science*, pages 161–171. Springer Berlin Heidelberg, 2009.

J.A. Nairn. Material point method simulations of transverse fracture in wood with realistic morphologies. *Holzforschung*, 61(4):375–381, 2007.

B. Pan. Recent progress in digital image correlation. *Experimental Mechanics*, 51(7): 1223–1235, 2011.

J. Réthoré, T. Elguedj, P. Simon, and M. Coret. On the use of nurbs functions for displacement derivatives measurement by digital image correlation. *Experimental Mechanics*, 50(7):1099–1116, 2010.

C.L. Santos, A.M.P. de Jesus, J.J.L. Morais, and J.L.P.C. Lousada. Quasi-static mechanical behaviour of a double-shear single dowel wood connection. *Construction and Building Materials*, 23(1):171–182, 2009. ISSN 0950-0618. doi: 10.1016/j.conbuildmat. 2008.01.005.

F. Thuvander, L.O. Jernkvist, and J. Gunnars. Influence of repetitive stiffness variation on crack growth behaviour in wood. *Journal of Materials Science*, 35(24):6259–6266, 2000.

L. Wagner, T. Bader, D. Auty, and K. de Borst. Key parameters controlling stiffness variability within trees: a multiscale experimentalnumerical approach. *Trees - Structure and Function*, (in press).

J. Xavier, S. Avril, F. Pierron, and J. Morais. Novel experimental approach for longitudinal-radial stiffness characterisation of clear wood by a single test. *Holzforschung*, 61(5):573–581, 2007.

J. Xavier, S. Avril, F. Pierron, and J. Morais. Variation of transverse and shear stiffness properties of wood in a tree. *Composites Part A: Applied Science and Manufacturing*, 40:1953–1960, 2009. Special Issue: CompTest 2008.

J. Xavier, A.M.R. Sousa, J.J.L. Morais, V.M.J. Filipe, and M. Vaz. Measuring displacement fields by cross-correlation and a differential technique: experimental validation. *Optical Engineering*, 51:043602, 2012.

J.C. Xavier, N. Garrido, J. Oliveira, J. Morais, P. Camanho, and F. Pierron. A comparison between the Iosipescu and off-axis shear test methods for the characterization of *pinus pinaster* Ait. *Composites Part A: Applied Science and Manufacturing*, 35(7-8):827–840, 2004.

R. Zhang and L. He. Measurement of mixed-mode stress intensity factors using digital image correlation method. *Optics and Lasers in Engineering*, 50(7):1001–1007, 2012.

A. Zink-Sharp, J.S. Stelmokas, and H. Gu. Effects of wood anatomy on the mechanical behavior of single-bolted connections. *Wood and Fiber Science*, 31(3):249–263, 1999.

Conclusions and further work

Wood is a hierarchical structure with a spectrum of length scales. When analysing and modelling wood at the meso scale (1-10 mm) on the transverse (RT) plane of symmetry, wood anisotropy and heterogeneity must be taken into account. These direction-dependent and local properties represent fundamental data in problems dealing with fracture mechanics, wood joints, wood drying and wood machining, for instance. Moreover, their quantitative evaluation on a spatial variability bases within the stem can provide relevant information for assessing and discussion wood quality. Besides, these patterns of properties within the stem can be used for validating non-destructive methods based on industrial X-ray computational tomography for assessing internal features of the stem for log grading and sawing optimisation.

In this work, a single ring-oriented mechanical tensile test was proposed for the characterisation of stiffness (compliance) orthotropic components in the RT plane and at the meso scale. In this test small rectangular specimens with different off-axis orientation (*i.e.*, rings curvature) along the radial direction were used, taking advantage of the wood structure variability itself to achieve a complex state of stress over de region of interest. A new approach for material parameter characterisation based on full-field measurements was developed. The so-called anisotropic-based (AbM) method and the virtual fields method (VFM) were chosen for tackle the problem of identification of global and local transverse elastic properties of wood at the growth ring scale.

Concerning to the identification of elastic properties, the AbM reveals suitable for global evaluation of E_R and G_{RT}, achieving consistent values that are in accordance with references, notwithstanding the initial hypothesis assuming an applied uniaxial stress state. This hypothesis could be relaxed in a compression test using suitable spherical bearing platens and lubrification for reducing friction. The local elastic properties concerning to the EW and LW tissues were then estimated from the global properties, as a function of mean density, combining the application of a micromechanical model (mixture law) and a unit cell model.

The VFM was applied to directly identify $Q_{11}(\sim E_R)$ and $Q_{66}(\equiv G_{RT})$ stiffness components associated to earlywood and latewood constituents within the annual ring structure. Image processing and analysis was implemented on the complex wood structure at the meso scale for classifying resin channels, earlywood and latewood layers. The output

binary images were then used to sort the strain fields for each layer. A regularisation procedure was proposed in order to extract representative strains associated to earlywood and latewood layers. This regularisation of the strain fields was found crucial because erroneous values were estimated in the vicinity of resin channels, since these regions within the annual ring represent a discontinuity on the tissue and therefore displacements measured by DIC are inaccurate (assumption: continuous based functions). These classified strain fields were processed by the VFM for local identification of stiffness parameters. The Q_{11} and Q_{66} latewood/earlywood ratios were found in the order of 1.32 and 2.45, respectively. These ratios suggest a linear relationship between elastic properties and density, rather than a cubic one based on cellular honeycomb models (Gibson and Ashby, 1997).

Regarding to the density-elastic properties relationships, generally, correlations between D_{mean} and E_R and G_{RT} were positive and statistically significant. Besides the average density, other parameters determined from X-ray micro-densitometry measurements showed significant correlations with the elastic constants in same cases. Specifically, D_{min}, LW_W and DE_W presented substantial and positive determination of E_R and G_{RT}. With regard to EW_W, when presented significant correlation with the moduli, it was always negative which, physically, makes sense because the greater the contribution of the EW fraction in the annual ring, the lower the E_R and G_{RT}.

Several issues arise from this work as future perspectives, which can be summarised as follows:

– New test methods should be investigated for determining all orthotropic components of wood in the RT plane at once in a single test. Eventually an unnotched Iosipescu test with suitable optimisation of free length and ring curvatures (Xavier et al., 2007) or a compression test on small specimens with off-axis angles oriented from 0° (radial direction) to 90° (tangential direction) (Garab et al., 2010) can be proposed. The compression test configuration will have the advantage of extending the current analysis to high-strain rate tests (*i.e.* $\dot{\varepsilon} = 10^{-2}$–$10^{-4}$) using the conventional split Hopkinson pressure bar (SHPB) set-up (Koerber et al., 2010). In alternative, additional tests should be proposed complementary to the ring-oriented tensile test for evaluating all orthotropic components of wood in the RT plane, including some tensile tests with specimens preferentially oriented along the T direction.

– As a future work this analysis should be extended to further position in the tree for assessing spatial variability of local properties within the stem. This is intended to be relevant data for assessing wood quality based on pattern variations of properties within the stem. Moreover, this information can be of major importance to validate multi-scaling modelling, which take into account the spatial variability of cell wall

constituents within the stem (*e.g.*, micro-fibril angle, chemical composition, local density....) (Wagner et al., (in press). Moreover, the numerical study carried you by Nairn (2007) using the material point method (MPM) of the transverse modulus of wood as a function of ring orientation and elastic properties taking into account heterogeneity and anisotropy could be properly validated.

– Improvement of strain fields regularisation using different approaches, such as global digital image correlation using regular displacement fields that are consistent with the period pattern of deformation within the annual growth ring, in a similar approach as proposed in (Leclerc et al., 2009). This issue is of relevance since the identification is rather affected when processing local strains associated to each constituent within each annual growth ring structure.

– Developing numerical analyses at the meso scale taking into account heterogeneity and cylindrical orthotropy. An elegant possibility would be using a morphological based model, such as the MPM, since the finite element analysis may have in this application some limitations: (*i*) the wood structure at the meso scale can be very complex, and therefore difficult to built up an FEA mesh; (*ii*) the mesh refinement (the number of elements) required to accurately resolve the wood structure at the scale of observation can be computationally expensive.

References

J. Garab, D. Keunecke, S. Hering, J. Szalai, and P. Niemz. Measurement of standard and off-axis elastic moduli and poisson's ratios of spruce and yew wood in the transverse plane. *Wood Science and Technology*, 44(3):451–464, 2010.

L.J. Gibson and M.F. Ashby. *Cellular solids. Structure and properties*. Cambridge University Press, 1997.

H. Koerber, J. Xavier, and P.P. Camanho. High strain rate characterisation of unidirectional carbon-epoxy im7-8552 in transverse compression and in-plane shear using digital image correlation. *Mechanics of Materials*, 42(11):1004–1019, 2010.

H. Leclerc, J.-N. Périé, S. Roux, and F. Hild. Integrated digital image correlation for the identification of mechanical properties. In A. Gagalowicz and W. Philips, editors, *Computer Vision/Computer Graphics CollaborationTechniques*, volume 5496 of *Lecture Notes in Computer Science*, pages 161–171. Springer Berlin Heidelberg, 2009.

J.A. Nairn. Material point method simulations of transverse fracture in wood with realistic morphologies. *Holzforschung*, 61(4):375–381, 2007.

L. Wagner, T. Bader, D. Auty, and K. de Borst. Key parameters controlling stiffness variability within trees: a multiscale experimentalnumerical approach. *Trees - Structure and Function*, (in press).

J. Xavier, S. Avril, F. Pierron, and J. Morais. Novel experimental approach for longitudinal-radial stiffness characterisation of clear wood by a single test. *Holzforschung*, 61(5):573–581, 2007.

Appendices

A Density variation patterns

124

TREE NUMBER 2
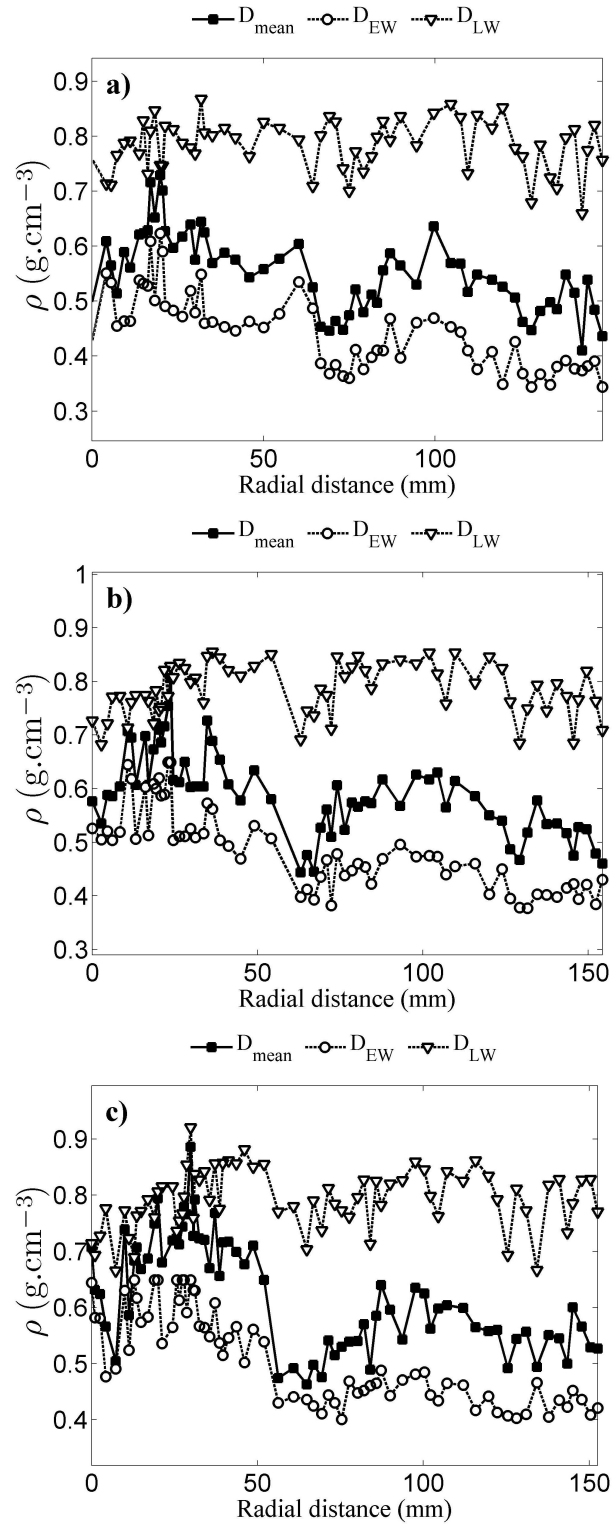
Figure 1: D_{mean}, D_{EW}, D_{LW} radial variation: (a) L3, (b) L2, (c) L1.
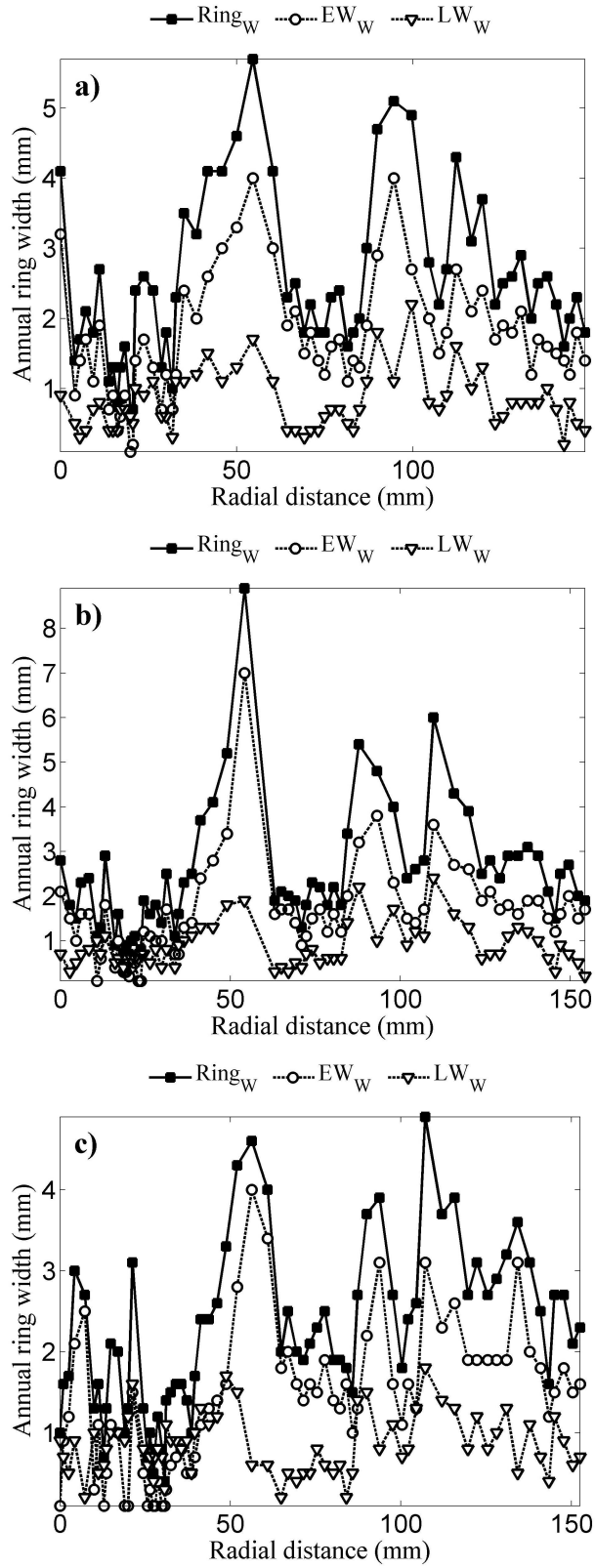
Figure 2: $Ring_W$, EW_W, LW_W radial variation: (a) L3, (b) L2, (c) L1.
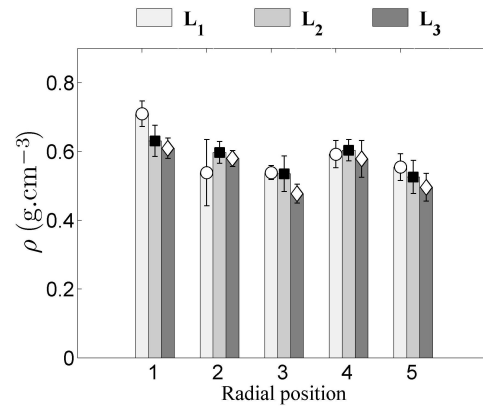
Figure 3: D_{mean} over radial and longitudinal positions variation.
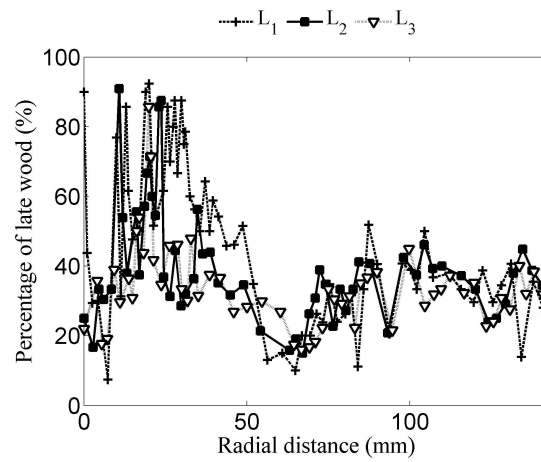
Figure 4: $\%LW$ over radial and longitudinal positions distribution.
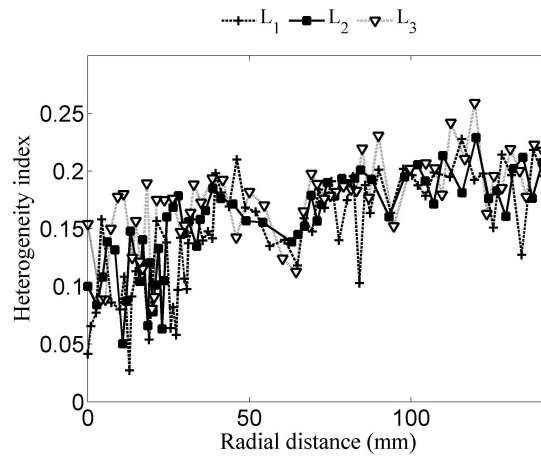
Figure 5: HI over radial and longitudinal positions distribution.

TREE NUMBER 3
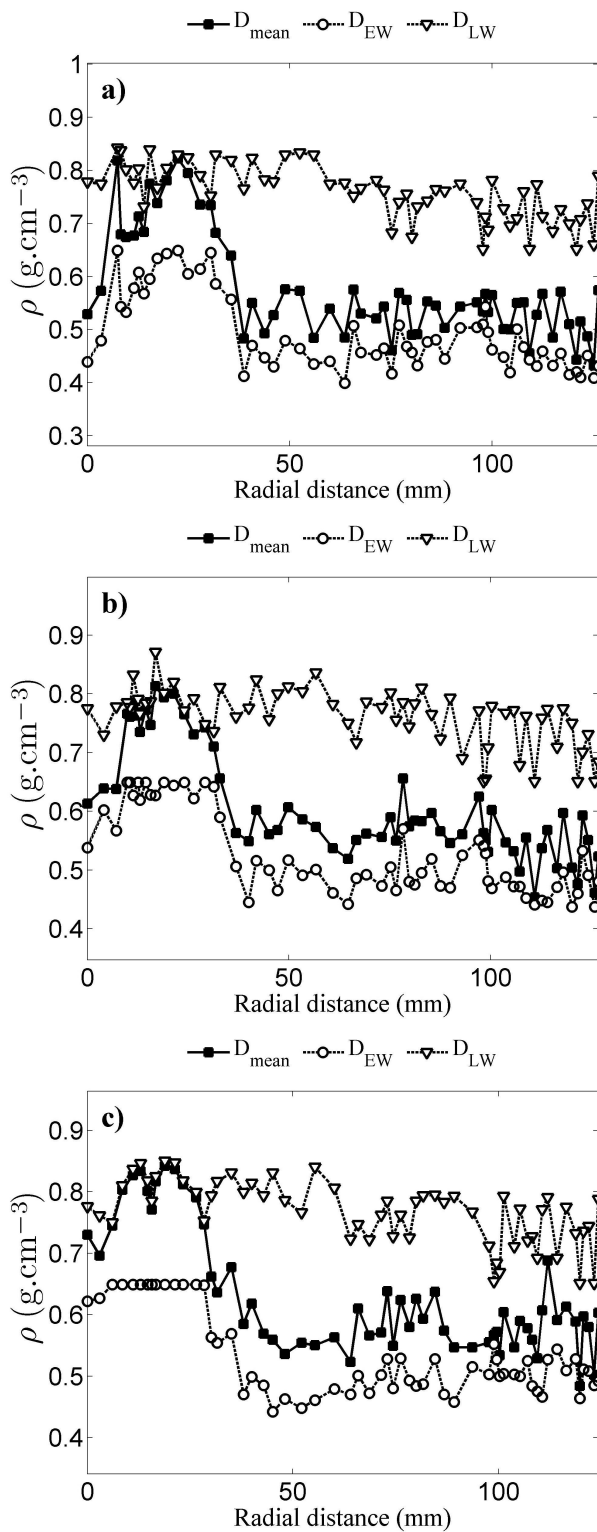
Figure 6: D_{mean}, D_{EW}, D_{LW} radial variation: (a) L3, (b) L2, (c) L1.
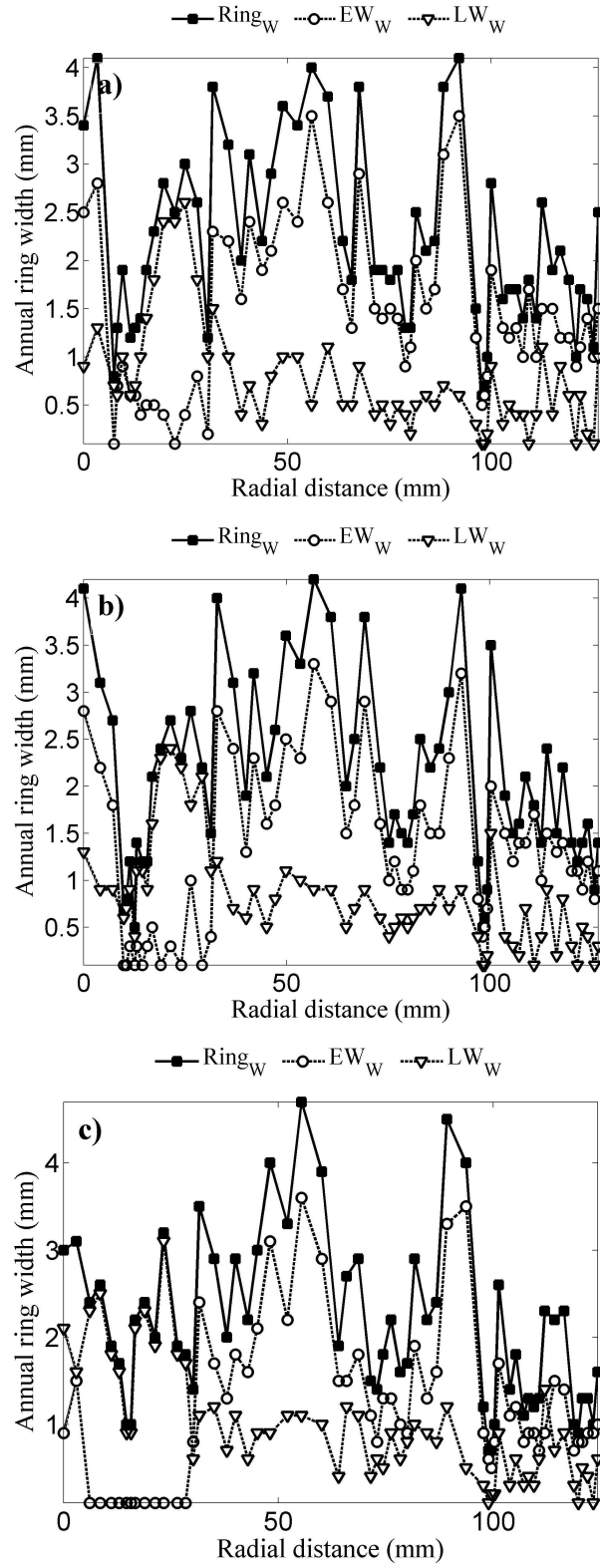
Figure 7: $Ring_W$, EW_W, LW_W radial variation: (a) L3, (b) L2, (c) L1.
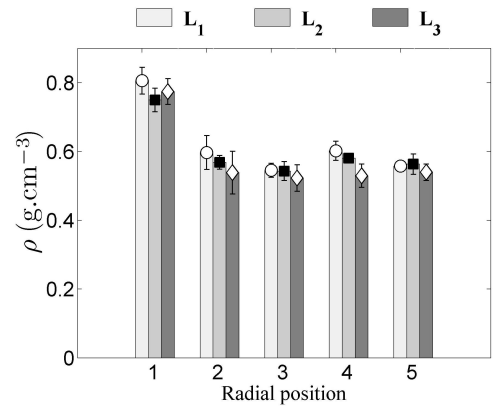
Figure 8: D_{mean} over radial and longitudinal positions variation.
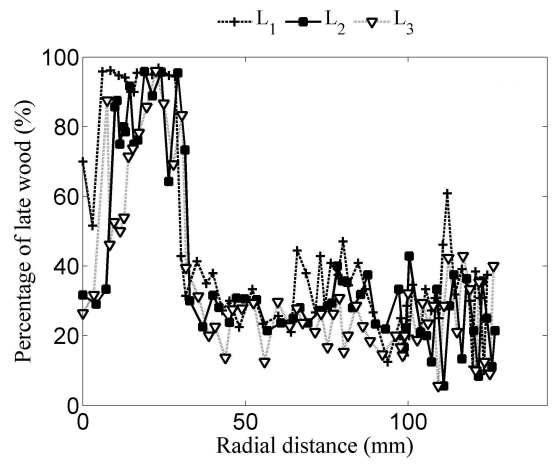
Figure 9: $\%LW$ over radial and longitudinal positions distribution.
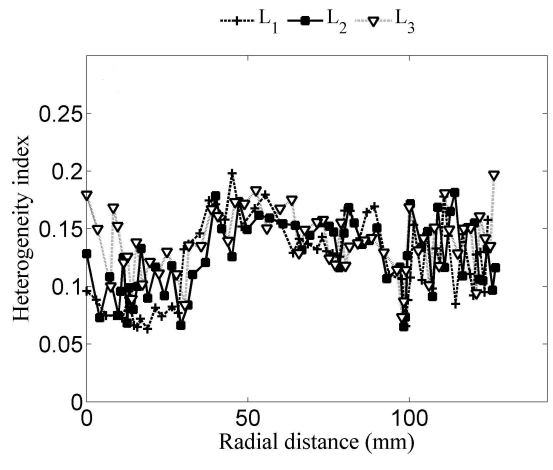
Figure 10: HI over radial and longitudinal positions distribution.

TREE NUMBER 4
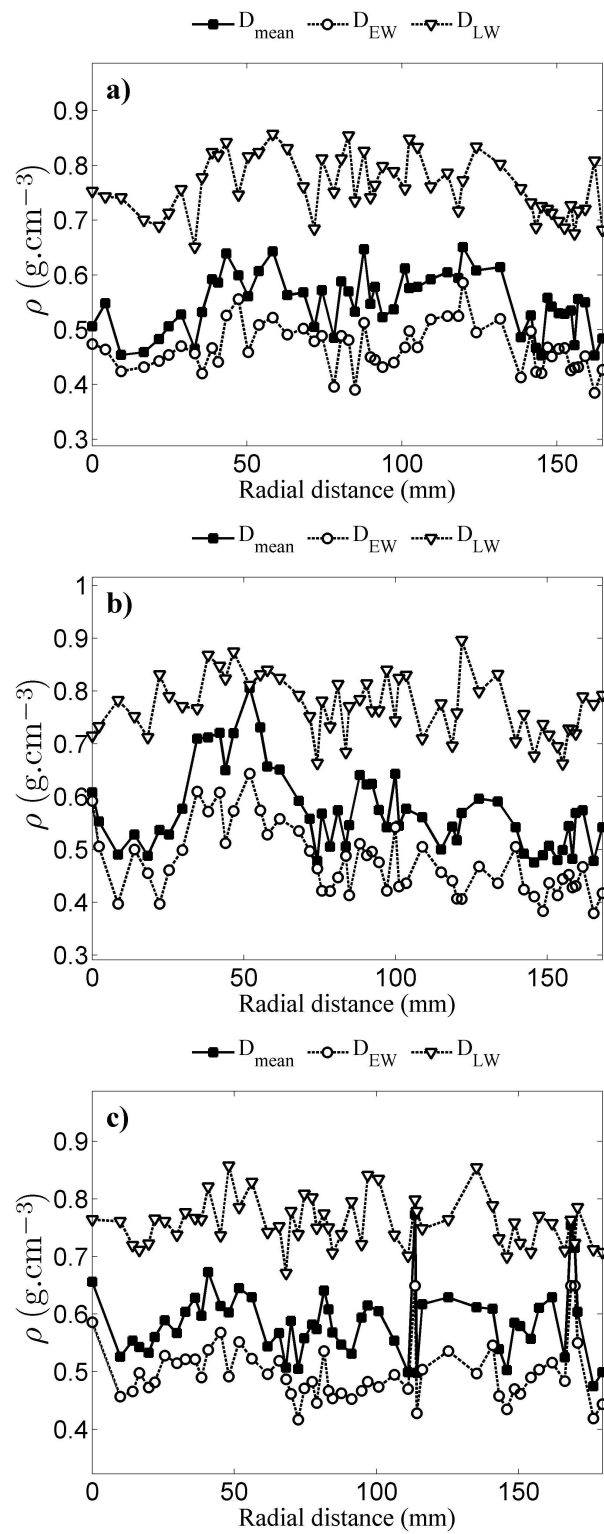
Figure 11: D_{mean}, D_{EW}, D_{LW} radial variation: (a) L3, (b) L2, (c) L1.
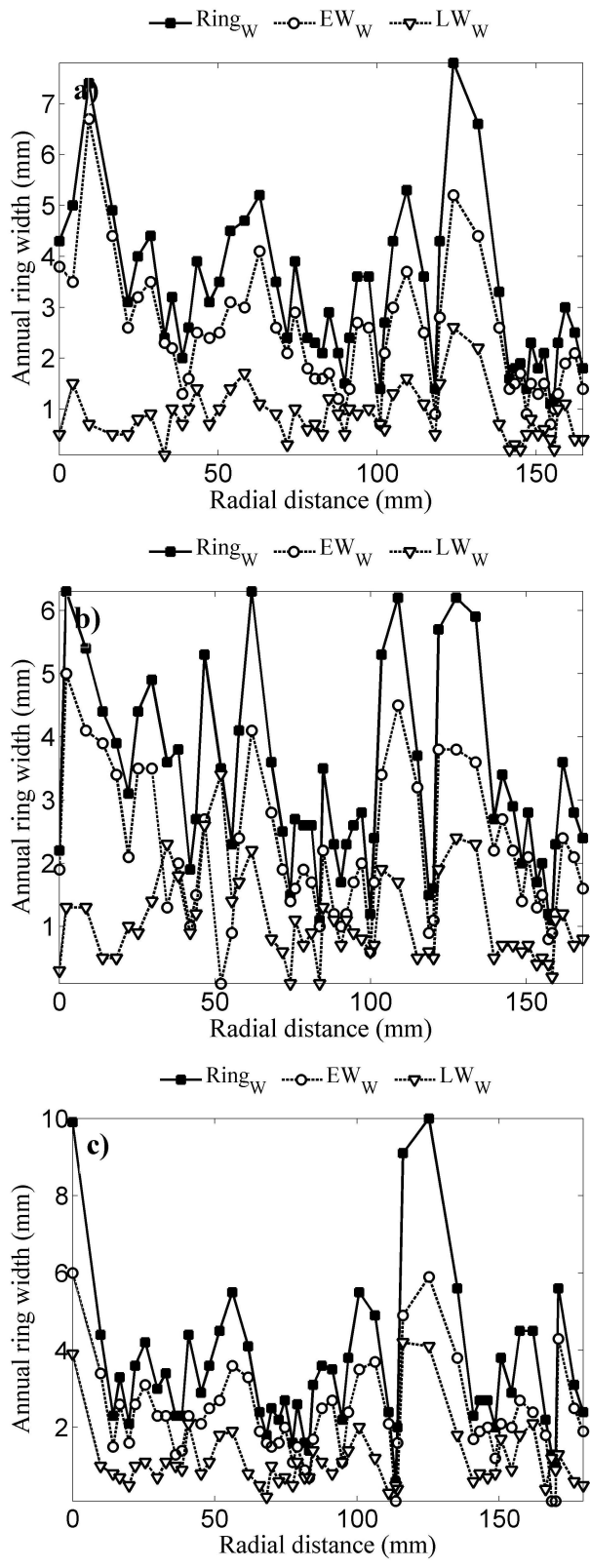
Figure 12: $Ring_W$, EW_W, LW_W radial variation: (a) L3, (b) L2, (c) L1.
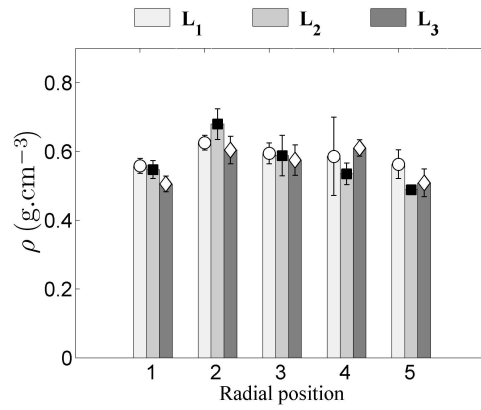
Figure 13: D_{mean} over radial and longitudinal positions variation.
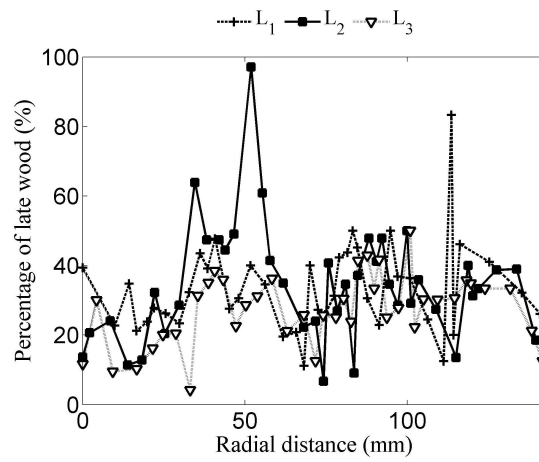
Figure 14: $\%LW$ over radial and longitudinal positions distribution.
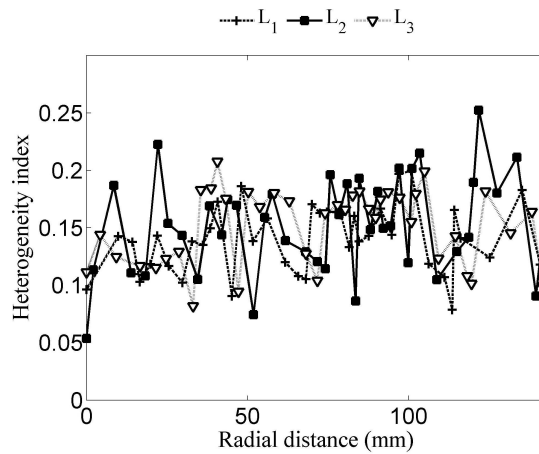
Figure 15: HI over radial and longitudinal positions distribution.

TREE NUMBER 5
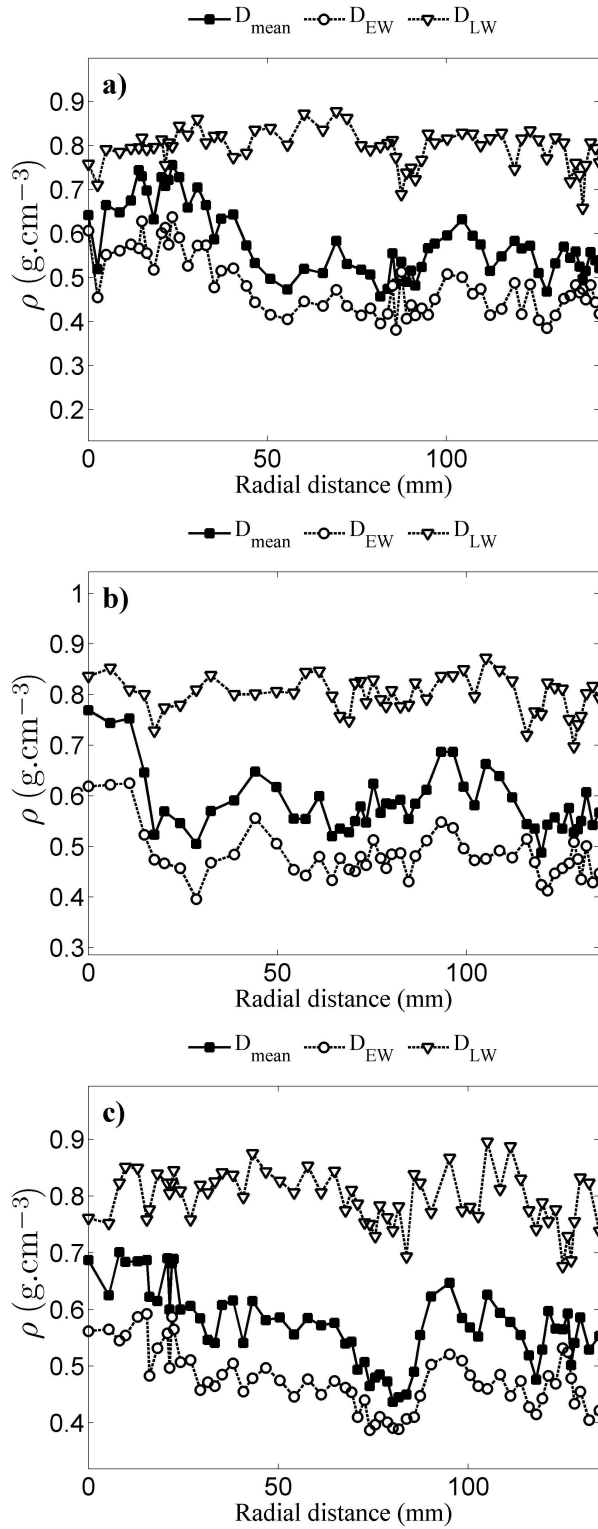
Figure 16: D_{mean}, D_{EW}, D_{LW} radial variation: (a) L3, (b) L2, (c) L1.
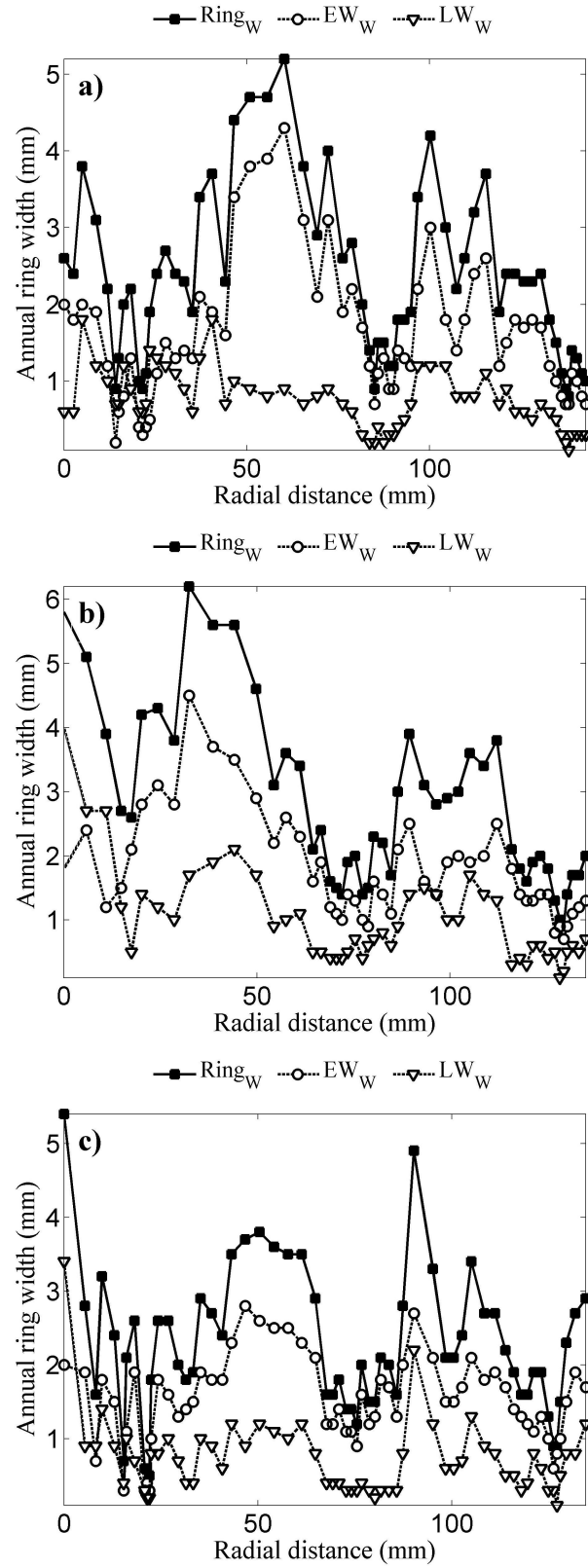
Figure 17: $Ring_W$, EW_W, LW_W radial variation: (a) L3, (b) L2, (c) L1.
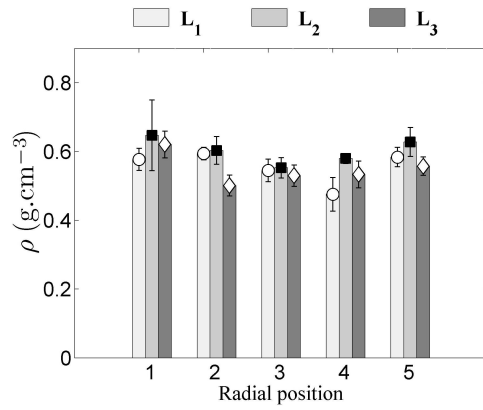
Figure 18: D_{mean} over radial and longitudinal positions variation.
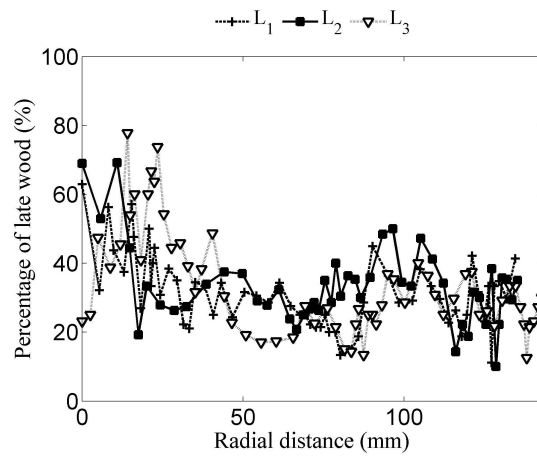
Figure 19: $\%LW$ over radial and longitudinal positions distribution.
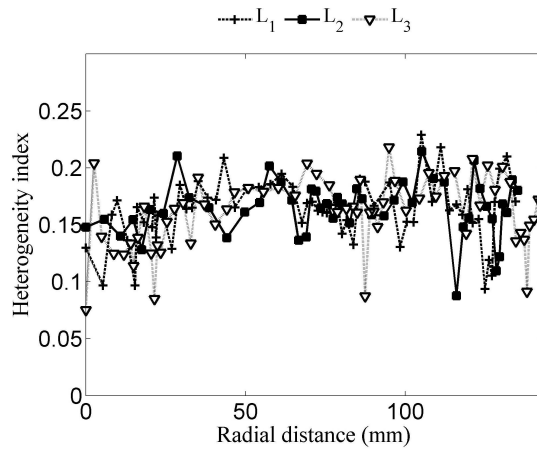
Figure 20: HI over radial and longitudinal positions distribution.

B Elastic properties variation patterns
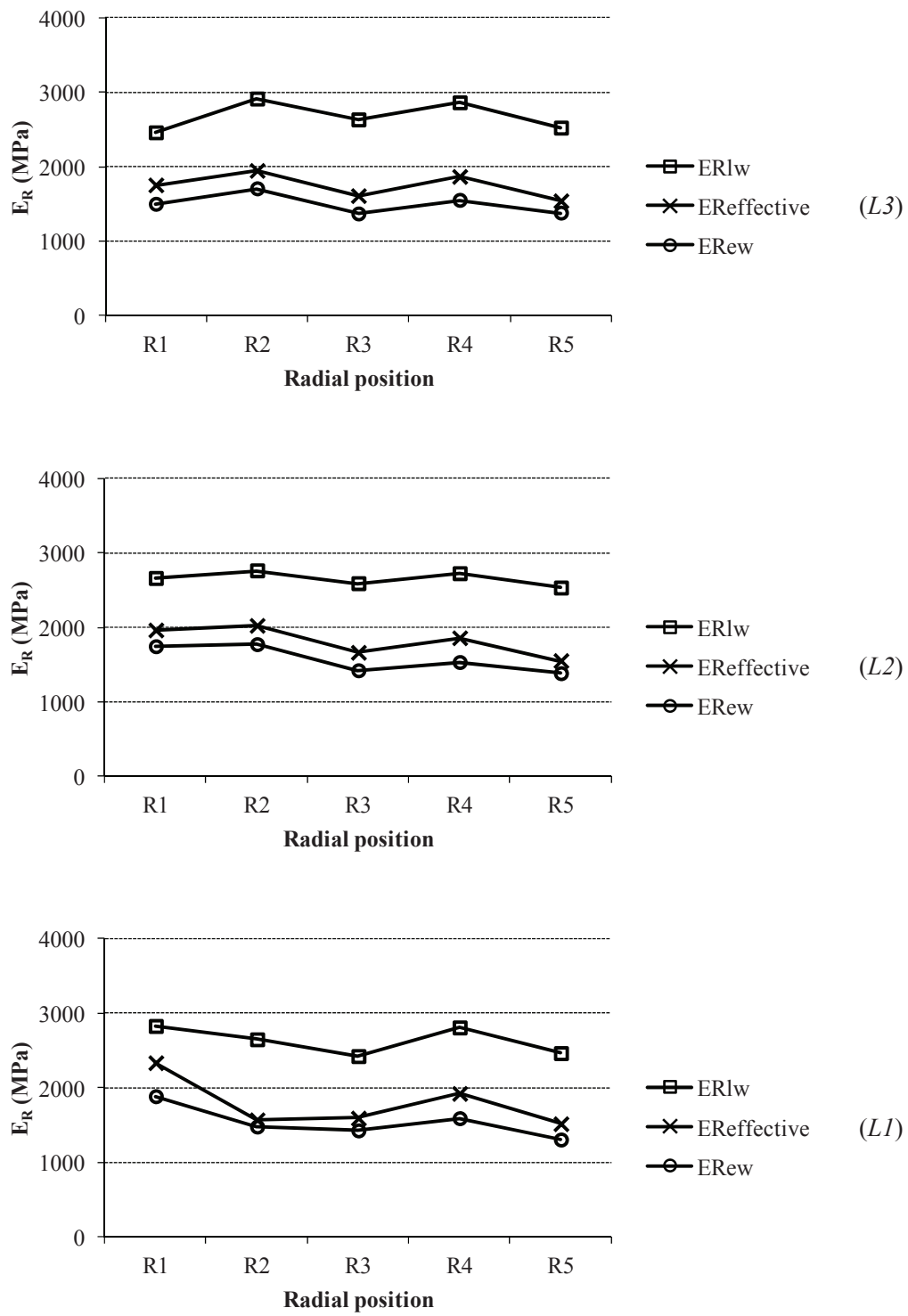
Figure 21: E_R radial variation for tree number 2.
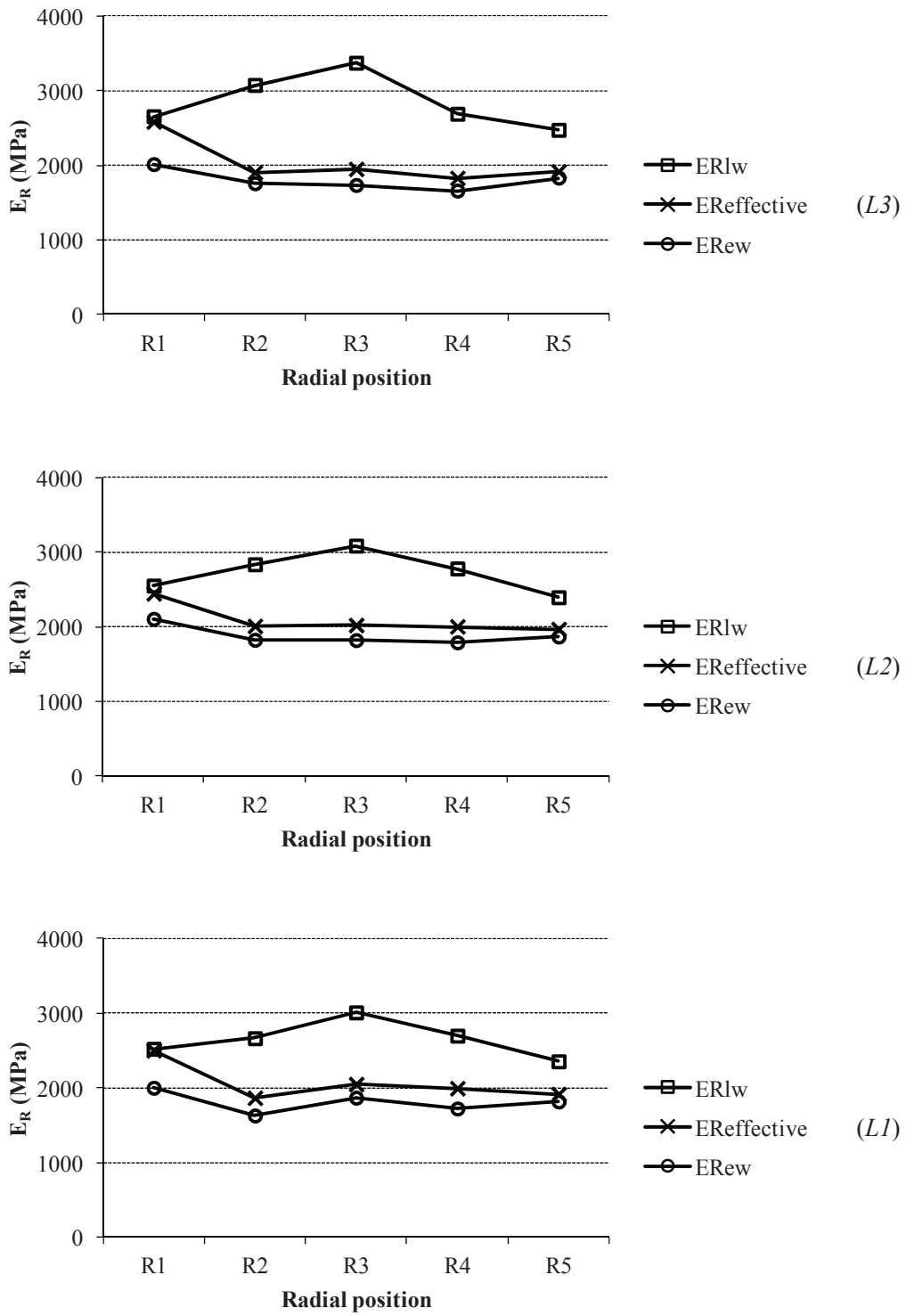
Figure 22: E_R radial variation for tree number 3.
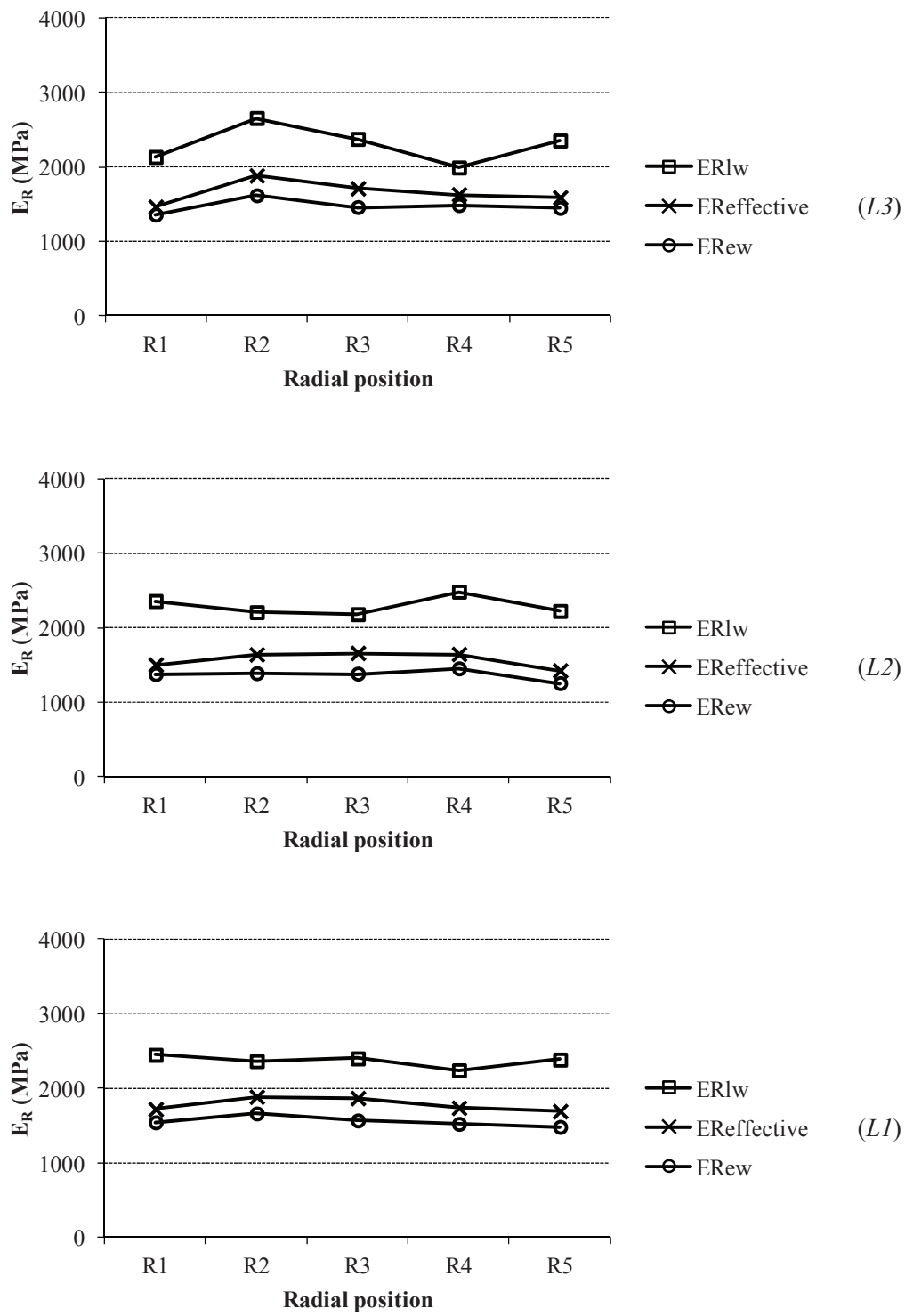
Figure 23: E_R radial variation for tree number 4.
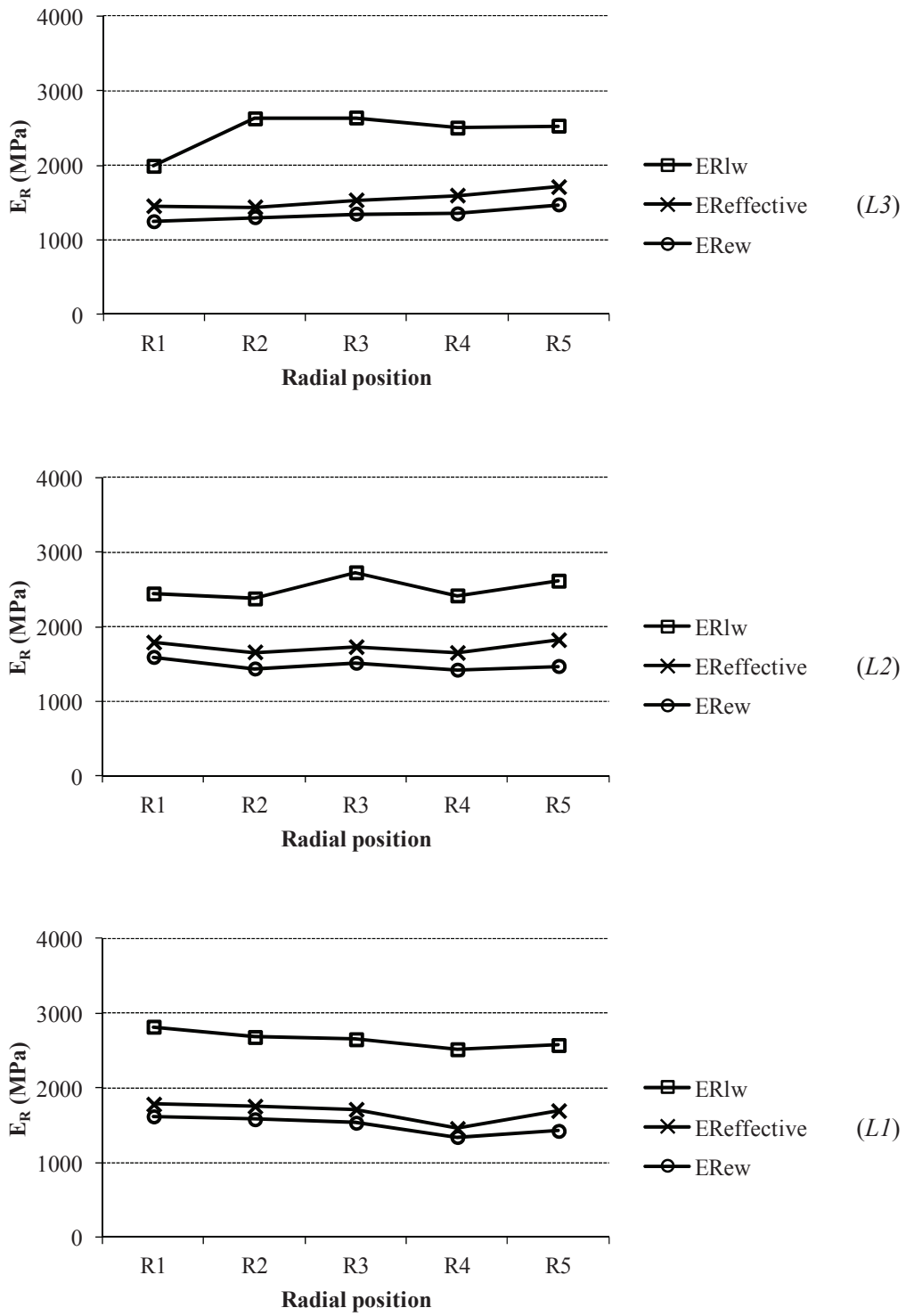
Figure 24: E_R radial variation for tree number 5.
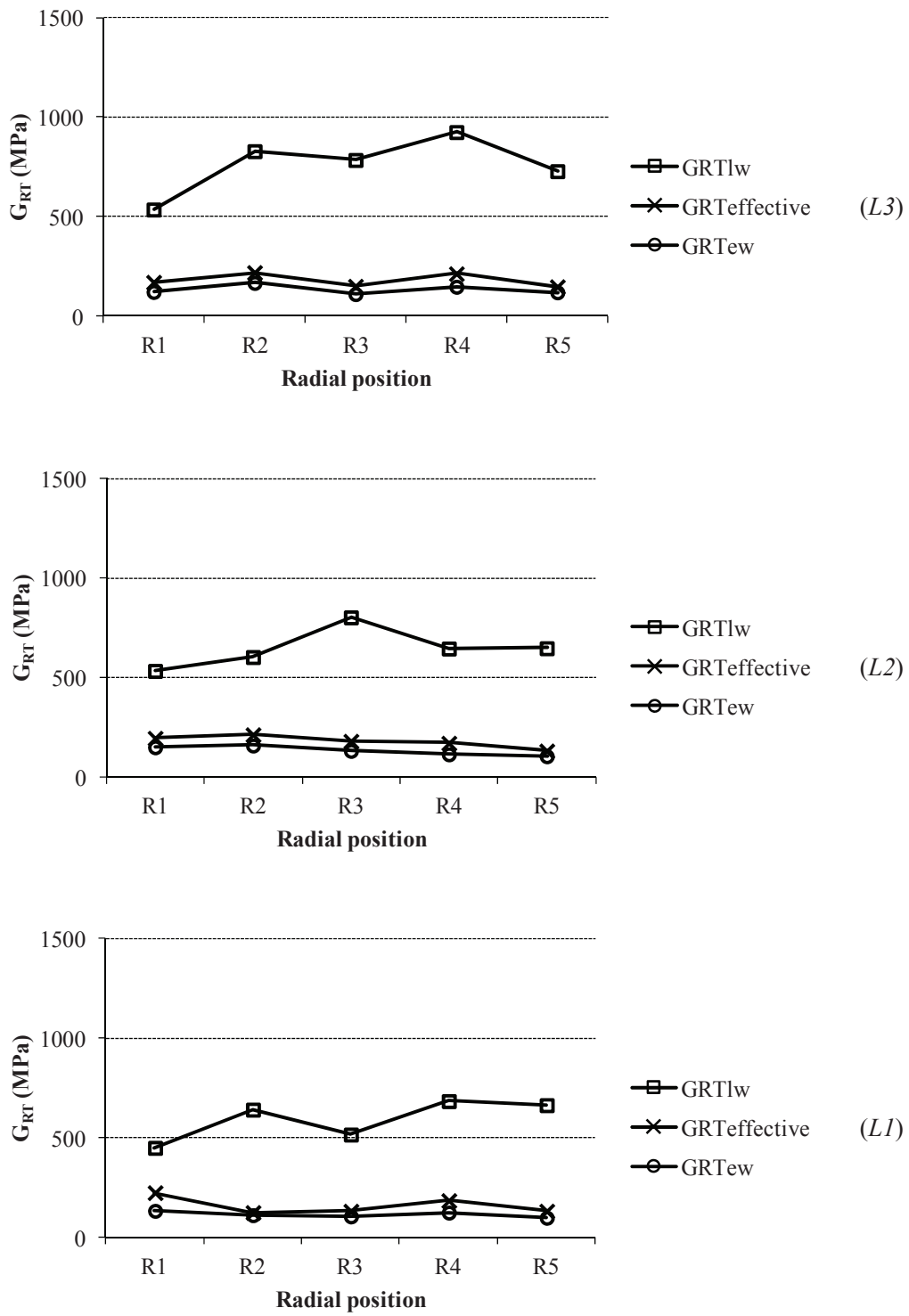
Figure 25: G_{RT} radial variation for tree number 2.
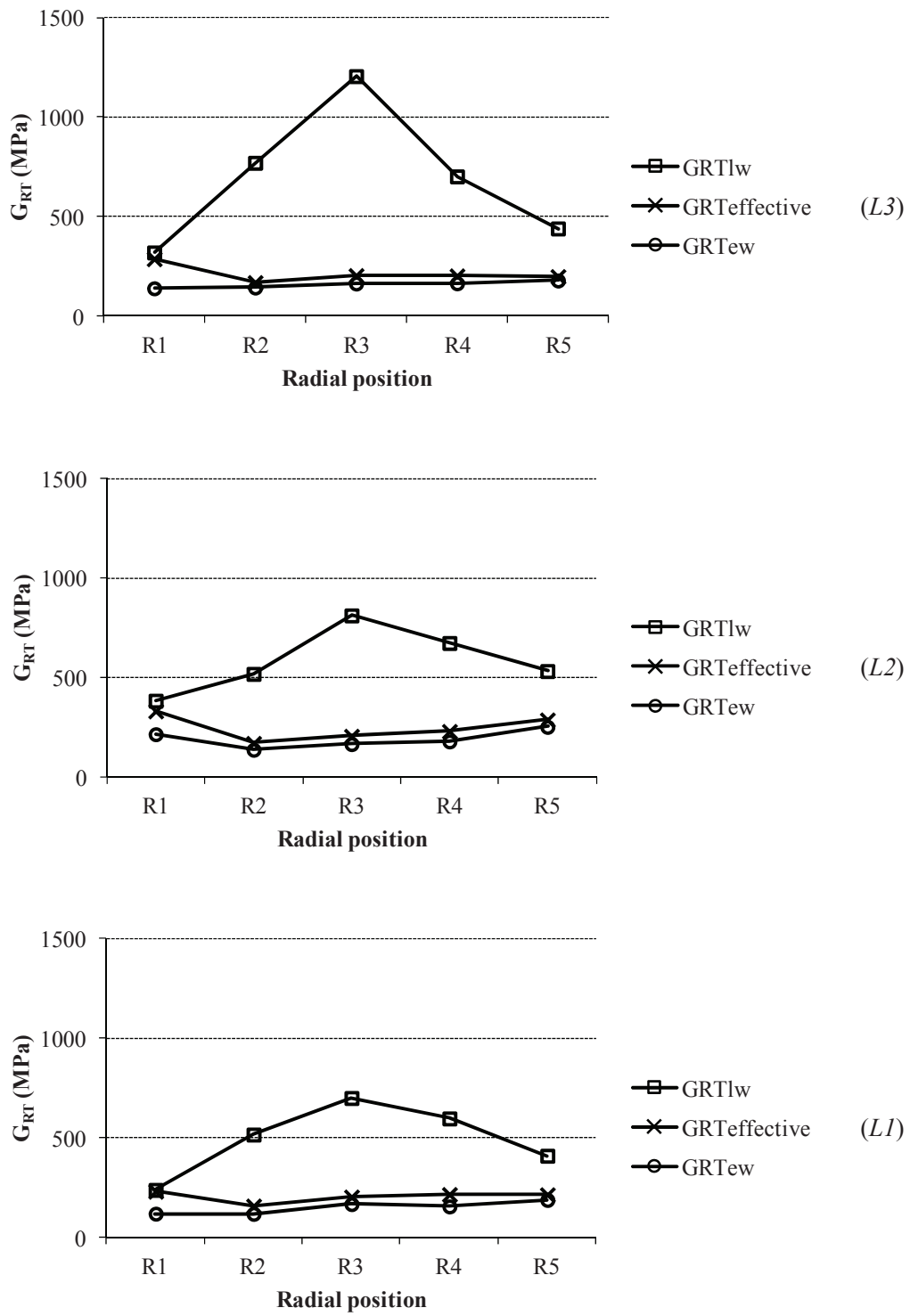
Figure 26: G_{RT} radial variation for tree number 3.
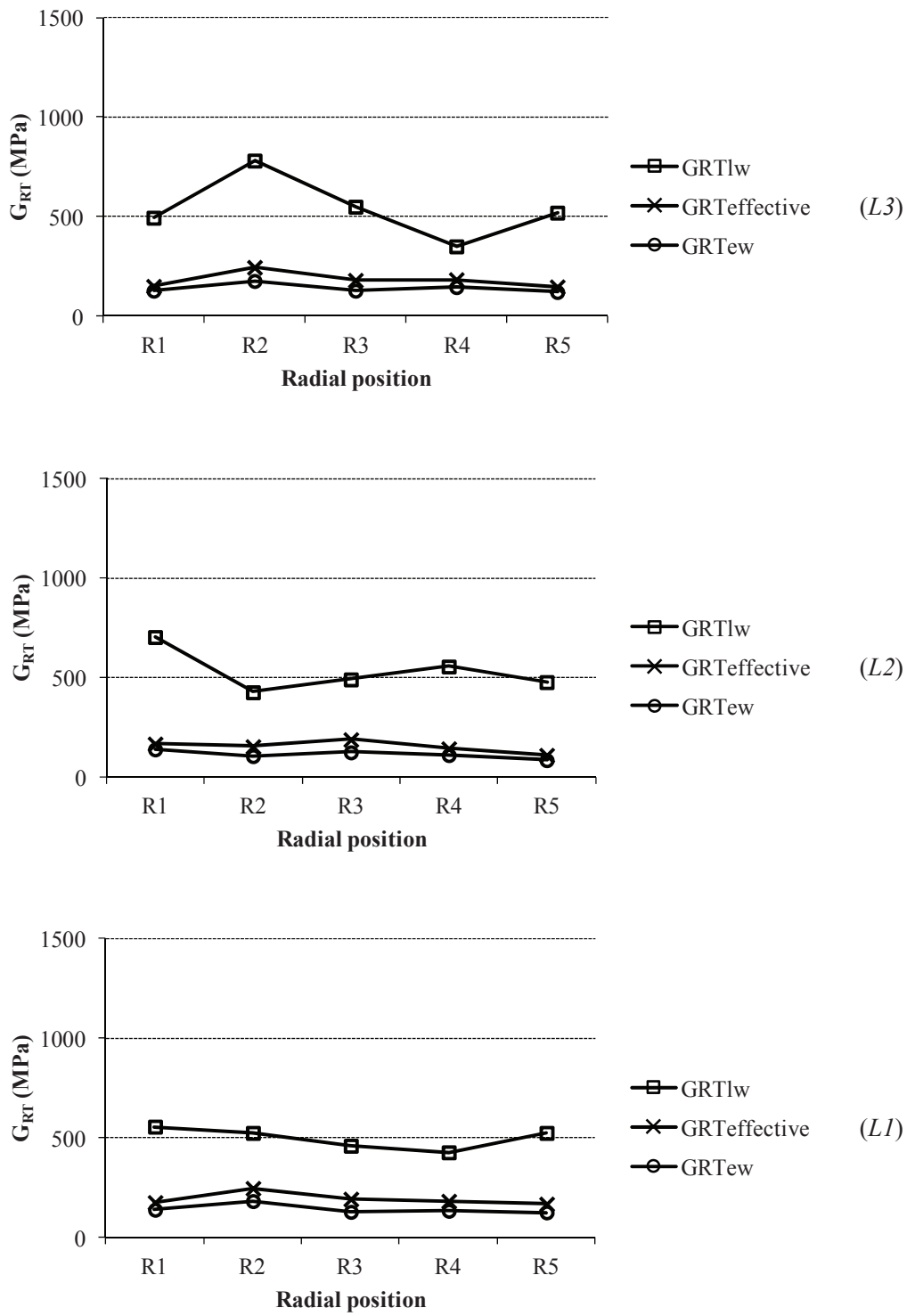
Figure 27: G_{RT} radial variation for tree number 4.
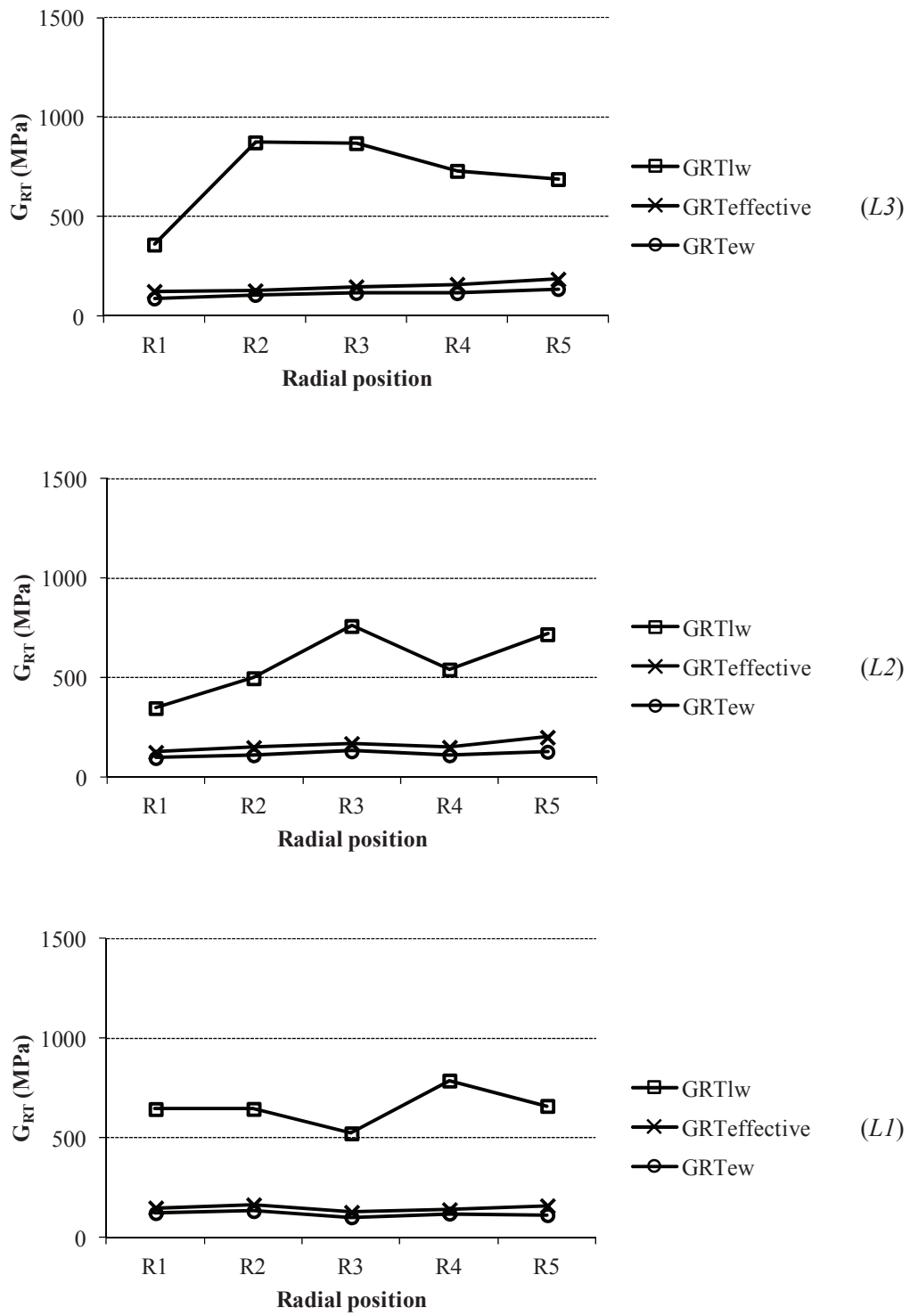
Figure 28: G_{RT} radial variation for tree number 5.
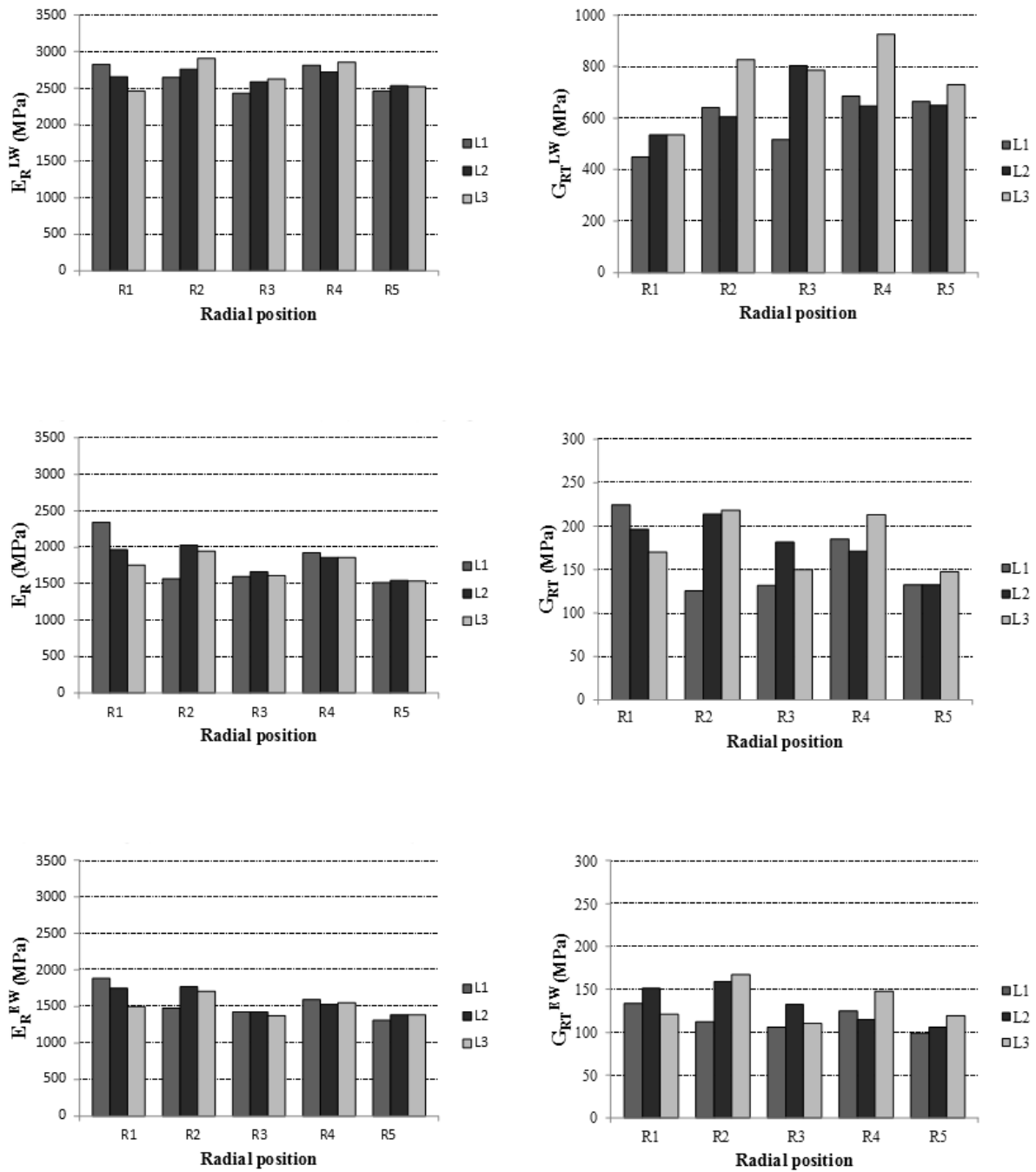
Figure 29: E_R and G_{RT} radial and longitudinal variation for tree number 2.
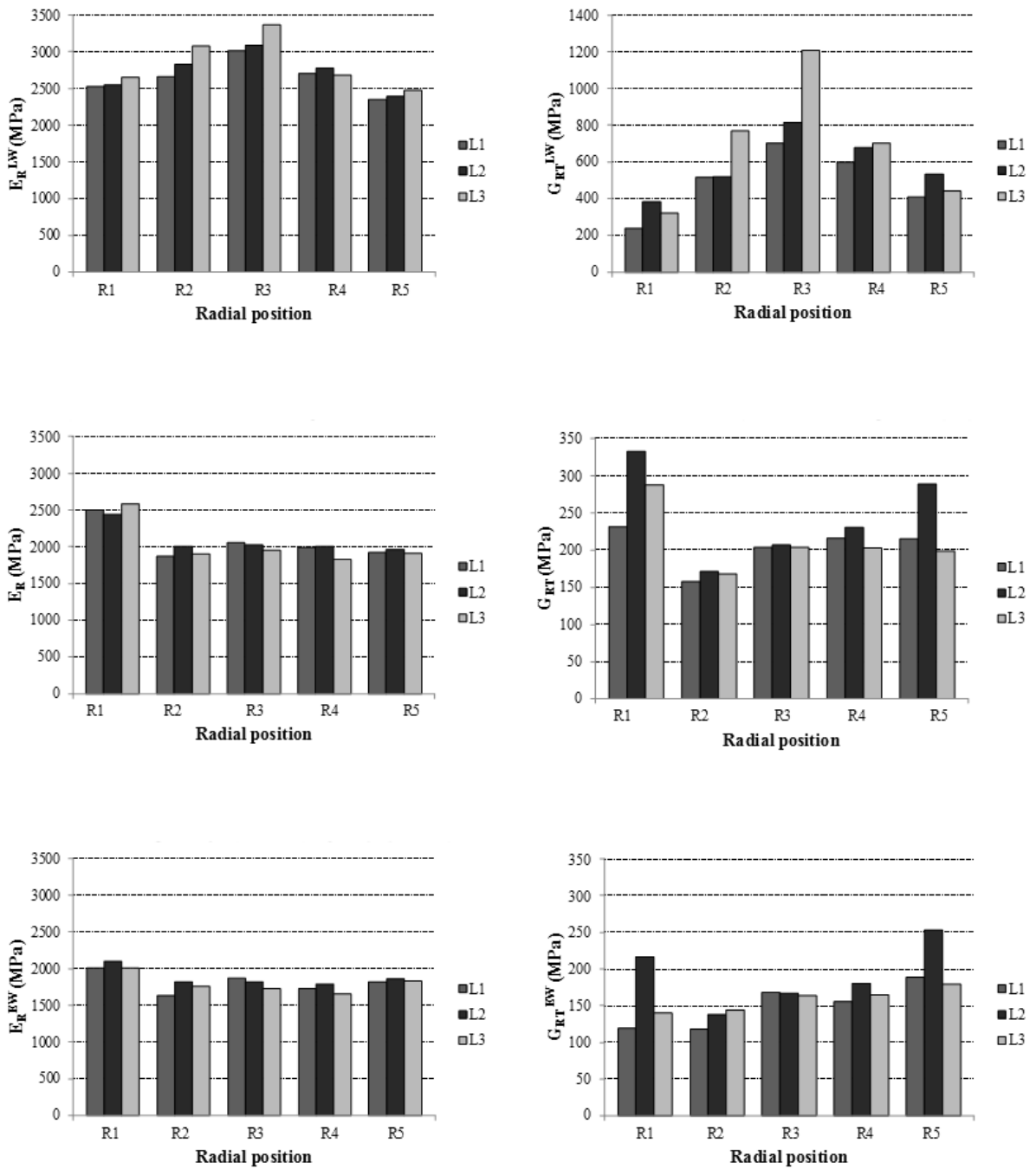
Figure 30: E_R and G_{RT} radial and longitudinal variation for tree number 3.
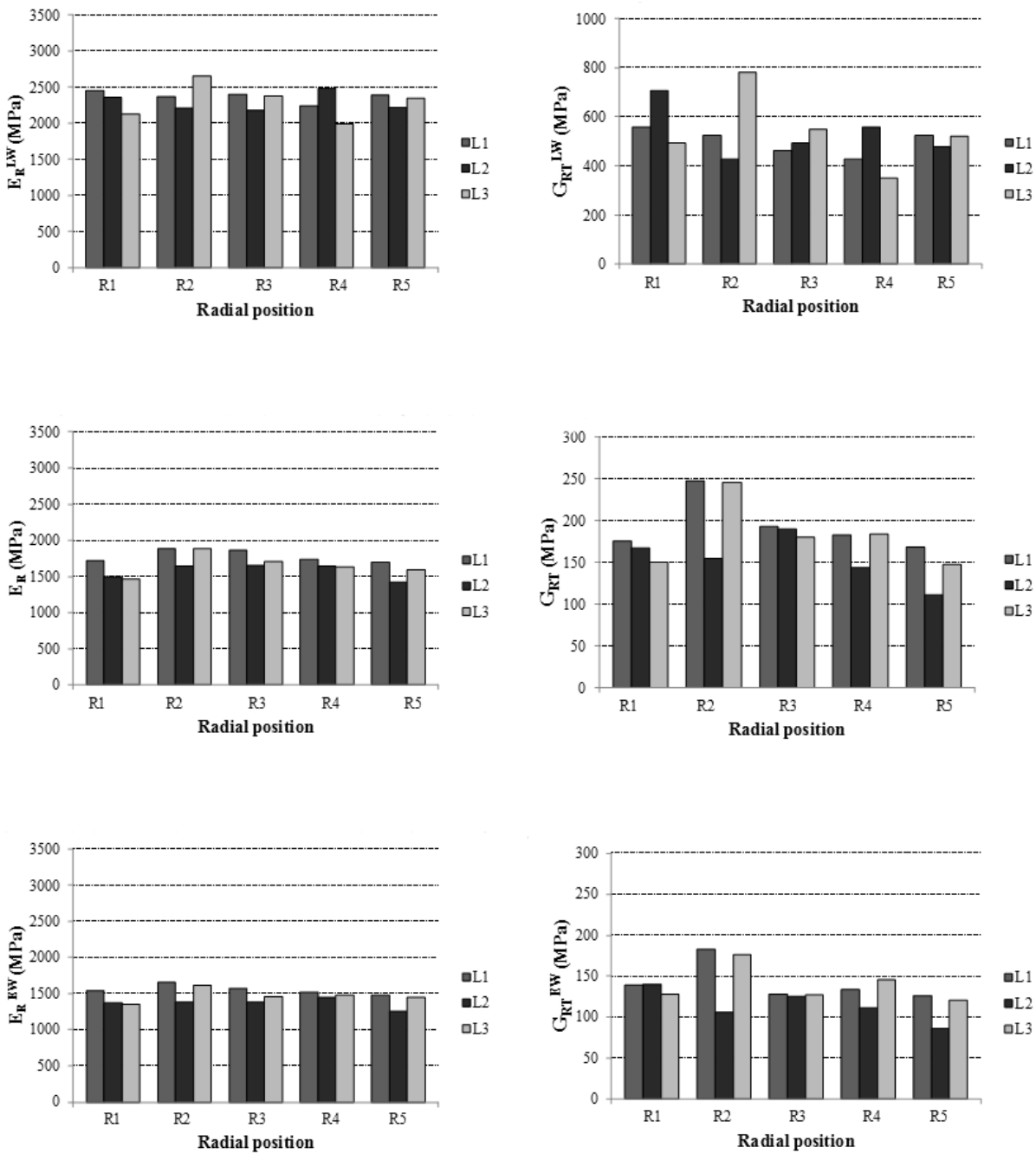
Figure 31: E_R and G_{RT} radial and longitudinal variation for tree number 4.
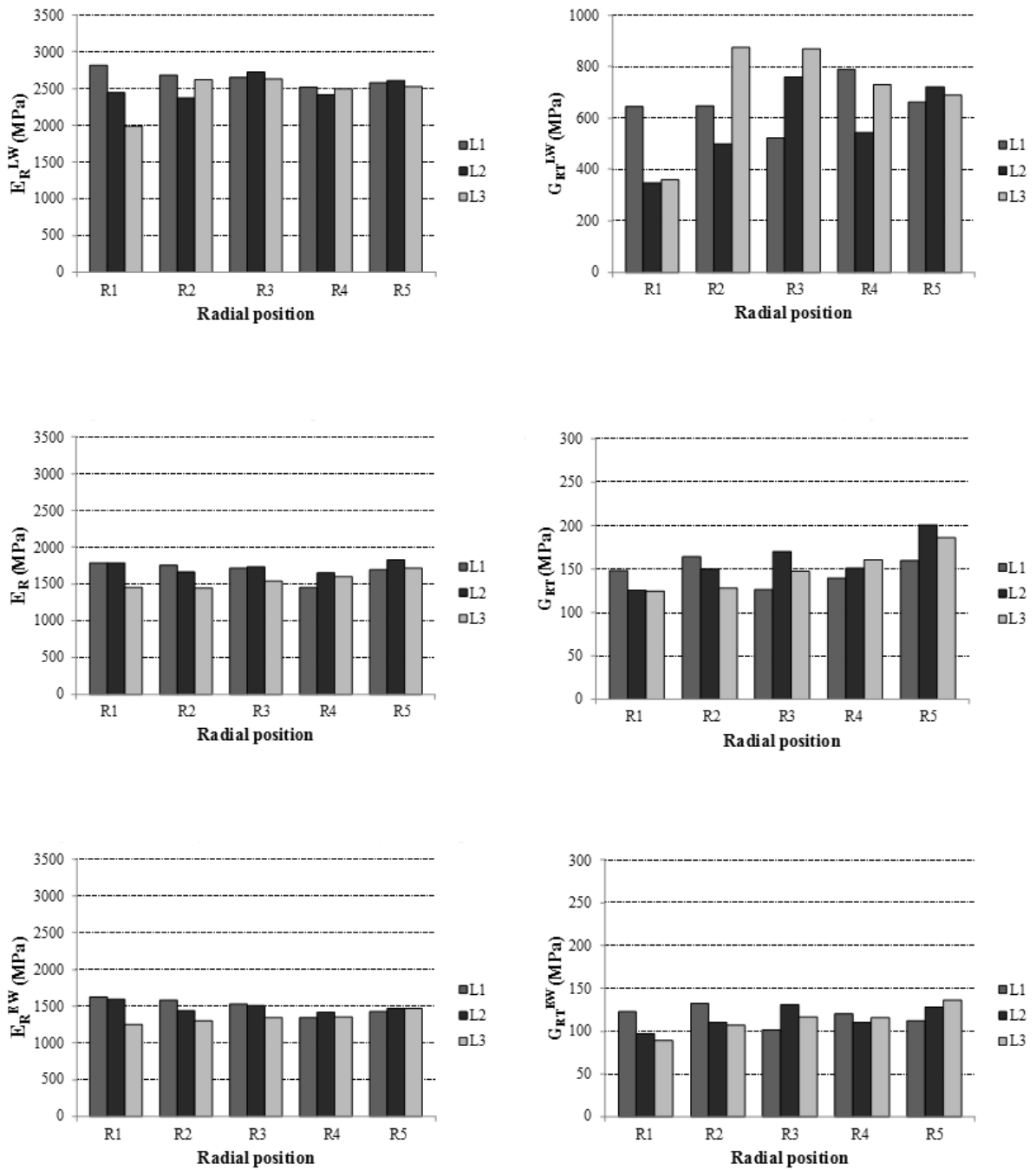
Figure 32: E_R and G_{RT} radial and longitudinal variation for tree number 5.

C Elastic properties-Density relationships
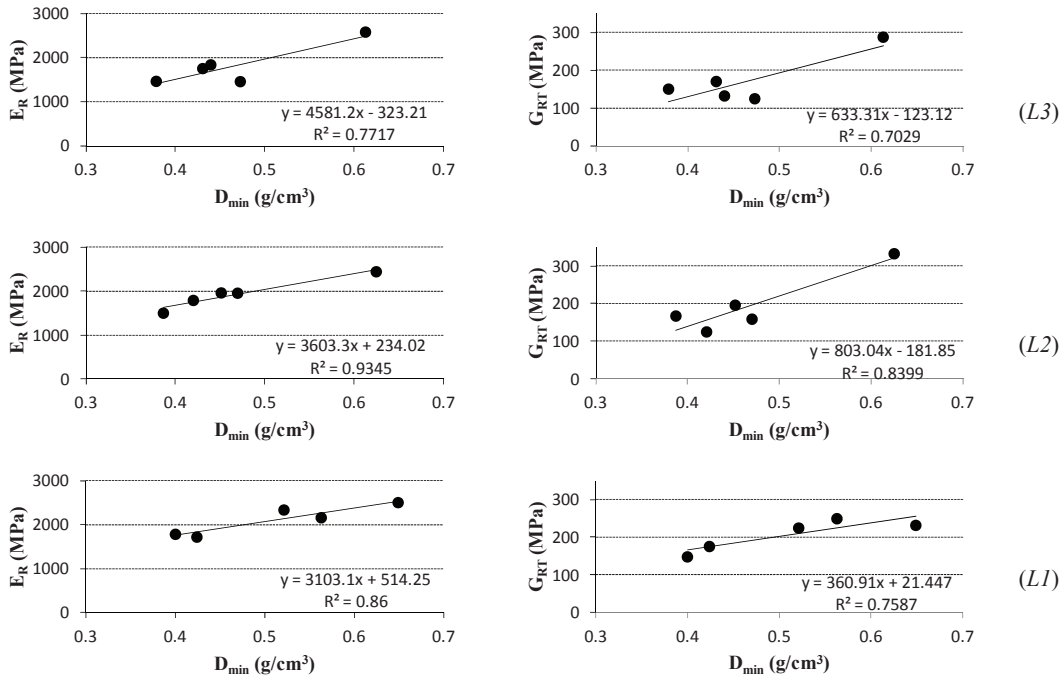
Figure 33: Linear fitting between E_R or G_{RT} and D_{min}: all trees at R1 position.
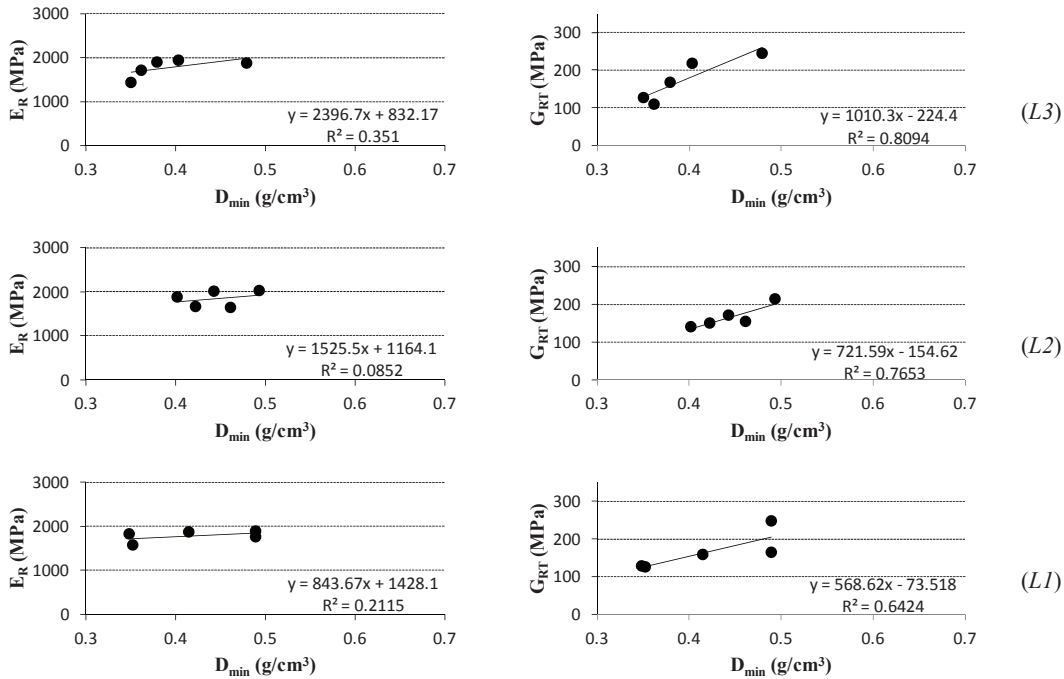
Figure 34: Linear fitting between E_R or G_{RT} and D_{min}: all trees at R2 position.
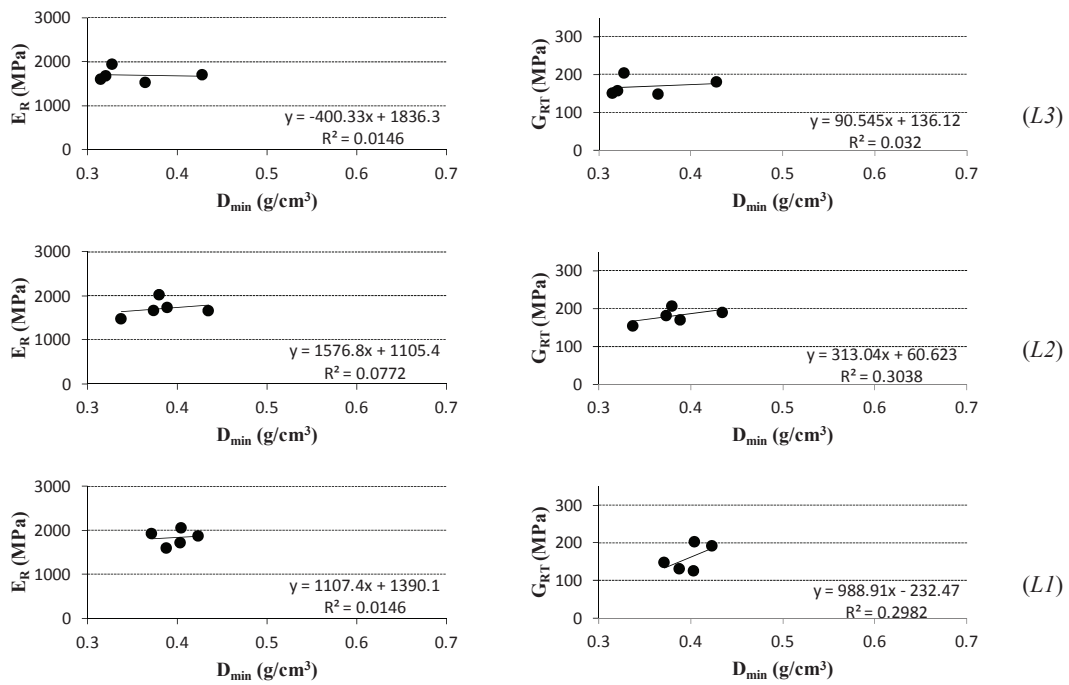
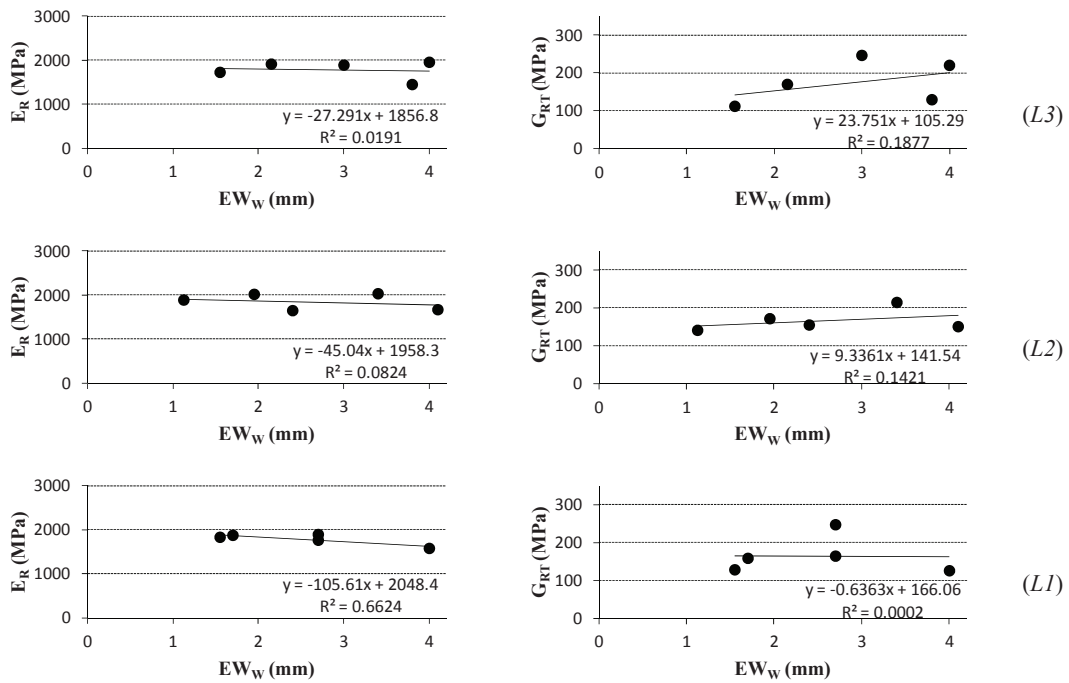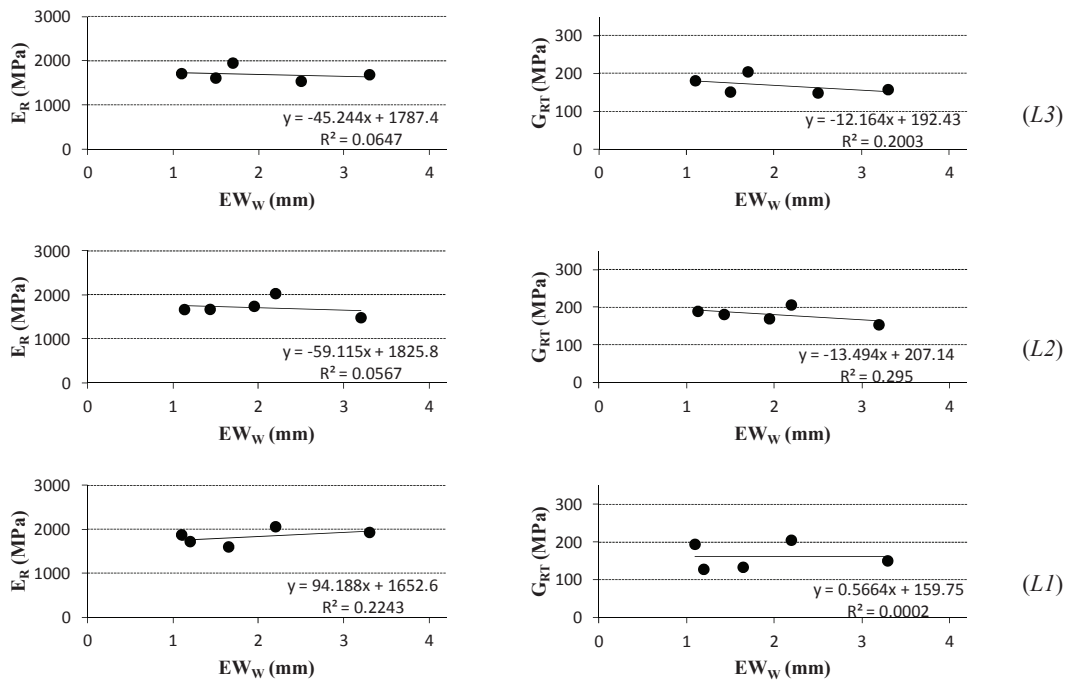Figure 35: Linear fitting between E_R or G_{RT} and D_{min}: all trees at R3 position.
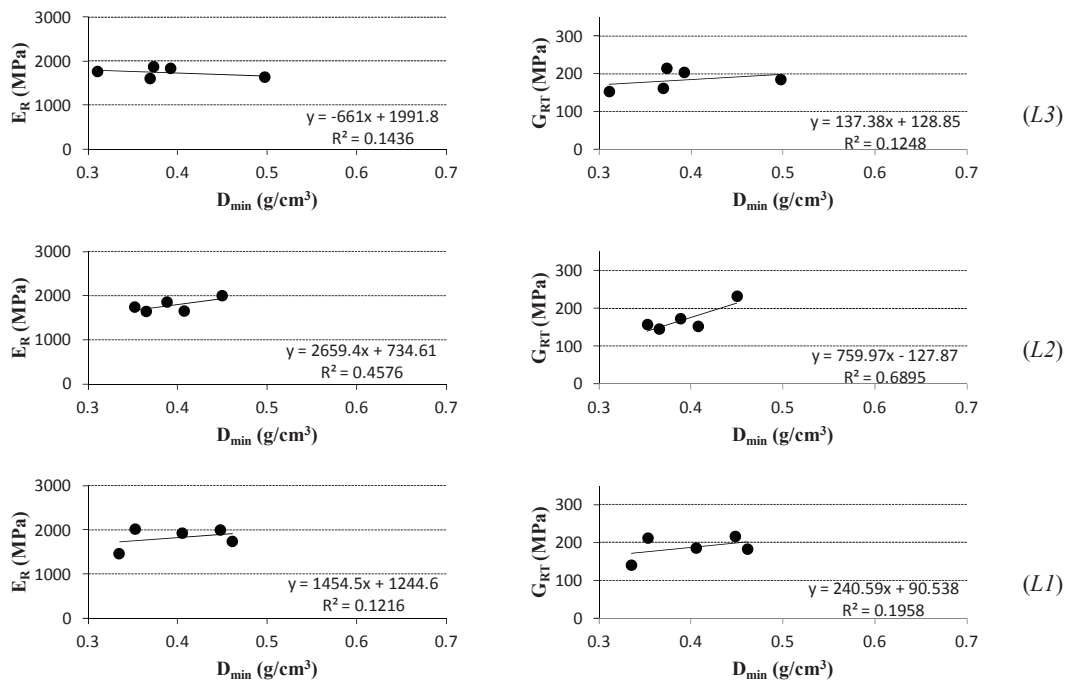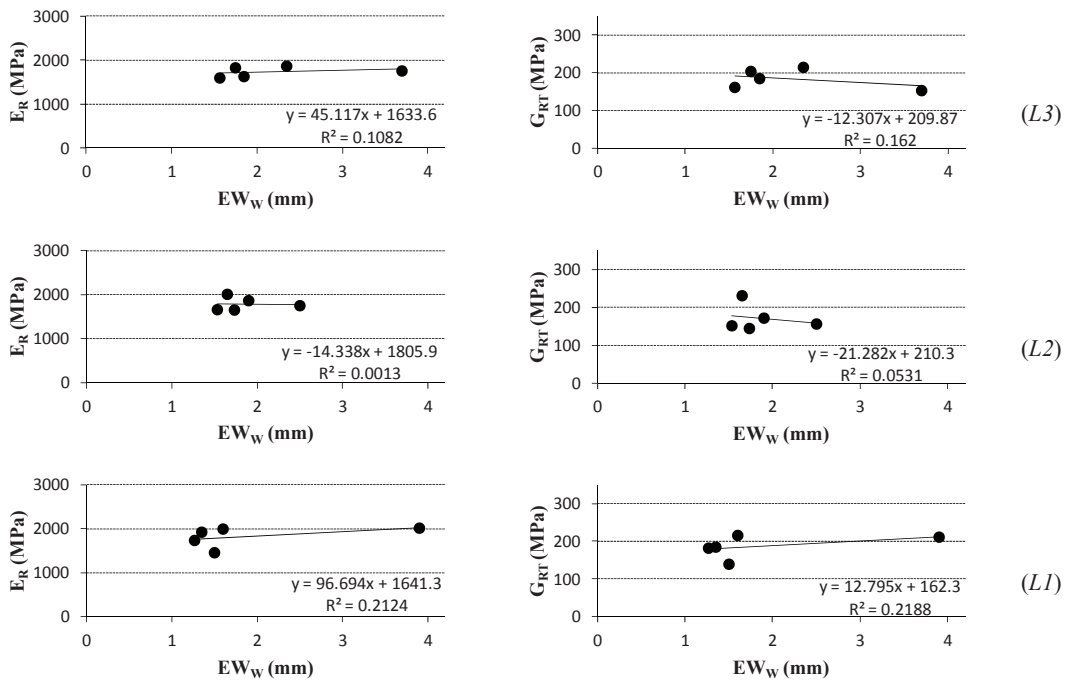

Figure 36: Linear fitting between E_R or G_{RT} and D_{min}: all trees at R4 position.
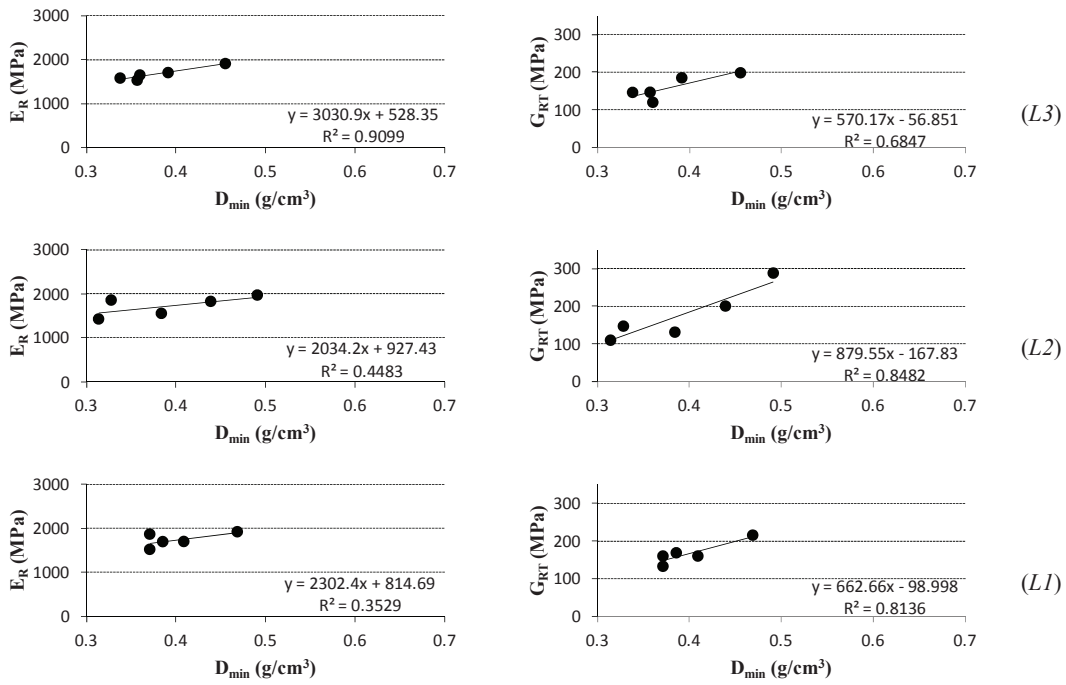
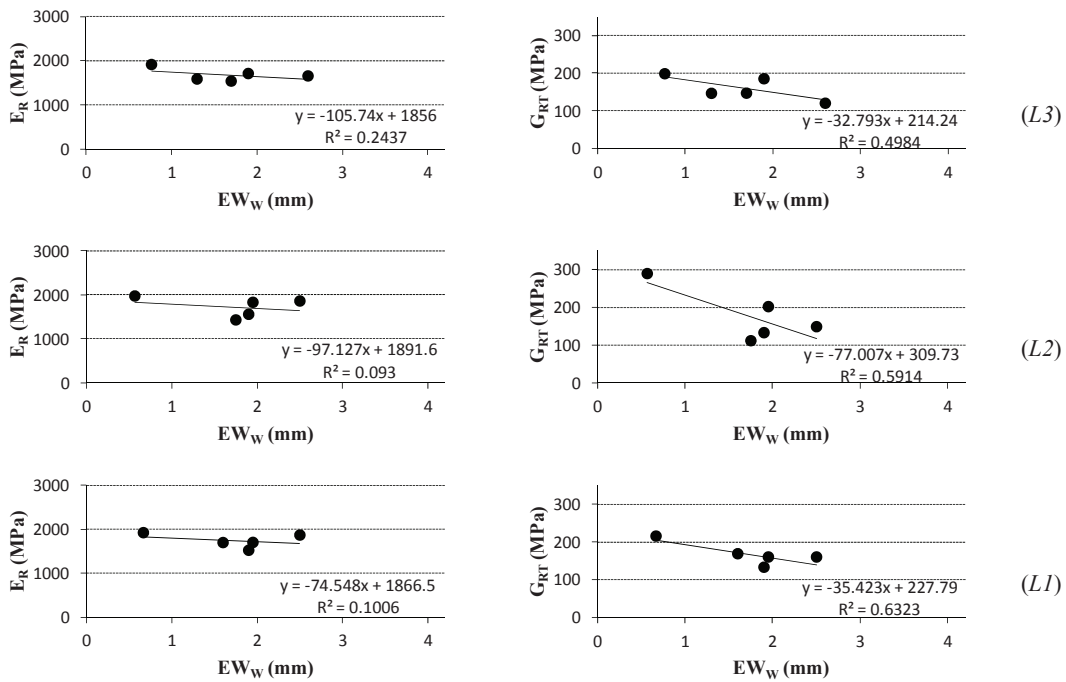Figure 37: Linear fitting between E_R or G_{RT} and D_{min}: all trees at R5 position.
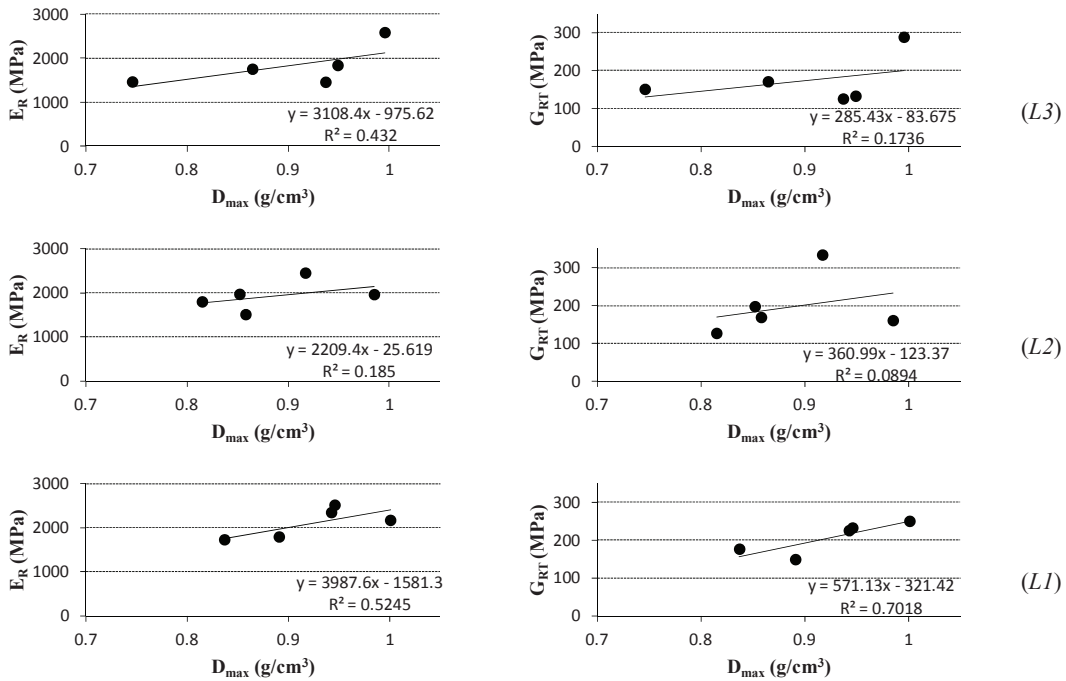
Figure 38: Linear fitting between E_R or G_{RT} and D_{max}: all trees at R1 position.
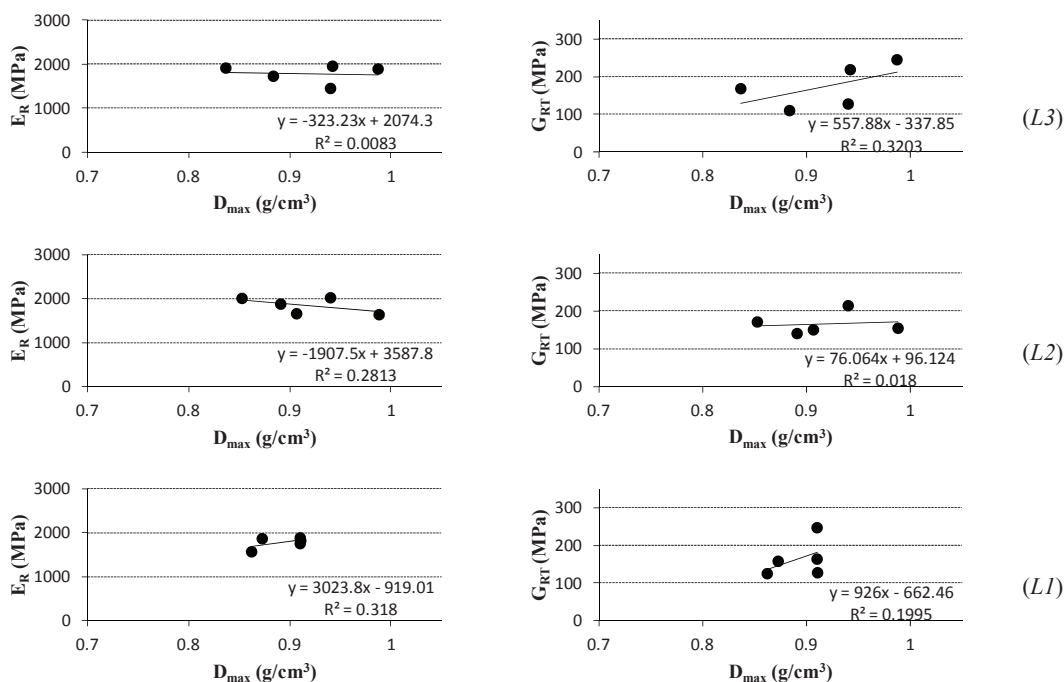
Figure 39: Linear fitting between E_R or G_{RT} and D_{max}: all trees at R2 position.
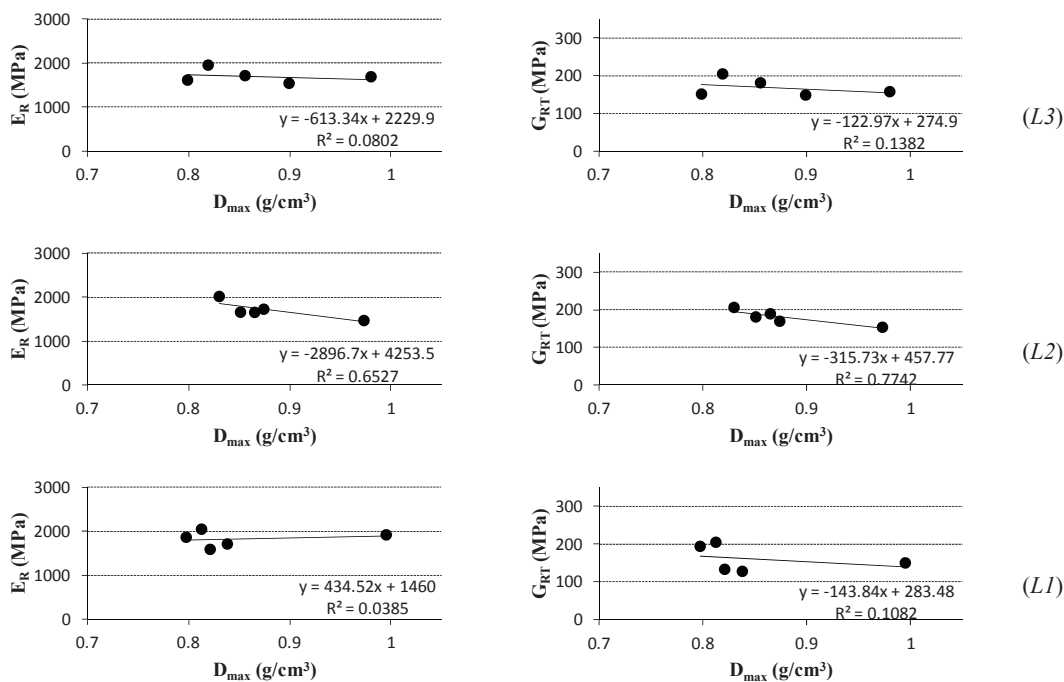
Figure 40: Linear fitting between E_R or G_{RT} and D_{max}: all trees at R3 position.
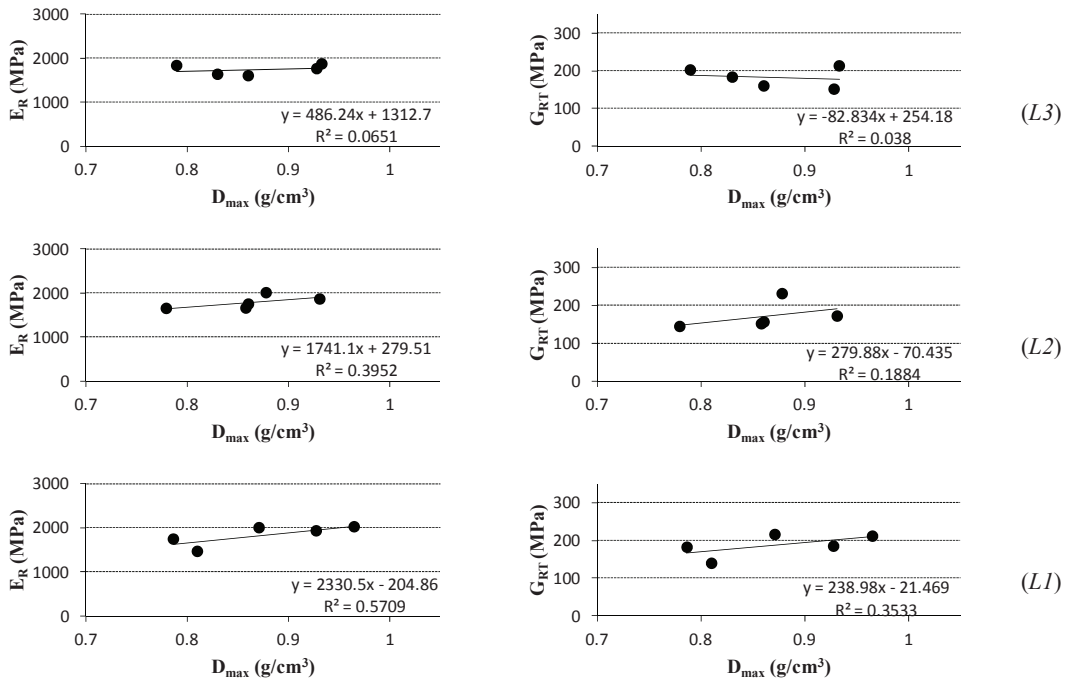
Figure 41: Linear fitting between E_R or G_{RT} and D_{max}: all trees at R4 position.
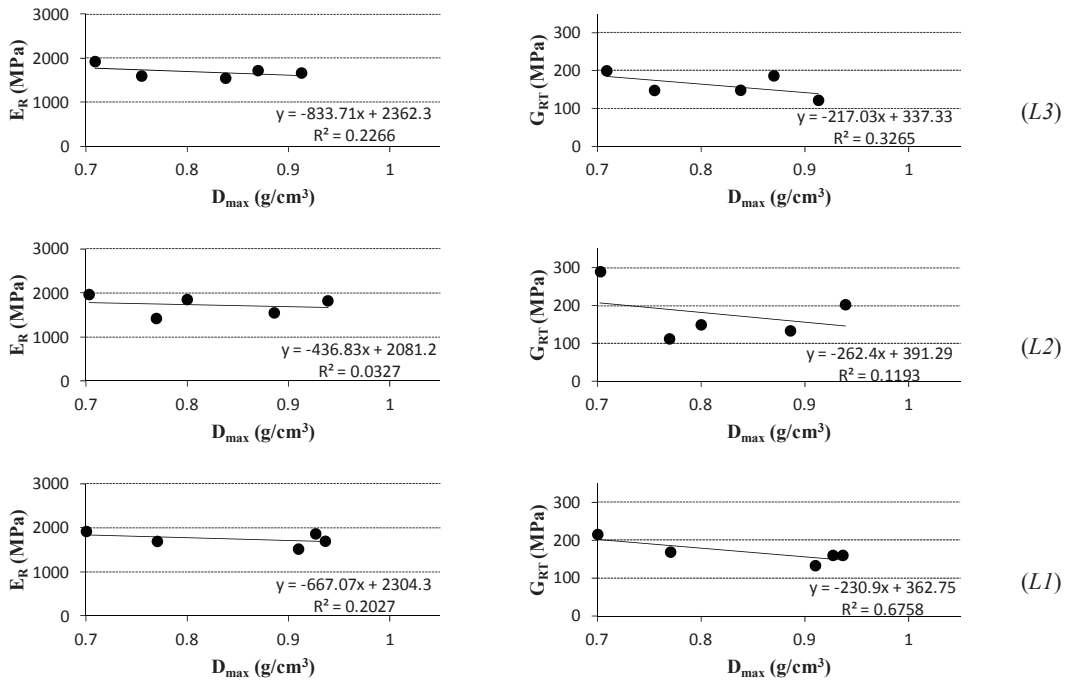
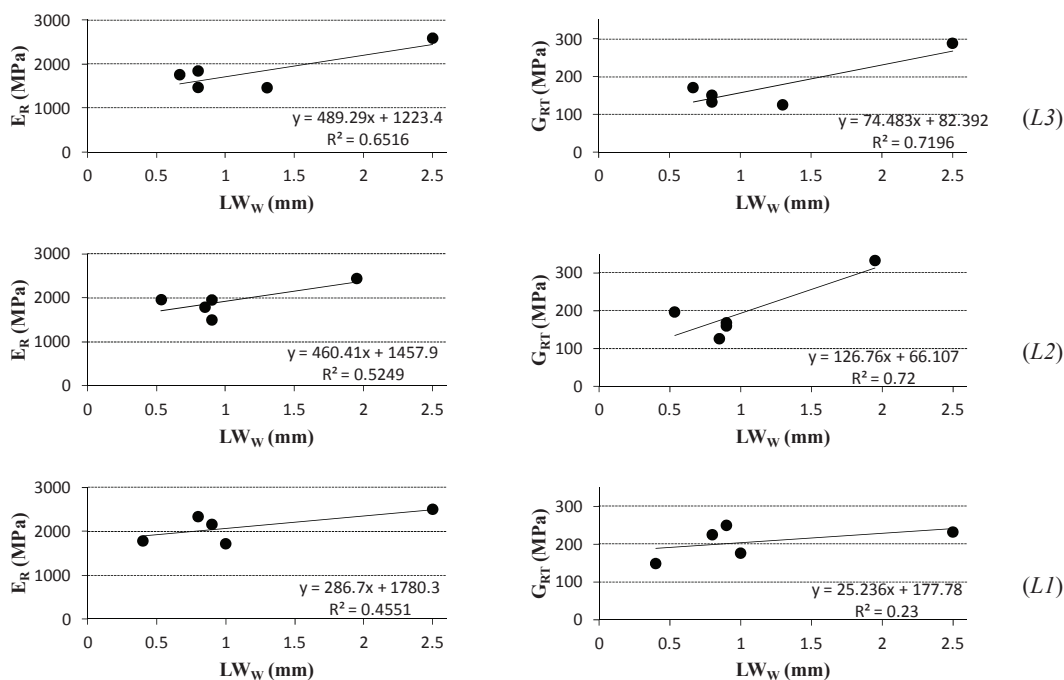Figure 42: Linear fitting between E_R or G_{RT} and D_{max}: all trees at R5 position.
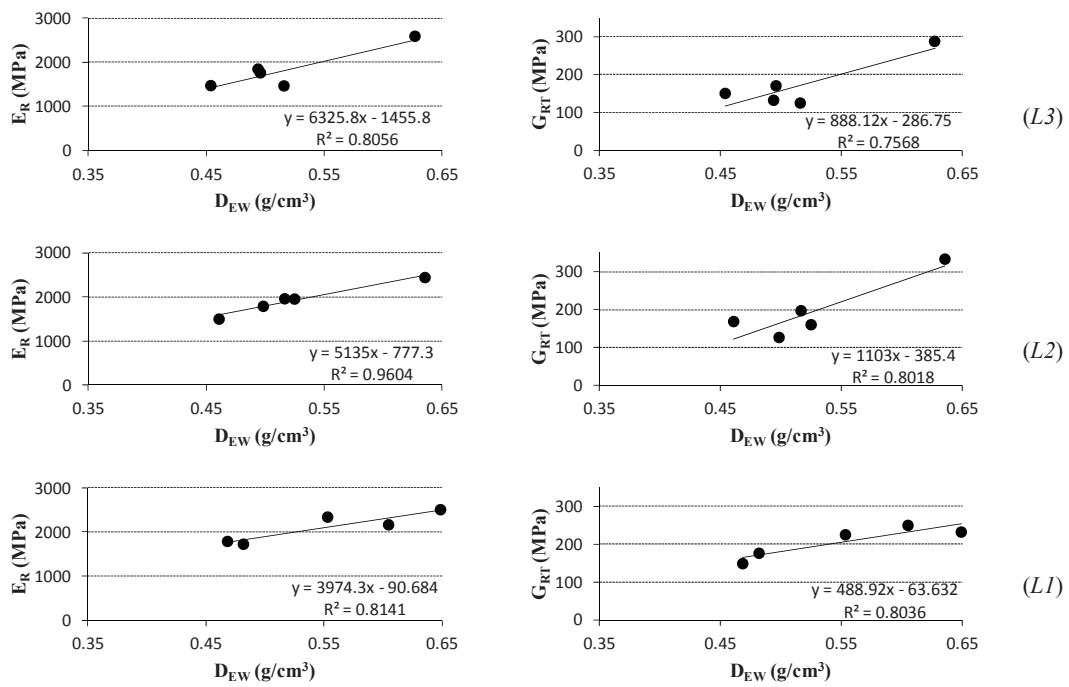
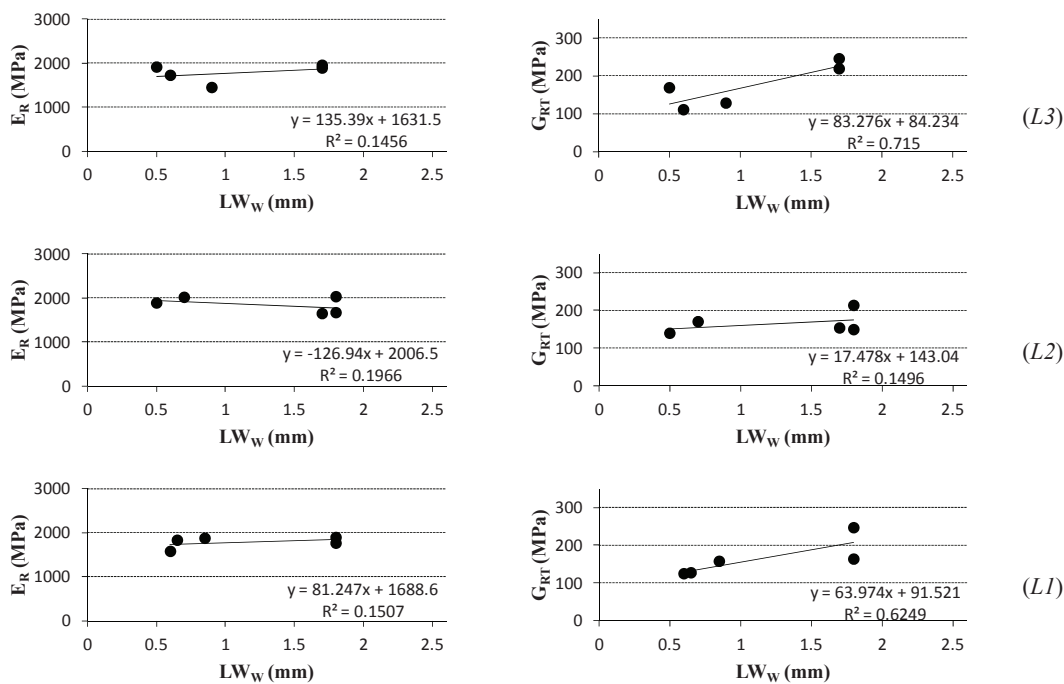Figure 43: Linear fitting between E_R or G_{RT} and D_{EW}: all trees at R1 position.
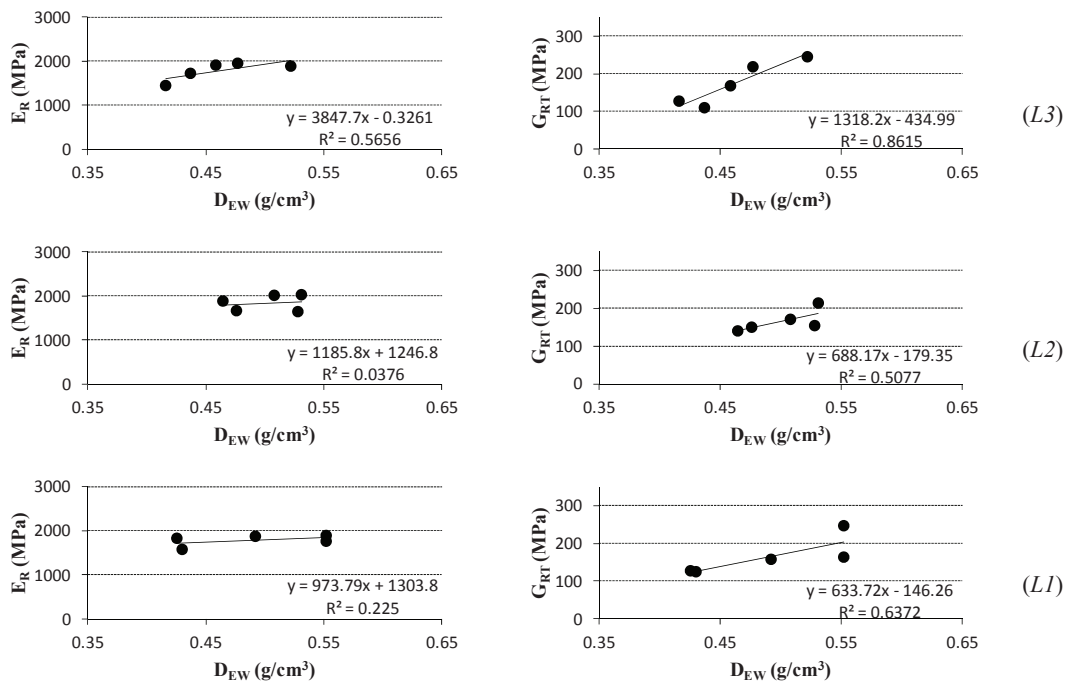
Figure 44: Linear fitting between E_R or G_{RT} and D_{EW}: all trees at R2 position.
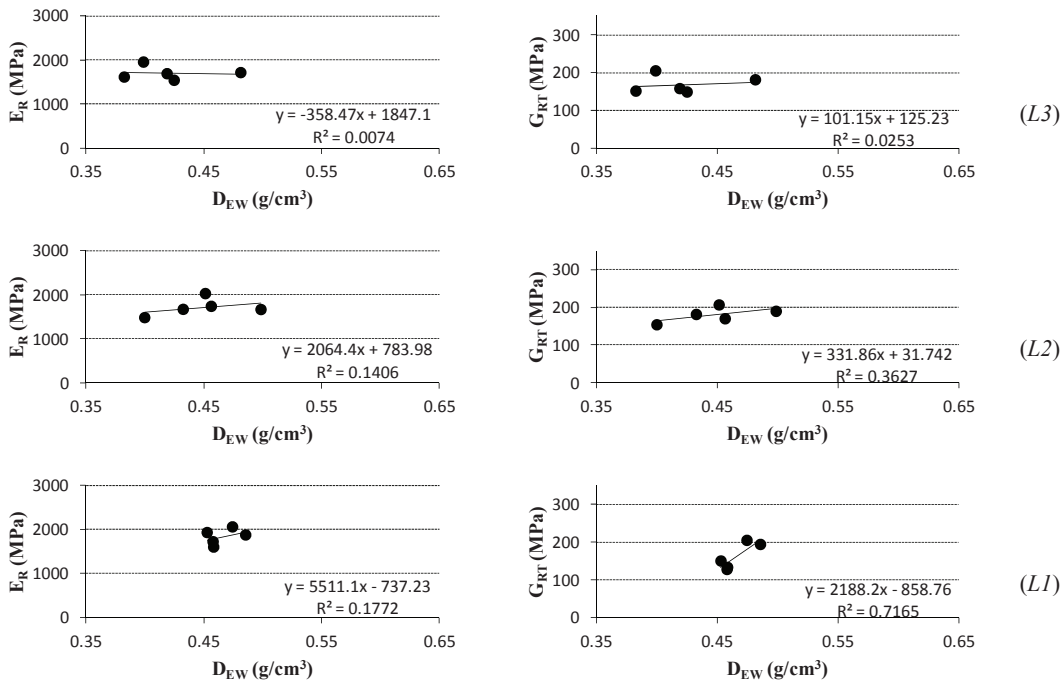
Figure 45: Linear fitting between E_R or G_{RT} and D_{EW}: all trees at R3 position.
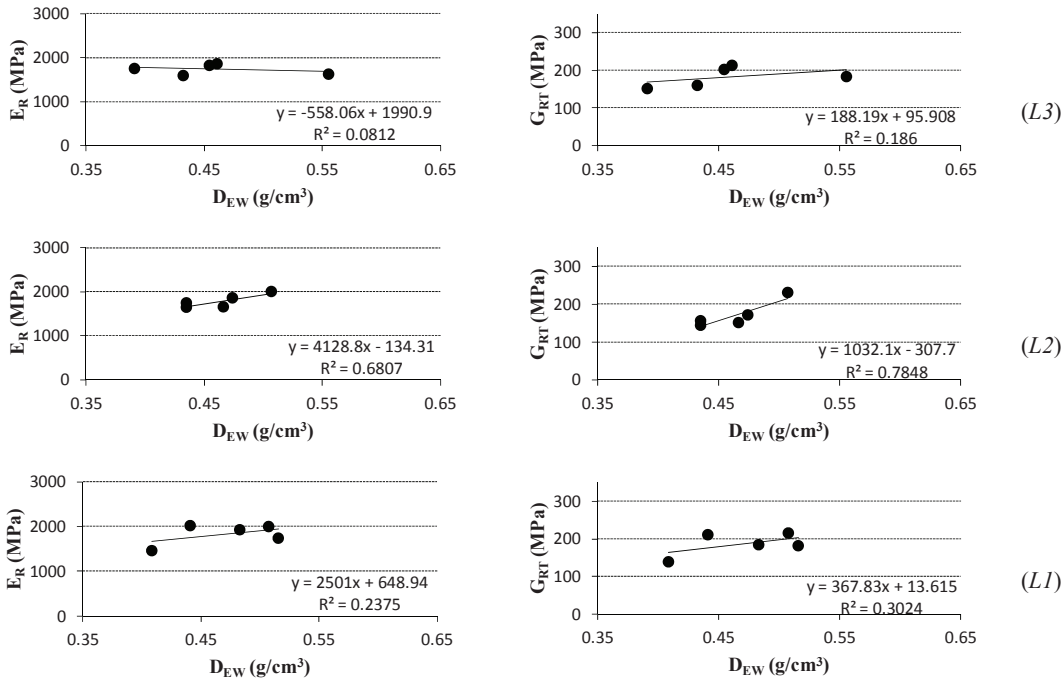
Figure 46: Linear fitting between E_R or G_{RT} and D_{EW}: all trees at R4 position.
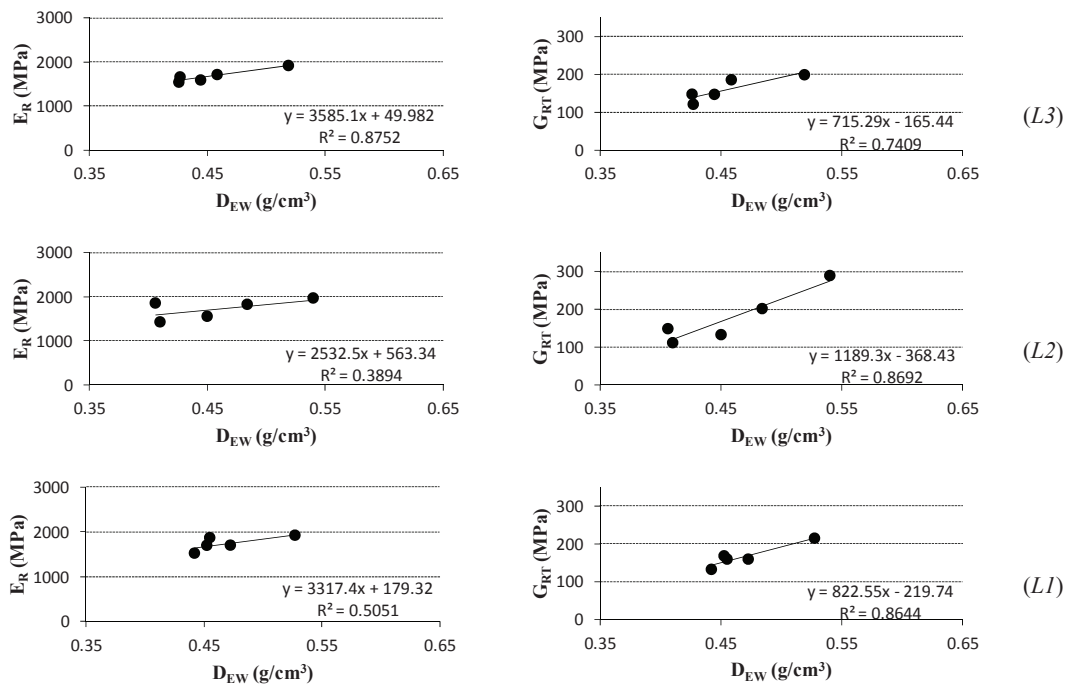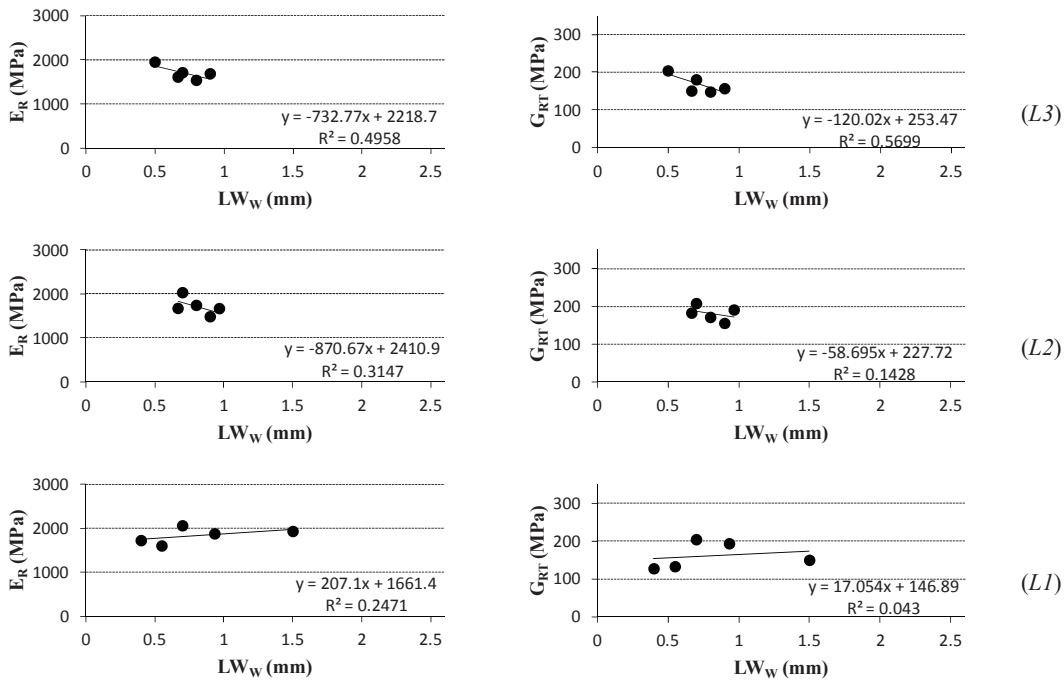
Figure 47: Linear fitting between E_R or G_{RT} and D_{EW}: all trees at R5 position.
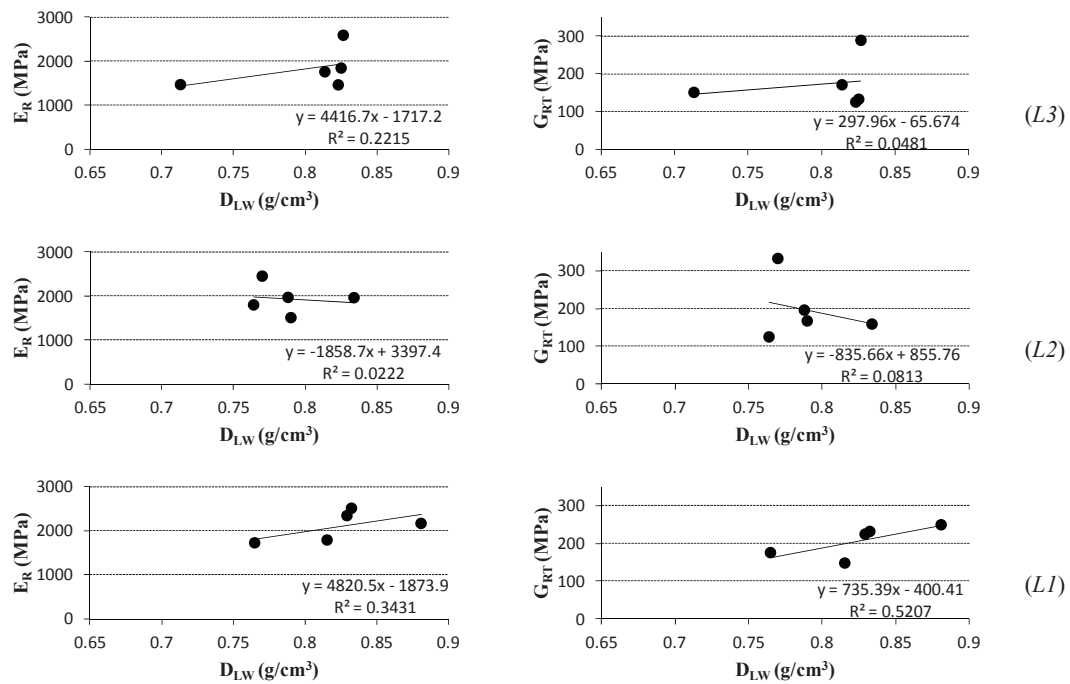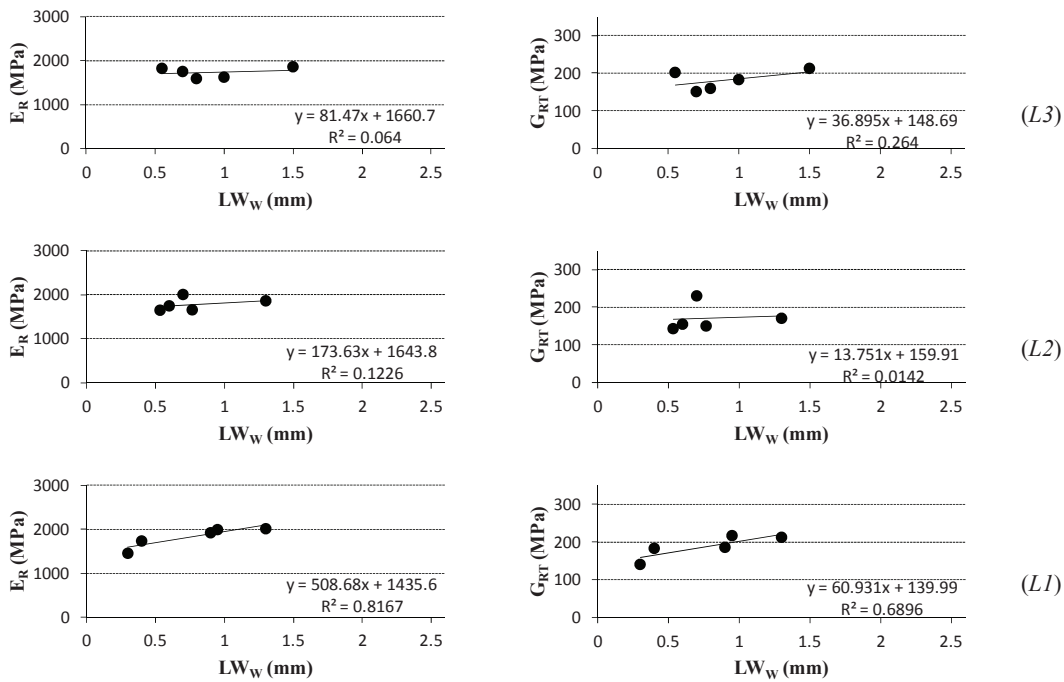

Figure 48: Linear fitting between E_R or G_{RT} and D_{LW}: all trees at R1 position.
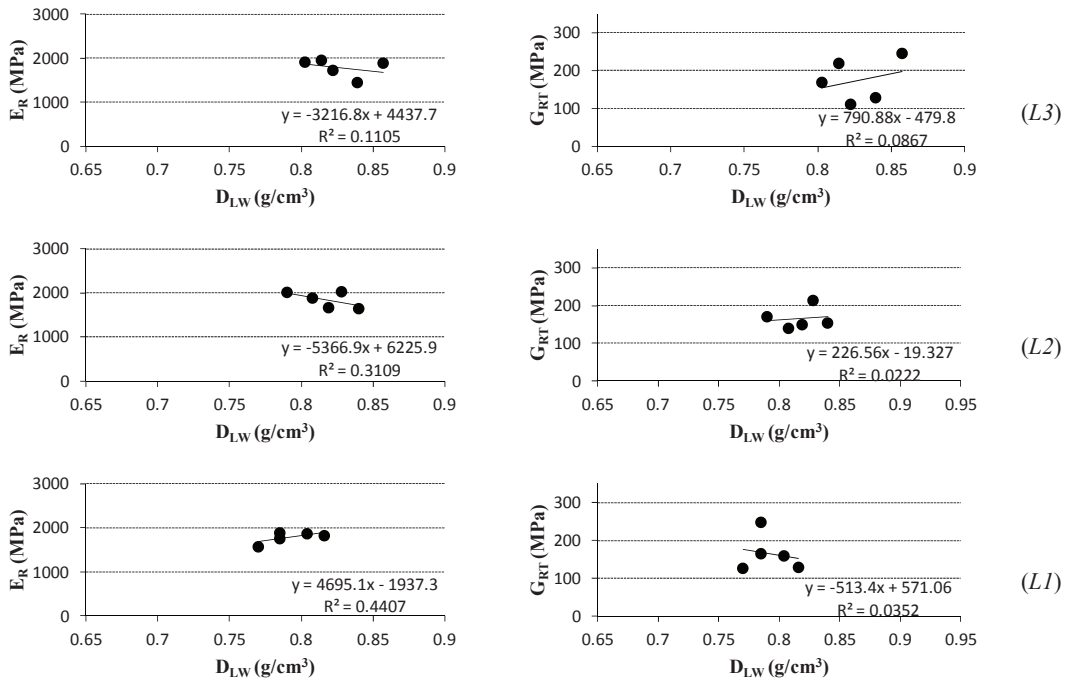
Figure 49: Linear fitting between E_R or G_{RT} and D_{LW}: all trees at R2 position.
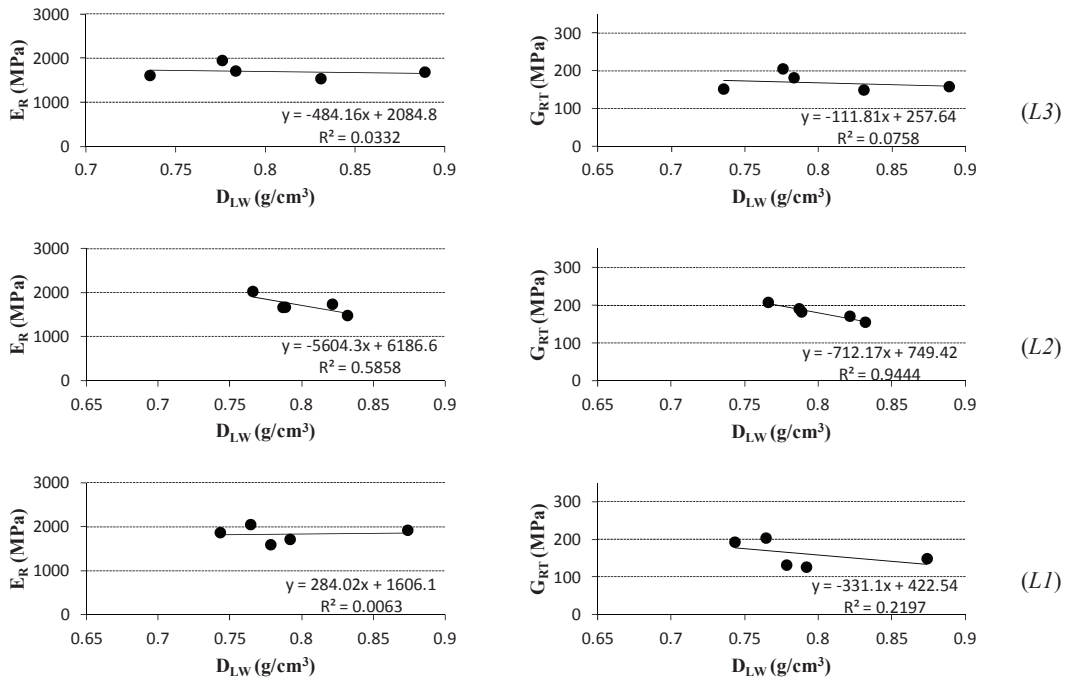
Figure 50: Linear fitting between E_R or G_{RT} and D_{LW}: all trees at R3 position.
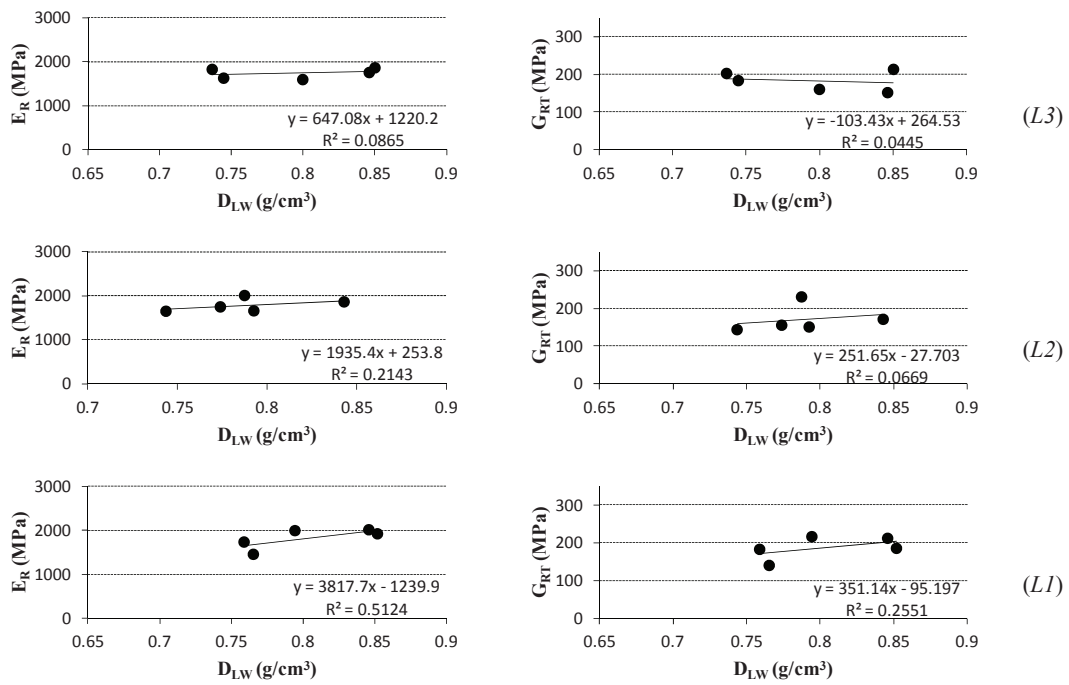
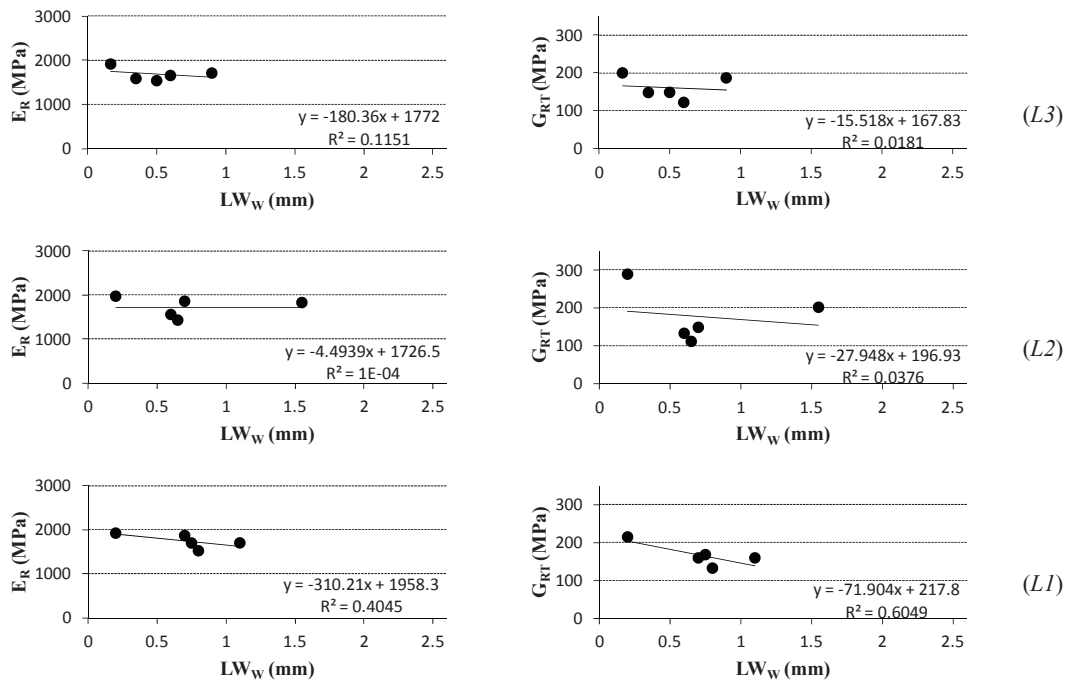Figure 51: Linear fitting between E_R or G_{RT} and D_{LW}: all trees at R4 position.
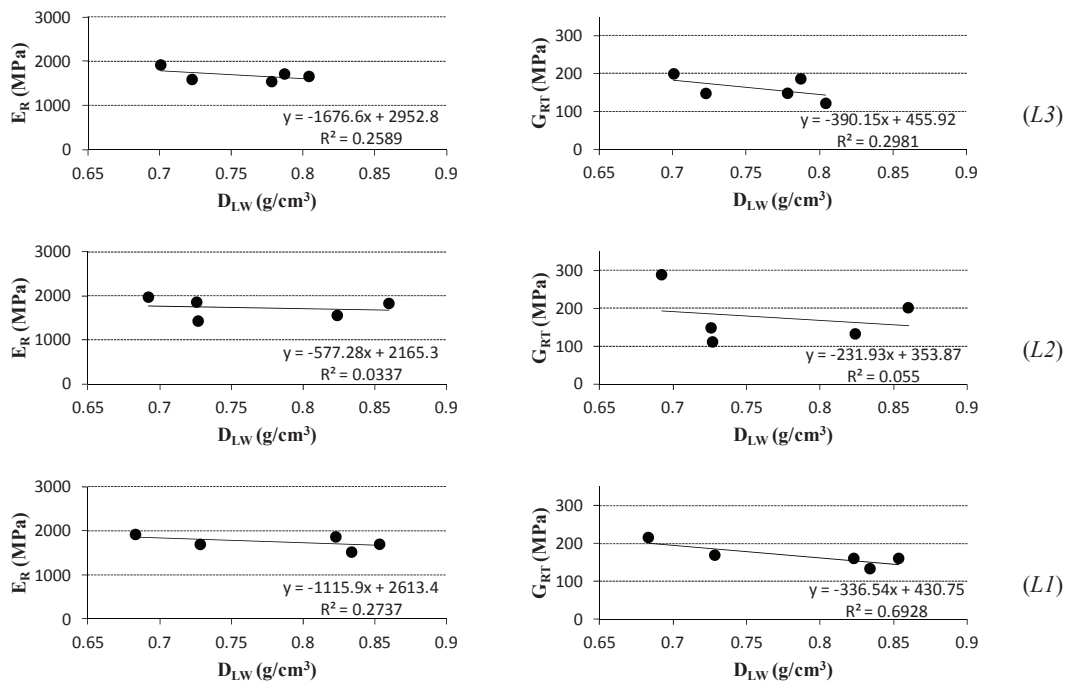
Figure 52: Linear fitting between E_R or G_{RT} and D_{LW}: all trees at R5 position.
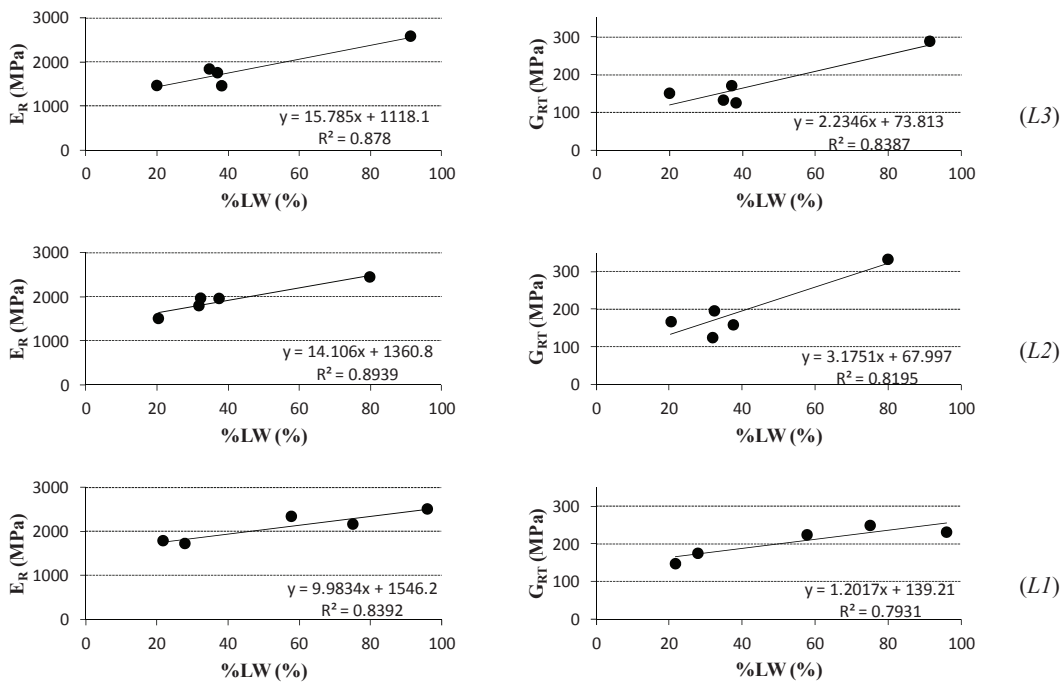
Figure 53: Linear fitting between E_R or G_{RT} and $\%LW$: all trees at R1 position.
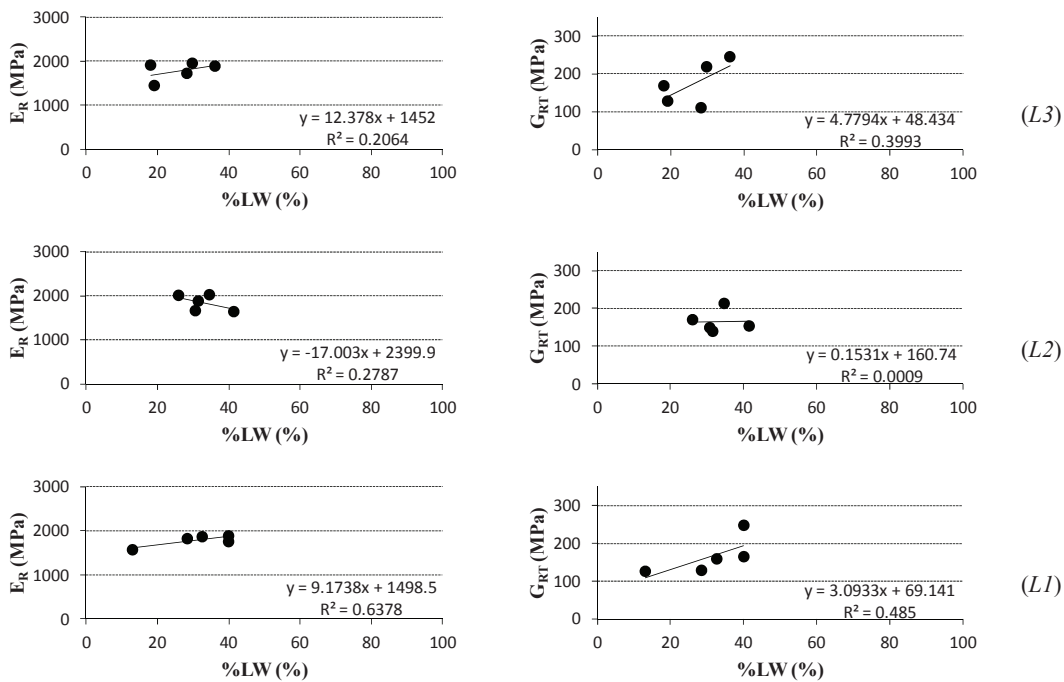
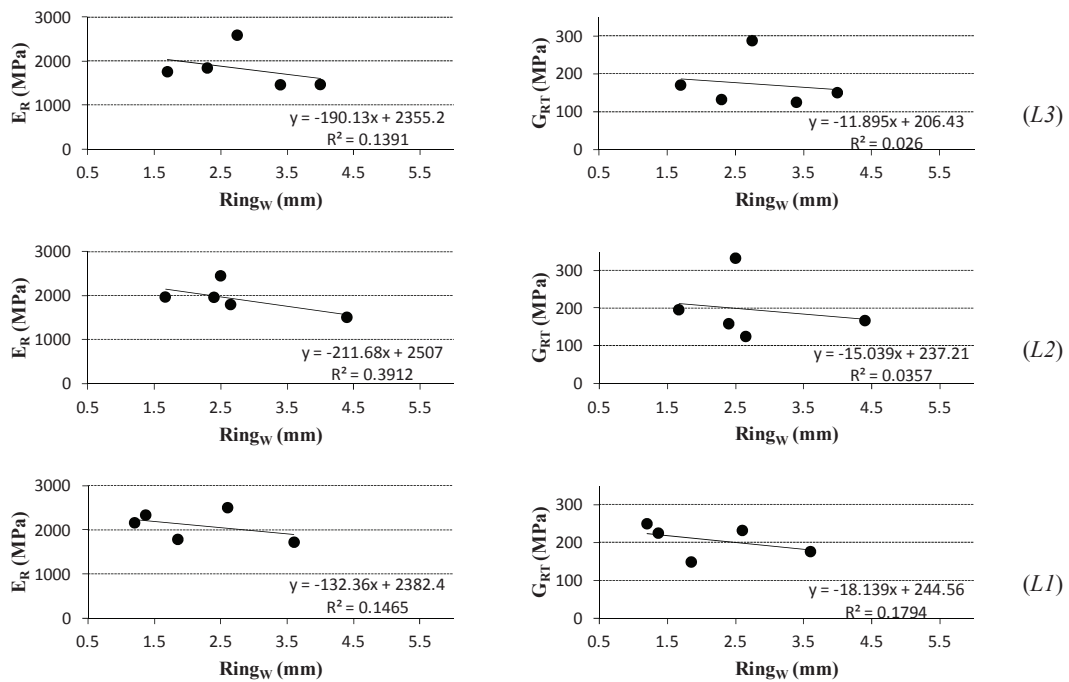Figure 54: Linear fitting between E_R or G_{RT} and $\%LW$: all trees at R2 position.
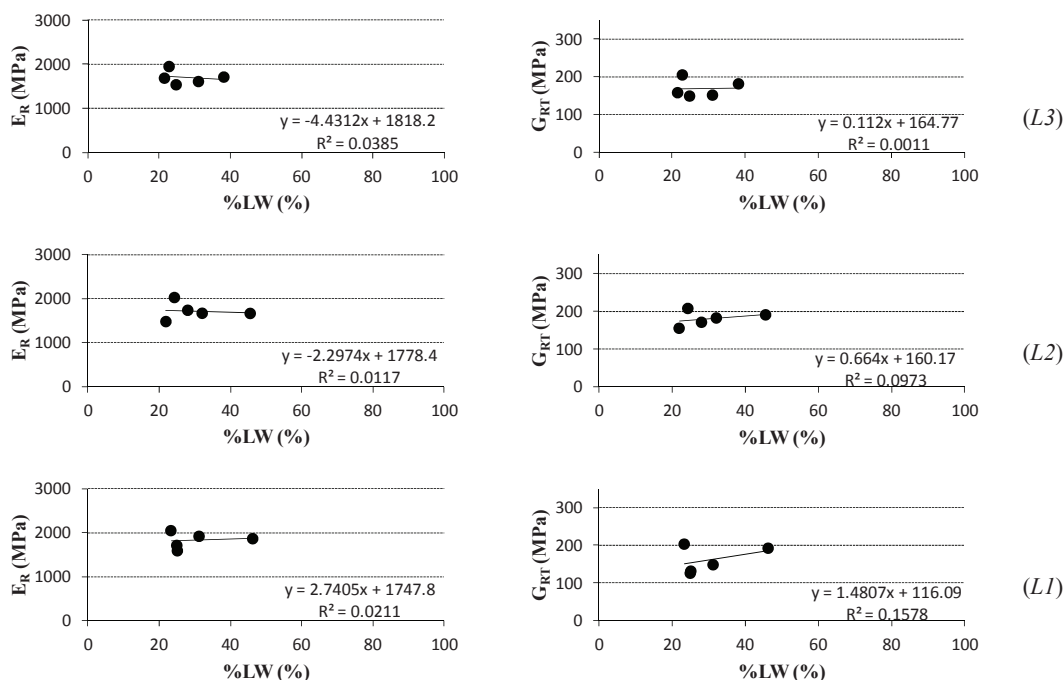
Figure 55: Linear fitting between E_R or G_{RT} and $\%LW$: all trees at R3 position.
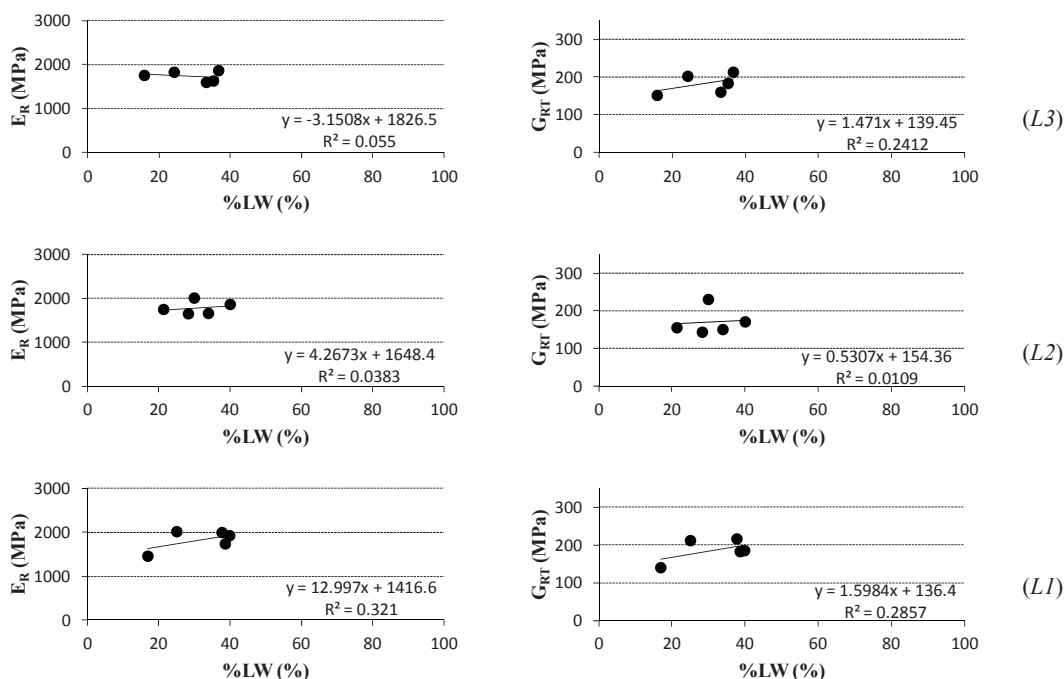
Figure 56: Linear fitting between E_R or G_{RT} and $\%LW$: all trees at R4 position.
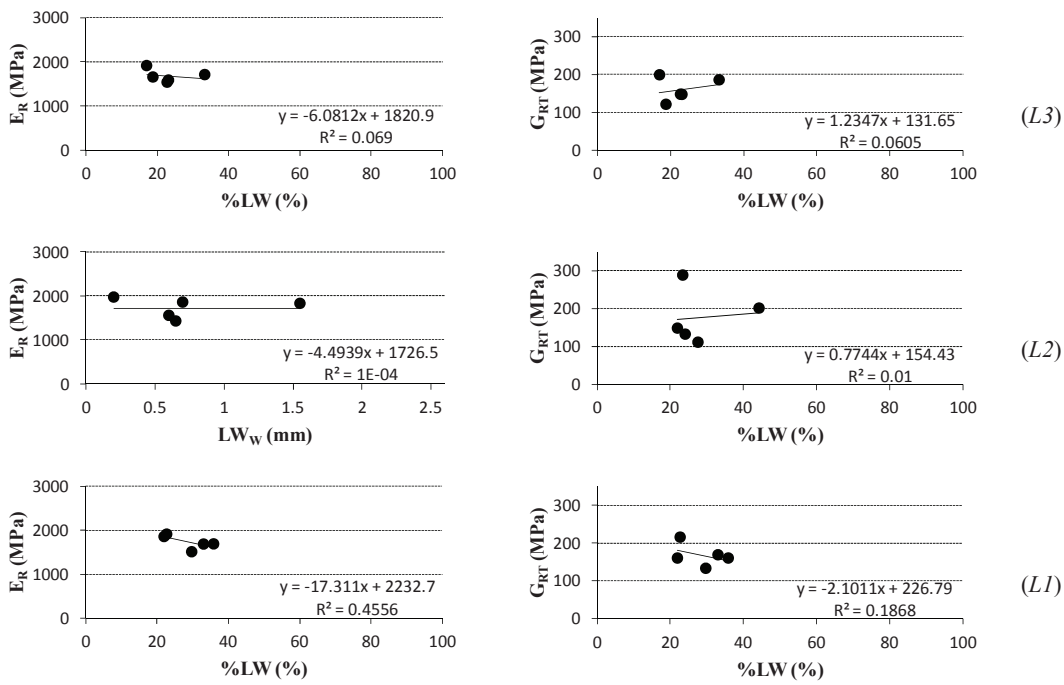
Figure 57: Linear fitting between E_R or G_{RT} and $\%LW$: all trees at R5 position.
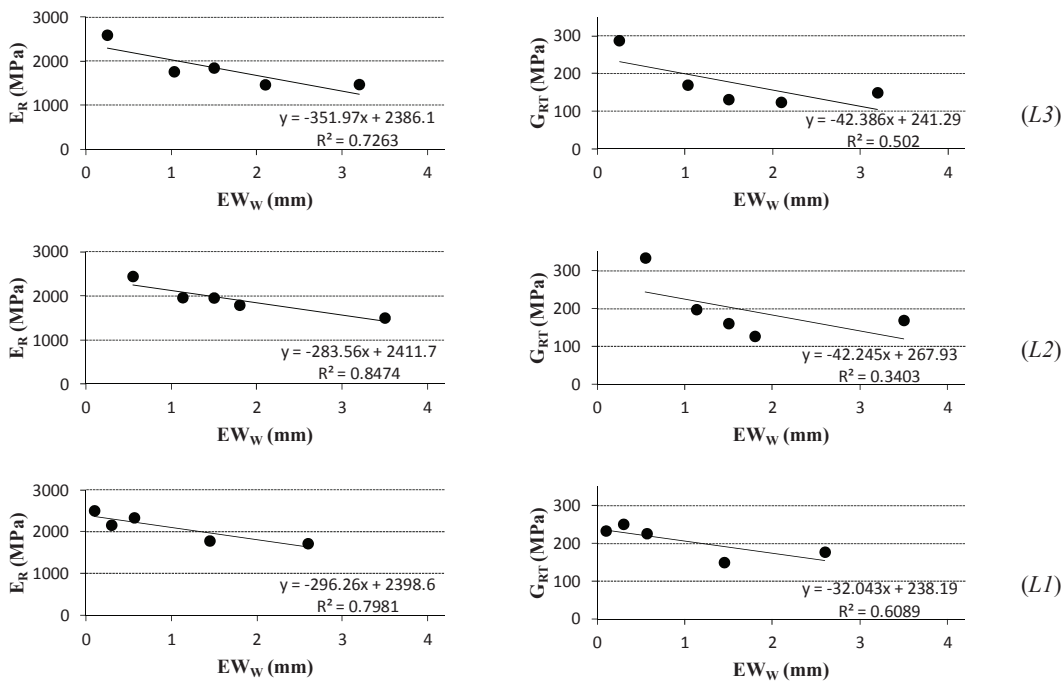
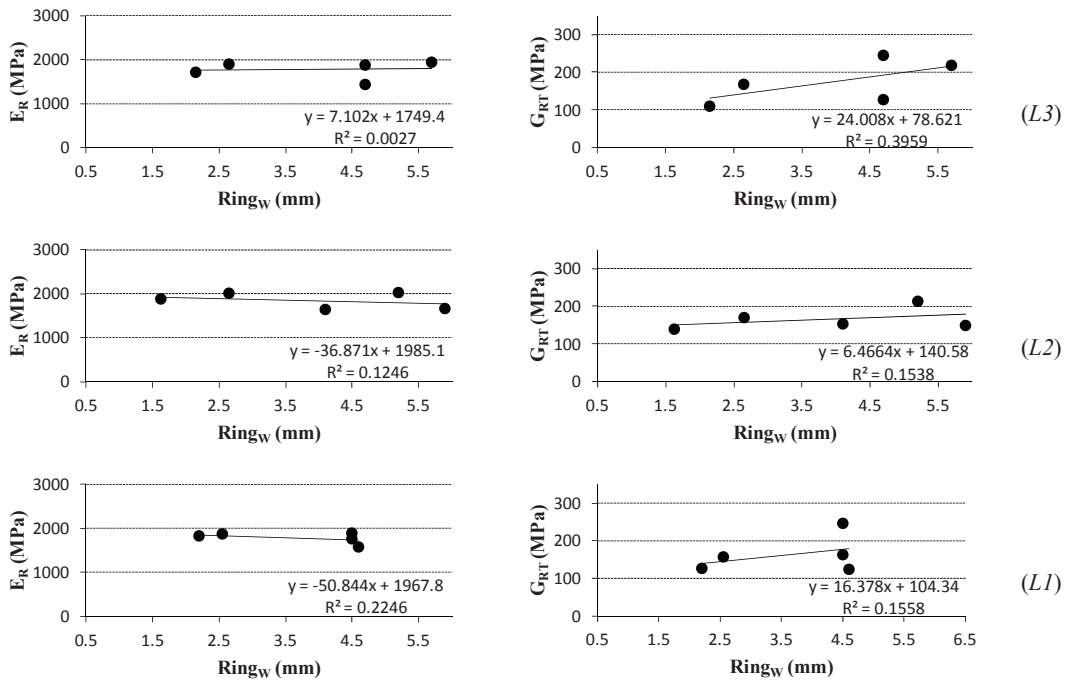Figure 58: Linear fitting between E_R or G_{RT} and EW_W: all trees at R1 position.

Figure 59: Linear fitting between E_R or G_{RT} and EW_W: all trees at R2 position.
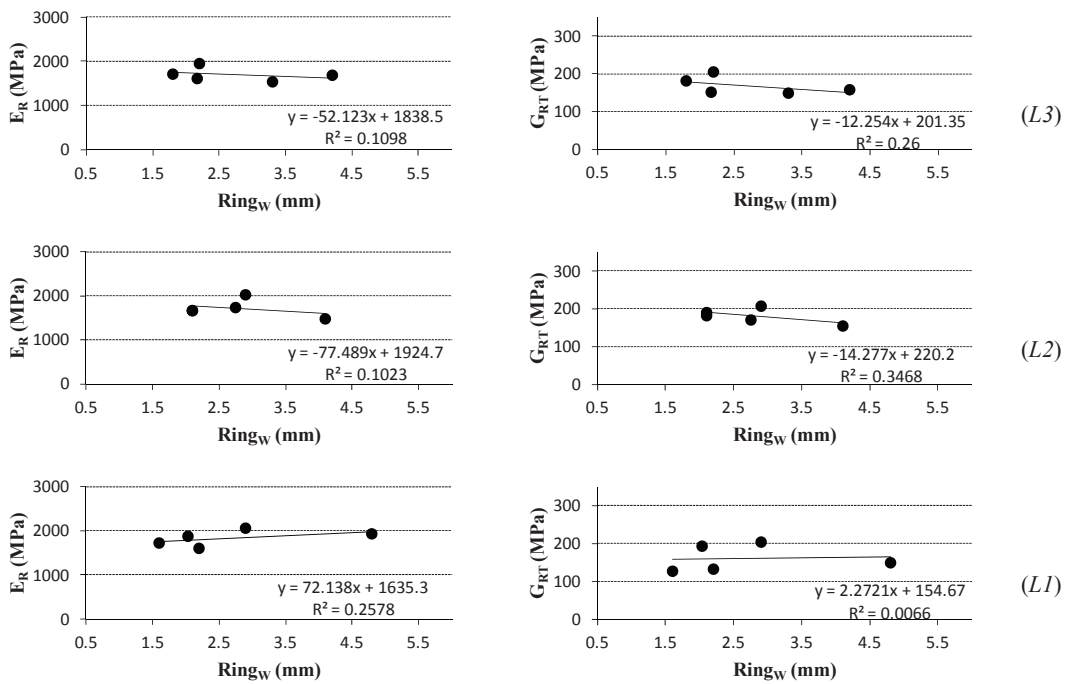

Figure 60: Linear fitting between E_R or G_{RT} and EW_W: all trees at R3 position.
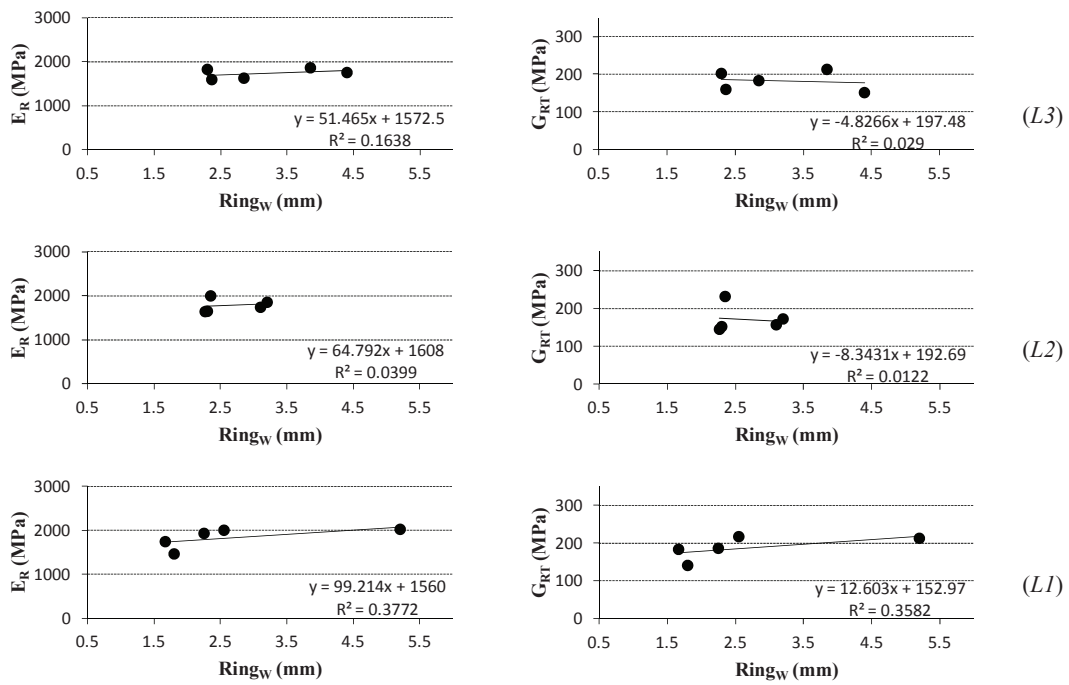
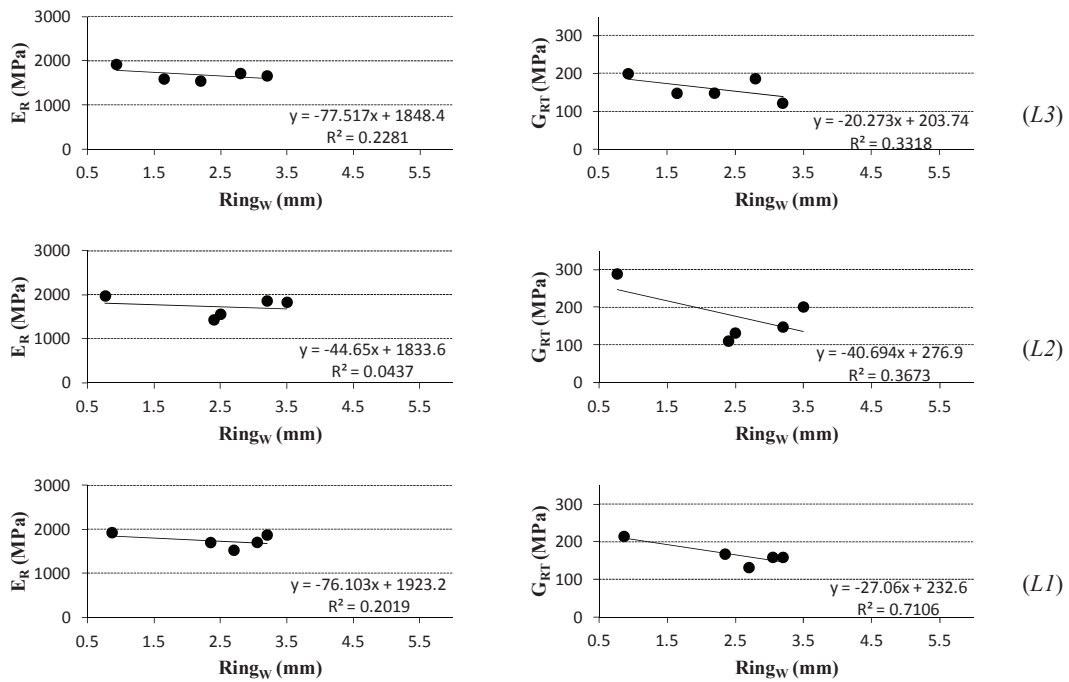Figure 61: Linear fitting between E_R or G_{RT} and EW_W: all trees at R4 position.

Figure 62: Linear fitting between E_R or G_{RT} and EW_W: all trees at R5 position.

Figure 63: Linear fitting between E_R or G_{RT} and LW_W: all trees at R1 position.

Figure 64: Linear fitting between E_R or G_{RT} and LW_W: all trees at R2 position.
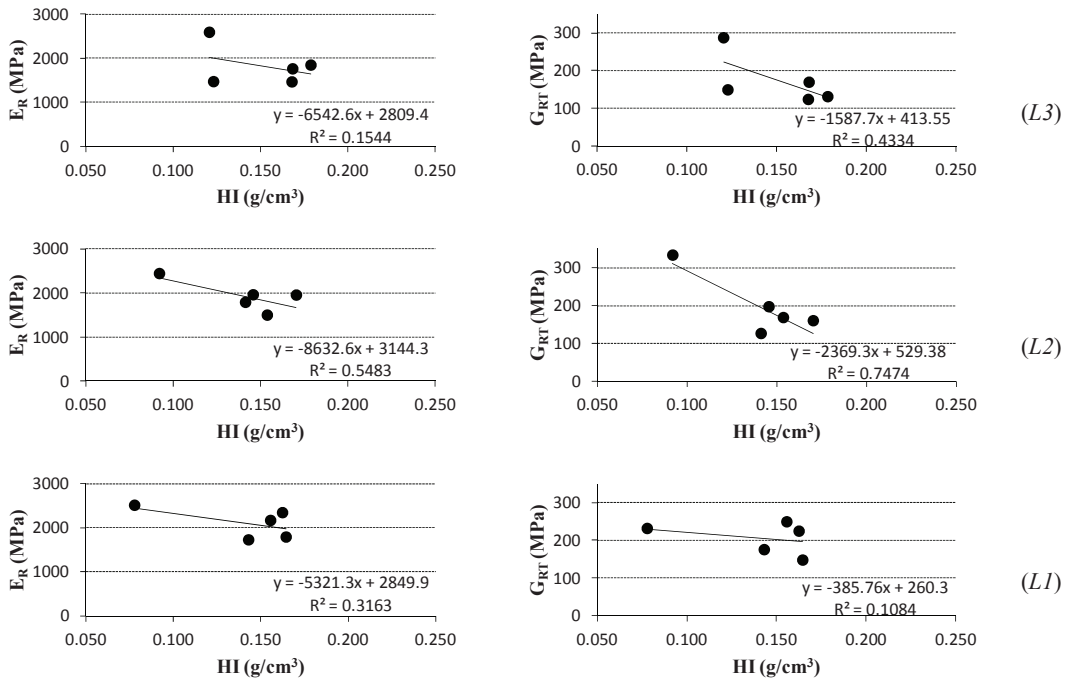
Figure 65: Linear fitting between E_R or G_{RT} and LW_W: all trees at R3 position.

Figure 66: Linear fitting between E_R or G_{RT} and LW_W: all trees at R4 position.

Figure 67: Linear fitting between E_R or G_{RT} and LW_W: all trees at R5 position.

Figure 68: Linear fitting between E_R or G_{RT} and $Ring_W$: all trees at R1 position.

Figure 69: Linear fitting between E_R or G_{RT} and $Ring_W$: all trees at R2 position.

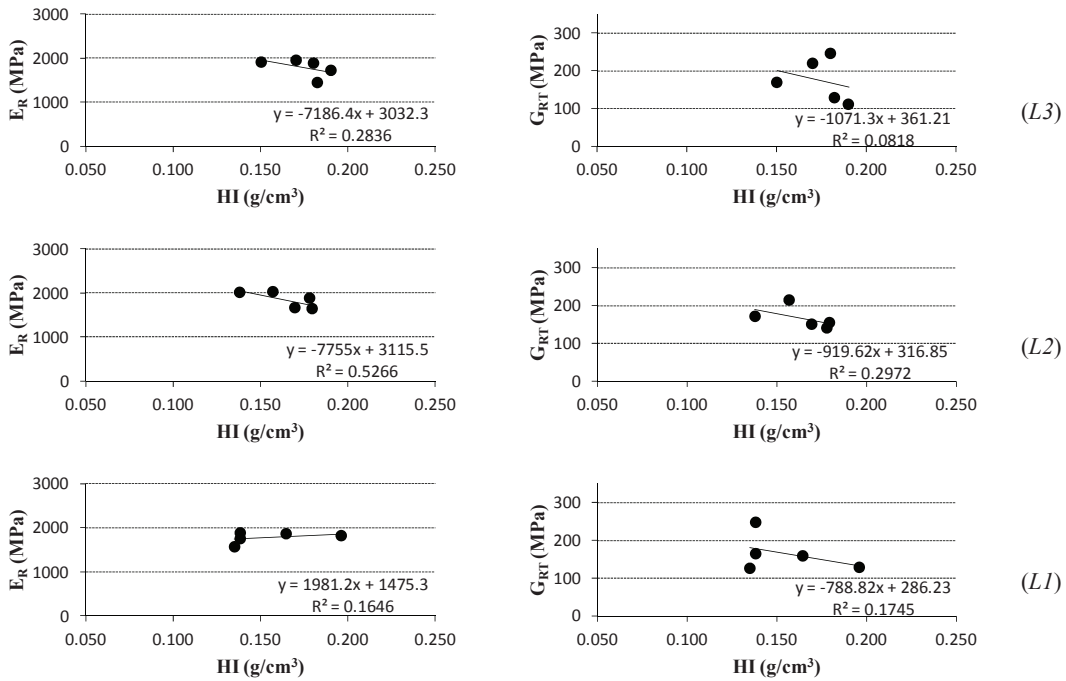Figure 70: Linear fitting between E_R or G_{RT} and $Ring_W$: all trees at R3 position.

Figure 71: Linear fitting between E_R or G_{RT} and $Ring_W$: all trees at R4 position.

Figure 72: Linear fitting between E_R or G_{RT} and $Ring_W$: all trees at R5 position.

Figure 73: Linear fitting between E_R or G_{RT} and HI: all trees at R1 position.

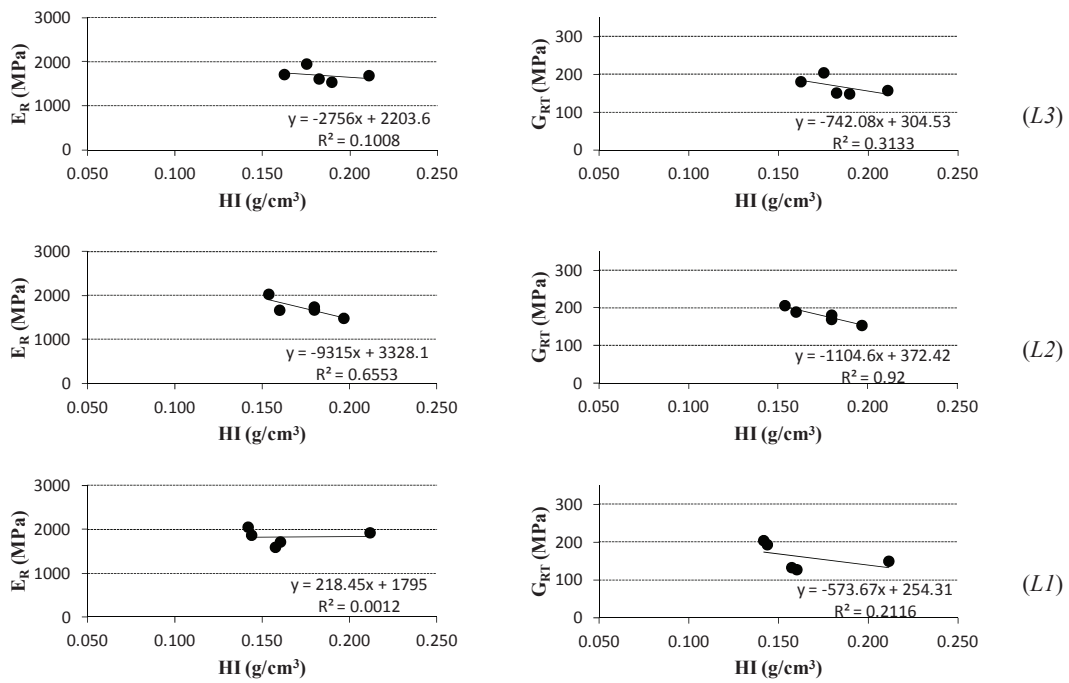Figure 74: Linear fitting between E_R or G_{RT} and HI: all trees at R2 position.

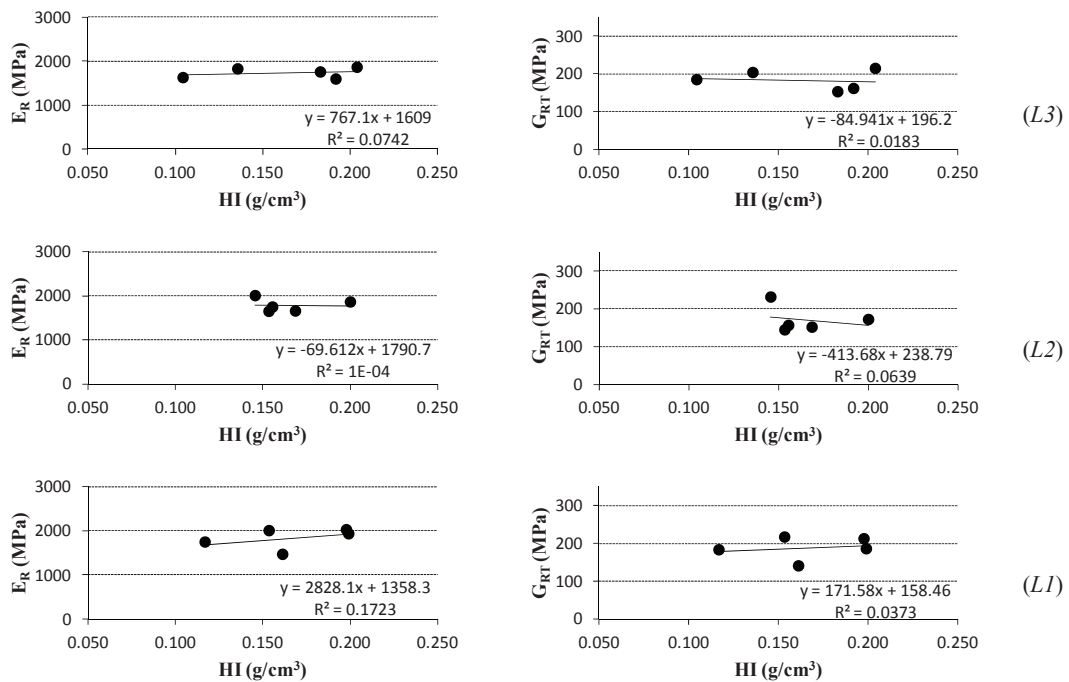Figure 75: Linear fitting between E_R or G_{RT} and HI: all trees at R3 position.

Figure 76: Linear fitting between E_R or G_{RT} and HI: all trees at R4 position.
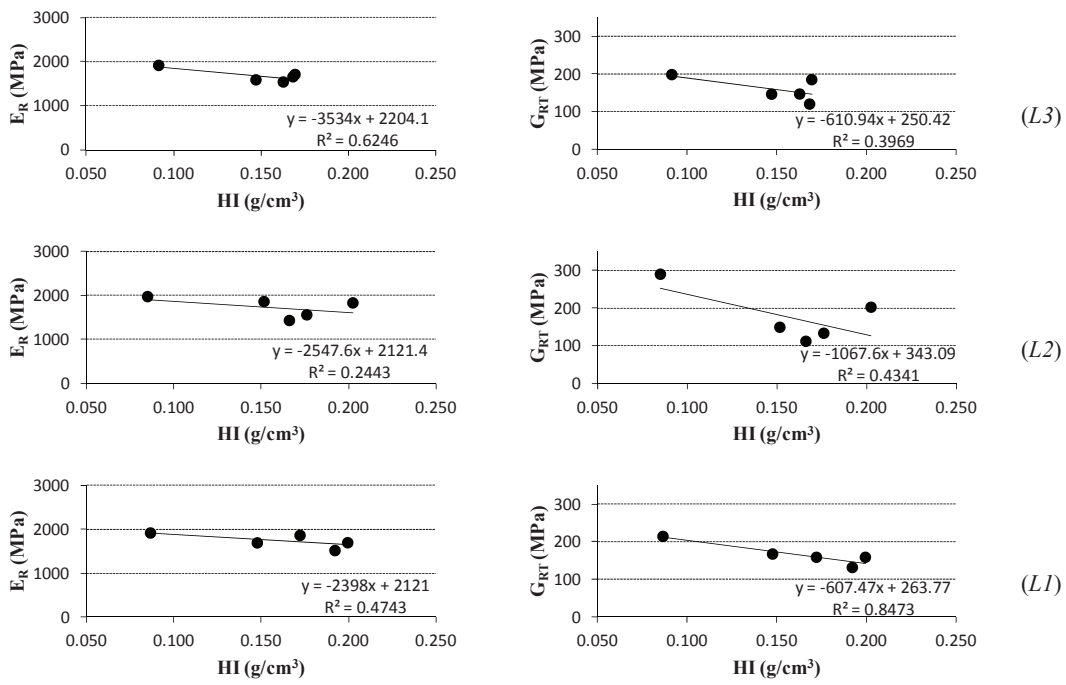
Figure 77: Linear fitting between E_R or G_{RT} and HI: all trees at R5 position.